Newcastle University

Finite element modelling of cell mechanics and cell-material interactions

A thesis submitted to the Faculty of Science, Agriculture and

Engineering for the Degree of

Doctor of Philosophy

by

Wenjian Yang

School of Engineering

Newcastle upon Tyne

November, 2020

To my family and my wife, Shuai Yu, for their support and unconditional love.

Abstract

Understanding cell mechanics subjected to external stimuli is important to design microniche to direct cell migration, differentiation and proliferation. However, previous models have not elucidated the mechanisms during the mechanotransduction process. Therefore, the main objective of this thesis is to develop different types of cell models including structure-based and continuum-based models to study the cell response during interactions with external stimuli. The structure-based cell model consisting of discrete cellular components was adopted to study the cellular responses during atomic force microscope (AFM) indentation tests, which revealed the significant contribution of stress fibres (SFs) to apparent modulus.

A continuum-based model has been developed to examine the effect of substrate thickness, lateral boundary and neighbouring cell on cell responses. In this model, the active behaviour of the cell was described by a SF formation model. Focal adhesion (FA) model driven by the SF contractility was implemented to account for the interactions with substrate. It has revealed that the thin layer of substrate enhanced the SF and FA formation. The SF concentration and integrin density decrease exponentially with increasing substrate thickness. Higher substrate stiffness attenuates the cell responses to thickness variation. Larger cell sizes promote the formation of SFs and enable deeper thickness sensing. Fixed lateral boundary of the substrate influences the SF and FA formation as well as the SF orientation. Soft substrate enables cells to sense the lateral displacement field created by another cell while stiff substrate hinders the cell-cell communication. Cell orients its SFs towards the neighbouring cell and could be influenced to polarize in this direction.

These predictions are consistent with experimental findings. Furthermore, the physics underpinned by the modelling has improved our understanding of the substrate boundary sensing and mechanics regulated cell-cell communications. This modelling framework could be potentially adopted for rational design of biomaterials in tissue engineering.

Acknowledgements

Throughout my PhD, I have met several people from whom I have received a great deal of support and assistance.

I would first like to give my sincere appreciation to my supervisor Dr.Jinju Chen for providing me the opportunity to pursue my dream in research. Her encouragement really motivated me when I am in frustration. I would also like to thank my co-supervisor, Prof. Jonathan Higgins, for sharing his ideas and invaluable knowledge.

I would like to thank Prof.Damien Lacroix and Prof. Lay Poh Tan for their useful discussions.

I would like to thank Jayathilake Pahala Gedara for sharing his knowledge and ideas when I am in the primary stage, motivating me to solve numerous research questions.

I would like to thank my friends, Yunyi Cao, Ma Luo, Xiaoyan Zhang, Rixia Zan and Lei Wang for enjoying the social life together. I would like to especially thank Ma Luo for his help during my thesis writing. Heartfelt thanks to all my friends who helped me during my days in Newcastle.

I would like to thank the Newcastle-Singapore Collaboration PhD scholarship for supporting my PhD.

In addition, I would like to thank my family, especially my parents-in-law and my wife, for their relentless support and care.

Contents

List of Tables

vi

List of Figures

Nomenclature and Abbreviations

Nomenclature

$\bar{k}_v$	Constant for the dissociation of contraction
$\dot{\varepsilon}_o$	Strain rate sensitivity parameter
$\bar{\eta}_{avg}$	Averaged fibre concentration along cell radius
$\bar{\bar{\xi}}_{avg}$	Averaged normalized integrin density along cell radius
$\bar{\sigma}_{avg}$	Averaged normalized fibre maximum principal stress along cell radius
$\bar{\sigma}_p$	Normalized stress fibre active principal stress
E_a	Apparent cell Young's modulus
E_{ctr}	Control cell apparent Young's modulus
E_s	Young's modulus of materials
R_c	Cell radius
R_p	Radius of spherical indenters
d_c	Cell-cell distance
k_b	Stress fibre dissociation rate
k_f	Stress fibre association rate
δ_{ij}	Kronecker delta
$\bar{\eta}$	Averaged stress fibre concentration
η_{max}	Maximum stress fibre concentration
$\bar{\bar{\xi}}_H$	Normalized high affinity integrin density

ξ_0	Total density of low and high affinity integrins
σ_{max}	Maximum stress allowed in the stress fibre
σ_o	Isometric stress fibre stress
σ_p	Stress fibre active maximum principal stress
Γ	Stress fibre variance
C	Stress fibre activation signal
R	Effective radius
d	Displacement of indenters or cells
$\boldsymbol{E}$	Green strain tensor
$\boldsymbol{F}$	Deformation gradient
$\boldsymbol{R}$	Rotation tensor
$\boldsymbol{S}$	Second *Piola-Kirchoff* stress
$\boldsymbol{U}$	Right Cauchy stretch tensor
$\boldsymbol{n}$	Surface normal
δ	Indentation depth
η	Stress fibre concentration
θ	Stress fibre activation signal decay constant
κ	Ratio of active stress to isometric stress
μ	Shear modulus of materials
ν	Poisson's ratio
ξ_H	High affinity integrin density

ϕ	Angle coordinate
σ	Cauchy stress

Abbreviations

2D,3D	Two-dimensional, three-dimensional
AFM	Atomic force microscopy
CSK	Cytoskeleton
ECM	Extracellular matrix
FA	Focal adhesion
FE, FEM	Finite element, Finite element method
RSS	Residual sum of squares
RVE	Representative volume element
SF	Stress fibre

Chapter 1. Introduction

Everyday thousands of surgeries are performed to repair or replace tissues that are injured in traumas and diseases. Tissue engineering tries to regenerate damaged tissues by using biomaterials scaffolds to guide the human cells to form new tissues (O'Brien, 2011). To facilitate the rational design of biomaterials scaffolds, it is essential to understand the interactions between cells and materials. Cells sense properties (physical, chemical or mechanical) of their immediate environment and interact with external materials to achieve a variety of physiological functions, including patterning tissues (Armstrong *et al.*, 2018), enabling damaged tissues to heal (Chantre *et al.*, 2019), or growing and differentiating (Wang *et al.*, 2012). In these processes, the internal properties of cells are changed by external stimuli. Therefore, elucidating the cell mechanics in cell-material interactions is critical and significant in biomechanical studies.

In two-dimensional cell culture, the cells are generally placed on a layer of substrate. Cues of materials (e.g. geometry and stiffness) are transduced by the cell-material adhesions into intracellular signals to regulate cell behaviours. The adhesion sites are formed at the cell-material interface (Curtis, 1964). In these cell-material focal adhesions (FAs), transmembrane receptors (e.g. integrins) are connected to ligands of materials, and they are linked to the contractile stress fibres (SFs) at the other side. Cells probe the mechanical properties of materials through adhesion sites by contracting the SFs. Signals will be transduced from adhesion sites to the cytoskeleton (CSK), which will reorganize itself corresponding to the stimuli and later transmit these signals to the nucleus through linker of nucleo-skeleton to CSK (LINC complex) (Lovett *et al.*, 2013), altering the nuclear properties such as nuclear shape (Lovett *et al.*, 2013), lamina compositions and chromatin organization (Swift *et al.*, 2013). The physical and mechanical properties of the substrate have been reported to influence the cell activities. For instance, the substrate stiffness has been reported to direct the cells into different lineages (Engler *et al.*, 2006). The thickness of the elastic substrate has been revealed to change the apparent stiffness that cells can sense (Lin *et al.*, 2010). Lateral boundaries of materials have been demonstrated to interrupt the fibre alignment in collagen matrix (Mohammadi *et al.*, 2014). The mechanical properties of the cells are modulated to adapt themselves to match the substrate stiffness (Solon *et al.*, 2007). However, there is a lack of studies about the

effect of the substrate geometry and stiffness on subcellular components behaviours. Additionally, the contributions of subcellular components to cell apparent stiffness have not been fully understood.

To investigate various aspects of cell-material interactions, considerable amount of experiment studies have been conducted to reveal the underlying mechanisms, however, single cell experiment does not offer a clear interpretation of cell-material interactions or substantial insight into the contributions of key biomechanical processes to cellular events. Therefore, computational models have been developed to better interpret the experimental results. Furthermore, computational models have also been developed to predict cellular processes such as cell contraction (De Santis *et al.*, 2011), migration (Ni and Chiang, 2007; Shenoy *et al.*, 2016), spreading (Nisenholz *et al.*, 2014) and CSK reorganisation (Ronan *et al.*, 2014) during interactions with materials. These computational models are mainly categorized into two types: structure-based and continuum-based models. The structure-based model deems the cellular components as discrete parts while the continuum-based model considers the cell as a homogeneous body. In current work, the structure-based model has been developed to predict the contributions of subcellular components to apparent cell stiffness. The continuum-based models have been developed to predict the self-organization of SFs in response to elastic substrates with different stiffness and thickness. The model has also been extended to predict how a cell senses the lateral boundary and its neighbouring cell.

1.1 Aims and Objectives

This project aims to construct single cell models and study the role of subcellular components in cell-material interactions.

The objectives of the project include:

- Develop a structure-based cell model to predict the subcellular components contributions in nanoindentation process and improve the understanding of nanomechanics of cells.
- Develop a continuum-based cell model to predict the response of cellular component, stress fibres, in substrate thickness sensing.
- Model the effect of substrate boundary on cell stress fibre formation.
- Model the cell behaviours in cell-cell communication on substrate with different stiffness.

1.2 Thesis structure

The thesis is divided into 7 chapters to describe each part of work.

Chapter 1 provides an introduction to the project, including the general background of the work, the aims and objectives of the project as well as structure of the thesis.

Chapter 2 presents the fundamental theory and research background. Basic knowledge of continuum mechanics about deformation, stress and linear elasticity are introduced. The contact mechanics is also described to illustrate the Hertz theory. The key processes of finite element method in Abaqus are presented to give a clear understanding about how the computational models are simulated.

Chapter 3 gives the technical details of the two types of cell models. For the structure-based model, the structure and sizes of all the components are provided. For the continuum-based model, the theory about how the SFs are associated in response to mechanical input is presented. The focal adhesion model that is coupled to SF formation model is explained. The implementation of these two models into the Abaqus user subroutine is described by flow chart.

Chapter 4 employs the structure-based model to study the role of subcellular components in nano-indentation process. Finite element cell model is employed to study the effect of indenter geometry and size on apparent cell stiffness. The variation of apparent stiffness is investigated when the indenters are placed at different positions.

Chapter 5 investigates the effect of the substrate thickness and stiffness on cell SF and FA formation with the continuum-based bio-chemo-mechanical model. The variations of SF concentration, SF active maximum principal stress and integrin density are studied with varying the substrate thickness and stiffness. The effect of cell size on cell response is studied as well.

Chapter 6 studies the effect of substrate lateral boundary on cell SF and FA formation. The SF concentration, active maximum principal stress, integrin density and SF orientation are studied when the distance of cell edge to laterally fixed boundary is changed. Cell-cell communication on the substrate with different stiffness is investigated when the cell-cell distance is varied.

Chapter 7 presents the conclusions and future work for the project. The limitations of current work are discussed and the ideas to further improve the modelling have been presented.

Chapter 2. Theory and Background

2.1 Introduction

In this chapter, the fundamental theory about continuum mechanics, contact mechanics, finite element modelling, relevant to the computational modelling work in this thesis, has been explained. Following this, a comprehensive review about cell mechanics and cell-materials interactions has also presented.

2.2 Continuum Mechanics

2.2.1 Notations and summation convention

In current work, vectors, tensors and matrix variables are denoted by bold symbols with notational brevity, Einstein summation convention is applied in variable calculations. Therefore, dot product of two vectors $\boldsymbol{u} = (u_1, u_2, u_3)$ and $\boldsymbol{v} = (v_1, v_2, v_3)$ could be described as

$$\boldsymbol{u} \cdot \boldsymbol{v} = u_1 v_1 + u_2 v_2 + u_3 v_3 = u_i v_i \ (i = 1,2,3.) \tag{2.1}$$

All the variables and abbreviations are listed at the beginning of this thesis.

2.2.2 Deformations and strain

In continuum mechanics, the deformation of a body is a "mapping" from its reference configuration to a current configuration in Lagrangian description. The position of a point P at reference configuration is denoted by a_1, a_2, a_3 while the position of the corresponding point P' in current configuration is represented by x_1, x_2, x_3 (Figure 2.1a). Thus, a displacement vector $\boldsymbol{u}$ is introduced:

$$u_i = x_i - a_i, \quad (i = 1,2,3.) \tag{2.2}$$

The velocity is defined as the derivative of displacement with respect to time:

$$\dot{u}_i = \frac{du_i}{dt}, \quad (i = 1,2,3.) \tag{2.3}$$

To further describe the transformation of the body, the deformation gradient tensor $\boldsymbol{F}$ is introduced and defined as (Irgens, 2008):

$$F_{ij} = \frac{\partial x_i}{\partial a_j} = \delta_{ij} + \frac{\partial u_i}{\partial a_j} = \delta_{ij} + u_{i,j}, \quad (i,j = 1,2,3.) \tag{2.4}$$

where δ_{ij} is the Kronecker delta with the following property:

$$\delta_{ij} = \begin{cases} 0 & i \neq j \\ 1 & i = j \end{cases} \tag{2.5}$$

The Jacobian determinant of $\boldsymbol{F}$ is defined as:

$$J = det|\boldsymbol{F}| \tag{2.6}$$
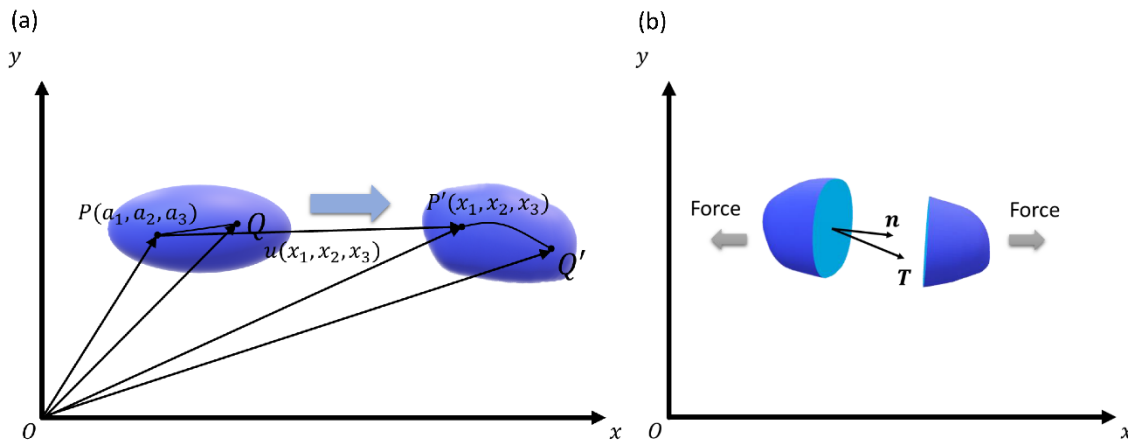
Figure 2.1 (a) Body deformation; (b) traction force in the body.

The transformation of the body could be considered as two steps: rotation followed by stretch or stretch followed by rotation. Considering rotation followed by stretch, the deformation gradient could be decomposed as:

$$\boldsymbol{F} = \boldsymbol{R} \cdot \boldsymbol{U} \tag{2.7}$$

where $\boldsymbol{R}$ represents the rotation matrix and $\boldsymbol{U}$ represents stretch. In 3-D space, the three eigenvalues of the tensor $\boldsymbol{U}$ are called the principal stretches represented by λ_1, λ_2 and λ_3. The volume change of the body can thus be written as the product of these stretches:

$$\frac{V}{V_0} = \lambda_1 \lambda_2 \lambda_3 \tag{2.8}$$

where V_0 is the original volume.

The Green strain tensor $\boldsymbol{E}$ is defined based on the deformation gradient:

$$E_{ij} = \frac{1}{2}\left(F_{ki}F_{kj} - \delta_{ij}\right) = \frac{1}{2}\left(u_{i,j} + u_{j,i} + u_{k,i}u_{k,j}\right) \tag{2.9}$$

If the first derivatives of displacement u_i are small, the squares and products of the partial derivatives are negligible. Therefore, we can obtain Cauchy's infinitesimal strain tensor:

$$\varepsilon_{ij} = \frac{1}{2}\left(u_{i,j} + u_{j,i}\right) \tag{2.10}$$

The logarithmic strain or true strain is defined as:

$$\boldsymbol{H} = \ln\left(\boldsymbol{U}\right) \tag{2.11}$$

where the tensor $\boldsymbol{H}$ is also called Hencky strain tensor in 3-D.

2.2.3 Stress

The stress state of a point in the deformed material body is usually described by the Cauchy stress tensor $\boldsymbol{\sigma}$. Traction vector $\boldsymbol{T}$ is the force vector acting on a cross-section divided by the area of the cross-section (Figure 2.1b). Cauchy's stress theorem can be used to obtain the traction at any cross-section in the body:

$$\boldsymbol{T} = \boldsymbol{n} \cdot \boldsymbol{\sigma} \tag{2.12}$$

where $\boldsymbol{n}$ is the cross-section surface normal vector.

The Cauchy stress tensor is used to describe small deformations of materials, while other stress measures are required for large deformations. Whereas the Cauchy stress relates the forces in the current configuration to the areas in the current configuration, the first Piola-Kirchhoff stress tensor $\boldsymbol{P}$ relates the forces in the current configuration to the reference configuration:

$$\boldsymbol{P} = J\boldsymbol{\sigma}F^{-T} \tag{2.13}$$

The second Piola-Kirchhoff stress tensor $\boldsymbol{S}$ expresses the stress relationship between the forces and areas in reference configuration:

$$\boldsymbol{S} = J\boldsymbol{F}^{-1} \cdot \sigma \cdot F^{-T} \tag{2.14}$$

In mechanics studies, stress and strain pairs are often used to calculate work and energy. The first Piola-Kirchhoff stress P is conjugated with deformation gradient F, while the second Piola-Kirchhoff stress S is conjugated with the Green strain E.

The stress tensor changes with different coordinates, it is useful to find the stress that are independent of coordinate. As the Cauchy stress tensor is symmetric in equilibrium (Irgens, 2008), it is possible to find a coordinate system described by its three eigenvectors, in which the stress tensor is diagonal. The diagonal components are the eigenvalues of the stress tensor. The principal stresses σ_1, σ_2 and σ_3 can be determined by eigenequation (Irgens, 2008):

$$(\boldsymbol{\sigma} - \sigma\boldsymbol{I}) \cdot \boldsymbol{n} = 0 \tag{2.15}$$

where σ is the principal stress to be determined; $\boldsymbol{n}$ is the normal of the principal planes. This can be expanded into:

$$\sigma^3 - I_1\sigma^2 + I_2\sigma - I_3 = 0 \tag{2.16}$$

where I_1, I_2 and I_3 are called the invariants of stress tensor:

$$I_1 = \sigma_{kk}$$

$$I_2 = \frac{1}{2}[(\sigma_{kk})^2 - \sigma_{ij}\sigma_{ij}]$$

$$I_3 = \det(\boldsymbol{\sigma}) \tag{2.17}$$

The stress tensor can be decomposed into two parts: hydrostatic and deviatoric stresses. The hydrostatic stress is related to the volume change while the deviatoric stress describes the shape change. The hydrostatic stress is:

$$\boldsymbol{\sigma_{hyd}} = \begin{bmatrix} \sigma_{hyd} & 0 & 0 \\ 0 & \sigma_{hyd} & 0 \\ 0 & 0 & \sigma_{hyd} \end{bmatrix} \tag{2.18}$$

where

$$\sigma_{hyd} = \frac{1}{3}\sigma_{kk} \tag{2.19}$$

The deviatoric stress is:

8

$$\boldsymbol{\sigma'} = \boldsymbol{\sigma} - \boldsymbol{\sigma_{hyd}} = \begin{bmatrix} \sigma_{11} - \sigma_{hyd} & \sigma_{12} & \sigma_{13} \\ \sigma_{21} & \sigma_{22} - \sigma_{hyd} & \sigma_{23} \\ \sigma_{31} & \sigma_{32} & \sigma_{33} - \sigma_{hyd} \end{bmatrix} \qquad (2.20)$$

The von Mises stress is a value usually used to determine if a given material will yield or fracture:

$$\sigma_v$$
$$= \sqrt{\frac{1}{2}\left((\sigma_{11} - \sigma_{22})^2 + (\sigma_{22} - \sigma_{33})^2 + (\sigma_{33} - \sigma_{11})^2\right) + 3(\sigma_{12}^2 + \sigma_{23}^2 + \sigma_{31}^2)} \qquad (2.21)$$

2.2.4 Linear elasticity

For small deformations, material exhibit linear elastic characteristics (e.g. the strain linearly proportionally to the stress). At large deformation, many materials begin to show the nonlinear elastic response or plastic deformation. The elastic deformation is fully recoverable. The plastic deformation is irreversible and not relevant to this work, which will not be discussed further. In principle, many materials may also be viscoelastic which is time-dependent elastic response which will also not be discussed. The major focus will be on the elastic response where the stresses in materials are only dependent on the strains and the deformation fully recoverable after the stresses are removed (Irgens, 2008). The material is elastically homogeneous if the elastic properties everywhere within the materials are the same. If the elastic properties are the same in every direction of a material point, the material is called elastically isotropic. When the strains in the materials are assumed to be very small, the strains can be described by the small deformation tensor (equation 2.10).

The stress-strain relationship of linear elastic material relates the second Piola-Kirchhoff stress and Green strain is given by:

$$S = C:E \qquad (2.22)$$

This can be written as:

$$S_{ij} = \frac{E_s \nu}{(1 - 2\nu)(1 + \nu)} E_{kk} \delta_{ij} + \frac{E_s}{(1 + \nu)} E_{ij} \qquad (2.23)$$

where E_s is the modulus of materials, ν is the Poisson's ratio, δ_{ij} is the Kronecker delta, E_{ij} is the Green strain.

2.3 Contact mechanics

Contact mechanics are essential for indentation (or nanoindentation) based techniques for mechanical characterisations. When two elastic solids are brought into contact, the Hertz model has been developed to predict the contact pressure and area shape of contact (Hertz, 1882). The surfaces in contact are assumed to be smooth enough, implying the absence of small surface irregularities, which may cause discontinuous contact or variations of local contact pressure. For contact between two spheres (Figure 2.2), the applied force F is related to the mutual displacement δ of two surfaces by (Johnson and Johnson, 1987):

$$F = \frac{4}{3} E^* \sqrt{R} \delta^{\frac{3}{2}} \tag{2.24}$$

where R is the effective radius obtained by

$$\frac{1}{R} = \frac{1}{R_1} + \frac{1}{R_2} \tag{2.25}$$

and R_1, R_2 are the radii of the two solids in contact. When a sphere is indenting a flat surface ($1/R_2 = 0$), the effective radius is equal to the radius of the spherical radius. (Figure 2.2).
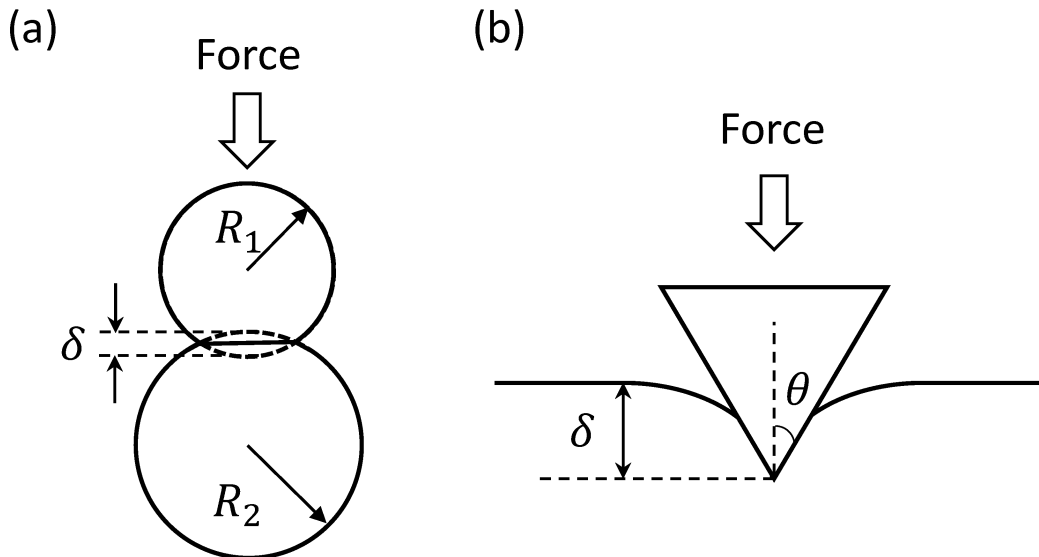
Figure 2.2 (a) Contact between two spheres; (b) contact between a cone and flat surface.

The contact modulus E^* is given by

$$\frac{1}{E^*} = \frac{1 - v_1^2}{E_1} + \frac{1 - v_2^2}{E_2} \qquad (2.26)$$

where E_1, E_2 are the elastic moduli, v_1, v_2 are the Poisson's ratio of the two elastic solids.

The Hertz theory of contact was further developed by Sneddon to describe the contact between a rigid conical indenter and an elastic half-space (Sneddon, 1965). The force-displacement relation is given by,

$$F = \frac{2}{\pi} \frac{E^* \cdot \tan\theta}{1 - v^2} \delta^2 \qquad (2.27)$$

where θ is the semi-included angle of the conical indenter (Figure 2.2). This equation is also applicable to the pyramid indenters (e.g. Berkovich indenter)

2.4 Finite element method

For most of the engineering problems, it is difficult to get analytical solutions. Therefore, numerical methods have been developed to obtain approximate solutions. The finite element method (FEM) is a numerical method to solve boundary value problems. FEM particularly subdivides the domain of interest into small parts called element. The problem in each element can be solved with simple equations rather than complicated expression in the whole domain. The governing equations in each element are assembled into a system of algebraic equations. These equilibrium equations are solved by some numerical techniques such as Newton-Raphson method. The main process of FEM is described below (Zienkiewicz *et al.*, 2005):

1) Mesh discretization of the continuous domain of interest;
2) Choose the shape function of the elements;
3) Derive the stiffness matrix of the elements;
4) Assemble overall stiffness matrix for the whole body;
5) Solve these equations to get nodal displacements, strains and stress in the body.

There are a number of FEM commercial softwares (e.g. ANSYS, ABAQUS, MSC software, COMSOL) developed to solve a wide range of engineering problems (Msc, 2004; Multiphysics, 2014; Systemes, 2015; Lee, 2020). In this study, ABAQUS is adopted. There are two programs mostly used in Abaqus: Abaqus/Standard and Abaqus/Explicit. Implicit solution technique is applied in the Abaqus/Standard

program, which is usually used to solve general linear and non-linear problems. On the other hand, the Abaqus/Explicit program uses explicit integration solution technique and has advantages over solving dynamic and highly discontinuous problems.

For some materials with complex behaviours, Abaqus/Standard provides the users with capability to define their customized material models by user subroutines coded by Fortran 77. In the user subroutine to defined material's mechanical behaviours (UMAT), the users need to provide constitutive equations for the mechanics of the specific materials. The stresses variable (STRESS) at each integration point are updated in each iteration with updated material Jacobian (DDSDDE). The detailed flowchart of FEM and user UMAT is presented in Figure 2.3.
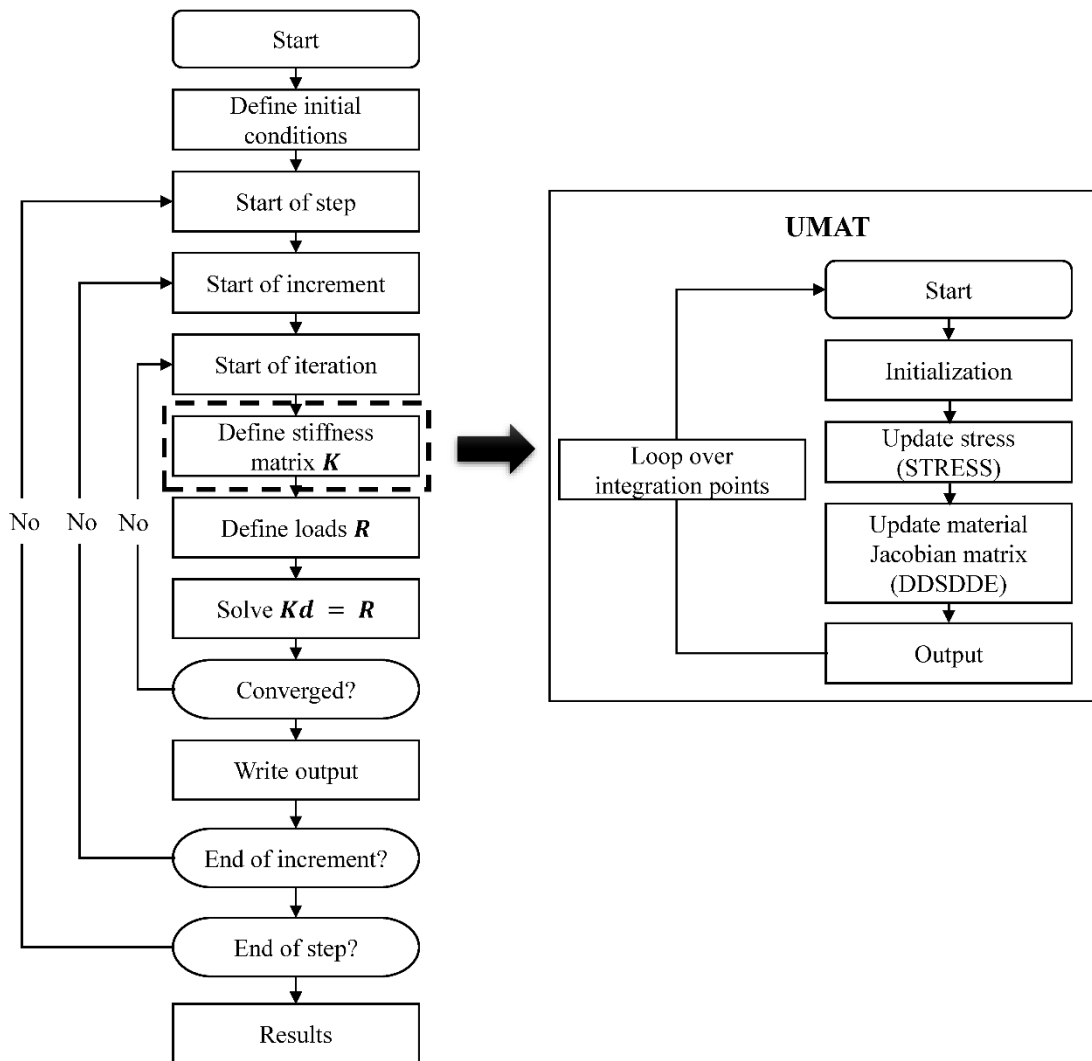
Figure 2.3 Flowchart of FEM and user subroutine UMAT in Abaqus.

2.5 Cell structure and cell mechanics

2.5.1 Cell structure

Most eukaryotic cells are comprised of a number of organelles including a plasma membrane, cytoplasm, nucleus and cytoskeleton, which play pivotal roles in various cell functions (Pollard *et al.*, 2016) (Figure 2.4). All the cell components are enclosed by the cell plasma membrane. Cytoplasm is a thick solution that mainly contains water, proteins and salts. The other organelles are located in the cytoplasm. Nucleus encapsulates the chromatin which forms chromosomes and stores genetic information. The cytoskeleton (CSK) works as a framework that provides mechanical support for the cell to maintain certain morphology and internal organization.

The cytoskeleton could be categorized into three major subtypes: actin filaments, intermediate filaments and microtubules. Actin filaments are first nucleated by several actin monomers and elongated by persistently adding monomers to their ends. They are highly dynamic in their stable state, where actin monomers keep assembling and disassembling (Lodish *et al.*, 2008). Bundles of aligned actin filaments can support filopodial protrusions, while branched actin filaments support the leading edges of migrating cells. Bundles of actin filaments can also collaborate with myosin motors to form stress fibres (SFs), enabling the cells to contract and generating forces in response to their external environment (Fletcher and Mullins, 2010a).

Microtubules are hollow cylinders formed by tubulins with a diameter of about 25 nm and length of 200 nm to 25 μm. During mitosis, microtubules rearrange themselves into mitotic spindle to segregate the chromosomes (Fletcher and Mullins, 2010b). Intermediate filaments are mid-sized compared to other two types with a diameter of about 10 nm. They can be crosslinked to each other to resist substantial forces. Intermediate filaments may help stabilize cell organelles such as nucleus.

2.5.2 Cell activities are regulated by material properties

During the 1970s and 1980s, the researchers have discovered the substrate stiffness can regulate cell proliferation and differentiation. For example, mammary epithelial cells tend to proliferate on rigid surfaces and differentiate on softer collagen gels (Emerman and Pitelka, 1977). The cell's ability to spread, exert force on extracellular matrix (ECM) and generate tension within CSK has also been identified by Ingber and Folkman (Ingber and Folkman, 1989). They hypothesised the inherent malleability of the matrix (i.e. stiffness) should be responsible for controlling the cell

growth and differentiation. Vailhe *et al.* also altered the mechanical properties by varying the concentration of fibrin gels, the stiffness of the gels was found to affect the capillary-like structure formation of human umbilical vein endothelial cells (HUVECs), and their results demonstrated the facility of soft gels for angiogenesis (Vailhé *et al.*, 1997). Despite the appreciation of cells to feel and respond to the stiffness of the material they grow on, robust experimental approaches were lacking until late 1990s. Pelham and Wang (Pelham and Wang, 1997) designed a thin polyacrylamide (PA) based, collagen coated flexible substrate within which the stiffness could be varied while the chemical environment remained constant, to clearly determine the effect of substrate stiffness on cell migration and focal adhesions. Cells were more locomotive and showed elevated lamellipodia activities on softer substrates, indicating the destabilized adhesions between cells and materials. The results revealed the ability of the cells to survey the mechanical properties of their surrounding environment. An important contribution of the study is that the PA substrates devised by the authors has since been utilised in the numerous studies to investigate the dependency of the cell behaviours on the substrate stiffness.
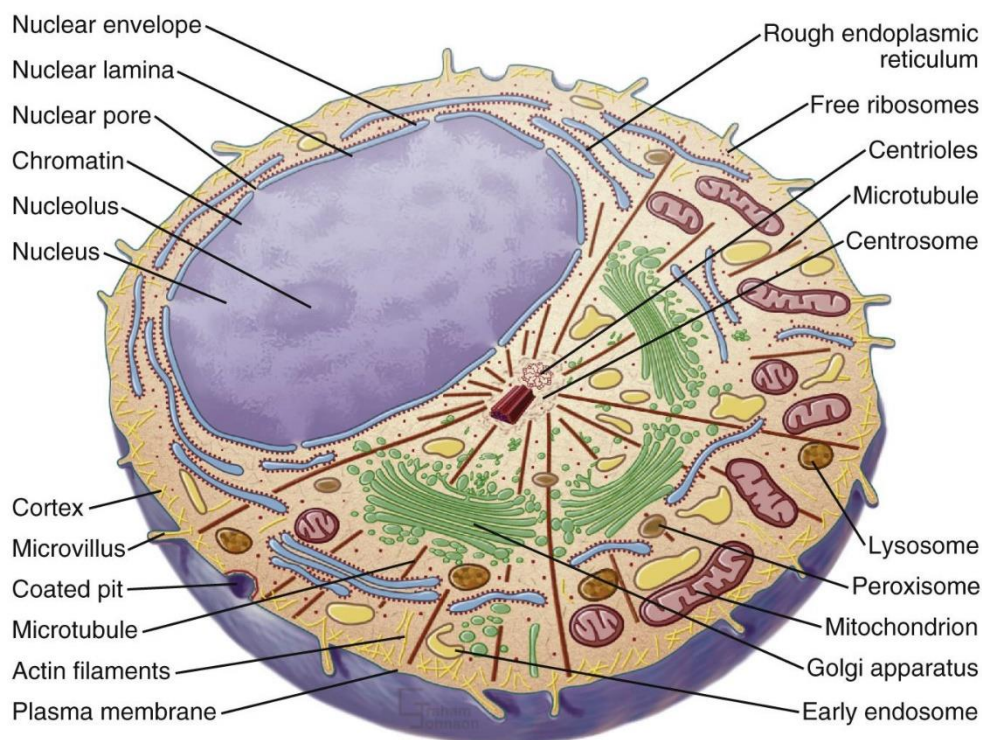
Figure 2.4 Basic cell structure (Pollard *et al.*, 2016).

After considerable amounts of research, substrate stiffness has become increasingly recognized as key to cellular processes ranging from motility, morphology and

differentiation. Engler *et al.* carried out a systematic study and reported that the human mesenchymal stem cells (MSCs) were directed into different lineages on different stiffness ranges (Figure 2.5) (Engler *et al.*, 2006). The authors cultured the MSCs on matrices with different stiffness ranges to mimic brain (E_{gel}~0.1-1kPa), muscle (E_{gel}~8-17kPa) and bone (E_{gel}~25-40kPa) elasticity. On soft gels, the cells exhibited branched, filopodia-rich morphology, consistent with those of neurons. Nevertheless, the MSCs on stiffer gels that mimic muscle and bone tissue environment exhibited similar morphology to those of myoblast and osteoblast, respectively. Along with directed differentiation, the cell contractility, measured as a mean cellular prestress, and cell cortical stiffness also scaled with matrix stiffness. It demonstrated that stiffer matrix produces stiffer and increasingly tensed cells.
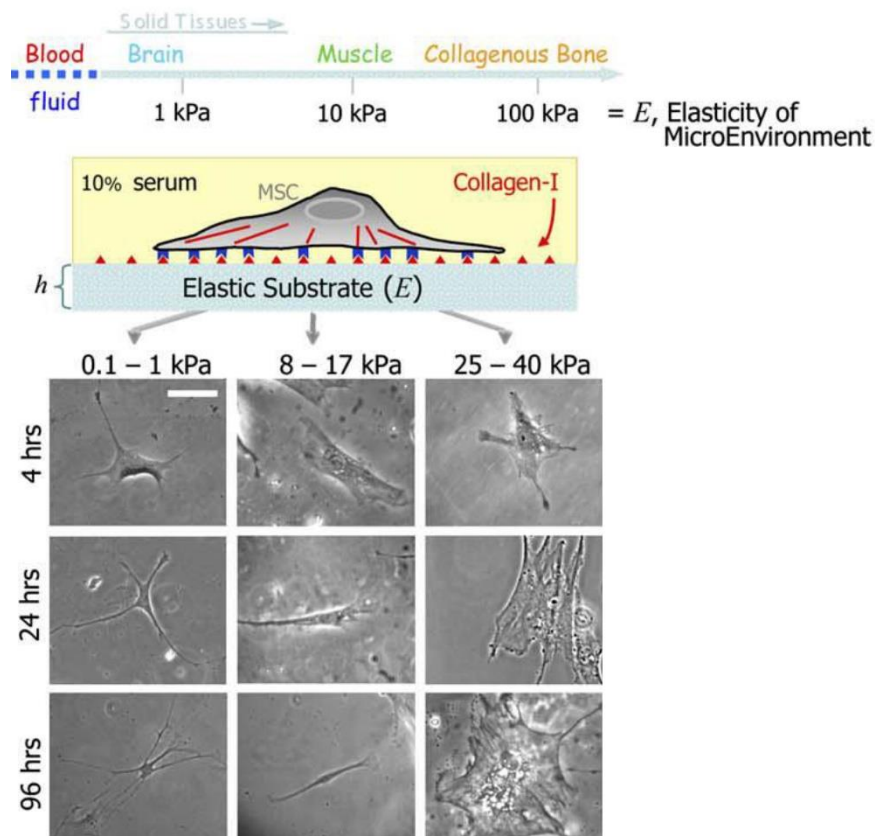
Figure 2.5 Human mesenchymal stem cells differentiate towards neurons, myoblasts and osteoblasts on soft (E_{gel}~0.1-1kPa), medial (E_{gel}~8-17kPa) and stiff (E_{gel}~25-40kPa) substrates, respectively (Engler *et al.*, 2006).

The effect of substrate stiffness on the cell differentiation was further extended by others to study the effect of substrate stiffness combined with other factors, such as growth factors (Park *et al.*, 2011; Wingate *et al.*, 2014; Floren *et al.*, 2016), substrate compositions (Rowlands *et al.*, 2008; Chen *et al.*, 2010; Suzuki *et al.*, 2010), surface

structure (Chuah *et al.*, 2015) and cell seeding density (Mullen *et al.*, 2013), on the differentiation of cells during cell-interactions. Taking the cell-material interaction from two dimension (2D) into three dimension (3D) to mimic more physiological environment, Pek *et al.* found the highest expressions of neural, myogenic and osteogenic transcription factors were on substrates with liquefaction stress of 7, 25 and 75 Pa respectively. Immobilization of adhesion peptide promoted both cell proliferation and differentiation of MSCs. These results were consistent with previous 2D research (Engler *et al.*, 2006). A recent study by Lee *et al.* explored the effect of dynamic physical properties of the external environment, that is switching substrate stiffness in

the midway of cell differentiation, on the subsequent cell differentiation (Lee *et al.*, 2014). When cells were transferred from soft (~0.5kPa) to stiff (~40 kPa) substrate after 10 days culture, their neurogenesis process were rewired to osteogenesis. However, MSCs transferred from stiff to soft hydrogels still maintained osteogenesis markers, suggesting a degree of irreversible activation. These results addressed the susceptibility of cells to biophysical properties of the materials, even after several weeks of culture.

Trappmann *et al.* argued that the changes in mesh (pore) size in PA gels rather than stiffness regulated the ECM tethering and thus cell differentiation (Trappmann *et al.*, 2012). However, Engler *et al.* had previously addressed that the adhesion and spreading of rat aorta smooth muscle cells on PA gels were not sensitive to the ligand density (Engler *et al.*, 2004a). Other studies also supported the stiffness sensing by studying cell differentiations on gels with different thickness which altered the effective stiffness that cells felt while maintain the cell-gel surface constant (Buxboim *et al.*, 2010; Takebayashi *et al.*, 2013). That is, thin gels with low modulus that increased the effective stiffness enabled the cells to exhibit same phenotype on stiff gels.

As the mechanical signals transmitted to the CSK via adhesions, the CSK organize itself and form stress fibres (SFs) when sufficient stimuli are provided. The study by Fu *et al.* revealed the strong correlations between cytoskeletal tension at early differentiation stage and ultimate differentiation of human MSCs. MSCs showed higher traction forces in osteogenic medium with culturing time 1 day or 3 days were more likely to commit osteogenesis after 7 days culture, suggesting cell contraction as an indicator of the cell fate (Fu *et al.*, 2010). It has been observed by Ghosh *et al.*

that fibroblasts on stiff substrate (4270 Pa) had linear, stretched arrays of actin microfilaments with uniform diameter while those on soft gels (95 Pa) a serpentine F-actin array of low density where most of microfilaments showed buckling (Ghosh *et al.*, 2007). The actin stretching of the cells on stiff substrate was also correlated with cell stiffness. Similar relationship between actin assembly and cell stiffness has been previously examined for hepatocytes (Bhadriraju and Hansen, 2002).

The cell tension regulated by matrix can lead to the translocation of mobile regulators as well, for instance transcription factors, at least in cellular mechanotransduction (Ho *et al.*, 2013). For example, the YAP and TAZ transcriptional tend to localize to nucleus in high tension cells cultured on stiff substrates and their entry into nucleus has been reported by numerous studies that they can trigger a wide range of downstream signalling cascades mediating complex cellular processes such as differentiation (Dupont *et al.*, 2011; Sun *et al.*, 2014). On the other hand, some factors, such as NKX-2.5, will enter the nucleus in response to low tension and repress the expression of genes (e.g., α-smooth muscle actin) that contributing to high tension states (Dingal *et al.*, 2015).

Recent studies have focused on how the stiffness regulate the nuclear behaviours, thus, modulating the cell gene expressions. Given the central role of the nucleus in transcriptional regulation, it has long been speculated that the nucleus could act as a cellular mechanosensor that can directly modulate gene expression in response to mechanical disturbances. External stimuli applied to a cell can be transmitted from the adhesion sites through the CSK to the nucleus, contributing to the nuclear behaviours such as deformations (Figure 2.6) (Caille *et al.*, 1998; Lombardi *et al.*, 2011; Morimoto *et al.*, 2012). These deformations could alter the structure of chromatin or conformation of nuclear proteins, such as the release of transcriptional regulators or translocation of chromatin segments away from transcriptionally repressive regions, thereby activating or repressing mechanosensitive genes (Booth-Gauthier *et al.*, 2012; Poh *et al.*, 2012; Isermann and Lammerding, 2013).

Experiments conducted by Lovett *et al.* and his partners reported that nuclear shape could be modulated by substrate stiffness (Lovett *et al.*, 2013). On soft substrates with a Young's modulus of 0.4 kPa, the nucleus exhibited round shape in vertical cross-section, however, the nucleus appeared flattened on stiff substrates with a modulus of 308 kPa. To determine the role of LINC complex played in the shape modulation, the LINC complex was disrupted and found nonsensitivity to substrate

stiffness, highlighting the importance of LINC complex in mechanotransduction. The authors also identified that the actomyosin cables on the apical surface of the nucleus do not contribute significantly to nuclear shape, as nuclear shape showed modest changes when disrupting F-actin cap. A limitation here is that whether the downward compression from the apical cortex or the pulling from CSK contributes to the nuclear shape changes is not determined, as it is difficult to distinguish the critical component when vertical rounding was observed with the disruptions of LINC complex and the simultaneously decreased cell spreading.
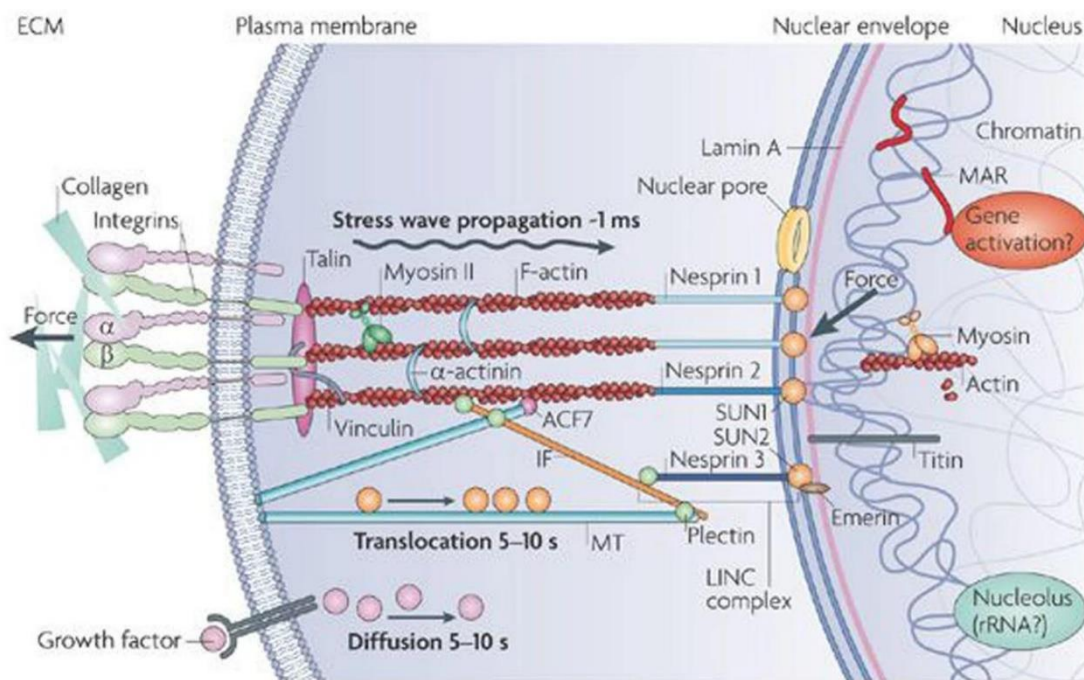
Figure 2.6 External forces trigger signalling process and are transmitted through cytoskeletal filaments to the nucleus (Bouzid *et al.*, 2019).

Lamins are intermediate filament proteins found in nearly all cell types attached at the inner face of nuclear envelope, including A-type and B-type lamins. Besides contributing to nuclear stiffness (Pajerowski *et al.*, 2007) and nuclear stability (De Vos *et al.*, 2011), they are also believed to modulate transcription (Shimi *et al.*, 2008) and speculated to regulate the genome (Wang *et al.*, 2009). Lamin-A has been reported to be the main contributor to nuclear softness when they are knocked down while maintaining the lamin-B (Pajerowski *et al.*, 2007). A recent study by Swift *et al.* addressed that lamin-A scaled with matrix stiffness (Swift *et al.*, 2013). The authors examined the proteomes for nucleus from brain to bone, and found that Lamin-A was increased 30 folds with tissue stiffness while lamin-B differed less than 3 folds. An absolute stoichiometry of the lamin isoforms (lamin-A:B) was found to exhibit a power law fit versus tissue stiffness (lamin-A:B ~ E0.6), indicating the dominance of lamin-A

18

in stiff tissues and lamin-B in soft tissues. Through growing tumours in the brain and flank, they also revealed that the matrix stiffness determines the tissue stiffness and lamin-A level. Furthermore, compared to MSCs on stiff matrix, the MSCs on soft matrix increased adipogenesis to 8%, but knockdown of partial LMNA increased adipogenesis to 20%, indicating the enhancement of matrix stiffness directed differentiation.

The effect of material geometry on cell behaviours, such as differentiation, adhesion and CSK remodelling have also been identified by several studies (Cheng *et al.*, 2009; Tay *et al.*, 2011; McNamara *et al.*, 2012). Through controlling the cell shape by substrate geometric features, cell shape, not cell-material contact area, has been addressed to govern individual cell's fate (Chen *et al.*, 1997; Chen *et al.*, 1998). It was pointed out by Kilan *et al.* that geometric shape of cells could regulate mechanochemical signals and paracrine/autocrine factors to control MSCs fates (Kilian *et al.*, 2010). In contrast, a study which studied cell-material interactions in three-dimensional environment, argued that neither cell nor nuclear morphology was required to determine cell fate (Huebsch *et al.*, 2010). Instead, they concluded that integrin-adhesion-ligand bonds were morphology-independent sensors of both matrix elasticity and dimensionality. They also concluded that cells interpret mechanically disparate substrates as having different adhesion-ligand presentations, even if their chemical compositions are identical. By guiding the contact of the cells, topological features of the substrates have been linked to chromosomal positioning and gene regulation (McNamara *et al.*, 2012). McNamara *et al.* plated the fibroblasts on microgrooved substrates and found the topography resulted in distinctions in the nucleoskeleton, nucleolar morphology and chromosomal positioning that correlated with gene expression.

Nanoscale disorder has been directly examined to stimulate human MSCs to produce bone mineral in vitro without osteogenic supplements (Dalby *et al.*, 2007). Dalby *et al.* cultured MSCs on surfaces with different nanopits structures and found the cells exhibited fibroblastic morphology on planar control surface while the cells showed discrete areas of intense cell aggregation and early nodule formation on the disordered square array (Figure 2.7) (Dalby *et al.*, 2007). By comparing the results from surfaces with disordered square array and those from planar control with dexamethasone, a corticosteroid that can induce bone formation, the authors confirmed the potential of the disordered materials to induce osteogenesis close to

that of the dexamethasone. They also found the ability of the nano-topographies to modulate adhesion formation of osteoprogenitor cells.

Nanotopography has also been examined to modulate the cell mechanical properties (Yim *et al.*, 2010). Yim *et al.* seeded human MSCs on both tissue-culture polystyrene (TCPS) which is stiff with Young's modulus of 2GPa, and poly(dimethylsiloxane) (PDMS) which is relatively soft with Young's modulus of 2~4 MPa. These two types of substrates were both patterned with nanogratings with different sizes. The cells on TCPS exhibited lower elastic moduli when attached to nanopatterned surfaces compared to those on unpatterned controls. The cells on PDMS had no significant differences, while showed significant lower moduli compared to those on TCPS. The viscoelastic properties also showed changes that paralleled those observed in the elastic properties.
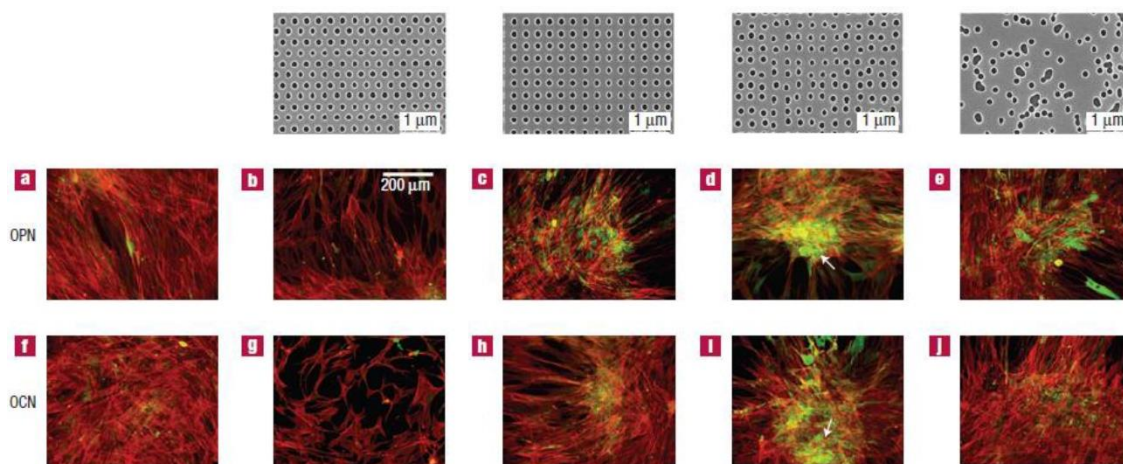
Figure 2.7 Bone-specific extracellular matrix proteins osteopontin (OPN) and osteocalcin (OCN) staining of osteoprogenitors after 21 days of culture (Dalby *et al.*, 2007). The top row shows images of nanotopographies of the materials. (a,f) Osteoprogenitors cultured on the control with planar surface lack positive OPN and OCN stain. (b,g) On hexagonal array, the cells have lost their cell adhesions; (c,h) On square array, cell numbers decreased compared with the control. (d,i) On disordered square array, bone nodule are formed (arrows); (e,j) On material with random array, cells have good populations with expression of OPN and OCN. Actin=red, OPN/OCN=green.

2.5.3 Cell-material adhesions are regulated by material properties

During interactions with surrounding materials, cells transmit extracellular signals through localized sites at which they are adhered to an extracellular matrix. Such small contact regions near the fibroblast cell periphery between cell membrane and substrate was discovered by Curtis *et al* (Curtis, 1964). Cell-material adhesions play critical roles in transmembrane signalling process to regulate cell morphology

(Prager-Khoutorsky *et al.*, 2011), differentiation (Kilian and Mrksich, 2012) and migration (Plotnikov *et al.*, 2012). Cell-materials adhesions are large, dynamic protein complexes that connect to materials by transmembrane proteins termed as integrins. In the intracellular domain, integrins are attached to the adaptor proteins such as vinculin, tensin and talin, which are linked to cytoskeletal elements. Integrin-mediated adhesions have be categorized into three types: focal complexes (FXs), focal adhesions (FAs) and fibrillar adhesions (FBs) (Zaidel-Bar *et al.*, 2004). Each of the adhesions has typical morphology and compositions. FXs are small dot (<1 μm^2) like nascent adhesions formed at the leading edge of the cell and mature into FAs. FAs are large (≥1 μm^2), elongated and stable adhesions serving as an important link between extracellular matrix and cytoskeleton. FAs involve more proteins including integrins, vinculin, talin and paxillin. FBs evolve from mature FAs which distinguish from FAs by high levels of tensin. Cells will generate different adhesions in response to different material stiffness. Rigid materials mainly give rise to the formation of FAs, while the soft materials result in the formation of punctate focal complexes. It has been speculated that the responses of cells to material stiffness originate from the adhesion sites, where mechanical inputs are translated into intracellular signals (Pelham and Wang, 1997). Cell-material adhesions have provided the cells with physical basis to sense the external environment.

It has been demonstrated that the morphology of focal adhesions is substrate stiffness dependent. The focal adhesions of fibroblasts on rigid substrate are elongated and oriented with the directions of stress fibres while those on soft substrate exhibit dot like adhesions oriented radially. Experiment showed the elongation of focal adhesion precedes the alignment of fibroblasts and it was proposed the focal adhesion elongation drives the polarization of fibroblasts (Prager-Khoutorsky *et al.*, 2011). To understand the underlying mechanisms of how cells sample the material stiffness through cell adhesions, Plotnikov et al. employed traction force microscope to visualise the distribution and dynamics of traction forces with single focal adhesion of migrating fibroblasts (Plotnikov *et al.*, 2012). Traction forces are asymmetrically distributed in single focal adhesion with the peak forces of most adhesions located at the adhesion centre or distal end. They further observed two different phenomena: the traction force within single focal adhesion exhibits stable force distribution with centred peak force or dynamically fluctuating both in positions and magnitude. This observation proposes the traction forces have two

states: weak state that forces are stable and strong state that forces are fluctuating with higher mean traction forces. The traction force states can be regulated by ECM rigidity in the range of ~20 kPa. Stiffer materials contribute to stable traction forces while softer materials promote fluctuating forces. Inhibition of the tension inside cells shifts the stable focal adhesions into tugging adhesions. This research helps gain an insight into the mechanism of ECM rigidity sampling and molecular mechanisms of focal adhesions.

Cell adhesions respond to external forces by changing their morphology and compositions. Experiments have been conducted to find the relationship between focal adhesion assembly and local forces. Balaban et al. fabricated PDMS elastomer and visualised the distortion of the materials by cells (Balaban *et al.*, 2001). The forces applied at adhesion sites were calculated by phase contrast. They found the local forces are correlated with focal adhesion orientation, total fluorescence intensity and area. FA elongation are mostly oriented in the direction of stress fibres and the directions of the force applied at FAs correlate with the main axes of the FAs. Forces scale with the area of the FA, indicating that a constant stress (5.5 ± 2 nN/μm^2) is applied at each FA site. Treatment of cells by chemicals to relax the forces exerted by actin filaments has resulted in the decrease of total intensity of FAs. It demonstrates the same time scale of force application and assembly of FAs.

Riveline et al. also studied the relationship between the force applied at the cell periphery and focal adhesion assembly level (Riveline *et al.*, 2001). Micropipettes applied at the cell dorsal surface were used to generate forces at the cell periphery. The growth of focal complexes into focal adhesions only located at the cell edge in the vicinity of the pipette tip. The direction of the growth is similar to that of the force. Green fluorescent protein study combined with interference reflection microscope revealed the same characteristics of the focal adhesions formed by applied force with those of the adhesions formed during cell spreading and migration. Disruption of actin filament results in that the external force can not induce the formation of focal adhesion. However, the inhibition of actomyosin do not prevent the focal adhesion formation upon force application. Hence, the external force can be considered to replace the function of actomyosin in actin filament contraction. This study highlighted the correlation between the forces at the adhesion sites and the focal adhesion formation.

The proteins in focal adhesion complexes will change their conformations and compositions upon receiving stimuli. They play crucial role in the process of adhesion formation. The transmembrane protein integrins have been reported to have two conformational states: a bent state with low affinity and a straight state with high affinity (Takagi *et al.*, 2002). Due to the conformational states, only the straight integrins can interact with external ligands on the materials. The integrins with low affinity can move freely in the cell membrane. Free integrins will cluster with bonded integrins at adhesion sites due to the binding of vinculin to talin (Geiger and Yamada, 2011). This process results in the formation and growth of cell adhesions. Vinculins have also been proved essential for myosin contractility dependent adhesion strength and traction force (Dumbauld *et al.*, 2013). To understand the molecular mechanisms of the mechanosensing in the focal adhesions, the differentiation of mesenchymal stem cells into different lineages were studied by modifying the affinity and density of material peptide ligands (Kilian and Mrksich, 2012). Materials with high affinity peptide ligands promote osteogenesis, those with low-affinity peptide at high density promote myogenesis and those with low-affinity peptide at low density promote neurogenesis.

2.5.4 Cell stress fibre formation are regulated by material properties

After the mechanical signals transmitted by the adhesions from external material, they are passed into the CSK to trigger cell internal structure reorganization (Parsons *et al.*, 2010). The actin cytoskeleton organization plays a fundamental role in regulating various cellular behaviours including differentiation (Pablo Rodríguez *et al.*, 2004), proliferation (Lepelletier *et al.*, 2006) and migration (Wang and Newman, 2003). Abnormalities of the cytoskeleton dynamics are correlated with many cell diseases such as cancer, neurological disorders and myofibrillar myopathies (Tojkander *et al.*, 2012). The most significant role of actin filaments is to provide forces for above-mentioned cellular activities. The force is generated by two mechanisms: actin polymerizations and myosin-II contraction on the filaments. The actin filaments are polymerized against the cell membrane to generate protrusion force. The actin filaments could also be cross-linked by myosin-II motor to form actomyosin bundles and provide the force for cells to sense external environment.

Stress fibres are mainly categorized into four types: dorsal and ventral stress fibres, transverse arcs and perinuclear actin cap (Tojkander *et al.*, 2012). Dorsal stress fibres are connected to the adhesion sites at their distal ends. They cannot contract

due to lack of myosin-II elements. Transverse arcs are anchored to the adhesion directly, but they transmit force via their links with the proximal ends of dorsal stress fibres. The contraction of transverse arcs has been shown to play a role in retrograde flow (Zhang *et al.*, 2003). Ventral stress fibres are the most observed structures that are anchored to the focal adhesions at both ends. Perinuclear actin cap is an actin structure that is located on the nucleus and believed to regulate nucleus shape (Khatau *et al.*, 2009b).

Formation of SFs has been related to some cellular proteins. Ridley and Hall pioneered an experiment to study how the SF formation was regulated by RhoA signal (Ridley and Hall, 1992). Micro-injection of RhoA protein into serum starved Swiss 3T3 cells immediately triggered the assembly of SFs. The downstream effectors of RhoA — Rho-associated protein kinase (ROCK) and the diaphanous-related formin mDia1 — have been shown to play different roles in regulate SF phenotype. ROCK activation only produces thick SFs with star-like pattern in the centre of the cell (Leung *et al.*, 1996). With overexpression of mDia1, the cell would only generate parallel SFs but not thick fibres (Watanabe *et al.*, 1997; Pellegrin and Mellor, 2007). These two activities are both essential in producing RhoA induced SF formation (Watanabe *et al.*, 1999). It was further discovered that Rho induced myosin light chain phosphorylation accompanied by increased contractility preceding the formation of SFs (Chrzanowska-Wodnicka and Burridge, 1996). Upon addition of inhibitor of contractility, the Rho-induced SFs was blocked. This result demonstrates that contractility of myosin-II stimulated by activated Rho drives the formation of SFs.

Experimental observations have demonstrated that the formation of stress fibres is stimulated by external forces. Franke et al. first demonstrated that critical level of fluid shear stress could induce the formation of stress fibres in endothelial cells (Franke *et al.*, 1984). It was further observed that the cells respond to the shear stress through adjusting their internal structures and strengthen their adhesions with basal substrate and neighbouring cells to resist being removed from the substrate (Galbraith *et al.*, 1998). Application of uniaxial stretch to the cells could bring about stress fibres aligned perpendicular to the direction of stretch (Dartsch and Betz, 1989; Yoshigi *et al.*, 2005) (Figure 2.8). In this process, the zyxin protein was observed to transfer from focal adhesions to actin filaments to thicken the stress fibres upon application of unidirectional cyclic stretch or shear stress to cells (Yoshigi *et al.*, 2005). The mechanical stretch and Rho protein cooperate to regulate the SF organization. In the

absence of Rho activation, the SF oriented in the direction of uniaxial stretch (Watanabe *et al.*, 1999).
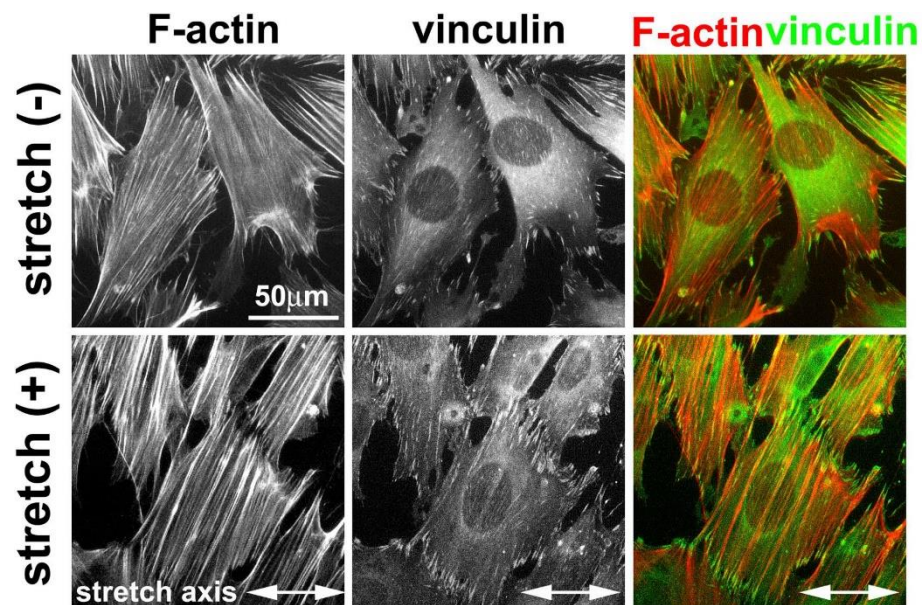
Figure 2.8 Fibroblasts on unstretched membranes (-) or subjected to uniaxial cyclic stretch (+; 1 hour at 15% and 0.5 Hz) aligned and reinforced their actin filaments (phalloidin staining), whereas the focal adhesion protein vinculin remained at adhesion sites (Yoshigi *et al.*, 2005).

2.5.5 Cells sense the physical boundaries and mechanical cues in the materials

1) Critical review about experimental work

As mentioned above, not only the substrate stiffness influence the cell behaviour, but also the geometry of the surrounding material can direct cell activities. In two-dimensional cell culture, cells are usually placed on a layer of substrate supported by a rigid glass base. The variation of the layer thickness is related to the apparent stiffness which the cells can sense (Lin *et al.*, 2010). The thickness sensing of cells has aroused a discussion about how deep the cells can feel, that is the critical thickness value with which the effect from the rigid support can be neglected. Early studies have approximated the substrate as a semi-infinite medium (Balaban *et al.*, 2001; Butler *et al.*, 2002). However, Butler et al. have proposed that the assumption of semi-infinite medium could not be accepted except the substrate displacement induced by the cell and cell size are small compared with the substrate thickness (Butler *et al.*, 2002). The substrate displacements induced by cells have been demonstrated to be higher on thicker substrate (Merkel *et al.*, 2007). Higher levels of SF and FA expression were also observed on thinner gels (Li *et al.*, 2018). To

determine the critical thickness, Engler *et al.* presented the cell spreading area has no difference on substrate with thickness of 5 µm from those on substrate with 70 µm thickness (Engler *et al.*, 2004b). The cell spreading observed by Buxboim *et al.* demonstrated the mesenchymal stem cells started responding to thickness variation at about 10~20 µm with a characteristic tactile length of less than about 5 µm on gels with stiffness of 1 kPa (Buxboim *et al.*, 2010). The experiment by Lin et al. showed the fibroblasts spreading area and traction force plateaued when the gel thickness was beyond 100 µm, which was the same length scale as cell size (Lin *et al.*, 2010). This indicates the stiffness sensing of cells is not just in the vicinity of focal adhesions. Myoblasts have been reported to sense the underlying glass when the substrate thickness was beyond 38 µm in terms of spreading area and differentiation (Li *et al.*, 2018). However, the critical thickness decreased to 18 µm in term of the cell proliferation. This may provide a perspective to the different definitions of critical thickness. Recently, the cell colonies have been demonstrated to sense deeper than isolated cells, highlighting the role of cell-cell interaction in mechanosensing process (Tusan *et al.*, 2018). For materials with different microstructure, the cells could even sense beyond 130 µm away from the substrate surface on fibrous materials due to the force propagation via fibres (Leong *et al.*, 2010; Mullen *et al.*, 2015).

Cells are able to sense the lateral mechanical cues that are located far away from the cell. Work by Lo et al. has shown the migration in response to substrate stretch (Lo *et al.*, 2000). A needle is inserted near the rear side of the cell in the substrate and pulled away from the cell, the cell moves towards the needle. However, when the needle is pushed towards the cell leading edge in the substrate, the cell migrates away from the needle. It is speculated the mechanical input is decreased or increased by the needle, thereby the CSK activity is weakened or strengthened.

Mohammadi et al. developed a rigid grids with different opening sizes to study 3T3 fibroblast cell behaviours on collagen gels (Mohammadi *et al.*, 2014). In smaller grids (200 µm wide), the mean number of cell extensions per cell is almost 2 times higher than that of cells in larger grids. The collagen fibres are more oriented in smaller grids. The matrix displacements in wider grids propagate to 500 µm away from the cell centroid while the displacements in smaller grids are interrupted by the lateral boundaries. Knockdown of β1 integrins or inhibition of non-muscle myosin II activity justified their contribution in lateral boundary sensing.

As cells continuously exert force on the substrate and generate strain gradients in the underlying material, another cell nearby may can sense the lateral strain field in the substrate and change its behaviours. Such cell-cell communication has been studied by Reinhart-King et al. as a function of matrix compliance for Bovine aortic endothelial cells (Reinhart-King *et al.*, 2008). It is demonstrated that cell migration behaviour changes with the strength of mechanical coupling between neighbouring cells. On polyacrylamide soft gels (~0.5 kPa), cells are likely to repeatedly touch neighbouring cells through setting out pseudopodial extension. On gels with intermediate stiffness (2.5~5.5 kPa), cells tend to contact, separate and retouch repeatedly for the duration of experiment. On stiffer gels (~ 33 kPa), cells generally touch and migrate away without the behaviours observed on soft substrate. Based on this observation, they presented the hypothesis that cells locally strain the substrate and create tension gradients and thus influencing the migration of nearby cells. The deformations induced by a cell on stiff substrates do not propagate a detectable distance from the cell edge and therefore cannot communicate through substrate efficiently. The interactions between cells and substrate studied by van Oers et al. also revealed a preferred substrate stiffness for cell-cell communication (van Oers *et al.*, 2014).

Winer et al. have reported that the lateral mechanical sensing ability of cells is dependent on cell type, substrate stiffness, and substrate type (Winer *et al.*, 2009). Fibroblasts have an average spread area of ~1800 μm^2 on polyacrylamide gel with shear modulus of 3.2 kPa. The cells have similar spread area of ~1900 μm^2 on nonlinear strain-stiffening soft fibrin gels with shear modulus of 60 Pa. It is attributed to the strains are applied on the gels by the cells. The soft fibrin gels are stiffened to have shear modulus of 3.7 kPa with 80% strain. Fibroblasts could deform the substrate beyond 250 μm laterally with averaged displacement of 1.5 μm on fibrin gels. However, the hMSCs with higher contractility displace the beads in the substrate up to 450 μm away from the cell centre. The long range force transmission in fibrous matrix is proposed to originate from the strain-induced alignment and strain-hardening behaviour of fibres in the matrix (Wang *et al.*, 2014; Hall *et al.*, 2016; Humphries *et al.*, 2017).

2) Critical review about modelling work

To derive the critical thickness of substrate, analytical and numerical methods have been applied in the cell depth-sensing studies. Maloney et al. have applied the theory

of elasticity to model the displacement and distortion of a focal adhesion with radius of 1 μm (Figure 2.9a) (Maloney *et al.*, 2008). The displacements and distortions in the substrate under the adhesion centre were compared with displacements on the substrate surface. The displacement in the substrate under the adhesion centre has 90% reduction compared to the surface displacement when the point is 3.42 μm (critical thickness) away from the substrate surface. When considering the 90% attenuation of distortion compared to that on the substrate surface, the critical thickness is around 1.58 μm. Different definitions of critical thickness have also been proposed in their work. It was suggested that the definitions of critical thickness should be ordered according to relevance in the design of finite-thickness coatings to elicit a predicted response of adherent cells. The computational model of Sen et al. studied the interfacial displacements and strains to elicit the threshold of gel thickness, which is around 2 μm for gels with stiffness lower than 8 kPa (Figure 2.9b)(Sen *et al.*, 2009). He et al. have modelled the cell as a pre-strained disk with strain of 0.1 (Figure 2.9c). It demonstrated the interaction depth to be the cell radius in terms of displacement decay in the substrate (He *et al.*, 2014).

Cells work as active gels to sense their external environment and exert force on the surrounding materials. To capture the active nature of cells, several models have applied initial stress or thermal strain in the cells to simulate the contraction (Sen *et al.*, 2009; He *et al.*, 2014). Sen *et al.* applied the prestress uniformly in the cells to study the effect of the substrate stiffness and thickness on the cell induced displacements and strains in the material. Alternatively, the internal strains could be generated by applying a temperature drop on the cells to represent the cell contractility (Notbohm *et al.*, 2012; Qu *et al.*, 2013; Nam *et al.*, 2014).
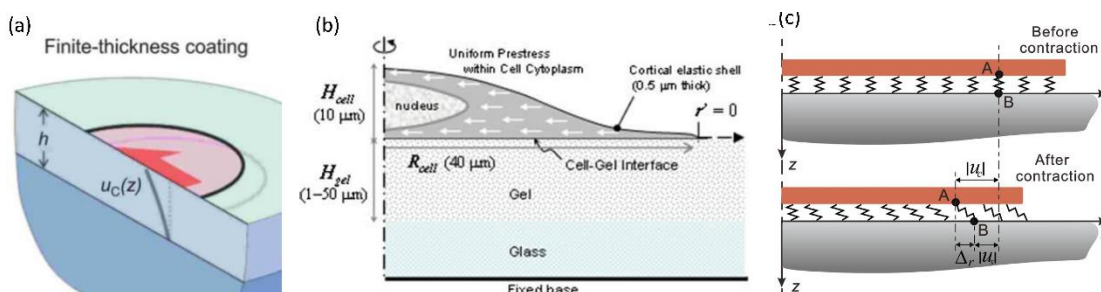
Figure 2.9 Schematics of different models to study cell thickness sensing: (a) focal adhesion area is pulled by a constant force to sense the depth of substrate (Maloney *et al.*, 2008); (b) an axisymmetric cell model consisting of cell cytoplasm and nucleus interacts with substrate with finite thickness (Sen *et al.*, 2009); (c) a layer of cell sense the material properties through cell adhesions (He *et al.*, 2014).

Nevertheless, the intracellular tensions are generated by the contraction of cell SFs along with several biochemical processes. During interactions with substrates, cells also form adhesions to probe the material properties. Therefore, SF and adhesion formation should be taken into account in the cell models. Several models have been developed to study the cell behaviours. Novak *et al.* characterized the adhesions as the local density of integrins bound to matrix, dependent on forces generated by SFs (Novak *et al.*, 2004). Integrins are allowed to diffuse along the cell membrane. The SF formation is dependent on adhesion size with random nucleation. This model was used to demonstrate the periphery localization of focal adhesions. Besser and Schwarz have considered more complicated biochemical and mechanical processes including myosin Ⅱ activation and Rho pathway to form a feedback loop (Besser and Schwarz, 2007). Vernerey and Farsad designed a constrained mixture model that accounts for four major elements of cell contraction: CSK, cytosol, SF and actin monomers (Vernerey and Farsad, 2011). The SF formation is described by mass exchange between actin monomers and polymers. Contraction of SFs is represented by length-tension and velocity-tension relation for muscle cells.

Deshpande *et al.* developed a bio-chemo-mechanical model to simulate the force dependent assembly and disassembly of stress fibres and focal adhesions by incorporating the dynamic reorganization of the CSK (Deshpande *et al.*, 2006) (Figure 2.10). An activation signal that triggers stress fibre formation was proposed in the model. The fibre formation rate was dependent on the activation signal and the dissociation rate of the fibres was dependent on the tension. The contraction rate of the stress fibres was linked to the stress by the cross-bridge dynamics. The model was able to capture the general features observed in experiments including: (1) the decrease of the forces generated by the cell with increasing the substrate compliance; (2) the influence of cell shape and boundary conditions on the development of structural anisotropy; (3) the high concentration of the stress fibres at the focal adhesions. The model has been extended to study the focal adhesions on patterned substrates (Pathak *et al.*, 2008). The model was further refined and applied in several studies to simulate cell behaviours on microposts (McGarry *et al.*, 2009), to study cell behaviours subjected to different loadings(Dowling *et al.*, 2012; Ronan *et al.*, 2012b; Ronan *et al.*, 2012a; Reynolds and McGarry, 2015; Weafer *et al.*, 2015). Recently, it was integrated into stochastic framework to predict the differentiation of

hMSCs in response to a range of environmental cues, including sizes of adhesive islands, stiffness of substrates (Suresh *et al.*, 2019).
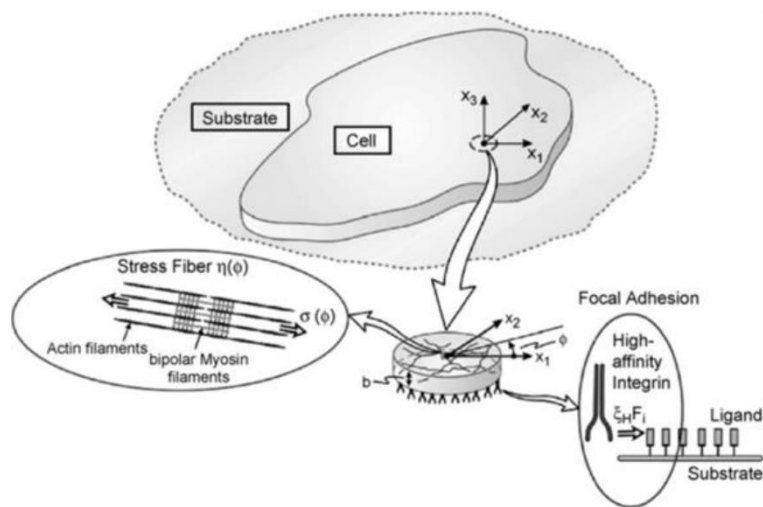
Figure 2.10 Schematic of the bio-mechanical model coupling cell contractility with focal adhesion formation (Deshpande *et al.*, 2008).

2.5.6 Characterisation of mechanical properties of living cells

1) Critical review about experimental work

Cells are exposed to external forces including shear, compression and stretch. Thus, these cells need certain level of stiffness to resist these loads. Changes in cell stiffness may cause disturb cell signalling process and result in diseases. For example, the cells with bladder cancer (Lekka *et al.*, 1999) or breast cancer (Guck *et al.*, 2005) showed a decrease in cell stiffness. An increase of cell stiffness was shown for chondrocytes in arthritis and airway smooth muscle cells (Trickey *et al.*, 2000) in bronchial asthma (An *et al.*, 2006). Therefore, quantifying the mechanical properties of the cells can provide information of the actual condition of the cell. Cell stiffness has been reported to depend on the stiffness of the material on which they adhere. Engler et al. showed that stiffer substrate produced stiffer and more tensed cells (Engler *et al.*, 2006). Solon *et al.* reported that fibroblast cells could adapt their stiffnesses to the values of external substrates with a saturation value of material rigidity of 20 kPa (Solon *et al.*, 2007). The cell stiffening are related to the expression of stress fibres as disruption of CSK components led to the decrease of cell stiffness (Barreto *et al.*, 2013).

To study the mechanical properties of cells, various experimental techniques (such as micropipette aspiration, cytocompression, nanoindentation) have been employed (Lim *et al.*, 2006). Among which, the nanoindentation technique taking advantage of

atomic force microscopy (AFM) has been widely used in experimental studies to probe the cell surface. Round or sharp indenters are selected for different situations. Cells are indented at different positions to collect holistic information due to its different mechanical properties at different positions (Aryaei and Jayasuriya, 2013). The load-depth-time profile is recorded during indentation of cells and interpreted by theoretical models such as Hertz model and its modifications to extract the Young's modulus.

As the cell is a heterogeneous body, the subcellular components including cortex, nucleus, CSK components play important roles in contributing to cell mechanical properties. Harris and Charras probed the Madin–Darby Canine Kidney II (MDCK-II) cells combined with confocal microscopy (Harris and Charras, 2011). They used cytochalasin D and latrunculin B to depolymerize the actin filaments and observed the two-fold decrease in cell elastic modulus. However, depolymerizing the microtubules with Nocodazole only causes ~25% decrease in cell elastic modulus. Inhibiting the myosin contractility has little effect on cell elasticity. Stiffness map presented by Rheinlaender and Schäffer directly showed the decrease throughout the cell after depolymerizing the actin filaments (Rheinlaender and Schäffer, 2013). Gavara and Chadwick have revealed the correlation between SF amounts and cell stiffness in mouse fibroblasts (Gavara and Chadwick, 2016). Aligned or thicker fibres will further reinforce the cell stiffness. The orientation of SFs could even cause non-axisymmetric membrane deformation and give rise to local mechanical anisotropy (Efremov *et al.*, 2019).

2) Critical review about modelling work

To better understand the intrinsic mechanism of cells during AFM measurement, various types of cell models have been developed. Some of the studies simply constructed part of the cells to explain their research questions (Chen and Lu, 2012; Garcia and Garcia, 2018; Efremov *et al.*, 2019; Guerrero *et al.*, 2019) (Figure 2.11c), or modelled the cells with simple geometry consisting of nucleus, membrane and cytoplasm (Vichare *et al.*, 2012; Ding *et al.*, 2017; Liu *et al.*, 2019) (Figure 2.11a and b). Gurrero et al. visualized the subcellular organelles with high-resolution AFM (Guerrero *et al.*, 2019). They developed a simple finite element model and illustrated the displacing the indenter away from the underlying SF decreases the apparent modulus of cells. Other subcellular components also have their contributions to cell stiffness. Vargas-Pinto et al. proposed that the presence of cell cortex could

contribute to the cell stiffness with overestimated stiffness when measured by sharp AFM tips (Vargas-Pinto *et al.*, 2013). Coceano et al. highlighted the nuclear region measurement of cell viscoelastic properties (Coceano *et al.*, 2015). However, the subcellular components could be perceived by the AFM tips (Guerrero *et al.*, 2019). These simple models do not reflect the contributions of cell complex structure to cell stiffness. To capture the heterogeneous feature of the cells, structure-based models are developed. Based on the idea that the living CSK is stabilized by the internal tensile prestress, the tensegrity model represents the CSK components with discrete elements (Ingber, 2003). The tension generating actin filaments are modelled as cables which were connected to struts that represents compression bearing microtubules. Barreto et al. have proposed a multi-structure cell model, which consists of cell cortex, cytoplasm, nucleus, SFs and microtubules (Barreto *et al.*, 2013) (Figure 2.11d). Prestress is applied in the SFs. Removal of microbutules or cell cortex both decrease the cell stiffness to nearly half of that of intact cell. However, the disruption of actin bundles has little influence on the cell stiffness. This research highlighted the importance of CSK elements in cell mechanics.
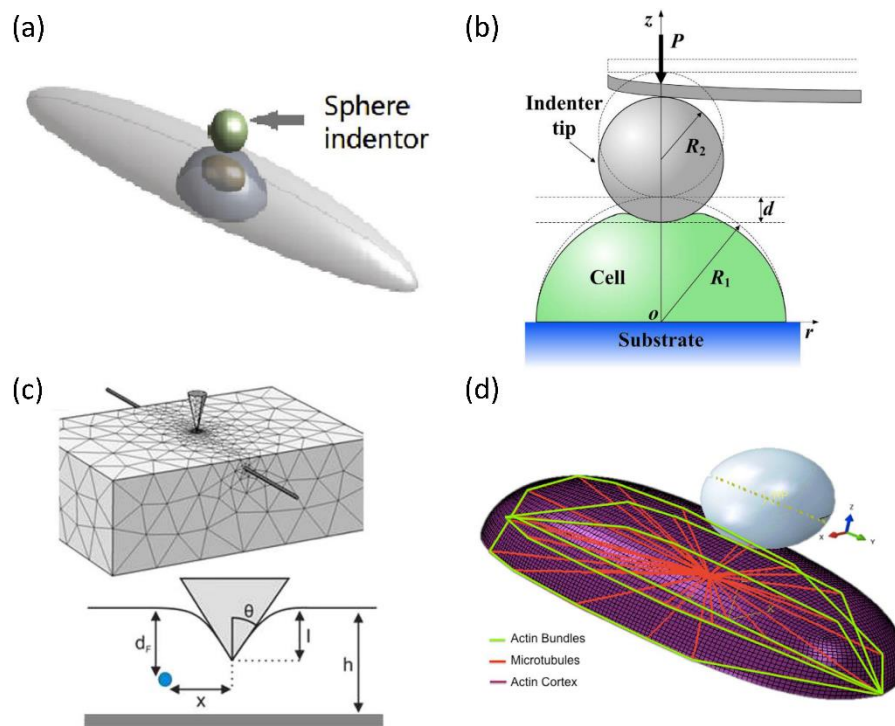
Figure 2.11 AFM indentation models from literature: (a) finite element cell model consisting of cell membrane, cytoplasm, nucleus and nucleolus (Liu *et al.*, 2019); (b) schematic of indentation of a hemispherical cell (Ding *et al.*, 2017); (c) schematic of indentation of a conical indenter on top of a SF (Guerrero *et al.*, 2019); (d) schematic of indentation of a structure-based cell model consisting of actin bundles, microtubules and actin cortex (Barreto *et al.*, 2014).

Chapter 3. Model Development

3.1 Introduction

This chapter describes two types of cell models including structure-based and continuum-based models. For the former, it is specially developed to understand the spatial dependent mechanical properties of cell during nanoindentation tests (Chapter 4). For the latter, it laid the foundation to study the role of stress fibres (SFs) in cell-material interactions (Chapter 5) and cell crosstalk (Chapter 6). In this chapter, we will explain these models, the key algorithms used and the key principles to implement these models via in-house developed code (Fortran) interfacing with the commercial finite element software (ABAQUS).

3.2 Structure-based cell model for nanoindentation tests

The structure-based cell model is an FE model of a representative adherent Human Bone Osteosarcoma Epithelial Cells (U2OS) developed in Abaqus 6.14. The cell geometry as described in (Barreto *et al.*, 2013; Barreto *et al.*, 2014) was used, which was also a representation of experimental measurements. The cell was constructed as semi-ellipsoid like shape with 19 μm length and 4 μm width. Although the real cell consists of various components, the model only considered key intracellular components such as nucleus, cytoplasm, cytoskeleton elements and a layer of actin cortex attached on the cytoplasm (Figure 3.1). Compared to its underlying cortex layer, the cell membrane has negligible contribution to mechanical stiffness of the whole cell. Thus, the thin cell membrane (~10nm) was not considered in the FE modelling. The cortex with a thickness of 0.2 μm was implemented in the finite element model. The nucleus was placed 0.5 μm away from the bottom surface. The actin stress fibre, a major component of cytoskeleton was modelled with prestrain. The equivalent prestress in the stress fibres is implemented in the model by user subroutine (UMAT). These stress fibres and microtubules were attached on the cell cortex or cell-material adhesions. The model includes 32 stress fibre elements and 33 microtubules in total. Although the number of the stress fibres is less than the amount in real cells, it can be regarded by stress fibre bundles which could represent the heterogeneity of the cell structure with good computational efficiency. The microtubules were modelled as star-shape structure emanating from a point near the nucleus membrane to represent that they originate from the centrosome.

Detailed description of the model will be presented in Chapter 4. In the method described above, the cell is passive with pre-strain, which is sufficient to capture the spatial-dependent cell mechanical properties which are often measured based on quasi-static tests. However, such a model cannot capture any active behaviours of cell (e.g. how it actively responds to the materials with different properties).
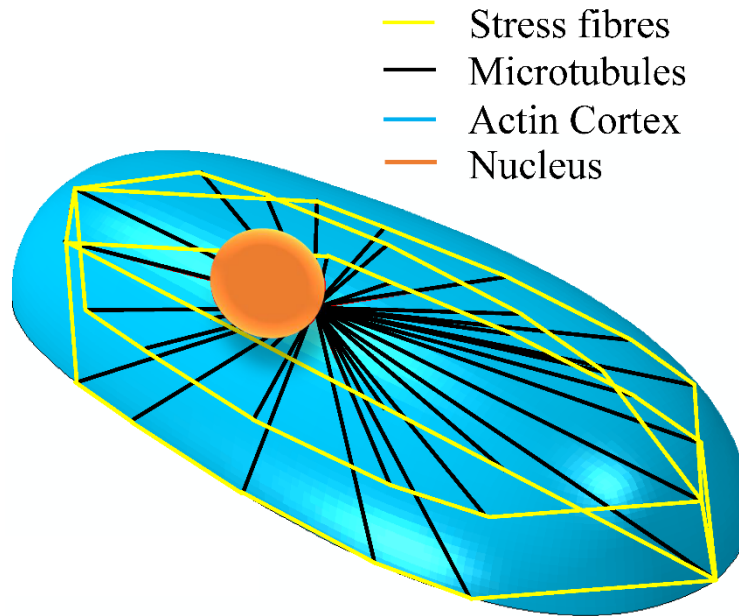
Figure 3.1 Structure-based cell model.

Theoretically, the above 3D structural based model can be dramatically improved by replacing the passive structures with active structures to enable the prediction of cell-materials interactions. However, the dynamical change of individual fibres in living cells will be very challenging and extremely expensive in terms of computational time. Therefore, continuum-based model has been proposed which can effectively capture the key features about the role of active stress fibres on cell-materials interactions and cell crosstalk. In this case, we need to consider the continuum model for the cell as active material (stress fibre formation and dissociation) and the adhesion model between the cell and materials. We will start with the description of the cell model.

3.3 Continuum-based cell model

The following section presents the details of the continuum-based cell model, which includes SF formation model and focal adhesion formation model.

3.3.1 Stress fibre formation model

Most living cells not only bear external forces as passive solids, but also actively generate contractile forces. The forces are mainly provided by the stress fibre (SF)

contractile bundles. As reviewed in Chapter 2, some key experimental observations should be considered for the development of SF formation model: (1) Cells respond to the external force perturbations and (2) sense the stiffness of underlying substrate.

The mechanical responses of SFs are summarized as three coupled phenomena: (1) An activation signal is essential to trigger the formation of actomyosin contractile units. (2) SF formation rate is dependent on the activation signal and the dissociation rate is dependent on the contraction force. (3) The contraction rate of SFs is related to the strain rate.

We choose the SF concentration rate formulation (Deshpande *et al.*, 2006) in 2D space as

$$\dot{\eta}(\phi) = \left(1 - \eta(\phi)\right)C\frac{k_f}{\theta} - (1 - \kappa)\eta(\phi)\frac{k_b}{\theta} \qquad (3.1)$$

where $\eta(\phi)$ is SF concentration at angle ϕ with the over-dot denoting the time derivative. k_f is the fiber association rate and k_b is the dissociation rate. C is the activation signal. $\kappa = \sigma(\phi)/\sigma_o(\phi)$ is ratio of active stress to isometric stress $\sigma_o(\phi)$, where

$$\sigma_o(\phi) = \eta(\phi)\sigma_{max} \qquad (3.2)$$

where σ_{max} being the maximum stress allowed in the SF.

This formulation means when the stress of SF is lower than isometric stress, the SF associates dependent on the signal and dissociates dependent on the stress inside. With the stress is higher than the isometric stress, the SFs will no longer dissociate.

The activation signal is provided by Deshpande et al. (Deshpande *et al.*, 2006).

$$C = e^{-\frac{t}{\theta}} \qquad (3.3)$$

where C represents the level of Ca^{2+} signal. t is the time and θ is the decay constant of time. The diffusion of the Ca^{2+} signal is faster than other time scales, therefore it is assumed the distribution of the signal is homogeneous along the cell membrane.

3.3.2 Contractile behaviour of stress fibres

The contraction behaviour of SFs is usually modelled by the Hill-based muscle contraction model, in which the stress in the fibre is dependent on the strain rate. Hence, the variation of stress in the SF (Deshpande *et al.*, 2006) is given by

$$\frac{\sigma(\phi)}{\sigma_o(\phi)} = \begin{cases} 0 & \dfrac{\dot{\varepsilon}}{\dot{\varepsilon}_o} < -\dfrac{\eta}{\bar{k}_v} \\[2mm] 1 + \dfrac{\bar{k}_v}{\eta}\left(\dfrac{\dot{\varepsilon}}{\dot{\varepsilon}_o}\right) & -\dfrac{\eta}{\bar{k}_v} \le \dfrac{\dot{\varepsilon}}{\dot{\varepsilon}_o} \le 0 \\[2mm] 1 & \dfrac{\dot{\varepsilon}}{\dot{\varepsilon}_o} > 0 \end{cases} \qquad (3.4)$$

where ε is the strain in a single stress fibre; $\bar{k}_v$ is the dimensionless constant for the dissociation of contraction and $\dot{\varepsilon}_o$ is the strain rate sensitivity parameter. This equation describes that the SF has no stress when in contraction while maintains isometric stress with high strain rate in stretch.
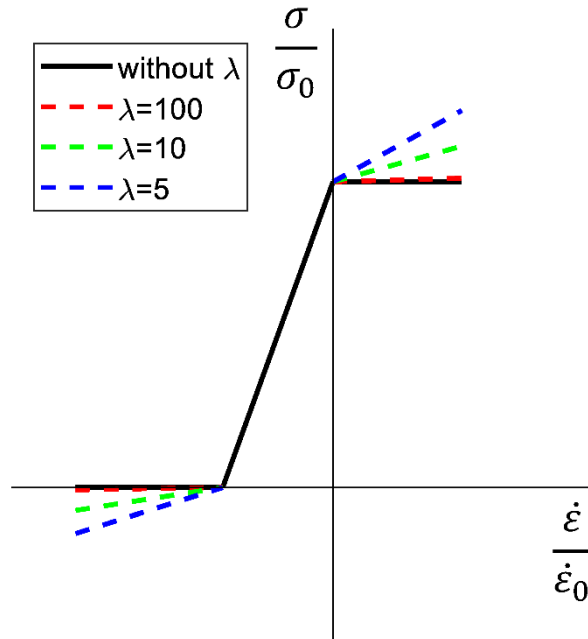
Figure 3.2 The modified Hill contraction model with different values of λ.

To improve the numerical efficiency, a parameter λ is introduced to allow the fibre stress to be slightly higher than the isometric value and to go slightly negative.

$$\frac{\sigma(\phi)}{\sigma_o(\phi)} = \begin{cases} \frac{1}{\lambda} + \frac{\bar{k}_v}{\eta\lambda}\left(\frac{\dot{\varepsilon}}{\dot{\varepsilon}_o}\right) & \frac{\dot{\varepsilon}}{\dot{\varepsilon}_o} < -\frac{\eta}{\bar{k}_v} \\ 1 + \frac{\bar{k}_v}{\eta}\left(\frac{\dot{\varepsilon}}{\dot{\varepsilon}_o}\right) & -\frac{\eta}{\bar{k}_v} \leq \frac{\dot{\varepsilon}}{\dot{\varepsilon}_o} \leq 0 \\ 1 + \frac{\bar{k}_v}{\eta\lambda}\left(\frac{\dot{\varepsilon}}{\dot{\varepsilon}_o}\right) & \frac{\dot{\varepsilon}}{\dot{\varepsilon}_o} > 0 \end{cases} \qquad (3.5)$$

Fibre stress-strain curve with different values of λ are compared to the original curve (Figure 3.2). In current study, λ is chosen to be 100.

3.3.3 Two-dimensional cell model

To model the anisotropic SF contraction behaviour, a 2D cell model is presented in this part. The characteristics of SFs are implemented in user defined material model (UMAT) of Abaqus (Version 6.14, Dassault Systemes, RI, USA).

1) Deformation and Rotations of an arbitrary fibre within an RVE

From the perspective of material properties, each material point of the cell is described by a representative volume element (RVE) (Figure 3.3). The RVE is comprised of several SFs contracting at orientation angles ϕ. Due to the deformation of the material, the orientation of the fibres will change with the rigid body rotations of material point.

$$\phi = \phi' + \frac{1}{2}\int_0^t \left(\frac{\partial \dot{u}_2}{\partial x_1} - \frac{\partial \dot{u}_1}{\partial x_2}\right) dt \qquad (3.6)$$

where $\dot{u}_i$ are the displacement rates and ϕ' is the orientation angle without considering material rigid body rotations. The strain rate in k-th fibre is obtained from the material strain rate by

$$\dot{\varepsilon}(\phi_k) = \dot{\varepsilon}_{11}cos^2\phi_k + \dot{\varepsilon}_{22}sin^2\phi_k + \dot{\varepsilon}_{12}sin2\phi_k \qquad (3.7)$$

2) Numerical integration of the RVE

After homogenization analysis, the active stress within the RVE is formulated as

$$\sigma_{ij}^a = \frac{1}{\pi}\int_{-\frac{\pi}{2}}^{\frac{\pi}{2}} \begin{pmatrix} \sigma(\phi)cos^2\phi & \frac{1}{2}\sigma(\phi)sin2\phi \\ \frac{1}{2}\sigma(\phi)\,sin\,2\phi & \sigma(\phi)sin^2\phi \end{pmatrix} d\phi \qquad (3.8)$$

To calculate the total active stress, numerical methods are employed to add up the contributions from each fibre. The trapezoidal integration scheme is applied over the range $[-\frac{\pi}{2}, \frac{\pi}{2}]$ with n intervals.

$$\int_a^b f(x)\,dx = \sum_{k=1}^{n-1} \frac{\Delta x}{2}(f(x_k) + f(x_{k+1})) = \frac{\Delta x}{2}f(x_1) + \Delta x \cdot \sum_{k=2}^{n-1} f(x_k) + \frac{\Delta x}{2}f(x_n) \quad (3.9)$$

For example, the σ_{11}^a can be expressed as

$$\sigma_{11}^a = \frac{1}{\pi} \int_{-\frac{\pi}{2}}^{\frac{\pi}{2}} \sigma(\phi)\cos^2\phi\,d\phi = \frac{1}{2n} \sum_{k=1}^{n} (\sigma(\phi_k)\cos^2\phi_k + \sigma(\phi_{k+1})\cos^2\phi_{k+1}) \quad (3.10)$$

where $\sigma(\phi_{n+1}) = \sigma(\phi_1)$.
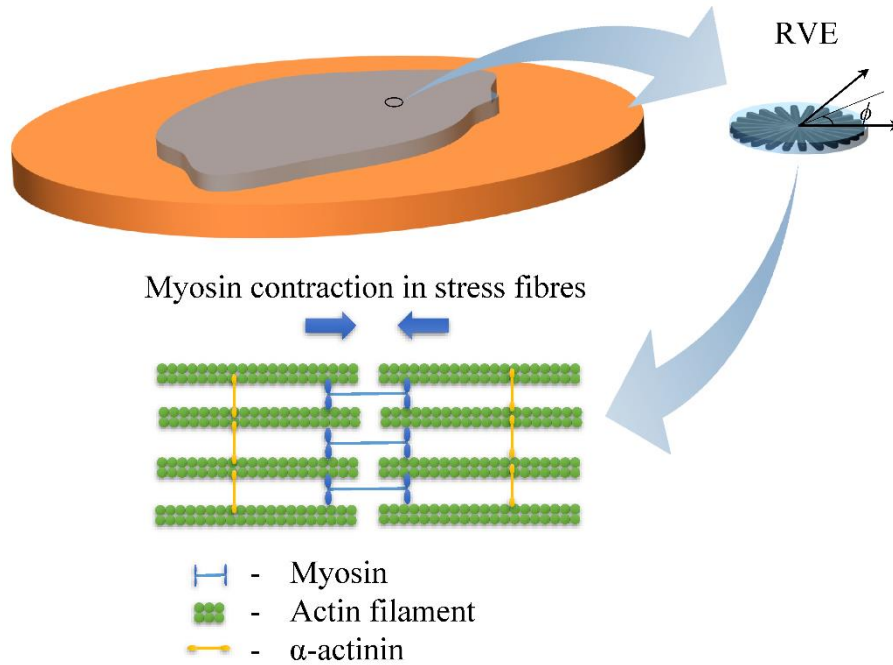
Figure 3.3 Two-dimensional cell model with stress fibre formation.

3) Constitutive Jacobian terms

The Jacobian matrix is required in UMAT in each iteration. The Jacobian matrix has three situations with different fibre contraction state. In this part, we present the deduction of Jacobian matrix.

The central difference method is applied to derive the partial differentiations. The central difference operators are

$$\dot{f}_{t+\frac{\Delta t}{2}} = \frac{\Delta f}{\Delta t}$$

$$f_{t+\frac{\Delta t}{2}} = f_t + \frac{\Delta f}{2} \tag{3.11}$$

Applying the central difference operator to the fibre strain rate equation (3.7), we can obtain

$$\Delta\varepsilon(\phi_k) = \Delta\varepsilon_{11} \cdot cos^2\phi_k + \Delta\varepsilon_{22} \cdot sin^2\phi_k + \Delta\varepsilon_{12} \cdot sin2\phi_k \tag{3.12}$$

Then the partial derivatives of fibre strain $\Delta\varepsilon(\phi_k)$ with respect to material strains are

$$\frac{\partial\Delta\varepsilon(\phi_k)}{\partial\Delta\varepsilon_{11}} = cos^2\phi_k$$

$$\frac{\partial\Delta\varepsilon(\phi_k)}{\partial\Delta\varepsilon_{22}} = sin^2\phi_k$$

$$\frac{\partial\Delta\varepsilon(\phi_k)}{\partial\Delta\varepsilon_{12}} = sin2\phi_k \tag{3.13}$$

Section 1: $\frac{\dot{\varepsilon}}{\dot{\varepsilon}_o} < -\frac{\eta}{\bar{k}_v}$

Substitute equation (3.2) into equation (3.5), we can obtain

$$\sigma = \left(\frac{\eta}{\lambda} + \frac{\bar{k}_v}{\lambda}\left(\frac{\dot{\varepsilon}}{\dot{\varepsilon}_o}\right)\right) \cdot \sigma_{max} \tag{3.14}$$

Apply the central difference operators in equation (3.14), we get

$$\frac{1}{2}\Delta\sigma + \sigma = \left(\frac{\frac{1}{2}\Delta\eta + \eta}{\lambda} + \frac{\bar{k}_v}{\Delta t \cdot \lambda}\left(\frac{\Delta\varepsilon}{\dot{\varepsilon}_o}\right)\right) \cdot \sigma_{max} \tag{3.15}$$

The partial derivative of fibre stress to strain is

$$\frac{\partial\Delta\sigma}{\partial\Delta\varepsilon} = \left(\frac{\partial\Delta\eta}{\partial\Delta\varepsilon} + \frac{2\bar{k}_v}{\Delta t \cdot \dot{\varepsilon}_o}\right) \cdot \frac{\sigma_{max}}{\lambda} \tag{3.16}$$

To get the term $\frac{\partial\Delta\eta}{\partial\Delta\varepsilon}$, we apply the central difference operators in equation (3.1), we obtain

$$\frac{\Delta\eta}{\Delta t} = \left(1 - \eta - \frac{1}{2}\Delta\eta\right)\frac{k_f C^*}{\theta} - \left(\eta + \frac{1}{2}\Delta\eta\right)\frac{k_b}{\theta} \tag{3.17}$$

where $C^* = C + \frac{\Delta C}{2}$. Then we find

$$\frac{\partial\Delta\eta}{\partial\Delta\varepsilon} = 0 \tag{3.18}$$

Therefore:

$$\frac{\partial\Delta\sigma}{\partial\Delta\varepsilon} = \frac{2\bar{k}_v \cdot \sigma_{max}}{\Delta t \cdot \dot{\varepsilon}_o \cdot \lambda} \tag{3.19}$$

Section 2: $-\frac{\eta}{\bar{k}_v} \leq \frac{\dot{\varepsilon}}{\dot{\varepsilon}_o} \leq 0$

Similarly, we can write the fibre stress as

$$\sigma = \left(\eta + \bar{k}_v\left(\frac{\dot{\varepsilon}}{\dot{\varepsilon}_o}\right)\right) \cdot \sigma_{max} \tag{3.20}$$

Apply the central difference operators:

$$\frac{1}{2}\Delta\sigma + \sigma = \left(\frac{1}{2}\Delta\eta + \eta + \frac{\bar{k}_v}{\Delta t}\left(\frac{\Delta\varepsilon}{\dot{\varepsilon}_o}\right)\right) \cdot \sigma_{max} \tag{3.21}$$

Perform the partial differentiation:

$$\frac{\partial\Delta\sigma}{\partial\Delta\varepsilon} = \frac{\partial\Delta\eta}{\partial\Delta\varepsilon} \cdot \sigma_{max} + \frac{2\bar{k}_v}{\Delta t \cdot \dot{\varepsilon}_o} \cdot \sigma_{max} = \frac{\partial\Delta\eta}{\partial\Delta\sigma}\frac{\partial\Delta\sigma}{\partial\Delta\varepsilon} \cdot \sigma_{max} + \frac{2\bar{k}_v}{\Delta t \cdot \dot{\varepsilon}_o} \cdot \sigma_{max} \tag{3.22}$$

We can rewrite it as

$$\frac{\partial\Delta\sigma}{\partial\Delta\varepsilon} = \frac{\frac{2\bar{k}_v}{\Delta t \cdot \dot{\varepsilon}_o} \cdot \sigma_{max}}{1 - \frac{\partial\Delta\eta}{\partial\Delta\sigma} \cdot \sigma_{max}} \tag{3.23}$$

Apply the central difference operators in equation (3.1):

$$\frac{\Delta\eta}{\Delta t} = \left(1 - \eta - \frac{1}{2}\Delta\eta\right)\frac{k_f C^*}{\theta} - \left(\eta + \frac{1}{2}\Delta\eta - \frac{\frac{1}{2}\Delta\sigma + \sigma}{\sigma_{max}}\right)\frac{k_b}{\theta} \tag{3.24}$$

We can get:

$$\frac{\partial \Delta \eta}{\partial \Delta \sigma} = \frac{k_b}{\sigma_{max}(\frac{2\theta}{\Delta t} + k_f C^* + k_b)} \tag{3.25}$$

Therefore:

$$\frac{\partial \Delta \sigma}{\partial \Delta \varepsilon} = \frac{2\bar{k}_v}{\Delta t \cdot \dot{\varepsilon}_o} \cdot \sigma_{max} \left(1 + \frac{k_b}{\frac{2\theta}{\Delta t} + k_f C^*} \right) \tag{3.26}$$

Section 3: $\frac{\dot{\varepsilon}}{\dot{\varepsilon}_o} > 0$

According to the equation (3.5), the fibre stress is written as

$$\sigma = \left(\eta + \frac{\bar{k}_v}{\lambda} \left(\frac{\dot{\varepsilon}}{\dot{\varepsilon}_o} \right) \right) \cdot \sigma_{max} \tag{3.27}$$

Apply the central difference operators and perform the partial differentiation, we find

$$\frac{\partial \Delta \sigma}{\partial \Delta \varepsilon} = \frac{\partial \Delta \eta}{\partial \Delta \varepsilon} \cdot \sigma_{max} + \frac{2\bar{k}_v}{\Delta t \cdot \dot{\varepsilon}_o \cdot \lambda} \cdot \sigma_{max} \tag{3.28}$$

We use the same method in Section 1 and get

$$\frac{\partial \Delta \eta}{\partial \Delta \varepsilon} = 0 \tag{3.29}$$

Therefore:

$$\frac{\partial \Delta \sigma}{\partial \Delta \varepsilon} = \frac{2\bar{k}_v \cdot \sigma_{max}}{\Delta t \cdot \dot{\varepsilon}_o \cdot \lambda} \tag{3.30}$$

4) Passive behaviour of material point

The passive behaviour of the cell is assumed to be elastic to represent the cellular components excluding SFs. In the 2D model, nucleus is neglected. The total Cauchy stress in the cell is calculated by adding active SF stress and passive stress together.

$$\sigma_{ij} = \sigma_{ij}^a + \sigma_{ij}^p \tag{3.31}$$

The passive behaviour of the cell material is elastic with constitutive stress-strain relationship:

$$\sigma_{ij}^p = S_{ij}F_{im}F_{jn} = \frac{1}{J}\left(\frac{E_c\nu}{1-\nu^2}E_{kk}\delta_{mn} + \frac{E_c}{1+\nu}E_{mn}\right)F_{im}F_{jn} \qquad (3.32)$$

where S_{ij} is the second Piola-Kirchhoff stress, F_{ij} is the deformation gradient and J is the determinant of $\boldsymbol{F}$, E_c is the material properties of cell cytoplasm.

3.3.4 Focal Adhesions Model

A cell makes contact to the materials via the formation of focal adhesion. Therefore, the focal adhesion model adopted in this project will be explained below.

1) Thermodynamics of focal adhesion proteins

Focal adhesions (FAs) are multi-protein structures that form mechanical links between the ECM and cell cytoskeleton. They transduce external mechanical signals into intracellular signals to direct cell behaviorus. FAs consists of integrins, talilns, paxillin and tensin. Integrins are transmembrane receptors that bind the substrate ligands and activating signal transduction pathways. Integrins play the most important role in cell mechanosensing process. Experimental observations have revealed that integrins have two configurations: bent or low affinity state and straight or high affinity state (Figure 3.3a) (Takagi *et al.*, 2002). Due to the geometrical configuration, only the high affinity integrins are allowed to form bounds with substrate ligand. The low affinity integrins can move along the cell membrane. The two integrin states can convert into the other state based on thermodynamic process.

The chemical potential of low affinity integrins at certain position (Deshpande *et al.*, 2008) is

$$\chi_L = \mu_L + kT\ln(\xi_L/\xi_R) \qquad (3.33)$$

where μ_L is the reference chemical potential of low affinity integrins, ξ_L is low affinity integrins density and ξ_R is the reference integrin density, k is the Boltzmann constant and T is the absolute temperature. High affinity integrins have a chemical potential

$$\chi_H = \mu_H + kT\ln(\xi_H/\xi_R) + \Phi(\Delta_e) - F\Delta_e \qquad (3.34)$$

where μ_H is the reference chemical potential of high affinity integrins, ξ_H is the high affinity integrins density. Upon binding with substrate ligands, the bonds between high affinity integrins and ligands will be stretched with the movement of cell

membrane. $\Phi(\Delta_e)$ is the energy stored in the bonds due to stretch and $F\Delta_e$ is the mechanical work done by stretching. Δ_e is the effective stretch of the bonds.

To achieve thermodynamic equilibrium along the cell membrane, the chemical potentials of low and high affinity integrins should fulfill the requirement

$$\chi_H = \chi_L \tag{3.35}$$

Here, we neglected the diffusion of integrins due to the small time scale of diffusion compared to other molecular time scales. The variation of proteins due to changes of membrane deformation is also neglected. The initial integrin density of both types is assumed to be ξ_0.
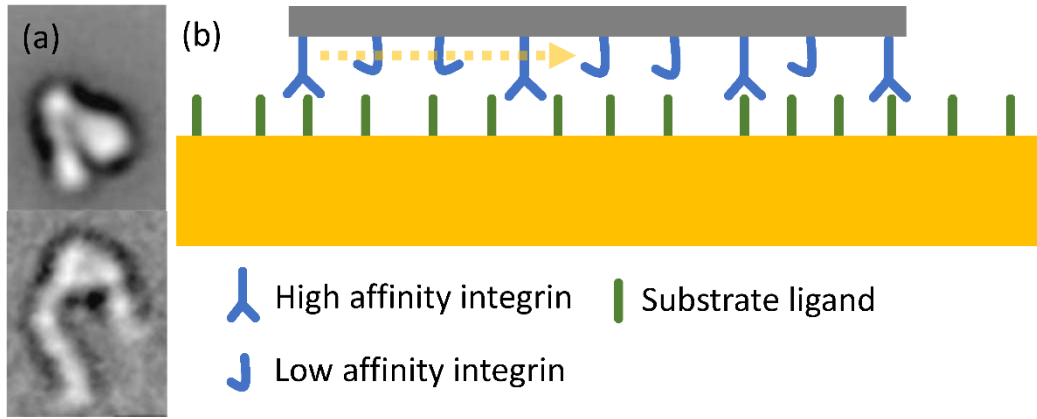
Figure 3.4 Integrins have two configurations: low affinity (top) and high affinity (bottom) (Takagi *et al.*, 2002). (b) Integrins slide over the substrate ligands.

Substitute equation (3.33-3.34) into (3.35), the relationship between ξ_L and ξ_H is

$$\frac{\xi_L}{\xi_H} = exp\left(\frac{\mu_H - \mu_L + \Phi(\Delta_e) - F\Delta_e}{kT}\right) \tag{3.36}$$

The total integrin density at each material point is $\xi_L + \xi_H = \xi_0$. Therefore, the low and high affinity integrin densities can be obtained by

$$\xi_L = (\xi_0 - \xi_L) \cdot exp\left(\frac{\mu_H - \mu_L + \Phi(\Delta_e) - F\Delta_e}{kT}\right) \tag{3.37}$$

$$\left(1 + exp\left(\frac{\mu_H - \mu_L + \Phi(\Delta_e) - F\Delta_e}{kT}\right)\right)\xi_L$$
$$= \xi_0 \cdot exp\left(\frac{\mu_H - \mu_L + \Phi(\Delta_e) - F\Delta_e}{kT}\right) \tag{3.38}$$

$$\xi_L = \frac{\xi_0 \cdot exp\left(\frac{\mu_H - \mu_L + \Phi(\Delta_e) - F\Delta_e}{kT}\right)}{1 + exp\left(\frac{\mu_H - \mu_L + \Phi(\Delta_e) - F\Delta_e}{kT}\right)} \tag{3.39}$$

$$\xi_H = \frac{\xi_0}{exp\left(\frac{\mu_H - \mu_L + \Phi(\Delta_e) - F\Delta_e}{kT}\right) + 1} \tag{3.40}$$

The interactions between integrins and ligands are modelled as relative sliding. The stretch energy is represented by the formulation (Deshpande *et al.*, 2008)

$$\Phi(\Delta_e) = \begin{cases} \frac{1}{2}\lambda_s\Delta_e^2 & \Delta_e \leq \Delta_n \\ -\lambda_s\Delta_n^2 + 2\lambda_s\Delta_n\Delta_e - \frac{1}{2}\lambda_s\Delta_e^2 & \Delta_n < \Delta_e \leq 2\Delta_n \\ \lambda_s\Delta_n^2 & \Delta_e > 2\Delta_n \end{cases} \tag{3.41}$$

where λ_s is the integrin-ligand bound stiffness. Δ_n is the peak length of the bound.

The force in the bound is related to the energy via

$$F = \frac{\partial\Phi(\Delta_e)}{\partial\Delta_e} \tag{3.42}$$

Hence, the force-stretch relation is

$$F = \begin{cases} \lambda_s\Delta_e & \Delta_e \leq \Delta_n \\ 2\lambda_s\Delta_n - \lambda_s\Delta_e & \Delta_n < \Delta_e \leq 2\Delta_n \\ 0 & \Delta_e > 2\Delta_n \end{cases} \tag{3.43}$$

2) Passive tractions between cell membrane and substrate

The cell-substrate interaction force can be considered as combination of specific and non-specific forces. Specific force refers to the interaction force between receptor and ligand, while non-specific forces arise from Van der Waals, electrostatic forces and hydrogen bonding. The non-specific force between cell and substrate is averaged throughout the cell membrane and is supposed to work only in the normal direction. It is assumed to be active on the area without integrins, while the non-specific force on integrins is neglected due to its low value compared to specific force in the bonds. The force-separation relationship (Ronan *et al.*, 2011) is defined by

$$T_1^P = \varphi_0^P \frac{\Delta_1}{\delta_p^2} e^{-\frac{\Delta_1}{\delta_p}} \tag{3.44}$$

where Δ_1 is the normal separation. The constant δ_p is the passive characteristic distance, and the constant φ_0^P is the passive interaction potential.

3) Bond stretching

The mixed mode bond stretching in 3D interface can be described in three states: (1) bond forms when the bond length Δ_e is greater than a threshold length Δ_0. It stretches until the bond force reaches peak value with length Δ_n ($\Delta_0 \leq \Delta_e < \Delta_n$); (2) bond slides until it is perpendicular to the substrate while maintaining peak bond length ($\Delta_e = \Delta_n$); (3) bond keeps stretching beyond the length Δ_n until the break of bond ($\Delta_n \leq \Delta_e \leq 2\Delta_n$).

4) Constitutive Jacobian terms

When implemented in the Abaqus user subroutine (UINTER), the focal adhesions model should consider the evolution of Jacobian matrix for the numerical integration. The relative displacements in three directions provided by UINTER should be adjusted to calculate the effective stretch due to the bond sliding. The relative displacement in UINTER is denoted by Δ_i (i=1,2,3).

Case 1: $\Delta_0 \leq \Delta_e < \Delta_n$

The normal force on the cell surface at each position consists of the binding force and normal non-specific force.

$$T_1 = -T_1^P - F_1 \xi_H \tag{3.45}$$

We may derive some partial derivatives of the terms on the right-hand side in equation (3.43). These partial derivatives are

$$\frac{\partial T_1^P}{\partial \Delta_j} = \frac{\varphi_0^P}{\delta_p^2} e^{-\frac{\Delta_1}{\delta_p}} \left(1 - \frac{\Delta_1}{\delta_p} \right) \delta_{1j} \ (j = 1,2,3.) \tag{3.46}$$

$$\frac{\partial F_i}{\partial \Delta_j} = \lambda_s \delta_{ij} (i, j = 1,2,3.) \tag{3.47}$$

$$\frac{\partial \xi_H}{\partial \Delta_j} = \frac{\lambda_s \xi_0 q_1 \Delta_j}{kT(q_1 + 1)^2} \, (j = 1,2,3.) \tag{3.48}$$

where

$$q_1 = \exp\left(\frac{\mu_H - \mu_L - \frac{1}{2}\lambda_s(\Delta_{tot})^2}{kT}\right) \tag{3.49}$$
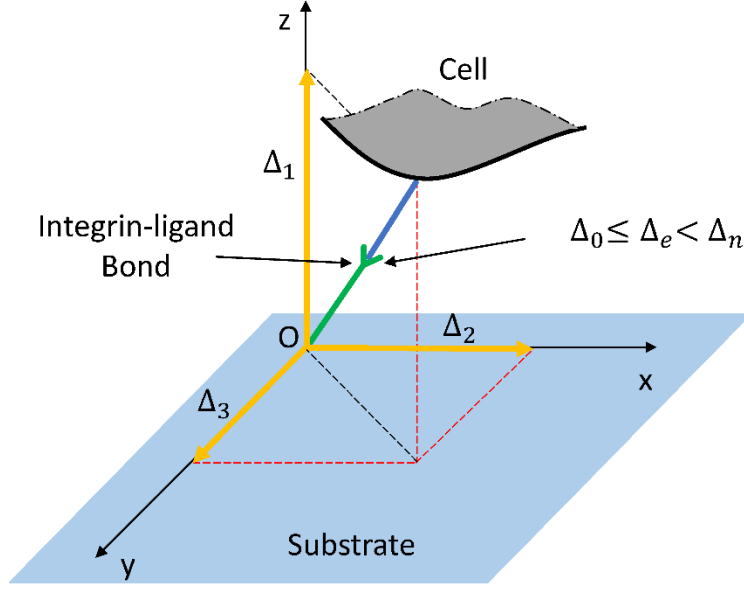
Figure 3.5 Schematic of integrin-ligand bond interaction during stretch. The origin of the coordinate denotes the position of the ligand in binding. Red dashed lines denote the relative displacement between cell and substrate in the three directions of axes.

Substitute equation (3.44-3.46) into equation (3.43)

$$\frac{\partial T_1}{\partial \Delta_j} = -\left(\frac{\partial T_1^P}{\partial \Delta_j} + \frac{\partial F_1}{\partial \Delta_j}\xi_H + \frac{\partial \xi_H}{\partial \Delta_j}F_1\right) \tag{3.50}$$

$$\frac{\partial T_1}{\partial \Delta_j} = -\left(\frac{\varphi_0^P}{\delta_p^2}e^{-\frac{\Delta_1}{\delta_p}}\left(1 - \frac{\Delta_1}{\delta_p}\right)\delta_{1j} + \delta_{1j}\frac{\lambda_s\xi_0}{q_1 + 1} + \frac{\lambda_s^2\xi_0 q_1 \Delta_1 \Delta_j}{kT(q_1 + 1)^2}\right) \tag{3.51}$$

The tangential forces are:

$$T_i = -F_i\xi_H \, (i = 2,3.) \tag{3.52}$$

Therefore, the tangential Jacobian terms are

46

$$\frac{\partial T_i}{\partial \Delta_j} = -\left(\frac{\partial F_i}{\partial \Delta_j}\xi_H + \frac{\partial \xi_H}{\partial \Delta_j}F_i\right)(i = 2,3. j = 1,2,3.) \tag{3.53}$$

Substitute equations (3.44-3.45) into equation (3.49)

$$\frac{\partial T_i}{\partial \Delta_j} = -\left(\delta_{ij}\frac{\lambda_s \xi_0}{q_1+1} + \frac{\lambda_s^2 \xi_0 q_1 \Delta_i \Delta_j}{kT(q_1+1)^2}\right)(i = 2,3. j = 1,2,3.) \tag{3.54}$$

Case 2: $\Delta_e = \Delta_n$

The bonds keep sliding on the substrate while maintaining the bond length Δ_n. The high affinity integrin density keeps constant during this sliding situation due to constant bond force.

$$\xi_H = \frac{\xi_0}{q_2+1} \tag{3.55}$$

where

$$q_2 = \exp\left(\frac{\mu_H - \mu_L - \frac{1}{2}\lambda_s \Delta_n^2}{kT}\right) \tag{3.56}$$
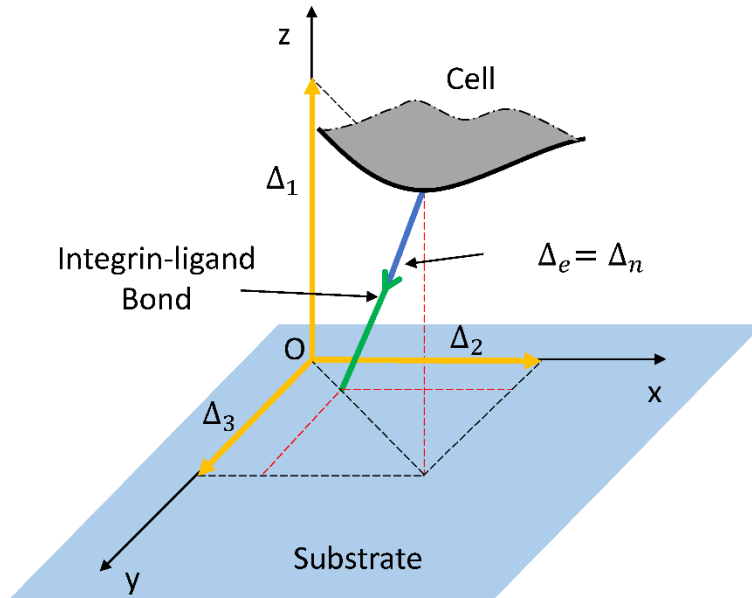
Figure 3.6 Schematic of integrin-ligand bond interaction during sliding ($\Delta_e = \Delta_n + \Delta_0$). The origin of the coordinate denotes the position of the ligand in binding. Red dashed lines denote the relative displacement between cell and substrate in the three directions of axes.

The Jacobian terms of normal traction force are

$$\frac{\partial T_1}{\partial \Delta_j} = -\left(\frac{\partial T_1^P}{\partial \Delta_j} + \frac{\partial F_1}{\partial \Delta_j}\xi_H\right) \quad (j = 1,2,3.) \tag{3.57}$$

where $F_1 = \frac{\Delta_1}{\Delta_n}F_{tot}$ is the bond force in the normal direction, and F_{tot} is the total force in the bond with $F_{tot} = \lambda_s \Delta_n$.

Substitute equations (3.43-3.44) into equation 3.53

$$\frac{\partial T_1}{\partial \Delta_j} = -\left(\frac{\varphi_0^P}{\delta_p^2}e^{-\frac{\Delta_1}{\delta_p}}\left(1 - \frac{\Delta_1}{\delta_p}\right)\delta_{1j} + \lambda_s\delta_{1j}\frac{\xi_0}{q_2 + 1}\right) \quad (j = 1,2,3.) \tag{3.58}$$

The tangential Jacobian terms are

$$\frac{\partial T_i}{\partial \Delta_j} = -\frac{\partial F_i}{\partial \Delta_j}\xi_H \quad (i = 2,3.\, j = 1,2,3.) \tag{3.59}$$

where the tangential force components are

$$F_i = \lambda_s\Delta_n \cdot \frac{\Delta_i}{\sqrt{\Delta_{tot}^2 - \Delta_1^2}} \cdot \sqrt{1 - \left(\frac{\Delta_1}{\Delta_n}\right)^2} \tag{3.60}$$

where $\Delta_{tot} = \sqrt{\Delta_1^2 + \Delta_2^2 + \Delta_3^2}$.

Therefore

$$\frac{\partial T_i}{\partial \Delta_j} = -\left(\frac{\delta_{1j}\lambda_s\Delta_n\Delta_1}{\sqrt{\Delta_n^2 - \Delta_1^2}}\frac{\Delta_i}{\sqrt{\Delta_2^2 + \Delta_3^2}}\right.$$
$$\left. + \lambda_s\Delta_n\sqrt{1 - \left(\frac{\Delta_1}{\Delta_n}\right)^2}\frac{\delta_{ij}(\Delta_2^2 + \Delta_3^2) - (\Delta_2\delta_{2j} + \Delta_3\delta_{3j})\Delta_i}{\left(\Delta_2^2 + \Delta_3^2\right)^{\frac{3}{2}}}\right)\xi_H$$
$$(i = 2,3.\, j = 1,2,3.) \tag{3.61}$$

Case 3: $\Delta_n < \Delta_e \leq 2\Delta_n$

The integrin-ligand bonds are perpendicular to the substrate surface, so the force in the bonds acts only in the normal direction. The integrin density is

$$\xi_H = \frac{\xi_0}{q_3 + 1} \tag{3.62}$$

where

$$q_3 = \exp\left(\frac{\mu_H - \mu_L - \lambda_s \Delta_n^2 + \frac{1}{2}\lambda_s(\Delta_1)^2}{kT}\right) \tag{3.63}$$

The bond force in the normal direction is dependent on normal relative displacement.

$$F_1 = \lambda_s(2\Delta_n - \Delta_1)\xi_H \tag{3.64}$$
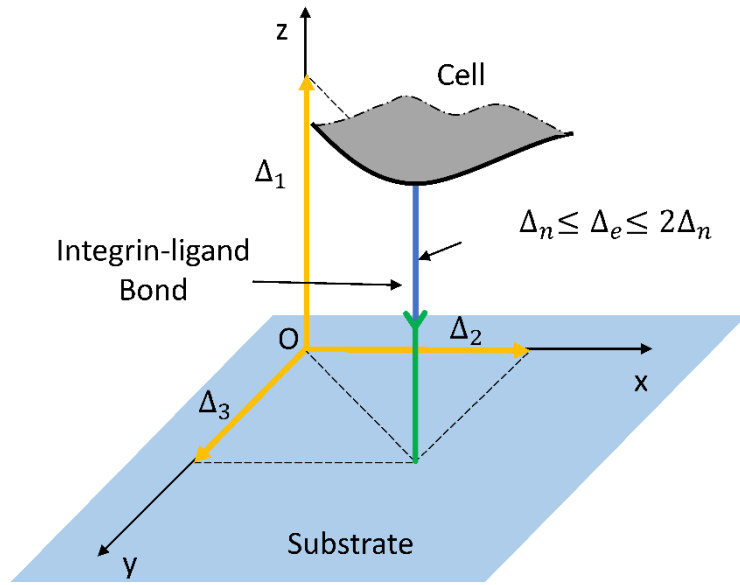
Figure 3.7 Schematic of integrin-ligand bond interaction when the bond is perpendicular to the substrate surface and its length is beyond its peak length ($\Delta_n < \Delta_e \leq 2\Delta_n$).

Thus, the normal traction force is

$$T_1 = -T_1^P - F_1\xi_H = -\left(\varphi_0^P \frac{\Delta_1}{\delta_p^2} e^{-\frac{\Delta_1}{\delta_p}} + \lambda_s(2\Delta_n - \Delta_1)\xi_H\right) \tag{3.65}$$

Therefore

$$\frac{\partial T_1}{\partial \Delta_1} = -\left(\frac{\varphi_0^P}{\delta_p^2} e^{-\frac{\Delta_1}{\delta_p}}\left(1 - \frac{\Delta_1}{\delta_p}\right) - \lambda_s \frac{\xi_0}{q_3 + 1}\right.$$
$$\left. - (2\Delta_n - \Delta_1)\frac{\xi_0 q_3}{(q_3 + 1)^2}\frac{\lambda_s^2 \Delta_1}{kT}\right) \tag{3.66}$$

The tangential traction forces on the cell membrane are zero. Hence, the Jacobian terms are zero.

$$F_2 = 0, T_2 = 0$$

$$F_3 = 0, T_3 = 0 \tag{3.67}$$

5) Overview of user subroutines calculations

The SF formation model is implemented in the UMAT of Abaqus. The overall calculation process is shown in Figure 3.8a:

(1) Define common blocks and initialize the parameters
(2) Calculate the passive stress
(3) Loop over angles to calculate the strain rate of each fibre, apply Runge-Kutta method to solve the ODEs and get the fibre activation level η and stress at the end of increment
(4) Calculate integrated active stress and total stress
(5) Update the Jacobian matrix

The FA formation model is implemented in the UINTER of Abaqus coupled with UMAT to simulate the cell response (Figure 3.8b). The overall process is:

(1) Determine the integrin-ligand bond length based on the passed-in relative surface displacements
(2) Calculate the passive traction
(3) Calculate the forces in the integrin-ligand bonds
(4) Calculate the total tangential and normal interface stress
(5) Update the Jacobian matrix
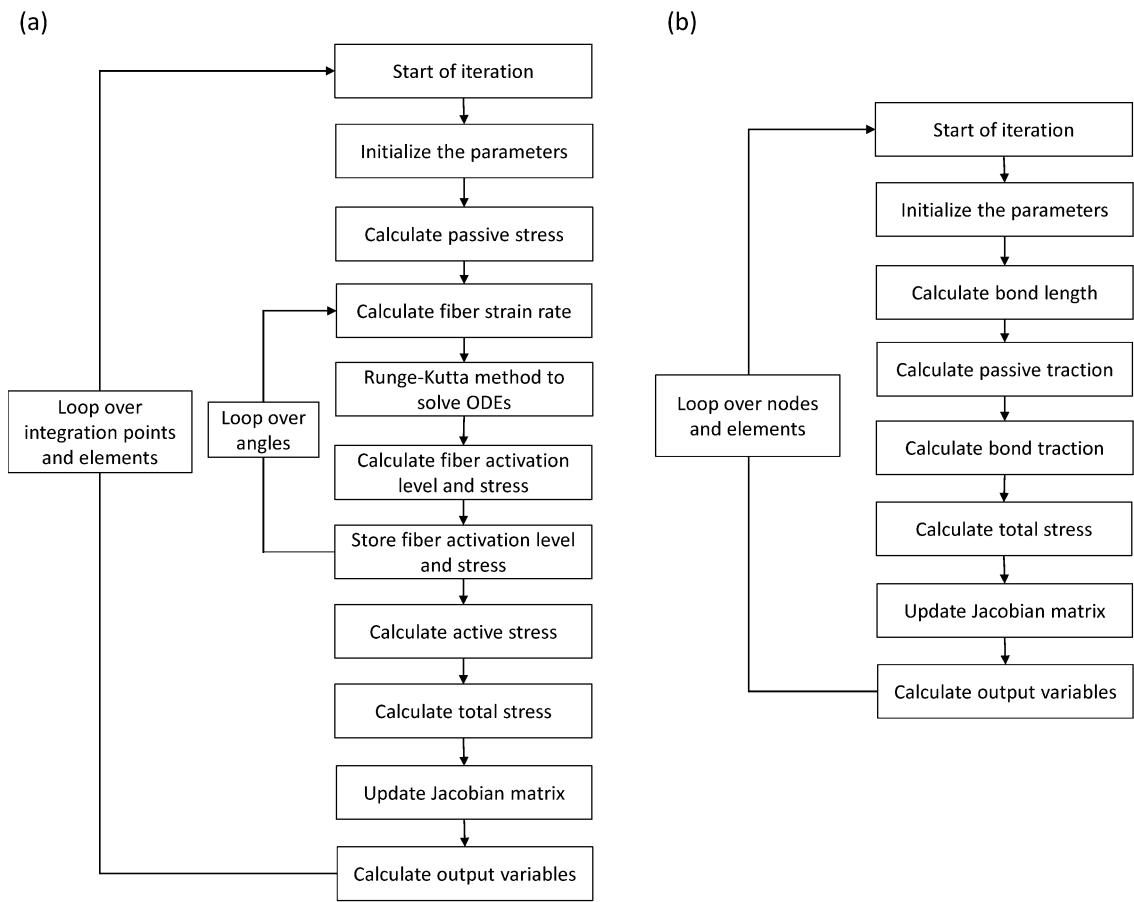
Figure 3.8 Flow chart of (a) UMAT of SF formation and (b) UINTER of focal adhesion formation.

Chapter 4. Revealing the nanoindentation response of a single cell using a 3D structural finite element model

4.1 Introduction

Knowledge of the mechanical properties of cells is crucial for understanding various cell behaviours including motility (Diz-Munoz *et al.*, 2013), differentiation (Chaudhuri and Mooney, 2012), and proliferation (Haugh *et al.*, 2011). Changes in cell elasticity have been correlated with cell abnormalities and various human diseases including cancer, malaria, and arthritis. Researchers have also shown that the elastic moduli of epithelial cancer cells in the human bladder are lower than those of normal cells due to reorganization of the cytoskeleton (Lekka *et al.*, 1999). Furthermore, red blood cells infected with malaria were found to be stiffer than normal cells, which may cause trapping and destruction of the cells in the reticuloendothelial system (Nash *et al.*, 1989). Several techniques have been developed to quantify the mechanical properties of living cells, including micropipette aspiration (Tan *et al.*, 2010), magnetic twisting cytometry (Puig-de-Morales-Marinkovic *et al.*, 2007), optical tweezers (Dao *et al.*, 2003), and nanoindentation (Li *et al.*, 2008). Atomic force microscopy (AFM) is a viable nanoindentation technique capable of revealing the structure and mechanical properties of cells. When integrated with other techniques, it would be even more powerful (Marcotti *et al.*, 2019). For example, AFM combined with fluorescence imaging has been applied to assess the stress fibre amount and stiffness of mouse fibroblasts (Gavara and Chadwick, 2016). Using AFM together with confocal microscopy, the nuclear stiffness of tumour cells was measured with simultaneous visualisation of the indentation process (Marina *et al.*, 2013). When combined with microfabricated well arrays, cells can be mechanically entrapped and automated indentation tests can be performed on a number of cells (Ng *et al.*, 2007). This requires use of computational modelling or a modified Hertz model to reliably extract the mechanical properties of cells due to the constraints induced by the wall (Chen, 2013).

To better interpret the nanoindentation experimental results, a number of computational models have been developed. Most assumed that cells are a homogenous material (Chen and Lu, 2012; Efremov *et al.*, 2017) or consist of homogenous cytoplasm and a nucleus (Ofek *et al.*, 2009; Liu *et al.*, 2019), while excluding the important structure components like actin stress fibres. When using

these simplified computational models, however, it is challenging to account for the microstructure heterogeneity induced indentation size effect of cells, particularly when using the sharp pyramid AFM probe. Furthermore, due to differences in protocol which aren't accounted for in these simple models, researchers will often find that their measured elasticities contradict what other labs reported for the same types of cell. This significantly hinders the deep understanding of the biomechanics of cells and affects data sharing in the scientific community. It was often concluded that these large discrepancies in the measured apparent cell moduli was due to different methods of sample preparation or variations in individual cells; however, it was also found that the cell modulus measured using AFM probes with different geometries can be vary significantly (Charras and Horton, 2002). For example, osteoblasts have been probed by Charras and Horton with both pyramidal and spherical indenters, yielding higher values with a pyramidal tip (E=14.0 kPa) than with a spherical indenter (E=3.2 kPa) (Charras and Horton, 2002). Carl and Schillers also reported higher values when measuring with a sharp probe as compared to when measurements were taken with a spherical one (Carl and Schillers, 2008). Vargas-Pinto et al. demonstrated that the stiff cell cortex could provide an explanation for why the apparent modulus was higher when measuring with sharp tips (Vargas-Pinto *et al.*, 2013). Stress fibres underlying the cell membrane could be resolved by nanomechanical maps, demonstrating the significant contributions to higher local stiffness of cells (Guerrero *et al.*, 2019).

So far, there is a lack of computational modelling which illustrates how the indenter geometry, size and indentation depth all affect the apparent cell modulus when considering the contributions of intracellular components. Therefore, in this chapter, we aim to develop a comprehensive computational model which considers the key structural components (i.e. cytoplasm, nucleus, cortex, microtubules and actin stress fibres) to study how AFM probe geometry, size and test protocols affect the measured apparent modulus of cells.

4.2 Methods

4.2.1 FE modelling

An FE model of a representative adherent Human Bone Osteosarcoma Epithelial Cells (U2OS) was developed in Abaqus 6.14. The same cell geometry as described in (Barreto *et al.*, 2013; Barreto *et al.*, 2014) was used, which was also used as a representation of experimental measurements. The cell was constructed as a semi-

ellipsoid like shape of 19 µm length and 4 µm width. Although the real cell consists of various components, the model only considered key intracellular components such as the nucleus, the cytoplasm, the cytoskeleton elements, and a layer of actin cortex attached on the cytoplasm (Figure 4.1). The cortex layer (~200 nm) is much thicker than that of cell membrane (~10 nm) (Clark *et al.*, 2013). Therefore, it is reasonable to consider that the cortex outcompetes the contribution of the cell membrane to the deformations. There is no need to create another 10 nm layer to deliberately represent the cell membrane. The nucleus was placed 0.5 µm away from the bottom surface. This simplified architecture of the intracellular structure in the cell model was created based on microscopic image of actin and microtubules distributions in adherent U2OS (Barreto *et al.*, 2013). The actin stress fibre, a major component of cytoskeleton was modelled with pre-strain, which is reported to be 0.24 ± 0.18 (Deguchi *et al.*, 2006). The prestress in the stress fibres is calculated to be 82 kPa and implemented in the model by user subroutine (UMAT). These stress fibres and microtubules were attached onto the cell cortex. The model includes 32 stress fibre elements and 33 microtubules elements in total. Although the number of stress fibres is less than the number in real cells, each fibre can be considered a bundle of fibres which should represent the heterogeneity of the cell structure with good computational efficiency. The microtubules were modelled as star-shape structures emanating from a point near the nucleus membrane (where a centrosome would be in a real cell).

The cytoplasm and nucleus were assigned linear hexahedron elements. Shell elements were used to represent the actin cortex. The stress fibres were modelled as truss elements with circular cross sections attached to the cell cortex nodes at both ends. The microtubules were modelled using beam elements with pipe section: these emanated from a node on the nucleus surface and interacted with the cell cortex and stress fibres at their ends. In order to study the indenter geometry effect on the apparent cell moduli, two types of indenters were employed in this study: spherical and conical indenter. The spherical indenter radius ranged from 1 to 5 µm to investigate how the apparent moduli varied with indenter radius. Semi-included angles of conical indenters ranged from 15˚ to 75˚: each had a rounded tip of radius 10 nm. The indenters were modelled as rigid bodies as they are much stiffer than intracellular components.

4.2.2 Apparent materials properties in FE model

There is no universal mechanical model for a living cell. Poroelastic or spring-dashpot based viscoelastic models have proven useful in many cases but can also fail to work in a few cases (Chen, 2014). Individual intracellular component would also exhibit time-dependent mechanical characteristics; however, these properties are difficult to be measured separately. Instead of assuming the time-dependent mechanical parameters based on viscoelastic or poroelastic models, we would prefer to choose a simple material model with only two materials properties (apparent Young's modulus and Poisson's ratio). Thus, all the cell components are assumed to be homogeneous, isotropic and elastic. Their elastic properties are summarized in Table 4.1, which were taken from experimental measurements or theoretical estimations reported in literature. In the present study, focus was directed towards the contribution of intracellular components on the apparent cell modulus. This is not currently well understood.
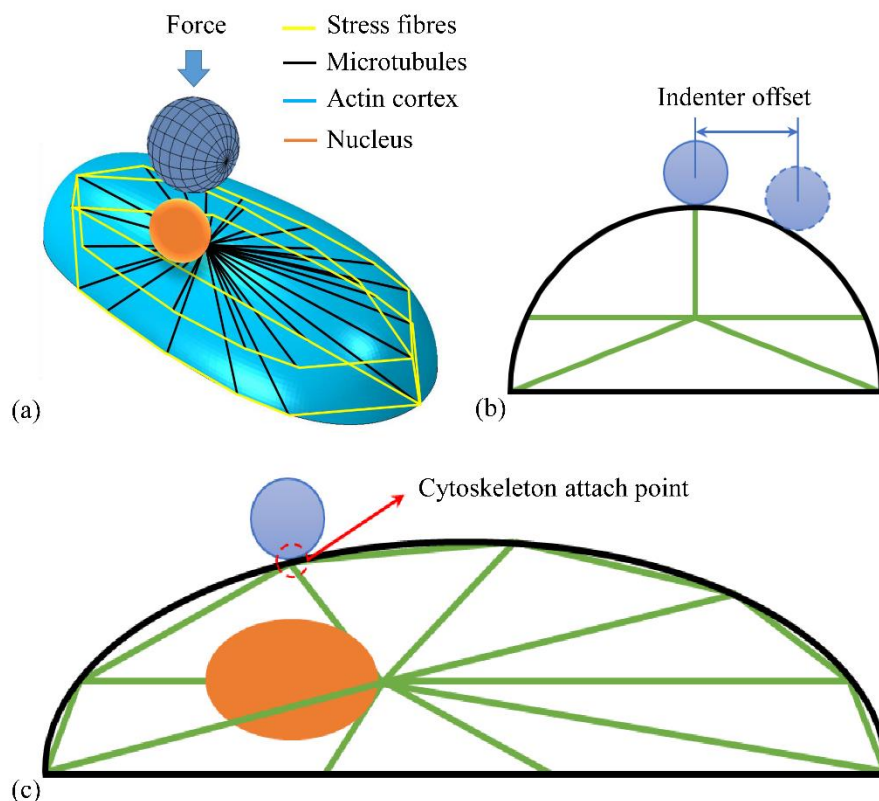
Figure 4.1 (a) The cell model consists of stress fibres, microtubules, the actin cortex, cytoplasm, and a nucleus. (b) and (c) Schematic views of the indentation positions relative to the cytoskeleton components. The cell is indented around the site where actin stress fibres are attached.

4.2.3 Boundary conditions

During experimental measurements, cells are often immobilised on a coverslip surface. The ventral surface of the cell was, therefore, fixed to prevent detachment from the coverslip. The nucleus, encapsulated in cytoplasm, was assumed to be bonded to the cytoplasm. An attachment point was defined in the contact area to allow the cytoskeleton to transfer external forces (Figure 4.1c). Indentation of 0.5 μm was applied at the top the nucleus (equivalent to what was used in prior experimental set-ups (Barreto *et al.*, 2013)). To quantify how the cell heterogeneity influences the apparent moduli, the indentation position on the cell surface was changed (Figure 4.1b). The indenter was subsequently displaced 0.1 ~ 1 μm from the original position.

	Poisson's ratio	Young's modulus	Number of elements
Cytoplasm	0.48	0.25 kPa (Canetta *et al.*, 2005; Barreto *et al.*, 2013)	95150
Nucleus	0.3	1 kPa (Guilak *et al.*, 2000)	5484
Actin cortex	0.3	2 kPa (Stricker *et al.*, 2010)	11748
Microtubules	0.3	2 GPa (Pampaloni and Florin, 2008)	277
Stress fibres	0.3	340 kPa (Deguchi *et al.*, 2006)	35

Table 4.1 Material properties of cellular components in the FE model.

4.2.4 Model calibration

Prior to comprehensive study, the model was validated against experiment data taken from [41]. For experimental measurements, nanoindentation tests of U2OS cells (N=18) were performed using spherical AFM probe of diameter 4.5 μm. As individual cells differ from one another, the force-displacement curves spread out. The force-displacement curves based on the 18 measurements reported in (Barreto *et al.*, 2013) were, therefore, averaged so that they could be compared to FE results. The loading rate in the experiments was so small (0.05 μm/s) that the apparent moduli of cells were similar to their equilibrium moduli. In the modelling, the Young's modulus of each intracellular component was set to the equilibrium modulus. It is, therefore, sensible to make direct comparison. As seen in Figure 4.2, there is no significant difference between the FE results and the averaged force-displacement

curve (p>0.95). The reported apparent cell modulus was 1.3 ± 0.8 kPa based on 18 measurements (Barreto *et al.*, 2013). The apparent cell modulus determined by FE is approximately 0.7 kPa which agrees with experimental results (1.3 ± 0.8 kPa) within measurement errors.
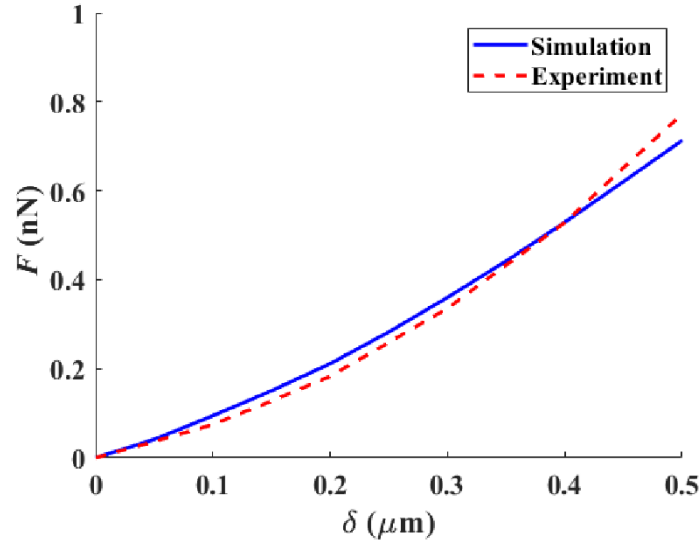
Figure 4.2 Comparison of the measured force-displacement curve (averaged based on 18 curves (Barreto *et al.*, 2013)) and FE simulation for nanoindentation tests of U2OS cells. There is no significant difference between FE results and the averaged force-displacement curve (p>0.95).

4.2.5 Data Analysis

The Hertz model has been widely adopted to interpret the AFM indentation results (Liu *et al.*, 2013; Guz *et al.*, 2014; Ding *et al.*, 2017). The materials evaluated in the Hertz model are assumed to be homogenous. Although the cell model in our study is inhomogeneous and the cell may experience a large deformation at larger penetrations, the Hertz model was still adopted to obtain the apparent cell modulus so that direct comparisons with experimental results reported in literature could be made. For the spherical indenter, the following formula was used (Johnson, 1985):

$$F = \frac{4}{3}\frac{E_a}{1 - v^2}\sqrt{R}\delta^{3/2} \qquad (4.1)$$

where F is the reaction force of the indenter, δ is indentation depth, and v is Poisson's ratio. E_a is the apparent cell modulus as a rigid indenter was used. R is the effective radius calculated from the spherical indenter (R_p) and curvature of cell (R_c) by the equation $1/R = 1/R_p + 1/R_c$.

For the conical indenters, the force-displacement relationship was given based on Sneddon's work (Sneddon, 1965):

$$F = \frac{2}{\pi} \frac{E_a \cdot \tan\theta}{1 - v^2} \delta^2 \qquad (4.2)$$

where θ denotes the semi-included angle of the conical indenter.

4.3 Results

4.3.1 Indenter size effect on the apparent cell moduli

In order to assess the effect of indenter size selection on the apparent Young's moduli determined by equation (4.1) or (4.2) depending on the indenter geometries, indentation studies with different indenter sizes were performed (Figure 4.3). Indentation studies showed a negative correlation between spherical indenter size and apparent modulus. The apparent modulus decreases slightly from 0.85 kPa to 0.62 kPa when the spherical indenter radius was increased from 1 to 5 µm (Figure 4.3b). When using a conical indenter, however, the measured modulus dramatically drops from 10.21 kPa to 0.96 kPa while increasing the semi-included angle of the cone (Figure 4.3d). The apparent moduli measured by conical indenters are significantly higher (can be more than 10 times higher) than the results obtained by their counterpart spherical indenters at given penetrations. The stress map show that, when small, both types of indenter produced higher stresses in the cell cortex, cytoplasm and CSK; large indenters, on the other hand, resulted in greater stress in the nucleus (Figure 4.6 and Figure4.7).

4.3.2 Indentation depth dependent moduli

The indentation depth dependent apparent moduli were analysed since the indentation depth also contributes to the apparent moduli (Figure 4.4). At a given indenter size, larger indentation depth produced lower and more stable apparent moduli both in spherical and conical indentations. When the radius or semi-included angle of the indenters was increased, the indentation depth dependent apparent moduli tended to converge. At relatively small penetrations, the spherical tip with a smaller radius (e.g. 1 µm) leads to an apparent modulus that is nearly twice that measured with a larger radius indenter (e.g.2~5 µm). Modelling also suggested that the apparent moduli measured are very similar at relatively large penetrations (e.g. 0.5µm, free from substrate effect) for a spherical probe with radius 3~5 µm. For the smaller radius probe, the apparent modulus drops by over 60% when the indentation penetration increases from 0.05 µm to 0.5 µm. On the other hand, the apparent modulus only drops by about 40% for the probes with larger radius. Such a geometry

dependent and indentation size effect is even more pronounced for the conical probes. At shallow penetrations, the sharpest probe leads to the apparent modulus that is nearly 15 times its counterpart measured with a much blunter tip (e.g. θ =75˚). Even at large penetrations (e.g. 0.5µm), the apparent modulus measured by the sharpest probe is still about 8 times that measured by the bluntest probe in this study.
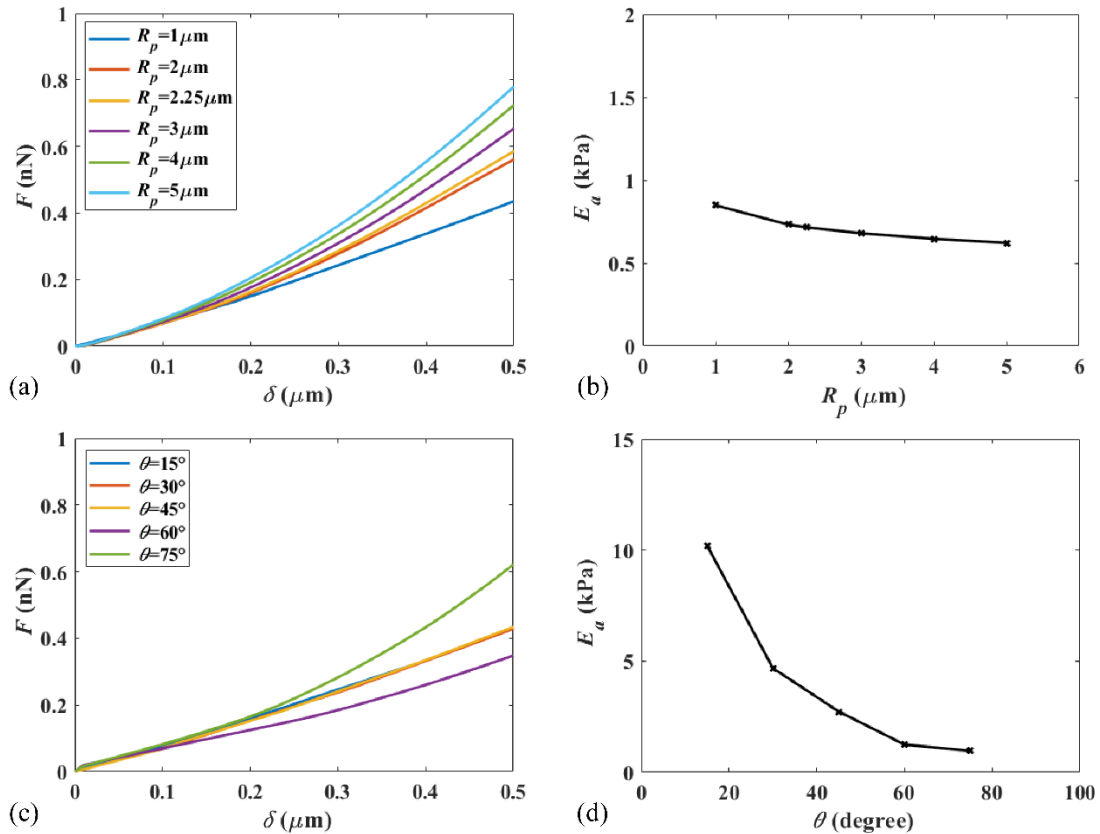
Figure 4.3 (a) and (c). Indentation force (F) versus depth (δ) of spherical indenters and conical indenters, respectively. (b) and (d) Measured apparent Young's moduli (E_a) versus indenter radius (R_p) of spherical indenters and semi-included angle (θ) of conical indenter, respectively.

4.3.3 Indenter position effect on the apparent cell moduli

To study the cell heterogeneity induced variations in apparent cell moduli, the indenters were displaced from the central position by up to 1 µm (Figure 4.5). The spherical indentation with 1 µm radius appears to be the most sensitive to offset values (the modulus decreases from 0.85 kPa to 0.43 kPa). In contrast, the apparent moduli measured in studies with other indenter sizes fluctuate in the range of 0.58 ~0.73 kPa. For sharp conical indenters (θ=15˚ and 30˚), the apparent moduli vary greatly from ~9.87 kPa to ~0.7 kPa. The blunt indenters (θ=60˚ and 75˚) produced relatively small variations within the range 0.95 kPa to 1.27 kPa. The stress maps of

intracellular components (Figure 4.6 and Figure 4.7) show much higher stresses when indenting on top of stress fibres.
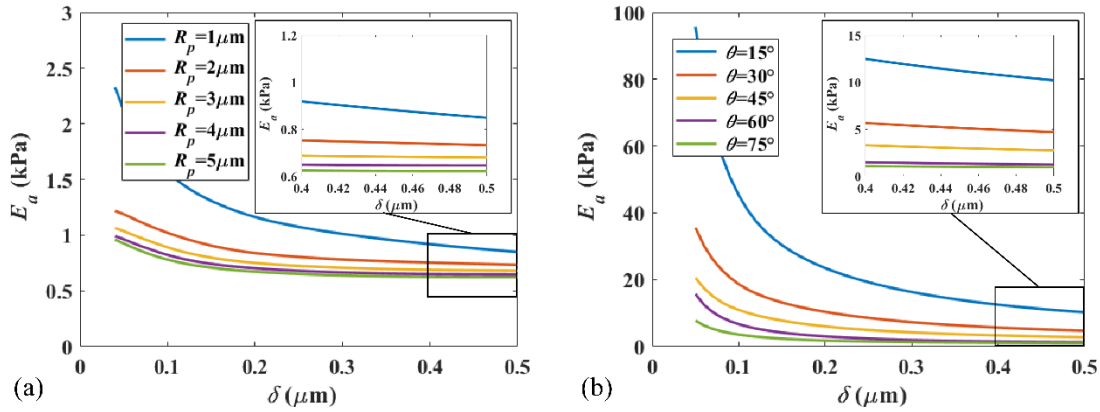
Figure 4.4 Indentation depth effect on measured apparent moduli with different indenter sizes. (a) Spherical indentation; (b) Conical indentation. Insets show the apparent moduli of the cell in the depth (δ) range of 0.4 ~0.5 µm.
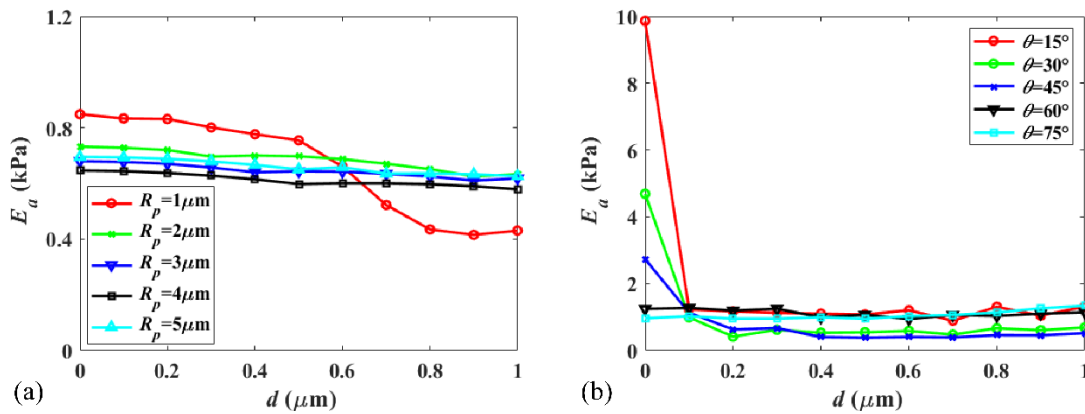
Figure 4.5 (a) Indentation position effect (with offset d from the stress fibre attach point) on measured apparent Young's moduli with different spherical indenter sizes. The moduli measured by indenters with R_p >1µm are stable when displacing the tips. For the indenter with R_p=1µm, the modulus drops when offset is beyond 0.5 µm. (b) Indentation position effect (with offset d from the stress fibre attach point) on measured moduli with different conical indenter sizes. For indenters with semi-included angle θ <60˚, the measured moduli fall dramatically upon displacement.

4.3.4 Heat map of cell modulus

To link the simulation results with experimental observations, we conducted a mapping analysis by indenting the top surface of the cell model with both types of indenters. Each indentation simulation has been conducted at 64 positions. Heat maps of apparent cell moduli derived by different sizes of indenters are presented in Figure 4.8. The apparent moduli (E_a) are normalised by the apparent moduli of a control cell model (E_{ctr}), in which CSK elements are removed. The noise from FE mesh and model geometry could, therefore, be reduced. Consistent with the results

60

of indenter size and geometry effects in Figure 4.3 and Figure 4.5, the apparent moduli near stress fibres measured by conical probes are significantly higher than those measure using spherical probes. The apparent cell moduli are higher near stress fibres in all cases. As the indenter becomes blunter (e.g. bigger semi-included angle or larger radius), the effect of stress fibres on localised apparent cell modulus was less significant.

4.4 Discussion

Our results have demonstrated that the apparent modulus decreases with indentation depth. Experimental results have also demonstrated that the apparent moduli decrease with the penetration and reach a plateau at large indentation depth regardless of probe shape and size (Ding *et al.*, 2018). It has been suggested that the indentation penetration should be restricted to less than 10% of cell thickness to avoid the effect of the substrate (Mathur *et al.*, 2001). Within the indentation community, it was often argued that the 10% rule was generally applicable for hardness measurements (Fischer-Cripps, 2000). Later, both experimental measurements and numerical simulations demonstrated that this rule is not stringent enough for a hard coating on a very soft substrate and too strict for a soft coating on a hard substrate (Cai and Bangert, 1995; Panich and Sun, 2004; Xu and Rowcliffe, 2004; Chen and Bull, 2009). Thus, such a 10% rule may not apply to modulus measurements of a thin layer on a substrate because the effective elastic deformation zone is much larger than the plastic deformation zone. Accumulative experimental evidence has, however, demonstrated that the rigid substrate has very little effect on the measured apparent modulus of cells even when the indentation penetration exceeds 10% or even 25% of the cell thickness (Mahaffy *et al.*, 2000). On the other hand, some other studies reported a stiffening effect with increasing indentation depth (Roduit *et al.*, 2009; Schillers *et al.*, 2010; Guz *et al.*, 2014) which was argued to be due to condensation of other cell organelles, e.g., the nucleus and the CSK during indentation. It should be noted that different type of cells can have very different morphologies and internal structure organisations. What was found in one type of cells may not apply to other type of cells.
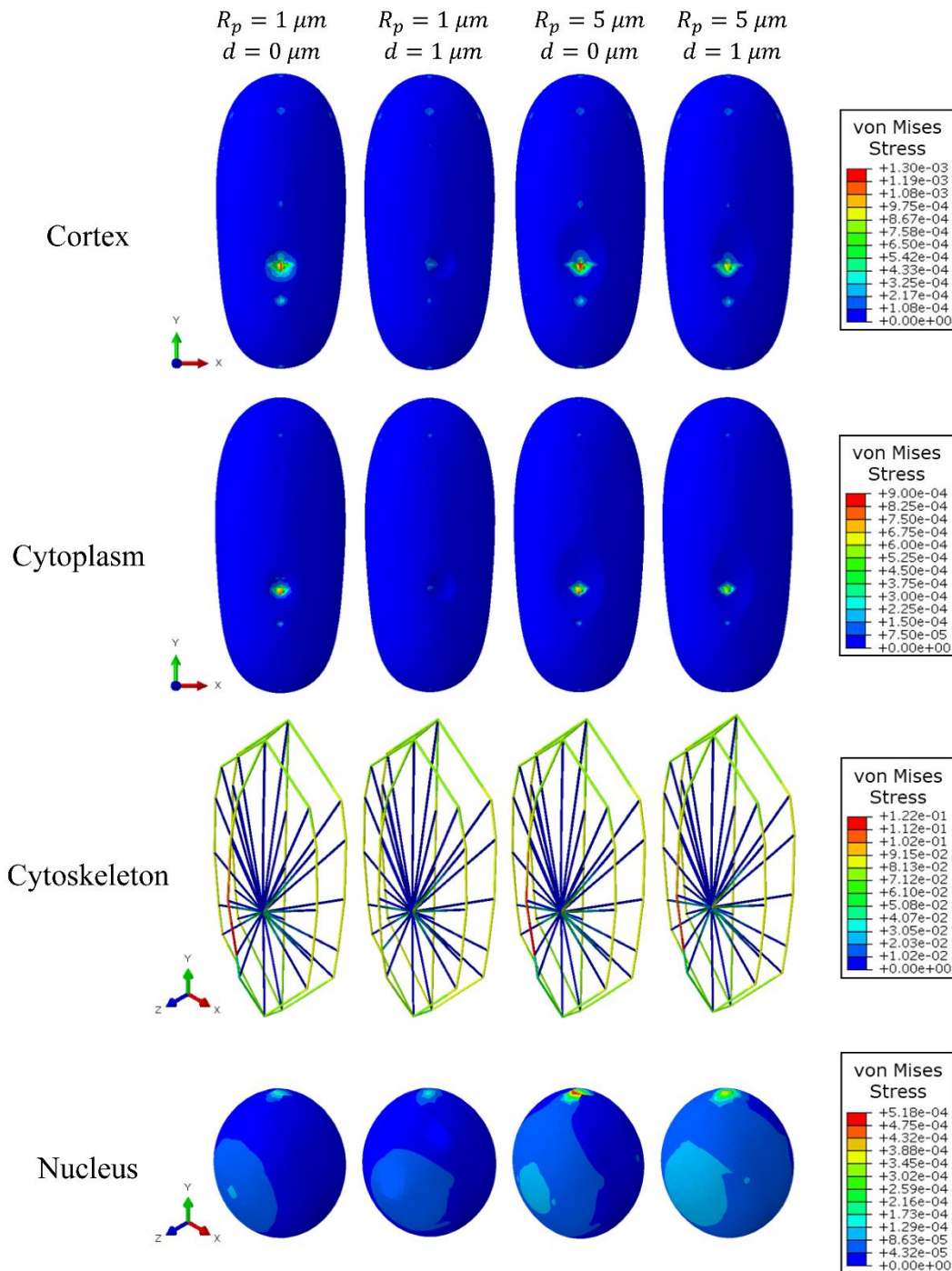
Figure 4.6 Stress map of cellular components indented by spherical indenters with different sizes (R_p=1, 5 μm) and positions (offset d=1, 5 μm).

For the given cell type modelled in this work, it seems that there was no significant effect from the substrate as no stiffening effect was observed at relatively large penetrations (e.g. at maximum penetration, 12% of the cell thickness). This might not rule out the substrate effect entirely as it could be coupled with the effect of the intracellular components, making it hard to isolate the substrate effect. The apparent softening effect with the indentation penetration was also observed experimentally and it was assumed to be due to stiffer region dominating behaviour at smaller

62

penetrations (Mathur *et al.*, 2001; Soufivand *et al.*, 2014). The FE model developed here (Figure 4.6 and 4.7) has confirmed such assumption that the indenters initially probe the stiff actin cortex and the CSK, which is significantly stiffer than the cytoplasm. As penetration is increased, the mechanical contribution of the soft cytoplasm also increases.
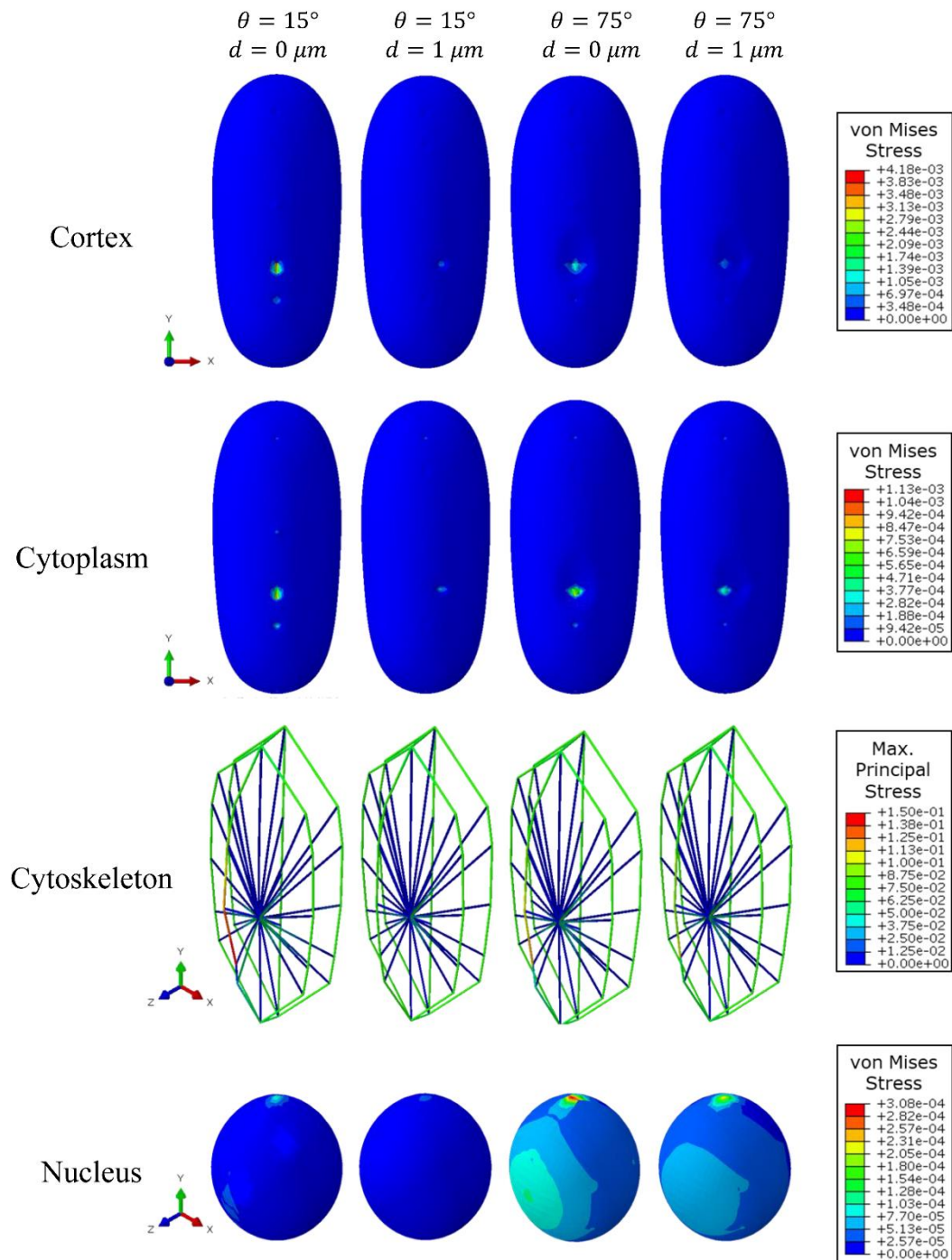
Figure 4.7 Stress map of cellular components indented by conical indenters with different sizes (θ=15˚, 75˚) and positions (offset d=1, 5 µm).

The cell is generally considered to be heterogeneous due to its different mechanical properties in different cell positions (Solon *et al.*, 2007). The heterogeneity of the cell in the model described here was created by attaching the CSK elements onto the cell membrane, enabling the probes to probe the effect of the CSK structure. CSK elements do contribute to the overall cell apparent moduli in our results (~0.72 kPa) compared to that without CSK (~0.31 kPa, equivalent to the cells with depolymerized actin fibres and micro-tubules) with spherical indenters (simulation data not shown). When the pyramidal indenters were used, Hofmann *et al.* also estimated that the region with the highest concentration of stress fibres are 3~10 times stiffer than surrounding areas free of these fibres or with very few fibres (Hofmann *et al.*, 1997). In general, all these quantitatively agree with our modelling predictions as shown in Figure 4.5b. The commonly used commercial pyramid AFM tips could be likened to the conical tips via their equivalent contact area (Sagadevan and Murugasen, 2014). The commonly used commercial pyramid AFM probes often have a semi-included angle between 10~70 ˚ and its equivalent conical probe will have slightly higher semi-apical angles based on geometrical calculations.
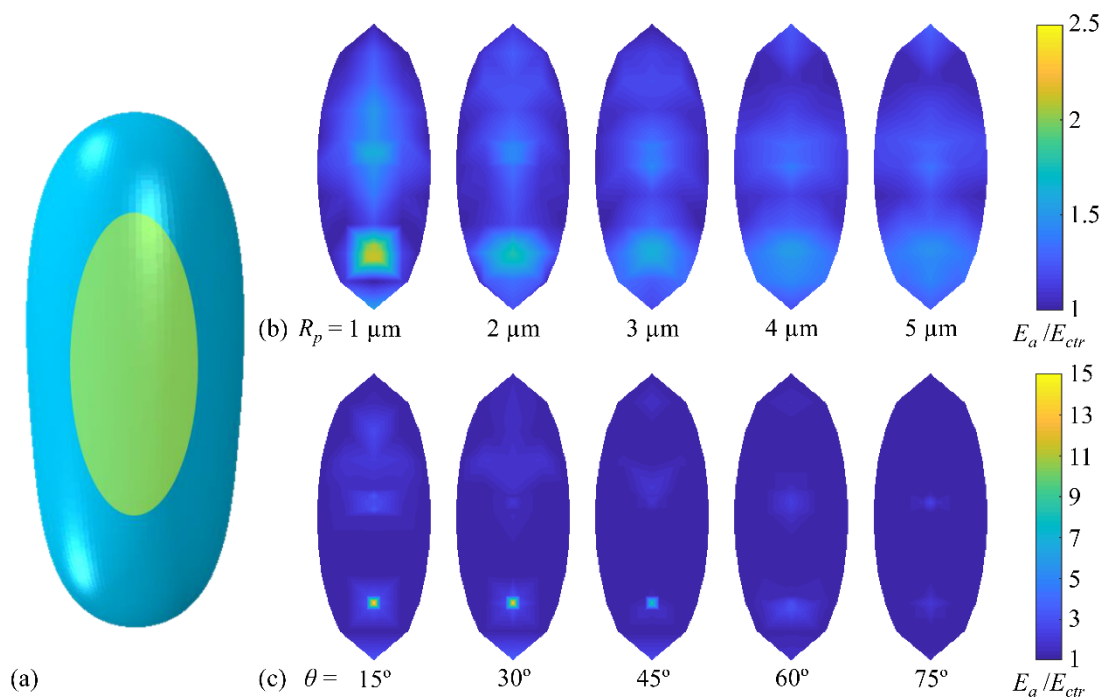
Figure 4.8 Heat maps of apparent cell moduli measured on the cell surface. (a) The area labelled with green is probed by the indenters. (b) Normalised apparent moduli (E_a/E_{ctr}) measured by spherical indenters are averaged by larger sizes. (c) Normalised apparent moduli measured by conical indenters are significantly higher near stress fibres, which are averaged out when using large sizes of probes.

When using these probes in practice, at very small penetration (e.g. 0.05 μm), the sharp pyramid can result in an apparent modulus which is almost 50 times of that generated by a spherical indenter. The commonly used spherical indenters have a radius between 1~5 μm. Even at a relatively large penetration (e.g. 0.5 μm) as adopted in many experimental measurements, the sharp pyramid can still lead to an apparent modulus which doubles that measured by a spherical indenter. These predictions semi-quantitatively agree with experimental measurements (Harris and Charras, 2011). Carl and Schillers attributed the higher apparent modulus measured by sharp tips to the higher applied pressure which results in local strain hardening (Carl and Schillers, 2008). Harris and Charras have reported on the underestimation of the contact area of sharp tips due to the potential contact between cell surface and AFM cantilever with indentation depth beyond critical value (Harris and Charras, 2011). This could explain the higher modulus measured by sharp tips with deep indentation. The results provided by Vargas-Pinto et al. showed significantly higher apparent moduli measured using sharp tips with lower penetration (0.4~0.9 μm) and longer tips (Vargas-Pinto *et al.*, 2013). The higher apparent modulus should, therefore, be attributed to other factors within the cell. The finite element results by Vargas-Pinto et al. suggested that the cortex may contribute to the higher values measured using conical tips (Vargas-Pinto *et al.*, 2013). These findings also agreed with our FE predictions about higher apparent moduli near stress fibres.

Together with fluorescence imaging, stiffness maps of cells were obtained using a scanning ion conductance microscope. These show the higher apparent moduli measured in the area with higher concentrations of stress fibres (Rheinlaender and Schäffer, 2013). Nanomechanical maps in a recent study clearly showed the higher apparent moduli near actin stress fibres with increasing indentations (Guerrero *et al.*, 2019). Our computed modulus mapping results are consistent with these experimental observations which emphasizes the contribution of stiff stress fibres to apparent cell modulus measurement. All these have demonstrated that the heterogenous cell model constructed here is sufficient to capture many important spatial-dependent cell mechanics at various conditions. For sharp indenters, we demonstrate the dramatic variation in measurements near stress fibres. At a given penetration, the contact areas of spherical indenters (or effective deformed volume) are much larger than those of conical indenters, as seen in Figure 4.6 and 4.7. Thus, the effect of the stress fibres on the localised apparent cell modulus is less

significant. If one would like to measure the stiffness of a localised area which can reflect the local concentration of actin fibres, sharp probes such as pyramidal and conical indenters should be employed.

4.5 Conclusions

In conclusion, a comprehensive three-dimensional cellular model which includes the key structural components of the cell has been developed to reveal how the AFM probe geometry and indentation size affect the apparent cell modulus measured during nanoindentation tests. This computational model is capable of predicting the spatial-dependent apparent cell modulus when using probes with different geometries, which cannot be achieved by the commonly used homogenous cell models.

In a semi-quantitative way, the model could predict why, in practice, the apparent modulus measured by commonly used pyramid probes is 2~50 times that measured by the commonly used spherical probes. This modelling also provides experimentalists a guideline on choosing the appropriate probes according to the research needs. This work has also demonstrated that the blunt conical probes (with semi-included angles above 60°) enables measurement of the averaged apparent cell modulus in the same way as what can be achieved with a relatively large spherical probe. This study presented the first 3D computational model for predicting the heat map of the whole apparent cell moduli and has suggested that modulus mapping by sharp conical probes can potentially reveal the relative concentration of stress fibres, which can be used to better understand the biophysics of cells. In principle, it is interesting to discuss the rate-dependent behaviour of the cell. It should be noted that the experimental viscoelastic properties for all the intracellular components in the modelling are not available. It will, therefore, be difficult for us to consider the rate-dependent behaviour of these structure components. Furthermore, for the experimental tests that were compared against, the loading rate was so small (0.05μm/s) that the apparent moduli of cells were similar to their equilibrium moduli. In the FE modelling, the Young's modulus of each intracellular component is the equilibrium modulus, which makes it sensible to compare our FE against experimental measurements reported in (Barreto *et al.*, 2013).

In the future, this model can be further extended by considering stress fibre density as measured in the lab and detailed attachment mechanisms of the fibres on the cell membrane to better understand how cells sense the mechanical niche and alter their

biomechanics. The understanding of the cells with complicated structure in the present work is valuable for fibre-reinforced engineering materials and many biological tissues (e.g. connective tissues) which can be regarded as fibre-reinforced materials with pre-stresses.

Chapter 5. Cell Response to Substrate Thickness

5.1 Introduction

In chapter 4, the cell is represented by a structure-based finite element model. However, the biochemical reactions and active reorganization of cytoskeleton (CSK) in the cell can not be described by such a model. To understand the active cell behaviour in response to external stimuli, continuum-based model is employed in this chapter.

In tissue engineering, biomaterials with various structures have been applied in cell culture. Cells are believed to feel the physical properties (such as mechanical properties, surface topographies) of their surrounding material. The materials provide support for cell adhesion. In turn, the cells exert forces on their substrates in response to the external stimuli. This process is known as mechanosensing, which has been reported to regulate cellular processes including differentiation (Engler *et al.*, 2006), division (Wang *et al.*, 2012), migration (Pelham and Wang, 1997) and morphology changes (Gupta *et al.*, 2015). For example, the mechanical property of materials, stiffness has been shown to direct the mesenchymal stem cells into different lineages (Engler *et al.*, 2006). However, many aspects of mechanosensing process remain elusive.

The study of integrin-mediated focal adhesions (FAs) has been largely focused on describing the cell mechanosensing process. Force induced FA growth has demonstrated its important role in mechanosensing process (Riveline *et al.*, 2001). For example, the CSK connected to FAs enabled the cell to sense a wide range of substrate stiffness   (Trichet *et al.*, 2012). During material stiffness sensing process, cells deform the material and can trigger ion channels on the cell membrane. During the cell-materials interactions, biochemical signals are transmitted to induce the formation of stress fibres (SF), which leads to increased intracellular tensions in proportion to the deformations. It has been reported that changes in CSK could tune the nucleus shape to regulate nuclear activities (Khatau *et al.*, 2009a).

The mechanical cues experienced by the cell consist of substrate modulus and geometry, notably the distance to the material boundaries, which can modulate the apparent stiffness experienced by the cells and therefore regulate cellular activities (Buxboim *et al.*, 2010; Leong *et al.*, 2010; Lin *et al.*, 2010; Li *et al.*, 2018). In principle, how deep can cell sense is also affected by cell spreading areas (Lin *et al.*, 2010),

cell proliferation (Li *et al.*, 2018) and differentiation (Leong *et al.*, 2010). Analytical studies have revealed the correlation between the depth-sensing of cell and the substrate displacements and strains (Maloney *et al.*, 2008; Sen *et al.*, 2009; He *et al.*, 2014). Several criteria about how deep cell can sense have been presented either based on displacement or strain of the cell induced substrate deformation (Maloney *et al.*, 2008; Sen *et al.*, 2009; He *et al.*, 2014). However, the relationship between the CSK organization and FA formation during the cell-substrate interactions have not been investigated.
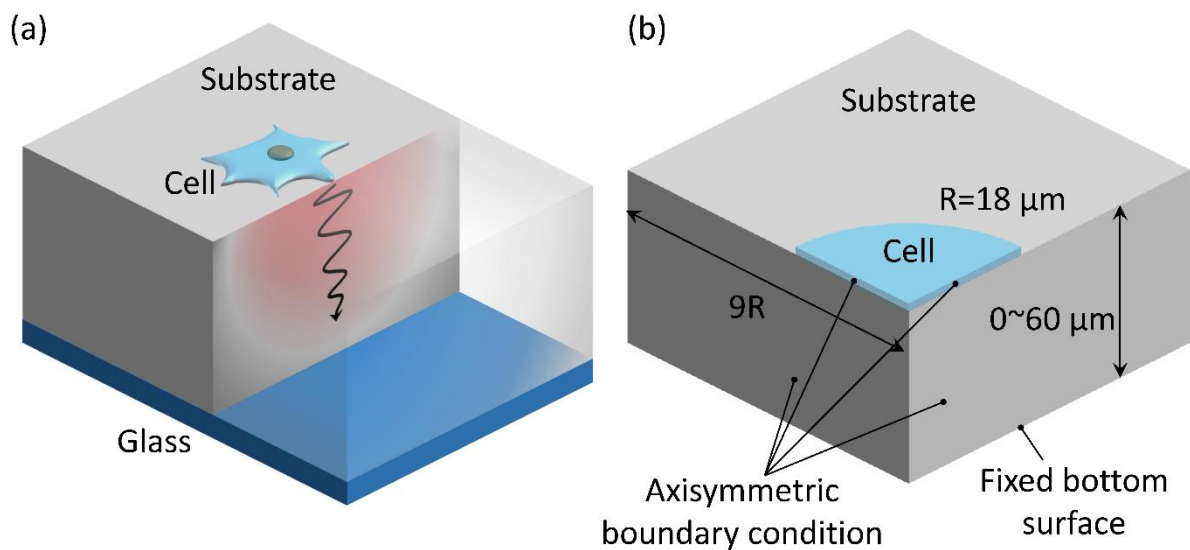
Figure 5.1 (a) Cell senses the underlying glass base when lying on substrate with finite thickness. (b) Cell-material interaction model geometry and boundary conditions.

In this chapter, a finite element (FE) model has been developed to study the effect of substrate thickness and stiffness on dynamic cell responses. To simulate the cell activities when interacting with materials, we need to consider the dynamic process of focal adhesion and stress fibre formation of the cell. These two processes need to be coupled to facilitate the dynamic response of cell triggered by interactions with the underlying substrate. In this chapter, a thermodynamics based focal adhesion model proposed by (Deshpande *et al.*, 2008) was adopted. A bio-mechanical model proposed by Deshpande et al was adopted for stress fibre (SF) formation (Deshpande *et al.*, 2007). Cell FAs and SF levels are represented by integrin density and SF concentration. With this proposed active cell model, it enables us to explore how the cell senses the thickness of an elastic substrate. Critical thickness that a cell can sense are determined by FA level, SF concentration and material displacement and strain.

5.2 Methods

5.2.1 Geometry and size

In our finite element model, the cell is modelled as thin layer on the substrate. The cell is chosen to be a disk and the initial cell area is around 1000 µm^2 with radius R_c=18 µm. Cell nucleus is neglected due to its little contribution to SF and FA formation. To investigate the role of substrate thickness on cell behaviour, the thickness of the substrate varies from 0 to 60 µm. This is to mimic the experimental protocols where hydrogel coatings are casted on coverslip (or petri dish). The lateral size of the substrate is nine times of the cell radius to ensure negligible contribution from the lateral boundary. The modulus of the glass coverslip is around 70 GPa, which is much larger than the modulus of the common materials used in tissue engineering. Hence, the glass is treated as rigid base. Due to the axisymmetry of the cell and material, a quarter of cell-material model is adopted to improve the computational efficiency. Axisymmetric boundary conditions are assumed for both the cell and substrate. The schematic of cell-substrate model was presented in Figure 5.1. The bottom surface of the substrate is fixed to represent its attachment to glass surface without any slip. To study the effect of substrate stiffness combined with thickness, substrate stiffness was varied from 1 kPa to 100 kPa which covers a wide range of stiffness for soft tissues (Engler *et al.*, 2006). To investigate how the cell size may behave differently in terms of the sensing the substrate, the cell size was varied from R_c=13 µm to R_c=28 µm which covers the cell sizes of fibroblast reported in literature (500 ~ 2500 µm^2) (Maloney *et al.*, 2008; Lin *et al.*, 2010).

The mesh size of the cell is around 0.2~1 µm with finer mesh near cell edge (see Figure 5.2). The mesh of contact surface of the substrate is similar to that of cell with coarse mesh away from the cell edge. The cell is modelled as active material which can generate contraction force upon external stimuli. The active behavior is coded via Fortran and implemented in Abaqus user subroutine UMAT. The contact interface between cell and substrate is modelled as adhesion growth model demonstrated in Chapter 3. The growth of the FAs is dependent on the relative displacement of the cell to the underlying matrix surface. This model (as detailed in Chapter 3) is coded in Fortran and implemented by the user subroutine UINTER in Abaqus. These two models are coupled together to simulate the response to the variation of substrate mechanical properties. The flow charts for the model coupling were provided in Chapter 3 and reproduced in Figure 5.3. The cell model is simulated with 1000

increments, which are about 2000 seconds to achieve stable state. For each simulation, it takes about 36 hours using 20 CPUs (AMD 3900X, 64 GB memory).
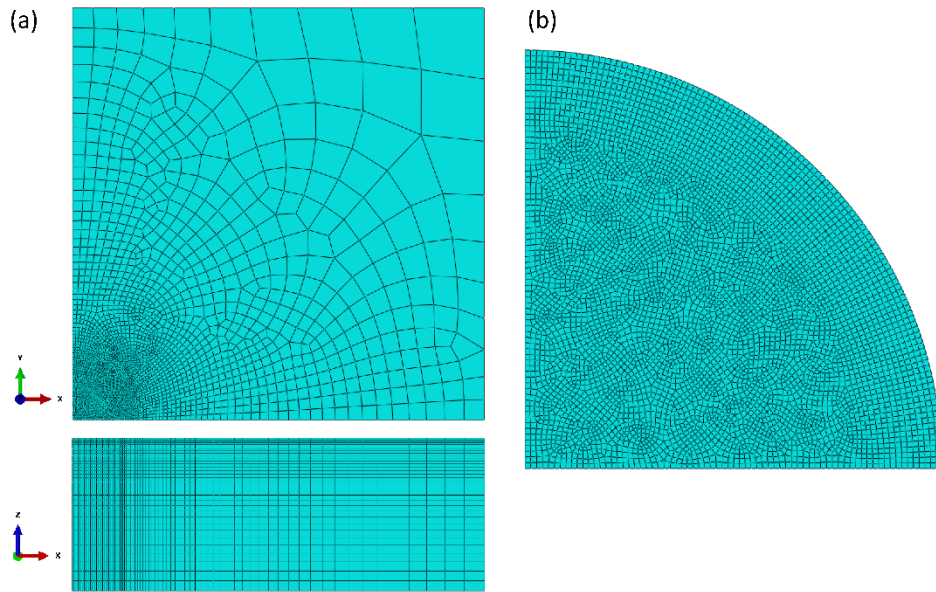
Figure 5.2 (a) Typical mesh of cell-material interaction model with substrate thickness h=60 µm, (top) top view of the mesh and (bottom) side view of the mesh; (b) enlarged mesh for the cell model.
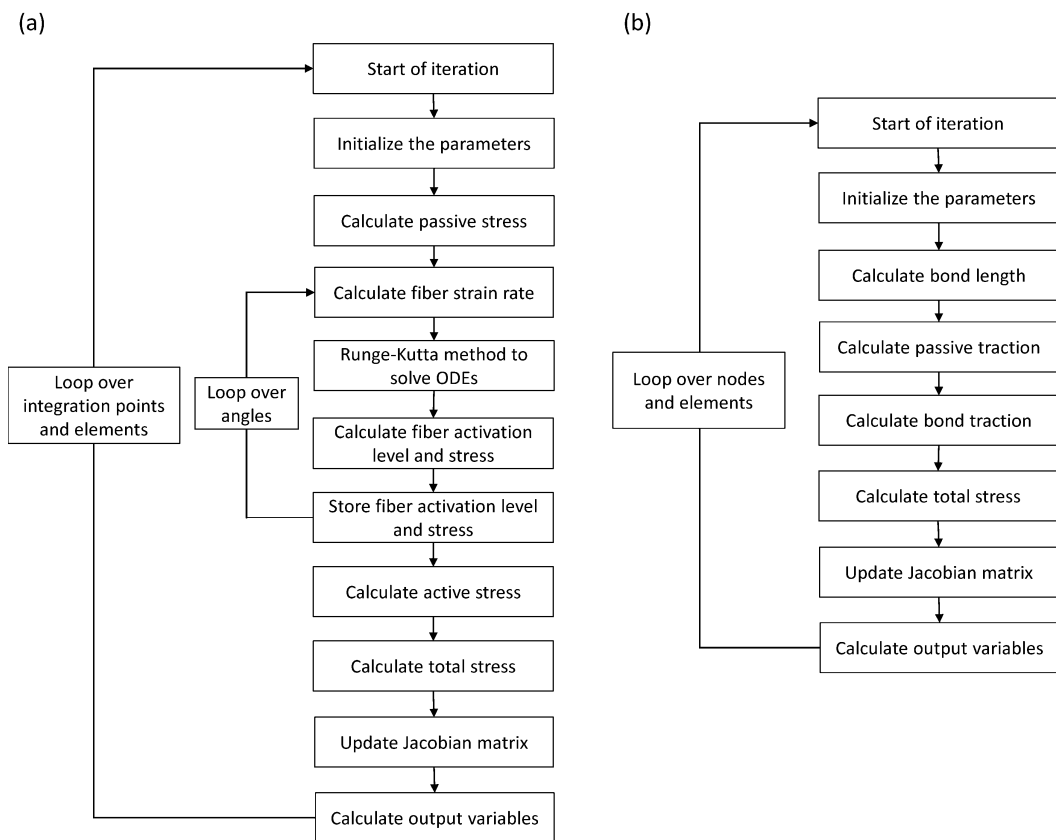
Figure 5.3 Flow chart of (a) UMAT of SF formation and (b) UINTER of focal adhesion formation. The SF formation algorithm applies to the cell body and the algorithm for focal adhesion formation applies to the cell-materials interface.

71

5.2.2 Model parameters

Most of the cell model parameters are adopted from previous study (Deshpande *et al.*, 2008; Pathak *et al.*, 2008). All these parameters are chosen to give the similar experimental observations in (Tan *et al.*, 2003) by Deshpande et al.(Deshpande *et al.*, 2006). The SF association rate k_f is 10 s^{-1} and disassociation rate k_b is 1 s^{-1}. The activation signal decay constant θ is 70 seconds. The strain rate sensitivity parameter $\dot{\varepsilon}_0$ is 0.003. The SF contractility parameter σ_{max} and Hill constant k_v are calibrated in (McGarry *et al.*, 2009) based on the average micro-post force obtained by (Yang *et al.*, 2007). The variation of the steady-state average force per post as a function of posts number shows good agreement with experiment data with σ_{max}=3.5 kPa and k_v=7. The Young's modulus of cell E_c is 0.8 kPa and Poisson's ratio is 0.3. The Young's modulus of the substrate is chosen to be 1 kPa with Poisson's ratio of 0.3 to represent soft gels. In the substrate stiffness effect study, it is varied from 1 kPa to 100 kPa to study the cell response on different physiological tissue stiffness. The cell-substrate interaction forces consist of active forces that involve binding forces of proteins and passive forces such as van der Waals force, hydrophobic forces and steric repulsion (Bell, 1978; Bell *et al.*, 1984). In the current work, the passive forces are considered to be active only in the normal direction to the substrate surface. They are averaged over the cell membrane and assumed to act on the part of membrane excluding the area occupied by the membrane proteins (Ronan *et al.*, 2014). The passive force is only related to the normal separation between the cell membrane and substrate surface. The active forces originate from the integrin-ligand bond interaction. The integrins can switch their configuration between high affinity and low affinity. While only the high affinity integrins are allowed to interact with substrate ligands when sliding over the substrate due to their geometrical higher length. The active forces are calculated according to the relative displacements of cell-substrate interface. Detailed information of the model is presented in Chapter 3. The parameters for the FA model follow those in (Ronan *et al.*, 2014). The chemical difference between high and low affinity integrins is μ_H-μ_L=2.14x10^{-20} J. The total density of low and high affinity integrins at each position is taken to be ξ_0=1000 µm^{-2}. The stiffness of each integrin-ligand bond is λ_s=0.15 nN/µm. The bond force peaks at maximum stretch Δ_n=0.13 µm. The passive characteristic distance is taken to be δ_p= 0.13 µm, and the passive interaction potential is ϕ_0^P =50 fJ.

5.2.3 Data analysis

The displacement on the substrate surface is denoted by u and the displacement of the substrate under the cell edge is denoted by u_z. To describe the deformation in the substrate, the maximum principal logarithmic strain ε_{log} is used:

$$\varepsilon_{log} = \ln(\varepsilon_p)$$

where ε_p is the maximum principal strain. The averaged value of ε_{log} along the cell radius is denoted by $\bar{\varepsilon}_{log}$.

To visualize the SF formation, the averaged fibre activation level is obtained by integrate over the angles at each integration point

$$\bar{\eta} = \frac{1}{\pi} \int_{-\pi/2}^{\pi/2} \eta d\phi \qquad (5.1)$$

To study the effect of thickness on SF formation in the circular cell, the averaged fibre concentration is integrated over the cell radius

$$\bar{\eta}_{avg} = \frac{1}{R_c} \int_{0}^{R_c} \bar{\eta} dr \qquad (5.2)$$

where R_c is the cell radius.

Similarly, the normalized active maximum principal stress is represented by

$$\bar{\sigma}_p = \sigma_p / \sigma_{max} \qquad (5.3)$$

where σ_p is the active maximum principal stress at the material point, σ_{max} is the maximum contractility of the SFs.

The averaged value of active maximum principal stress along the cell radius is

$$\bar{\sigma}_{avg} = \frac{1}{R_c} \int_{0}^{R_c} \bar{\sigma}_p dr \qquad (5.4)$$

The normalized high integrin density is described by

$$\bar{\xi}_H = \xi_H / \xi_0 \qquad (5.5)$$

where ξ_H the integrin density on the cell surface, ξ_0 is the total density of low and high affinity integrins at each material point.

The averaged value of integrin density along cell radius is given by,

$$\bar{\xi}_{avg} = \frac{1}{R_c}\int_0^{R_c} \bar{\xi}_H dr \tag{5.6}$$

To investigate the effect of input parameter variations (substrate thickness, stiffness and cell size) on critical thickness, the output parameters (displacement, strain, SF concentration, SF stress and integrin density) are fitted against the substrate thickness (h/R_c) are fitted with exponential model as suggested in (Tusan *et al.*, 2018)

$$y = y_0 + (y_\infty - y_0)e^{-cx} \tag{5.7}$$

where x is the value of the substrate thickness, y is the value of averaged interfacial displacements, maximum principal logarithmic strain, SF concentration, SF active maximum principal stress and averaged integrin density. To reveal how deep the cell can sense for cells with different size, the critical thicknesses are determined when 50% (half-maximum) (Tusan *et al.*, 2018) and 10% of maximal values (Maloney *et al.*, 2008) of averaged interfacial displacement, interfacial maximum principal logarithmic strain, averaged SF concentration and averaged SF active maximum principal stress are reached.

5.3 Results

5.3.1 Effect of substrate thickness on cell response and cell-induced substrate deformation

Fibroblast cell model with SF formation and FA formation was simulated on an elastic substrate with thickness from 1 µm to 60 µm. To investigate the changes in the substrate, the cell induced displacement and logarithmic strain are shown in Figure 5.4. The displacement in thin substrate is restricted on the surface while it goes deeper in the thick substrate. The highest displacement and strain are both found near the cell edge. However, high logarithmic strain is mainly located near substrate surface in a thick substrate compared to that in a thin substrate. Higher radial displacements are induced by the cell on a thick substrate compared to those on a thin substrate (Figure 5.5a). The substrate displacements of cell-material interface are radially averaged, and it gradually converged on substrate with thickness beyond $h/R_c>3$ (Figure 5.5b). The interfacial logarithmic strain levels off with $h/R_c>0.5$. As see in Figure 5.5c, the localised substrate displacement decreased when it is away

74

from cell edge in all cases. It appears that there was little difference in substrate displacement for the pair of 1µm and 2µm thick substrates, or the pair of 3 µm and 4 µm. For the thicker substrate, it is evident that there is steep change of substrate displacement when it is away from the cell edge. Such a change is less steep for the thinner substrate. As seen in Figure 5.5d, the averaged substrate interfacial log strain appears to decrease exponentially with the ratio of substrate thickness over cell radius (h/R_c).
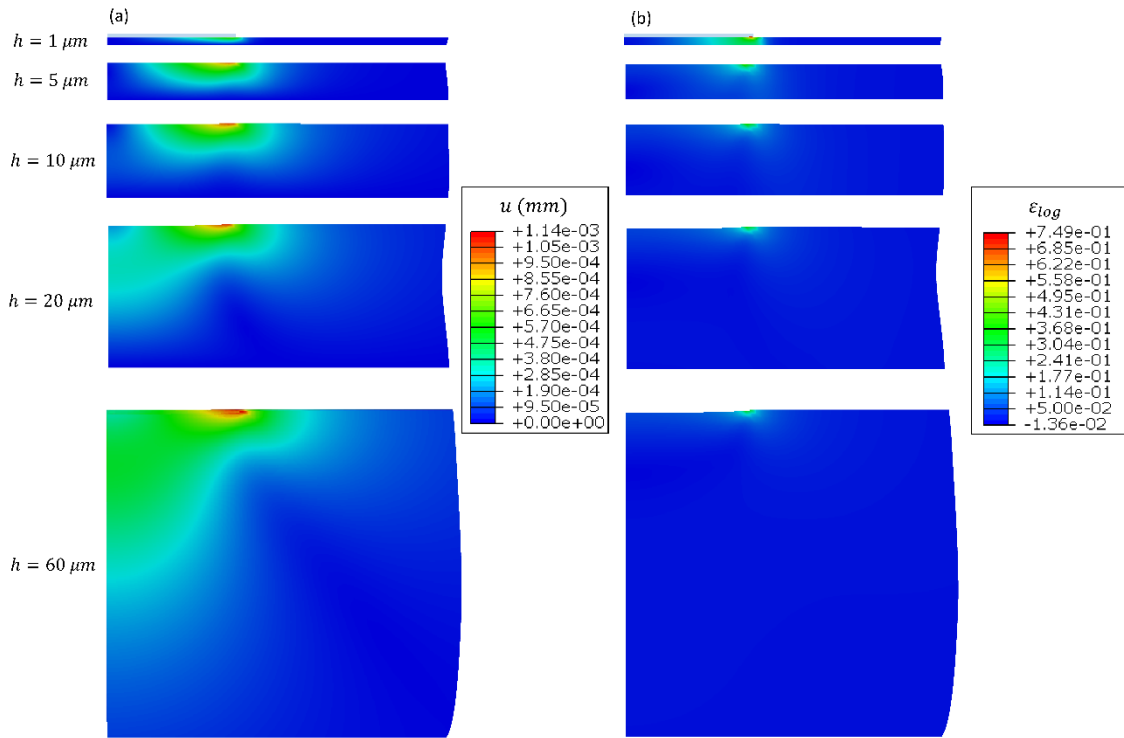
Figure 5.4 Contour plot of (a) displacement and (b) maximum principal logarithmic strain in substrates with thickness from h=1 µm to h=60 µm.

Figure 5.6 shows the contour plot of SF concentration within the cell when a cell is seeded on a substrate with thickness h ranging from 0 to 60 µm. The thickness value h=0 µm denotes the cell interaction with rigid substrate. The SF concentration dropped significantly with the increase of substrate thickness. In general, the SF concentration gradually decreases from the centre to cell edge. SF activation level is highest near the cell centre due to higher active stress (Figure 5.7 and Figure 5.9a), which results in lower disassociation of SFs. Figure 5.7 shows the contour plot of the SF formation induced active maximum principal stress within cell when a cell is seeded on materials with thickness h ranging from 0 to 60 µm. The SF formation induced active maximum principal stress changes in the same way as the SF concentration. Figure 5.8 and Figure 5.9e displays the corresponding contour plot of

cell integrin density ξ_H/ξ_0 at the interface between the cell and substrate. FAs of the cell were formed due to relative cell-substrate displacement. Cell integrins are mostly located near cell edge while few are near cell centre (Figure 5.8). The integrin density of cell at the cell edge on rigid surface is significantly higher than those on elastic material. With increasing the substrate thickness, integrin density generally increases with similar trend.
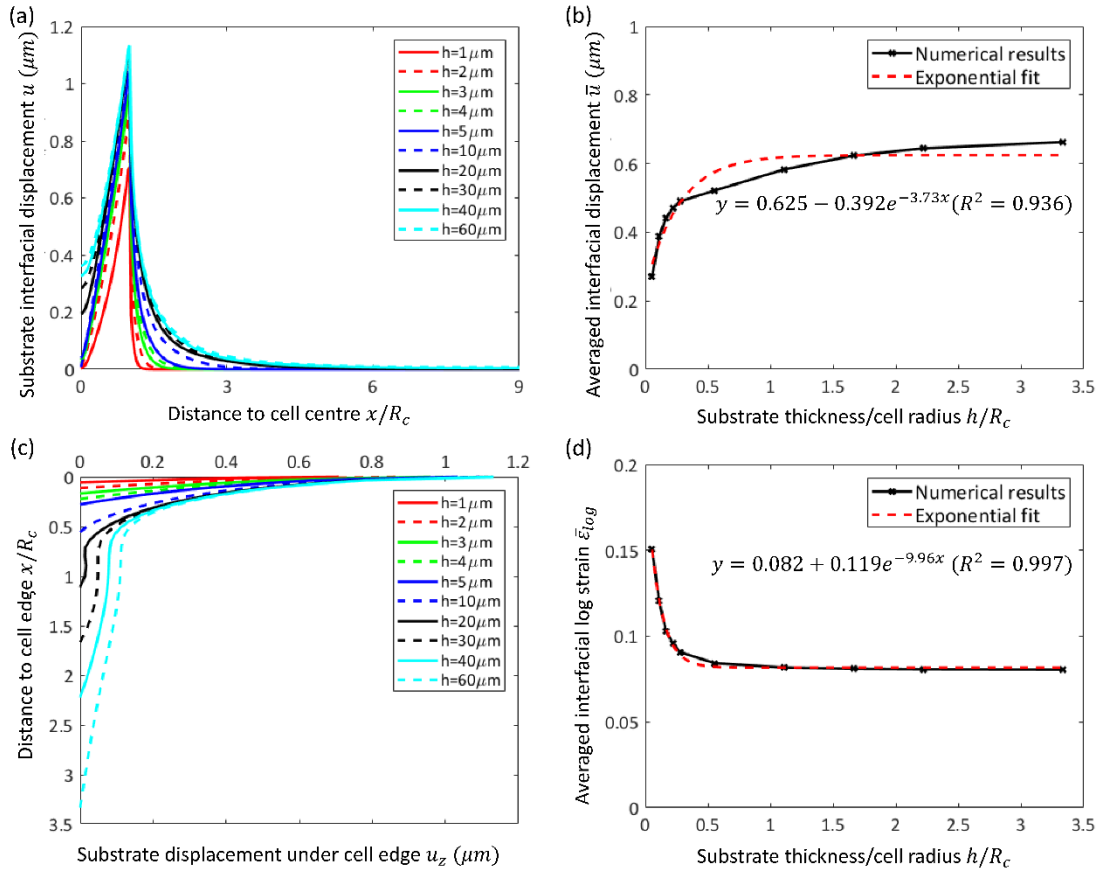
Figure 5.5 (a) Cell induced substrate interfacial displacement along the cell radius; (b) averaged interfacial displacement in matrix with different thickness; (c) substrate displacement variation under the cell edge; (d) averaged interfacial logarithmic strain in substrate with different thicknesses.

Figure 5.9b, d and f show the exponential fits for SF concentration, SF active maximum principal stress and integrin density. The fitted formulations are used to obtain the critical thicknesses based on these variables. The obtained equation parameters and critical thickness are presented in Table 5.1. The critical thickness determined by half-maximum rule based on averaged interfacial displacement is around 3.35 μm, while the other variables give 1.25~1.93 μm. The critical thickness derived by 10% of maximum rule for averaged interfacial displacement is 11.13 μm, while other variables give 4.16~6.41 μm.
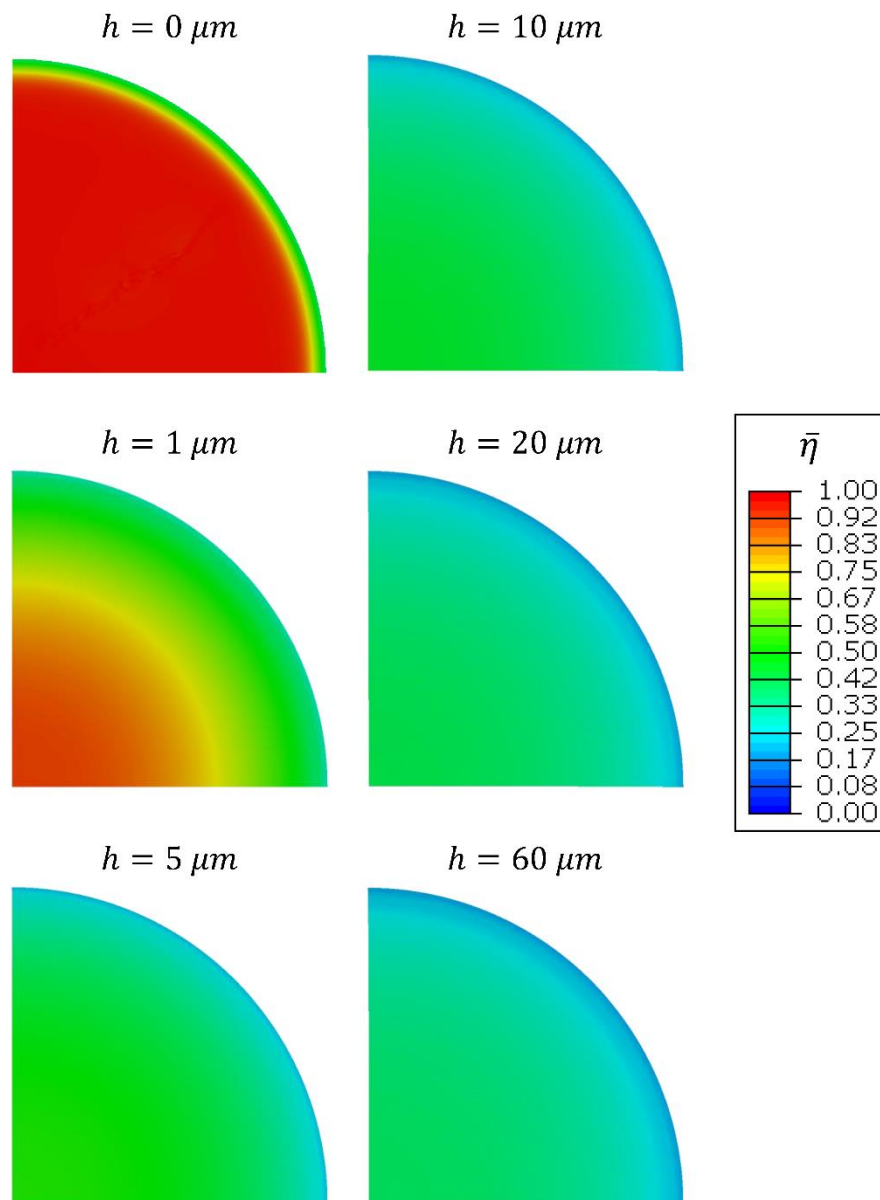
Figure 5.6 Contour plot of SF concentration within the cell when a cell is seeded on materials with thickness h ranging from 0 to 60 μm (h= 0 μm denotes the interaction with rigid substrate).

5.3.2 Effect of substrate stiffness on cell response and cell-induced substrate deformation

To study the role of substrate stiffness in regulating cell behaviour, effect of substrate stiffness combined with variation of substrate thickness were simulated. Substrate stiffness was varied from 1 kPa to 100 kPa with thickness varying from 0 to 60 μm. Figure 5.10 shows the contour plots of substrate displacements and maximum principal logarithmic strains. Higher displacements and maximum principal logarithmic strains were observed near the cell edge. Displacements and strains gradually decreased with increasing the substrate stiffness. The averaged interfacial

displacements and maximum logarithmic strains converged on stiff substrate (Figure 5.11b and d). The averaged interfacial displacements and strains have lower values on stiff substrate (Figure 5.11a and c). For the situations $E_s \geq 10$ kPa, the displacements and strains have little difference. Therefore, these trends are not fitted with exponential model.
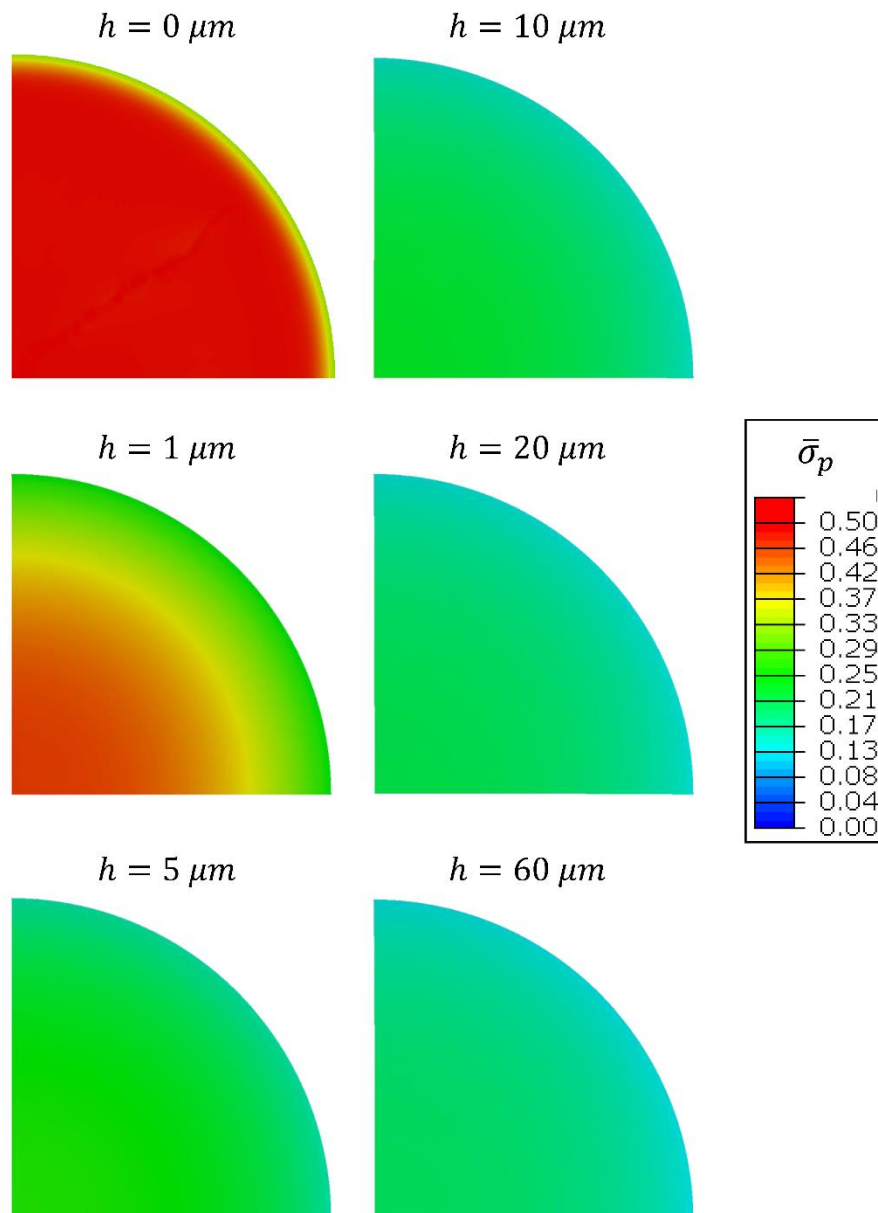
Figure 5.7 Contour plot of the SF formation induced active maximum principal stress within cell when a cell is seeded on materials with thickness h ranging from 0 to 60 μm. (h= 0 μm denotes the interaction with rigid substrate).
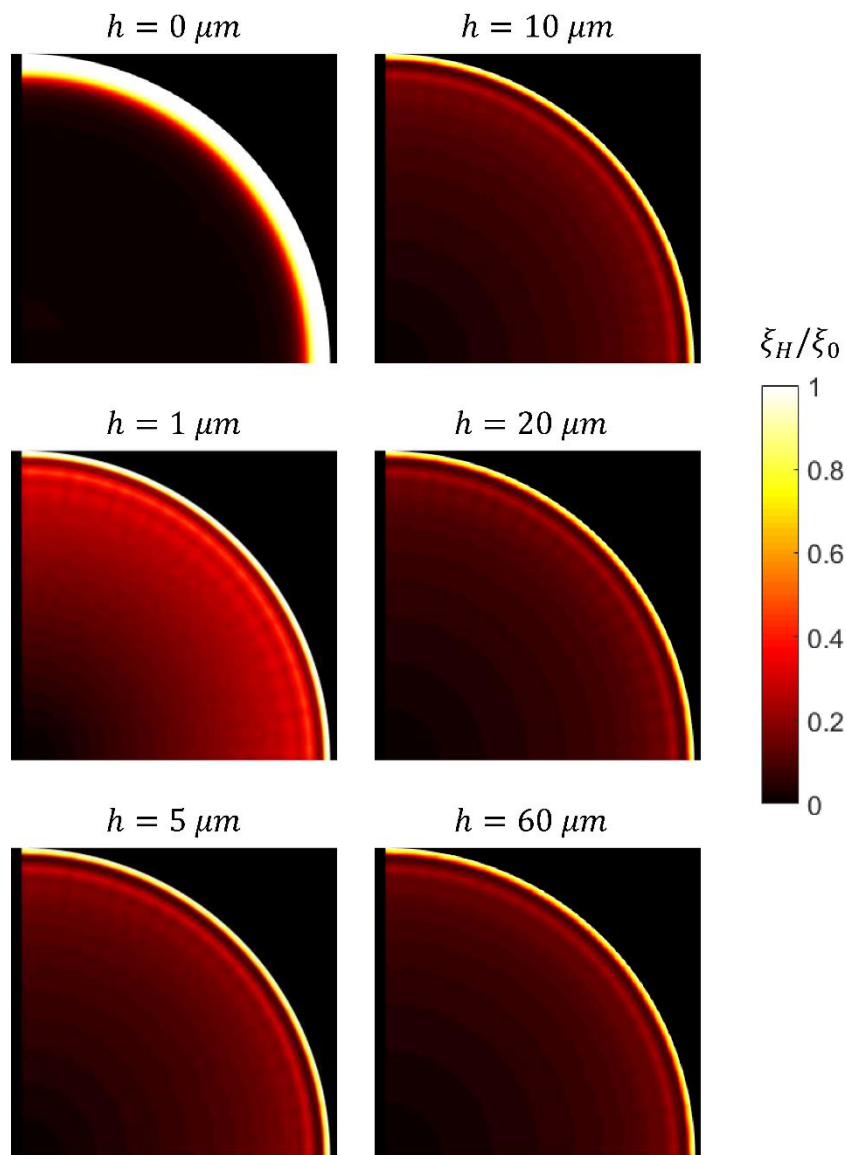
Figure 5.8 Contour plot of cell integrin density ξ_H/ξ_0 at the interface between the cell and substrate. The substrate thickness h varied from 0 to 60 μm ($h = 0\ \mu m$ denotes the interaction with rigid substrate).

Figure 5.12 shows the SF concentration and integrin density variation along the cell radius on substrate with different stiffnesses. The levels of SF and FA on soft substrate (1 kPa) are significantly lower than those on stiff substrate ($E_s \geq 10$ kPa). On substrate with stiffness $E_s \geq 10$ kPa, the SF concentration, active stress and integrin density almost converge and have little difference when varying substrate thickness (Figure 5.12b, d, and e). Due to the little variations of SF concentration, active stress and integrin density on substrate with $E_s \geq 10$ kPa when varying substrate thickness, they are not fitted with exponential model. It demonstrates that this type of cell is very sensitive to the change of stiffness when the substrate stiffness is below 10 kPa. Therefore, only the critical thicknesses on substrate with stiffness lower than 10 kPa

are plotted (Figure 5.16a). Generally, the critical thickness increases with substrate stiffness and is determined to be in the range 1.25~7.37 μm for the half-maximum rule.
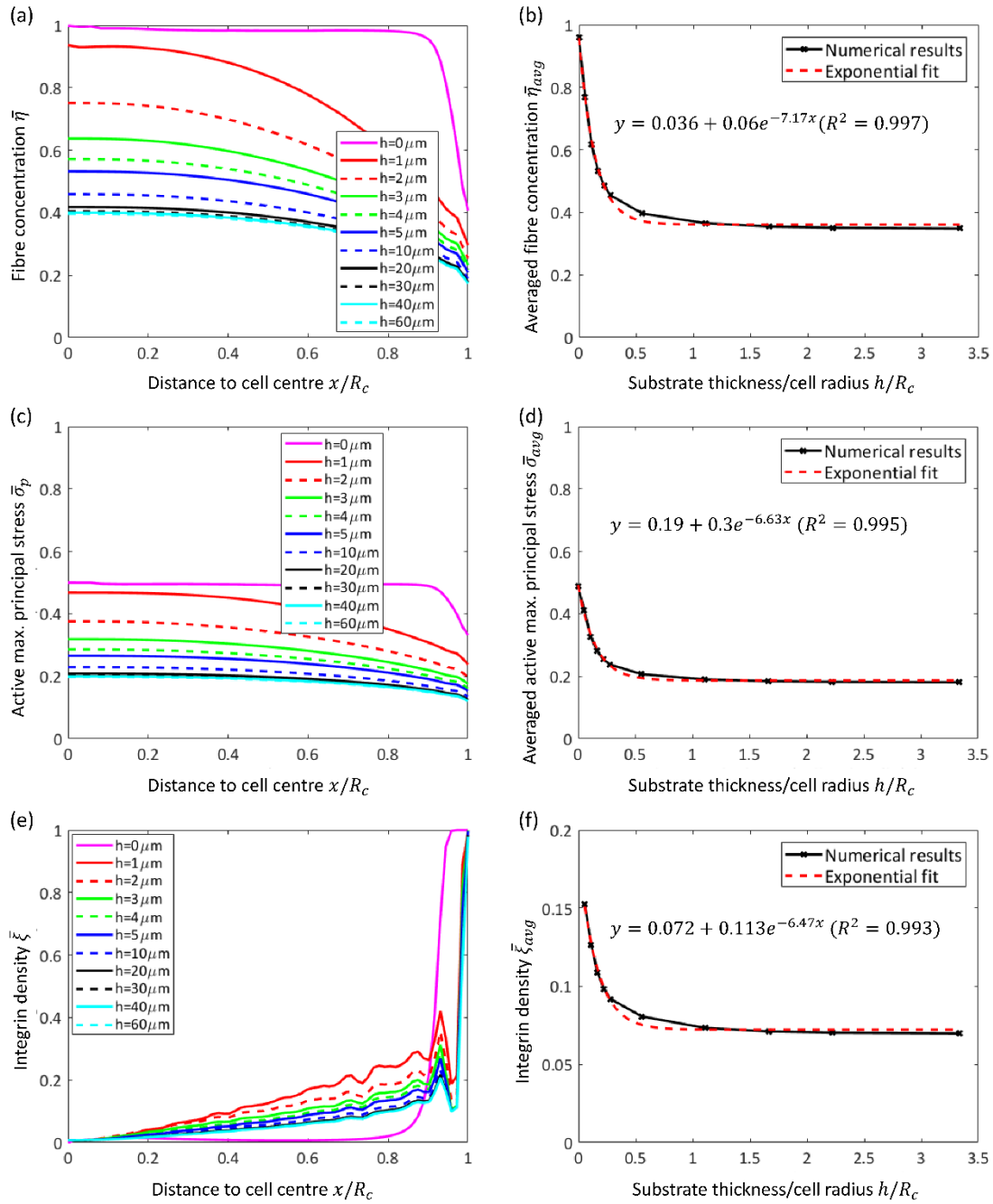
Figure 5.9 (a) SF concentration, (c) Sf active maximum principal stress and (e) integrin density along the cell radius for a cell seeded on materials with thickness h ranging from 0 to 60 μm (h= 0 μm denotes the interaction with rigid substrate). Variation of averaged (b) SF concentration, (d) SF active maximum principal stress and (f) integrin density along cell radius. Red dashed lines are the exponential fit of the numerical results.
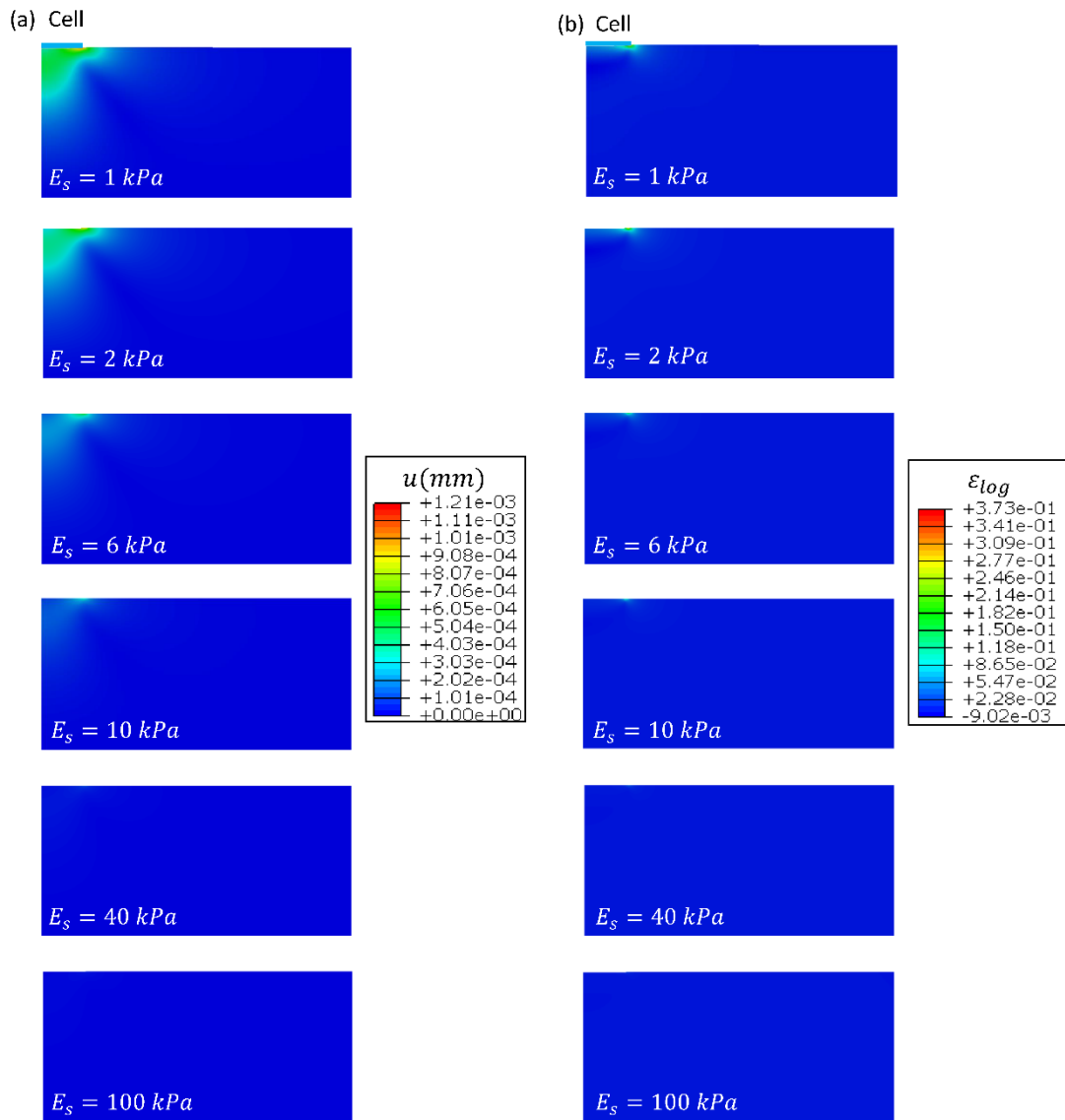
Figure 5.10 Contour map of (a) displacement and (b) maximum principal logarithmic strain of the substrate (thickness h=60 μm) with different stiffnesses.

5.3.3 Effect of cell size on cell response and cell-induced substrate deformation

Figure 5.13 shows the contour map of substrate displacements and maximum principal logarithmic strains. Larger cell produced significantly higher displacements and strains, and the displacements propagated deep into the substrate. The radially averaged interfacial displacements almost scale with cell size on thick substrate while gradually decrease on thin substrate (Figure 5.14b). The maximum principal logarithmic strains generally decrease with increasing cell size (Figure 5.14d). The averaged displacements and strains both show exponential trends with larger cells exhibit higher displacements and strains (Figure 5.14a and c).
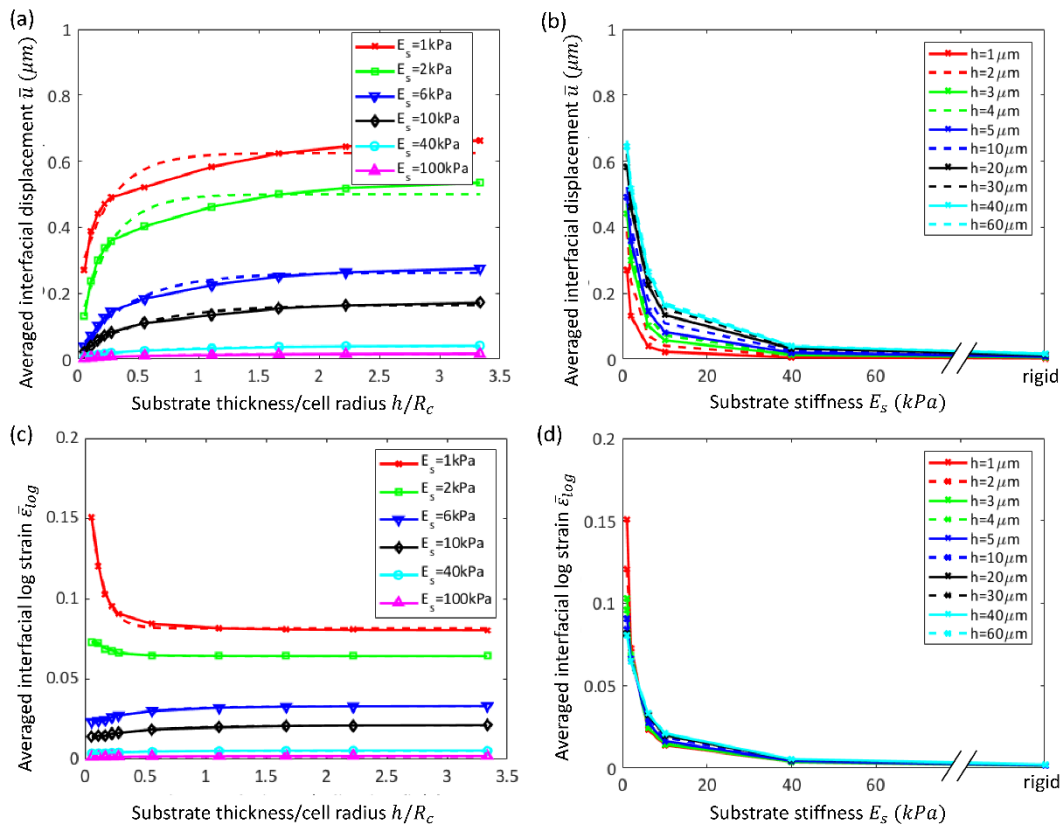
Figure 5.11 The combined effect of substrate stiffness and thickness on (a) averaged interfacial displacements and (c) averaged interfacial maximum principal logarithmic strain along cell radius. The dashed lines are their exponential fit of corresponding numerical results. Effect of substrate stiffness on (b) averaged interfacial displacements and (d) averaged interfacial maximum principal logarithmic strains along cell radius with substrate thickness $h = 60 \ \mu m$.

Variables	y_0	y_∞	c	R^2	Half maximum (μm)	10% maximum (μm)
Displacement	0.625	0.233	3.73	0.936	3.35	11.13
Max. Principal Log strain	0.082	0.201	9.96	0.997	1.25	4.16
SF concentration	0.361	0.958	7.17	0.997	1.74	5.78
Active max. principal stress	0.187	0.492	6.63	0.995	1.88	6.25
Integrin density	0.072	0.185	6.47	0.993	1.93	6.41

Table 5.1 Critical thickness determined by averaged substrate interfacial displacement, maximum principal strain, SF concentration, active maximum principal stress and integrin density.

The averaged SF concentration, active maximum principal stress and integrin density decrease and converged with increasing substrate thickness (Figure 5.15a, c and e). The SF concentration and active maximum principal stress on substrate with thickness h= 60 μm increase with cell size, while integrin density decrease when increasing cell size (Figure 5.15f).
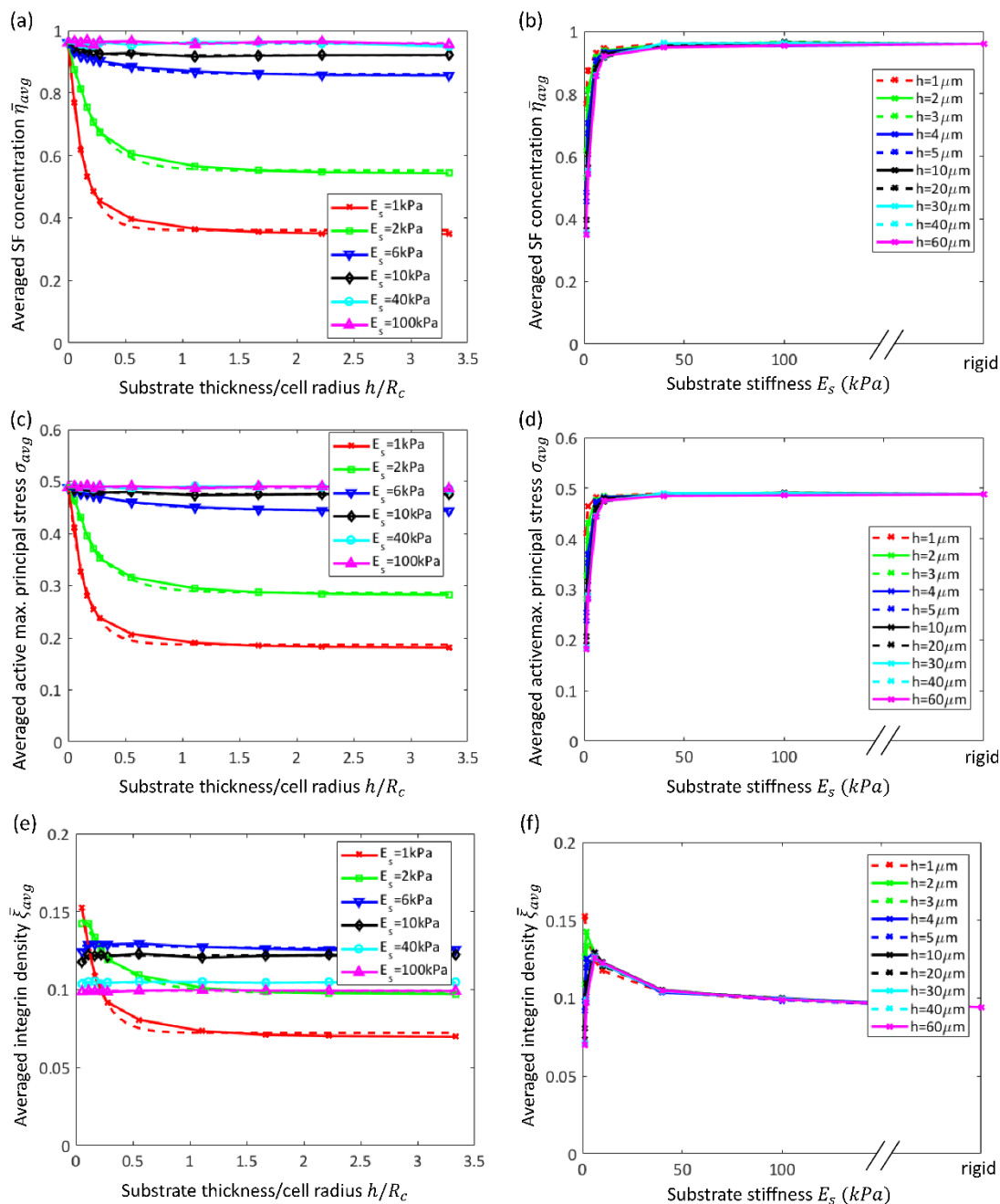
Figure 5.12 Effect of substrate stiffness and thickness on (a) averaged SF concentration, (c) averaged SF active maximum principal stress and (e) averaged integrin density along cell radius. The dashed lines are their exponential fits of corresponding numerical results. Effect of substrate stiffness on (b) averaged SF concentration, (d) averaged SF active maximum principal stress and (f) averaged integrin density along cell radius with substrate thickness $h = 60 \ \mu m$.

Critical thicknesses determined by averaged substrate interfacial displacements, substrate maximum principal logarithmic strain, averaged cell SF concentration, averaged cell SF active maximum principal stress and averaged integrin density for different cell sizes are shown in Figure 5.16. The critical thicknesses are in the range of 0.95~5.74 µm with the half-maximum rule, while they range from 3.14 µm to 19.08 µm for the 10% of maximum rule. For most of these variables, critical thickness increases with cell size except the averaged interfacial displacement.
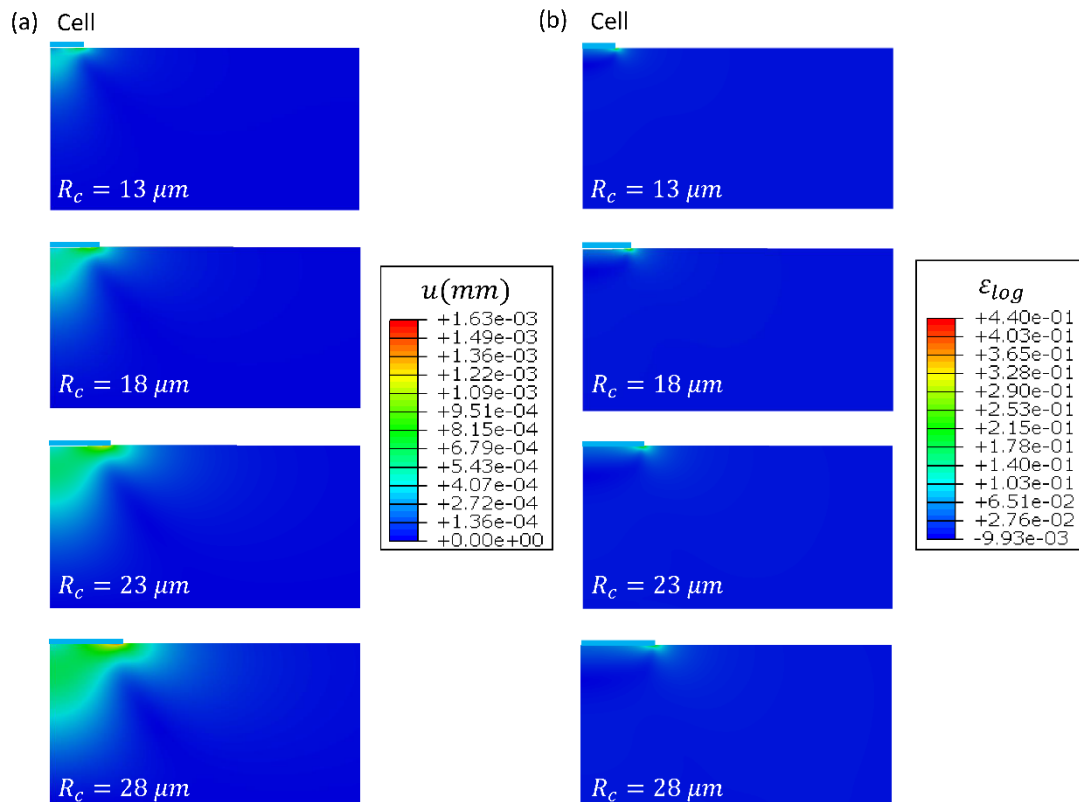
Figure 5.13 Contour map of (a) substrate displacements and (b) their maximum principal logarithmic strains induced by different cell sizes.

5.4 Discussion

The current study presents a computational investigation of SF and FA formation of a bio-chemo-mechanical cell model on different substrate thickness and stiffness, considering the variation of cell size. Cell force microscopy has shown that the lateral substrate displacement increased with substrate thickness for a given material (Merkel *et al.*, 2007). The theoretical analysis by Maloney et al. has also predicted similar trend of cell traction induced substrate displacement (Maloney *et al.*, 2008). The computational modelling by Sen et al. showed the interfacial substrate displacement and maximum principal logarithmic strain increased with substrate thickness and gradually reached a plateau (Sen *et al.*, 2009). The modelling results

presented here (Figure 5.5b and d) are consistent with all these experimental and modelling results reported in literature.

On thick substrate, the cell has low level of SF and FA, while high concentration of SF and FA are predicted on thin substrate (Figure 5.6 and Figure 5.8). Small displacement and higher logarithmic strain are produced on thin substrate due to its fixed bottom boundary, which suggests that the cell feels the rigid body. When increasing the substrate stiffness, both SF concentration and FA integrin density of the cell increase exponentially. When the substrate stiffness exceeds 10 kPa, the averaged interfacial substrate displacements, averaged interfacial maximum principal logarithmic strain, SF concentration and integrin density is almost independent on substrate thickness for a substrate thicker than 1 μm (Figure 5.11 and Figure 5.12). In such case, their critical thicknesses for the stiff substrates appears to be less than 1 μm. Larger cell size enables the deeper sensing capability (Figure 5.14 and Figure 5.15).
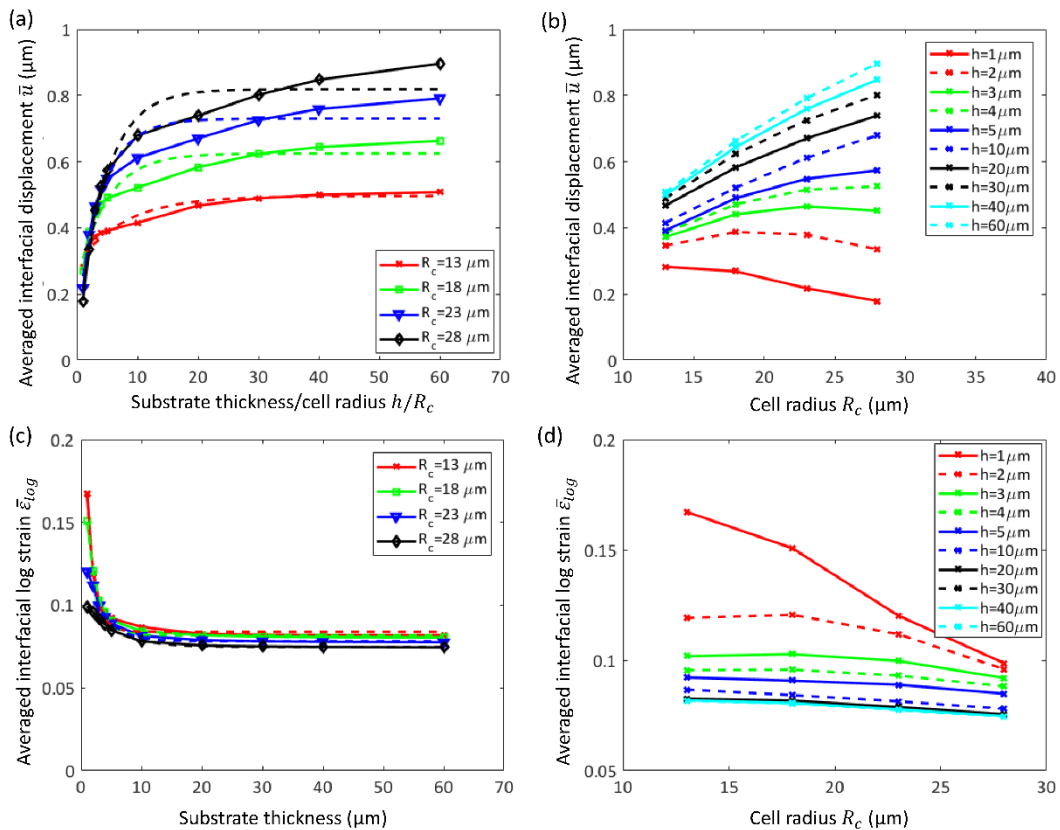
Figure 5.14 Effect of cell size and substrate thickness on (a) averaged interfacial displacements and (c) averaged interfacial maximum principal logarithmic strain along cell radius. The dashed lines are their exponential fit of corresponding numerical results. Effect of cell size and substrate thickness on (b) averaged interfacial displacements and (d) averaged interfacial maximum principal logarithmic strain along cell radius with substrate thickness $h = 60\ \mu m$.
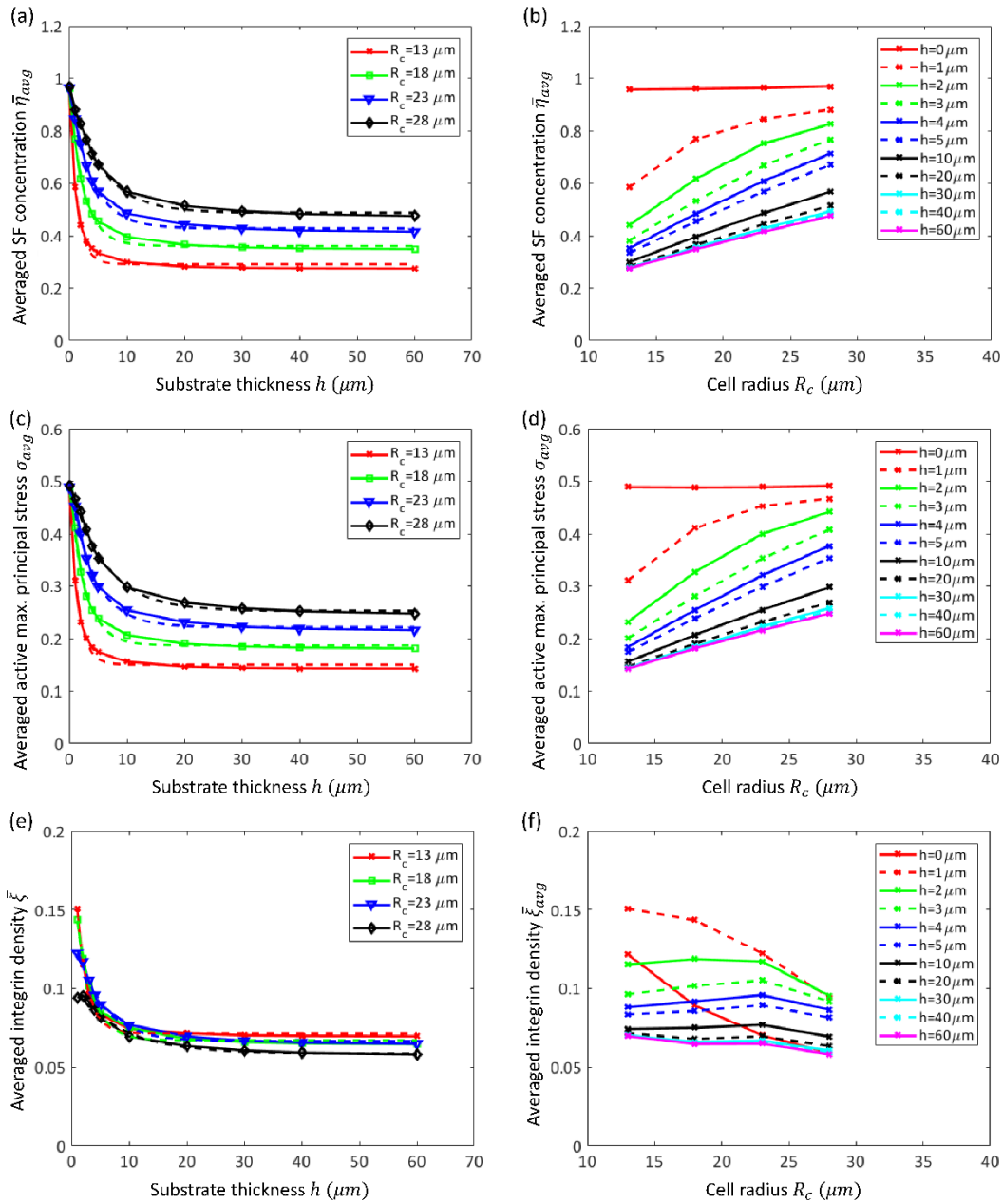
Figure 5.15 Effect of substrate thickness and cell size on (a) averaged SF concentration, (c) averaged SF active maximum principal stress and (e) averaged integrin density along cell radius. The dashed lines are their exponential fit of corresponding numerical results. Effect of cell size on (b) averaged SF concentration, (d) averaged SF active maximum principal stress and (f) averaged integrin density along cell radius with substrate thickness $h = 60\ \mu m$.

Our modelling predicted the increased SF and FA expression when a cell interact with a stiffer substrate, which is consistent with experiment observations (Zemel *et al.*, 2010). The concentration and active maximum principal stress of SFs were saturated when the substrate stiffness increased beyond 10 kPa, which suggests that a typical cell is more sensitive to stiffness change for softer materials with stiffness below 10 kPa. Cells tend to exert higher traction force on stiff substrate to balance

86

their internal tension (Ghibaudo *et al.*, 2008). Higher cell tension will contribute to the formation of SF. The FA level is also promoted on stiff substrate due to the higher force they experienced by the CSK tension, which contributes to the growth of FA (Riveline *et al.*, 2001). In our cell model, higher cell stress induces greater relative displacement between cell and substrate, producing higher level of FA as stated in Chapter 3.
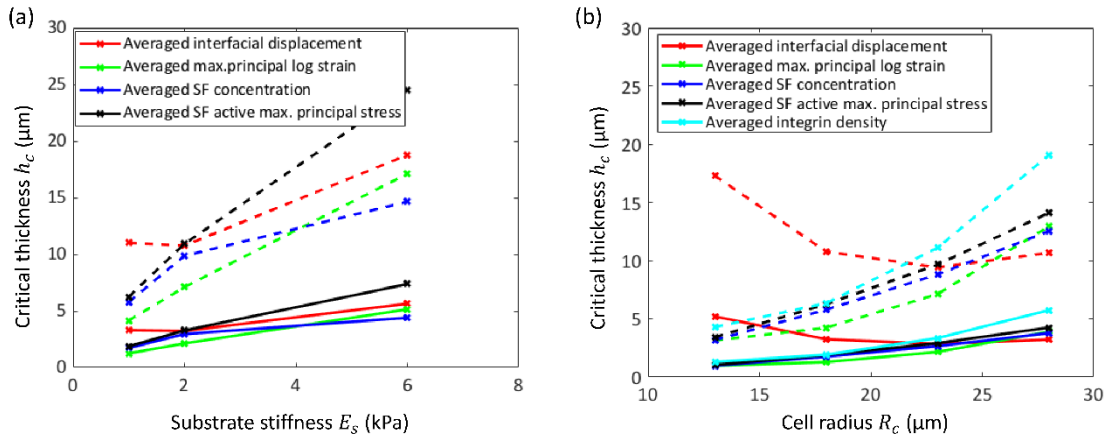
Figure 5.16 Critical thicknesses determined by averaged substrate interfacial displacements, substrate maximum principal logarithmic strain, averaged cell SF concentration, averaged cell SF active maximum principal stress and averaged integrin density for different substrate stiffnesses and cell sizes, solid lines denote the values derived by half-maximum rule, dashed lines denote the values derived by 10% of maximum rule.

The elastic gel has been approximated as semi-infinite medium in experiment studies (Balaban *et al.*, 2001). However, some studies have proposed that cell behaviours could be regulated by finite substrate thickness, including spreading area (Lin *et al.*, 2010), migration(Kuo *et al.*, 2012), and FA size (Li *et al.*, 2018). Therefore, efforts have been made to determine the critical thickness of substrate, beyond which the effect from the rigid support could be neglected. Cell spreading area was often used to calculate the critical thickness in experimental studies (Buxboim *et al.*, 2010). With increasing the substrate thickness, the cell spreading area leveled off to a plateau. The half-maximum of the spreading area was considered as the critical thickness in some studies (Tusan *et al.*, 2018). In some simulation studies, the percentage of maximal displacement or strain was used to determine the critical values, for example, 10%, 50% and 90% of displacement at the substrate depth compared to the surface have been used to determine a FA thickness-sensing (Maloney *et al.*, 2008). The depth, at which the displacement in the substrate decays to 1% of that on the substrate surface, has also been employed to give a critical thickness of 1.15 of

cell radius (He *et al.*, 2014). In previous work, the threshold of thickness has been proposed to depend on the substrate displacement, which should be small enough compared to gel thickness and cell size to eliminate the effect of thickness (Butler *et al.*, 2002). It was also suggested that critical thickness should be around the cell size (He *et al.*, 2014). However, Engler et al. showed that the critical thickness was less than 5 μm, which is much lower than the cell size (~50 μm) (Engler *et al.*, 2004b). In current study, the critical thicknesses are obtained to be up to 0.97~1.93 μm on substrate with stiffness of 1 kPa with half-maximum rule for variables excluding substrate displacement (Table 5.1). Increasing the cell size to R_c=28 μm leads to the deeper sensing of cells with critical thickness of 1.29~5.74 μm. Simulation by Sen et al. has given a critical value around 3 μm for cell size R_c=40 μm with substrate stiffness of 1 kPa obtained by substrate interfacial displacements (Sen *et al.*, 2009). It is comparable with the results by our predictions.

It is found that SF and FA formation have little change with thickness variation on stiff substrates with E_c≥10 kPa (Figure 5.11 and Figure 5.12). It demonstrates the cell stiffness sensing range to be lower than 10 kPa, which is consistent with the predictions in (Ronan *et al.*, 2014). In the range 1~10 kPa, critical thickness scales with substrate stiffness. He et al. have demonstrated the cell sensing depth did not change with substrate stiffness (He *et al.*, 2014). As the cell is modelled as a pre-strained disk in their work, the cell generates constant traction on all the types of substrates. However, the contraction force generated by the cell in our model considers the active response to external environment. Stiffer substrate favours the generation of SF stress (Deshpande *et al.*, 2006), and thus higher sensing depth. Our study has found the sensing depth of the cell could be enhanced with larger cell radius (Figure 5.13). Large cells have higher levels of SF concentration and integrin density. Therefore, the support of thicker substrate could be sensed.

5.5 Conclusions

In current work, the bio-chemo-mechanical cell model considering SF formation and FA growth is employed to study the how deep the cell can sense. The fibroblast cell model is predicted to form high levels of SF and integrin density on thin and stiff substrate. Larger cell can generate higher level of averaged SF active stress and integrin density. The critical thickness for the fibroblast on substrate with stiffness of 1 kPa yielded by the cell responses is around 1.74~6.41 μm, which is consistent with

experimental findings. Such a critical thickness is also dependent on substrate stiffness and cell size.

The modelling framework developed here can be extended to other cell types and can lead to improved understanding of the mechanosensing process during interaction with substrate with different stiffness and geometry. As such, it can potentially guide the materials design for tissue engineering applications.

Chapter 6. Cell Response to Substrate Lateral Mechanical Cues

6.1 Introduction

In chapter 5, a bio-chemo-mechanical model has been developed to study the stress fibre (SF) and focal adhesion (FA) formation in response to substrate stiffness and thickness. In current chapter, this model is applied to further understand how the cell responds to a rigid surface perpendicular to the cell (or its rigid lateral boundary) and its neighbouring cell.

Cells have a complex intracellular apparatus to sense their external material environment. The materials are deformed by the cell contraction and their mechanical cues are transferred to the cell, i.e. two-way interactions. Such mechanosensing process is important in a wide range of cellular activities, including division (Subramanian and Lin, 2005), migration (Pelham and Wang, 1997), morphology (Trichet *et al.*, 2012) and differentiation (Wen *et al.*, 2014).

Much work on cellular mechanosensing has examined the effect of mechanical cues from the underlying substrate (Buxboim *et al.*, 2010; Lin *et al.*, 2010; He *et al.*, 2014), in which case the substrate is parallel to the cell. However, it remains elusive how the cell responds to the stiffer materials that is perpendicular to the cell. A special case is the rigid surface, which can be simplified as constrained lateral boundaries of the materials (Figure 6.1a). It has been revealed that physical boundaries interrupt the process of cell-mediated fibre alignment in the collagen matrix and promoted the fibroblast cell extensions (Mohammadi *et al.*, 2014). The cell is capable to sense a stiffer material far away. During the formation of new tissue in wound healing, the fibrin matrix is replaced with granulation tissue, forming a new substrate for epidermal cell migration at later stages of the repair process (Wang *et al.*, 2012). Furthermore, cells will migrate to the stiff region on substrate with stiffness gradients (Lo *et al.*, 2000). As cells could sense signals away from them, they also sense the mechanical strains created by other neighbouring cells through the underlying compliant substrate (Reinhart-King *et al.*, 2008) (Figure 6.1c). Upon feeling the neighbours, the migration of the cells is hindered compared to isolated cells.

During interactions with substrate, cells assemble and dissemble SFs and FAs dynamically. It has been proposed SFs could contribute to the cell migration process (Tojkander *et al.*, 2012). Therefore, the bio-chemo-mechanical cell model considering the formation of SF and FA is employed in current study to understand their response

to lateral mechanical cues. Meanwhile, the lateral cell-cell communication is also studied to investigate how the cell transmit mechanical signals to another cell through the shared substrate.
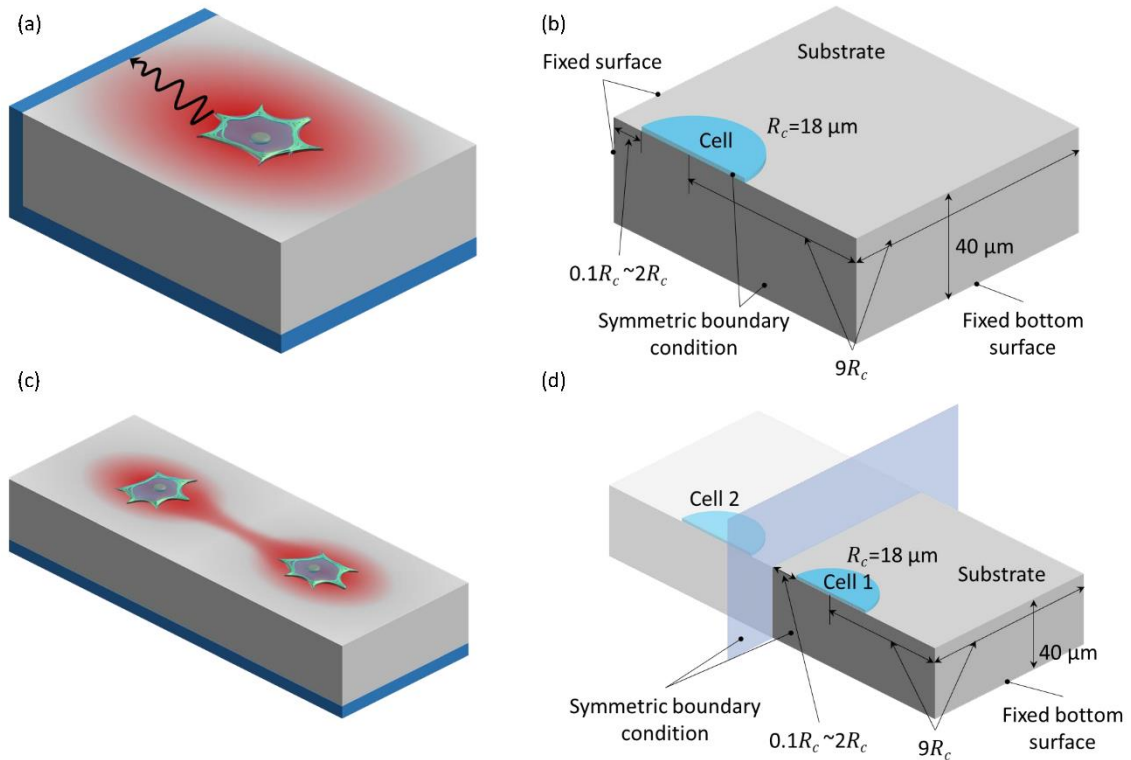
Figure 6.1 Schematic of (a) cell lateral boundary sensing and (c) cell communication on substrate. FE model geometry and boundary conditions of (b) cell lateral boundary sensing and (d) cell-cell communication.

6.2 Methods

6.2.1 Geometry and size

The finite element model settings are similar to those in chapter 5. The cell is modelled as thin layer on the substrate. The cell is chosen to be round and the initial cell area is around 1000 μm² with radius R_c=18 μm. Cell nucleus is neglected due to its little contribution to stress fibre and focal adhesion formation. For the study of lateral boundary sensing of cells, only half of the cell is considered due to the symmetry of the model to improve the computational efficiency (Figure 6.1b). The cell is placed near the fixed boundary with distance d from $0.1R_c$ to $2R_c$. The lateral distance from the cell centre to the free boundary of the substrate is nine times of the cell radius to ensure negligible contribution from the free boundary. Substrate thickness is chosen to be 40 μm as we have shown that little effect from the rigid support with this thickness in Chapter 5. The modulus of the glass is around 50~90 GPa, which is much larger than the modulus of the common materials used in tissue

engineering. Therefore, the glass is considered as rigid base. Symmetric boundary conditions are assumed for both the cell and substrate. The bottom surface of the substrate is fixed to represent its attachment to glass surface without any slip. Other unspecified surfaces are assigned with free boundary conditions. To study the cell-cell communications, one cell is placed with $d_c = 0.2R_c \sim 4R_c$ away from the other cell (Figure 6.1d). For computational efficiency, only one cell is considered and the middle surface between the two cells is assigned with symmetric boundary condition. Other boundary conditions and geometric sizes are shown in Figure 6.1d, which are similar to those of lateral boundary sensing study. The substrate is sufficiently thick so that only the lateral fixed boundary matters.

Typical mesh views of the cell and substrate with $d=1R_c$ are shown in Figure 6.2. The mesh size of the cell is assigned to be 0.25 μm, while the mesh size of the substrate in contact with the cell is 0.6 μm with coarse mesh away from the cell edge. The cell is modelled as active material with the ability to generate contraction force upon external stimulus. The active material is implemented in Abaqus user subroutine UMAT. The contact interface between cell and substrate is modelled as adhesion growth model demonstrated in Chapter 3. The growth of the focal adhesions is dependent on the relative displacement of the cell to the underlying matrix surface. This model is implemented by the user subroutine UINTER in Abaqus. These two models are coupled together to simulate the response to the variation of substrate mechanical properties.

6.2.2 Model parameters

Most of the cell model parameters are adopted from previous study (Deshpande *et al.*, 2008; Pathak *et al.*, 2008). All these parameters are chosen to give the similar experimental observations in (Tan *et al.*, 2003) by Deshpande et al. (Deshpande *et al.*, 2006). The SF association rate k_f is 10 s⁻¹ and disassociation rate k_b is 1 s⁻¹. The activation signal decay constant θ is 70 seconds. The strain rate sensitivity parameter $\dot{\varepsilon}_0$ is 0.003. The SF contractility parameter σ_{max} and Hill constant k_v are calibrated in (McGarry *et al.*, 2009) based on the average micro-post force obtained by (Yang *et al.*, 2007). The variation of the steady-state average force per post as a function of posts number shows good agreement with experiment data with σ_{max}=3.5 kPa and k_v=7. The Young's modulus of cell E_c is 0.8 kPa and Poisson's ratio is 0.3. The Young's modulus of the substrate is chosen to be 1 kPa with Poisson's ratio of 0.3 to represent soft gels. As the sensitivity range of the fibroblast model is restricted

in 10 kPa, the substrate stiffness is varied from 1 kPa to 10 kPa to study the substrate stiffness effect.
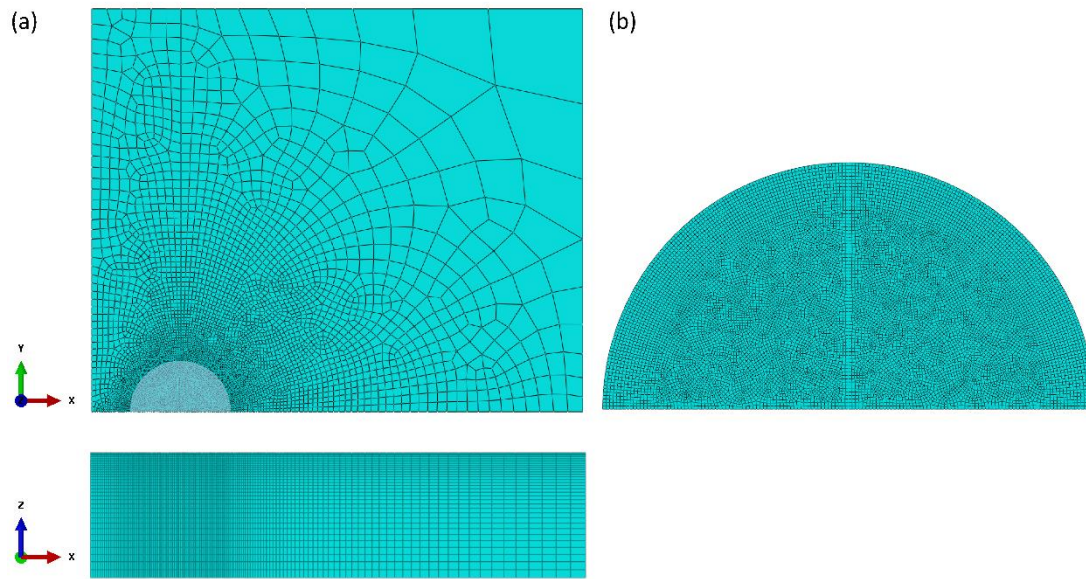
Figure 6.2 (a) Typical mesh of substrate with thickness h=40 µm, (top) top view of the mesh and (bottom) side view of the mesh; (b) enlarged mesh for the cell model.

The cell-substrate interaction forces consist of active forces that involve binding forces of proteins and passive forces such as van der Waals force, hydrophobic forces and steric repulsion (Bell, 1978; Bell *et al.*, 1984). In the current work, the passive forces are considered to act in the normal direction to the substrate surface. They are averaged over the cell membrane and assumed to act on the part of membrane excluding the area occupied by the membrane proteins (Ronan *et al.*, 2014). The passive force is only related to the normal separation between the cell membrane and substrate surface. The active forces originate from the integrin-ligand bond interaction. The integrins have two configurations: high affinity and low affinity, which can convert into each other according to the chemical potentials. However, only the high affinity integrins are allowed to interact with substrate ligands when sliding over the substrate due to their geometrical higher length. The active forces are calculated according to the relative displacements of cell-substrate interface. Detailed information of the model is presented in Chapter 3. The parameters for the FA model follow those in (Ronan *et al.*, 2014). The chemical difference between high and low affinity integrins is μ_H-μ_L=2.14x10^{-20} J. The total density of low and high affinity integrins at each position is taken to be ξ_0=1000 µm^{-2}. The stiffness of each integrin-ligand bond is λ_s=0.15 nN/µm. The bond force peaks at maximum stretch

Δ_n=0.13 μm. The passive characteristic distance is taken to be δ_p= 0.13 μm, and the passive interaction potential is ϕ_0^P =50 fJ.

6.2.3 Data analysis

The displacement on the substrate surface is denoted by u and the deformation is described by the maximum principal logarithmic strain ε_{log}. To visualize the SF formation, the averaged fibre activation level is obtained by integrate over the circular area at each integration point

$$\bar{\eta} = \frac{1}{\pi} \int_{-\pi/2}^{\pi/2} \eta d\phi \qquad (6.1)$$

The normalized active maximum principal stress is represented by

$$\bar{\sigma}_p = \sigma_p/\sigma_{max} \qquad (6.2)$$

where σ_p is the active maximum principal stress at the material point, σ_{max} is the maximum contractility of the SFs.

The normalized integrin density is described by

$$\bar{\bar{\xi}} = \xi/\xi_0 \qquad (6.3)$$

where ξ is the high affinity integrin density on the cell surface, ξ_0 is the total density of low and high affinity integrins at each material point.
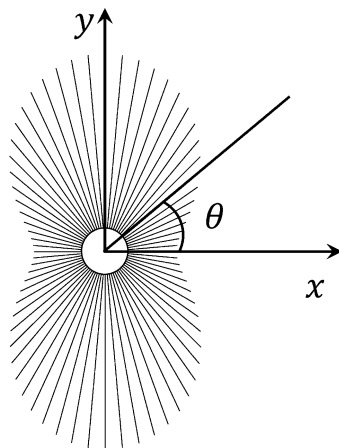
Figure 6.3 An example of the SFs activation at each direction of each material point. The line segment length denotes the SF concentration (η) magnitude.

In current cell model, the SFs at each material point are assumed to be described by 36 SFs uniformly distributed in a circle (Figure 6.3, see model details in Chapter 3).

These SFs may be activated by the tension with certain actin concentration. Higher actin concentration implies higher active stress. The active stresses in these SFs are used to determine the active maximum principal stress at the material point. The direction of the active maximum principal stress is used to represent the orientation of the biologically assembled SF. Obviously, the direction of the active maximum principal stress is related to angles of the maximally activated SFs. To study the level of SF orientation, the SF variance at each material point is defined as:

$$\Gamma = \eta_{max} - \bar{\eta} \tag{6.4}$$

where η_{max} is the maximal value of fibre concentrations among the directions of material point. In Figure 6.3, this example shows that the maximal SF concentration (η_{max}) is at the direction of y-axis with highest SF variance at y-axis direction. Therefore, the biologically associated SF at this point is most probably polarized toward y-axis.

In order to study the influence of lateral boundary or another cell, the variables results along the cell radius are compared with those of control models, which are simulated on substrate without any lateral mechanical cues. The differences are described by residual sum of squares (RSS):

$$RSS = \sum_{i=1}^{n} (f_b^i - f_{ctr}^i)^2 \tag{6.5}$$

where f_b^i is the result influenced by lateral boundary or another cell, f_{ctr}^i is the result from the control model.

The RSS are fitted with exponential model to quantify how far the cell could sense the boundary laterally.

$$y = y_0 + (y_\infty - y_0)e^{-cx} \tag{6.6}$$

The critical decay distances are determined when 50% (half-maximum) and 10% of maximal RSS values of radial interfacial displacement, interfacial maximum principal logarithmic strain, SF concentration, SF variance, SF active maximum principal stress and integrin density are reached.

6.3 Results

6.3.1 Effect of laterally fixed boundary on cell responses

Figure 6.4 and Figure 6.5 show the substrate displacements and maximum principal strains with distance of cell edge to laterally fixed boundary ranging from $0.1R_c$ to $2R_c$. The cell induced displacements and strains have higher values near the cell edge. The displacement and strain patterns are significantly influenced by the lateral boundary when the distance is $d \leq 0.5R_c$ (Figure 6.4a). While the side of cell near the boundary induces few displacements with $d = 0.1R_c$, the other side created significantly higher displacements towards the boundary. In contrast, the maximum principal logarithmic strains have little difference except higher values at cell edge near the laterally fixed boundary with $d = 0.1R_c$ (Figure 6.4b and Figure 6.5c).
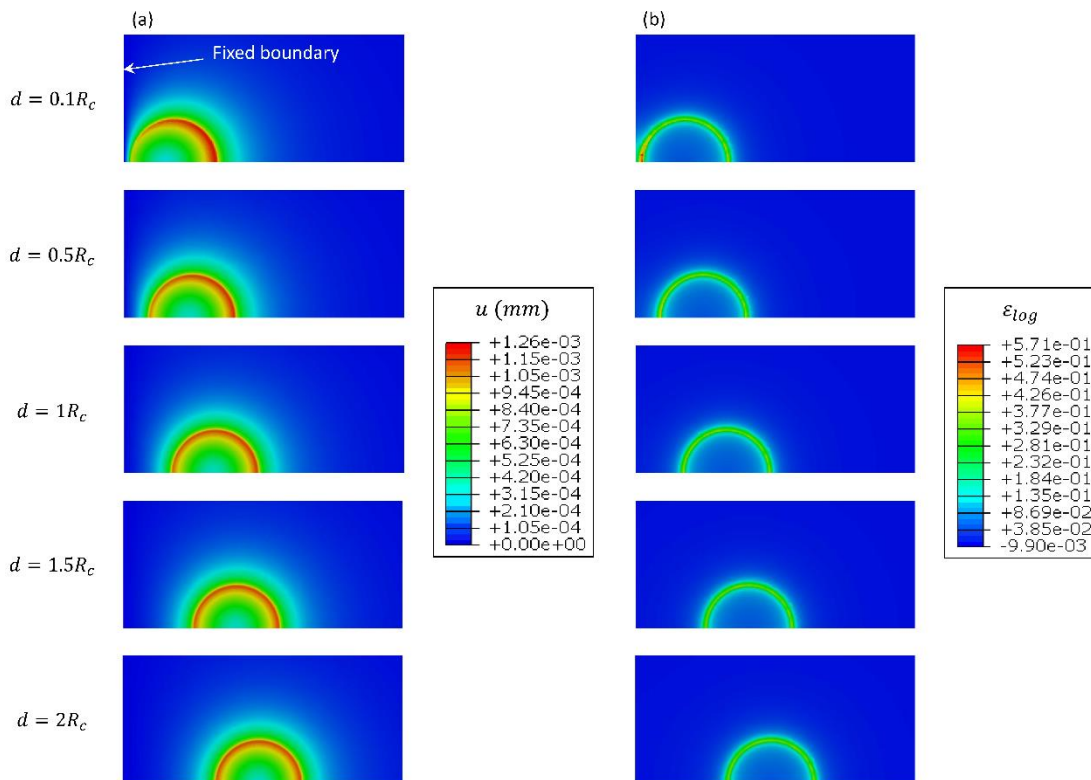
Figure 6.4 Contour plot of (a) displacement and (b) maximum principal logarithmic strain in the substrates with displacing the cell laterally away from the fixed boundary.

The variations of SF concentration, SF active maximum principal stress and SF variance when displacing the cell away from the lateral boundary are shown in Figure 6.6, Figure 6.7 and Figure 6.8. The high values of SF concentrations and SF active maximum principal stresses are mostly located in the cell centre with nearly symmetric pattern. However, high concentrations and stresses are shifted towards the fixed boundary when the cell is near the boundary with $d = 0.1R_c$. The highest SF

variance is observed at cell edge (Figure 6.8). The orientations of SFs are directed along the cell edge. Nevertheless, the SFs inside the cell are oriented towards the fixed boundary with shorter distances. With increasing the distance from the cell edge to fixed boundary, the SFs tend to form circular patterns inside the cell. The circular histogram plots clearly show the polarization of SFs towards the fixed boundary and exhibited lack of sensitivity to the lateral boundary with greater distances. In contrast, the variations of integrin density give little difference (Figure 6.9), except the small fluctuations near cell edge when moving the cell away from the boundary (Figure 6.10g).
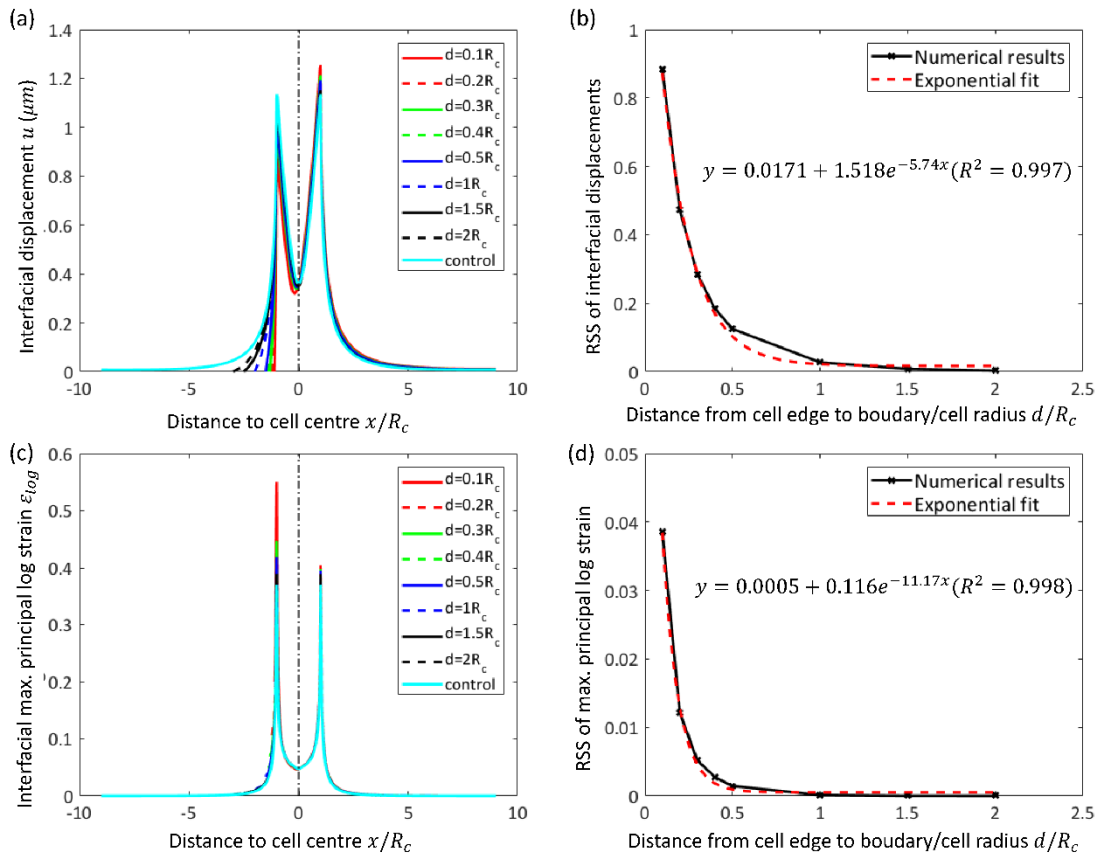
Figure 6.5 Substrate interfacial (a) displacements and (c) maximum principal logarithmic strains along the radial direction of the cell with different distances from cell edge to laterally fixed boundary. The lateral boundary is located at the negative side of x axis. Residual sum of squares (RSS) of (b) interfacial displacements and (d) maximum principal logarithmic strains along the radial direction of the cell compared to the values induced by the cell on substrate without laterally fixed boundaries. The red dashed lines are the exponential fittings of RSS values with equations shown nearby.

Figure 6.10 shows the SF concentration, SF active maximum principal stress, SF variance and integrin density along the cell radius and their RSS values compared to those from control model. It is demonstrated by Figure 6.10e that the SF orientation

could sense the lateral boundary with $d = R_c$. The RSS values exponentially decreased, indicating the attenuated influence from the lateral boundary (Figure 6.5b and d). The estimated sensing distance based on the half maximum rule is $0.06R_c$~$0.12R_c$. While considering sensing the 10% of maximum values, the sensing distance is $0.23R_c$~$0.4R_c$. If we assume that the cell could sense the 1% of maximum values of these variables, the sensing distance will extend to $0.41R_c$~$0.8R_c$.

$d = 0.1R_c$ $d = 1.5R_c$

$d = 0.5R_c$ $d = 2R_c$

$\bar{\eta}$

0.42
0.39
0.35
0.32
0.28
0.25
0.21
0.18
0.14
0.11
0.07
0.04
0.00

$d = 1R_c$

Fixed boundary   Substrate

d Cell
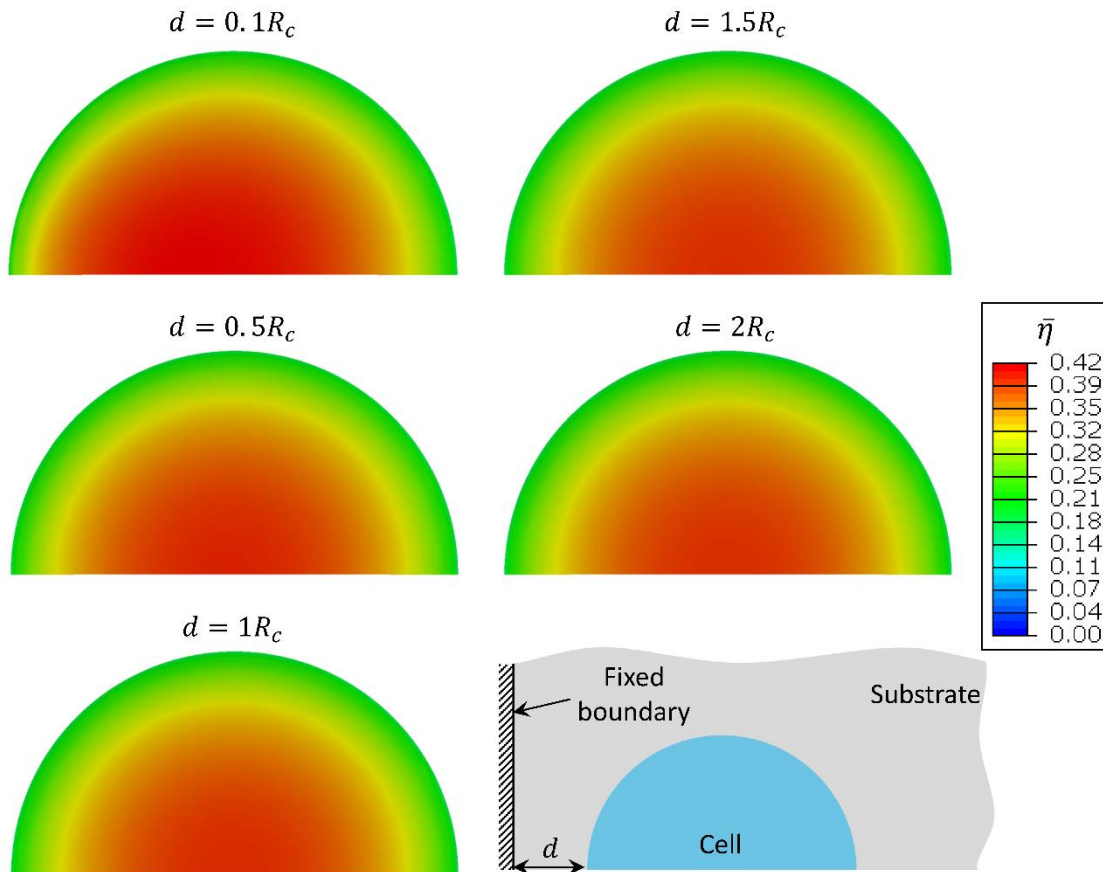
Figure 6.6 Contour plot of SF concentration of the cell with displacing the cell laterally away from the fixed boundary. The bottom right figure shows the schematic of cell position relative to the lateral boundary.

6.3.2 Cell-cell communication on elastic substrate

Cells could communicate with other cells nearby on compliant substrate through sensing the deformations created by other cells. In current work, we studied how far the cell could sense another similar cell on elastic substrates. Figure 6.11 shows the contour plot of substrate interfacial displacements and maximum principal logarithmic strains with different cell-cell distances. Due to the attraction of another cell, the cell induces higher dispalcements at the side far away from the other cell. and creates greater logarithmic strains near the other cell. With increasing cell-cell distance, the influence from the other cell is attenuated. The displacements and logarithmic strains

along the cell radius in Figure 6.12a and c demonstrate their variations in accordance with Figure 6.11.
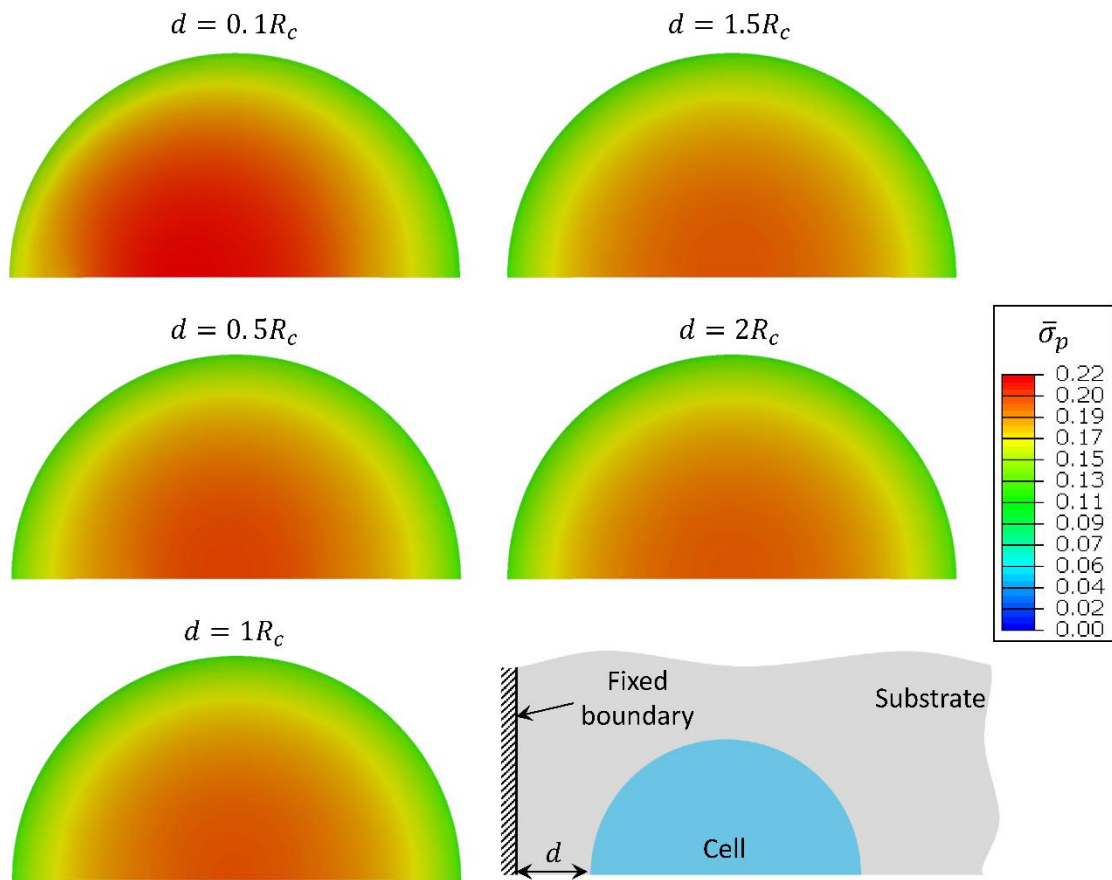
Figure 6.7 Contour plot of SF active maximum principal stress of the cell with displacing the cell laterally away from the fixed boundary. The bottom right figure shows the schematic of cell position relative to the lateral boundary.

Figure 6.13, Figure 6.14 and Figure 6.15 show the variations of SF concentration, SF active maximum principal stress and SF variance when displacing the cell away from the other cell. The higher SF concentrations and SF active principal stresses are shifted towards the other cell with $d_c = 0.2R_c$. While the cell SF concentrations and SF stresses are insensitive to the nearby cell with $d_c \geq 0.6R_c$. SFs are oriented towards the neighboring cell with polarized SF pattern (Figure 6.15). The cell integrin density has little difference in response to difference cell- cell distances (Figure 6.16), with small fluctuations near cell edge (Figure 6.17g). The radial SF concentration, SF active maximum principal stress, SF variance and integrin density are used to compare with the result of control model. The RSS values of these variables in Figure 6.17 decreases exponentially with increasing cell-cell distance. Three different criteria were used to determine the critical intervals to enable effective mechanical cue induced cell-cell communication: 1) RSS=0.5*maximum RSS, the cells could

communicate with each other within distance of $0.22R_c$; 2) RSS=0.1*maximum RSS, the cell can connect to the other cell within distance of $0.36\sim0.71R_c$; 3) RSS=0.01* maximum RSS, the cells could talk to each other within $1.43R_c$.
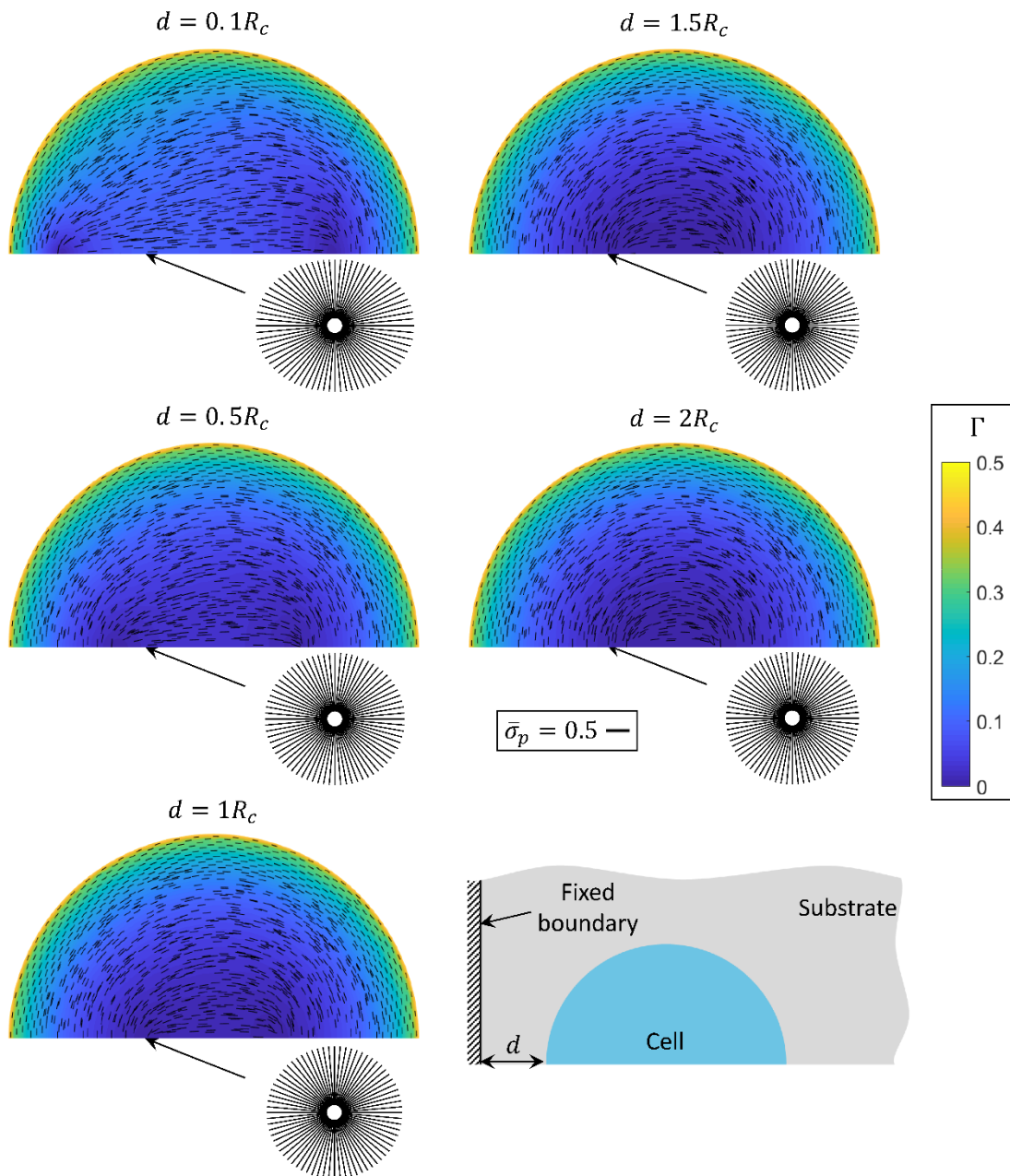
Figure 6.8 Contour plot of SF variance of the cell with displacing the cell laterally away from the fixed boundary. The bottom right figure shows the schematic of cell position relative to the lateral boundary. The line segments denote the magnitude of the active maximum principal stresses ($\bar{\sigma}_p$) and their directions. The circular histogram plots represent the SF stress in each direction at the indicated point.

As smaller deformation could be induced on stiff substrate, we studied the effect of substrate stiffness on cell lateral mechanical sensing. When the cell-cell distance is fixed to be $0.2R_c$, the radial distributions of SF concentration, SF active principal

stresses, SF variance and integrin density of cells on substrate with different substrate stiffnesses are shown in Figure 6.18. Higher substrate stiffness significantly attenuated the interfacial displacements and logarithmic strains (Figure 6.18a and b). The displacements and strains do not propagate far from the cell edge on stiff substrate. Although the SF concentration, stress and variance increase with substrate stiffness, they are gradually shaped to be symmetric about the centre of the cell with increasing the substrate stiffness. The cell tends to be insensitive to the boundary on stiff substrate.
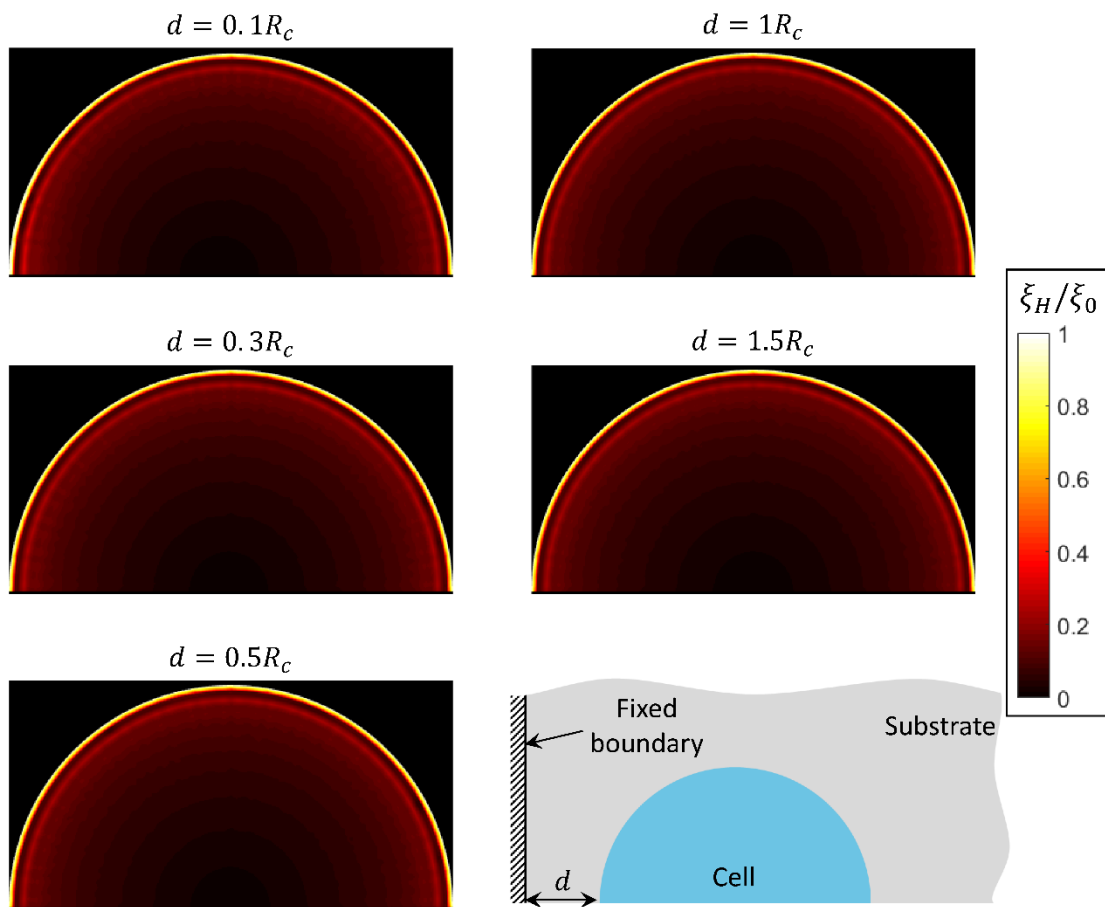
Figure 6.9 Contour plot of integrin density within the cell with displacing the cell laterally away from the fixed boundary. The bottom right figure shows the schematic of cell position relative to the lateral boundary.
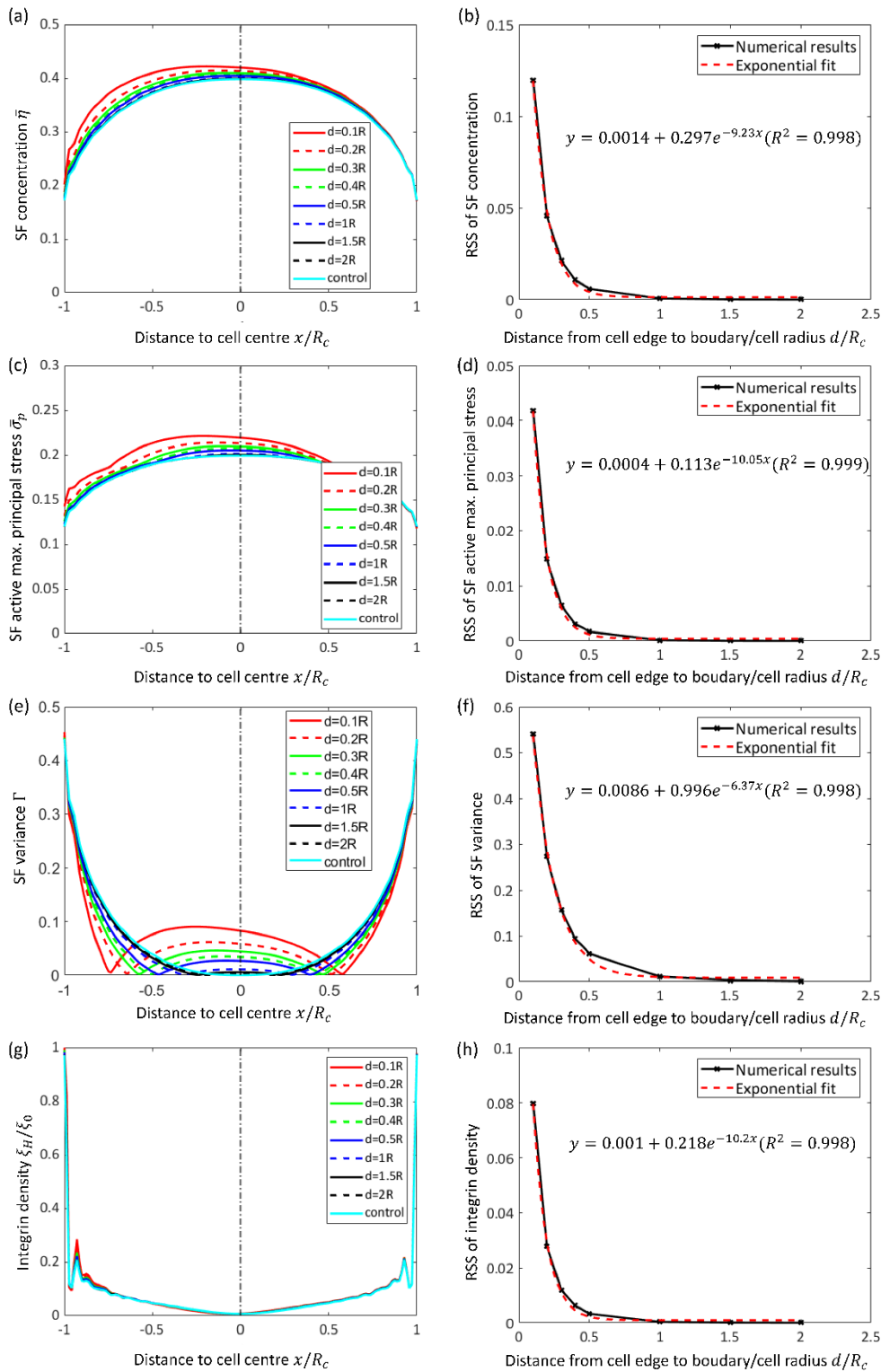
Figure 6.10 (a) SF concentration, (c) SF active maximum principal stress, (e) SF concentration variance, and (g) integrin density along the cell radius with different distances from the cell edge to lateral fixed boundary. The lateral boundary is located at the negative side of x axis. Residual sum of squares (RSS) of (a) SF concentration, (c) SF active maximum principal stress, (e) SF concentration variance, and (g) integrin density, compared to the values of a cell with no lateral boundary.The red dashed lines are the exponential fittings of RSS values with equations shown nearby.
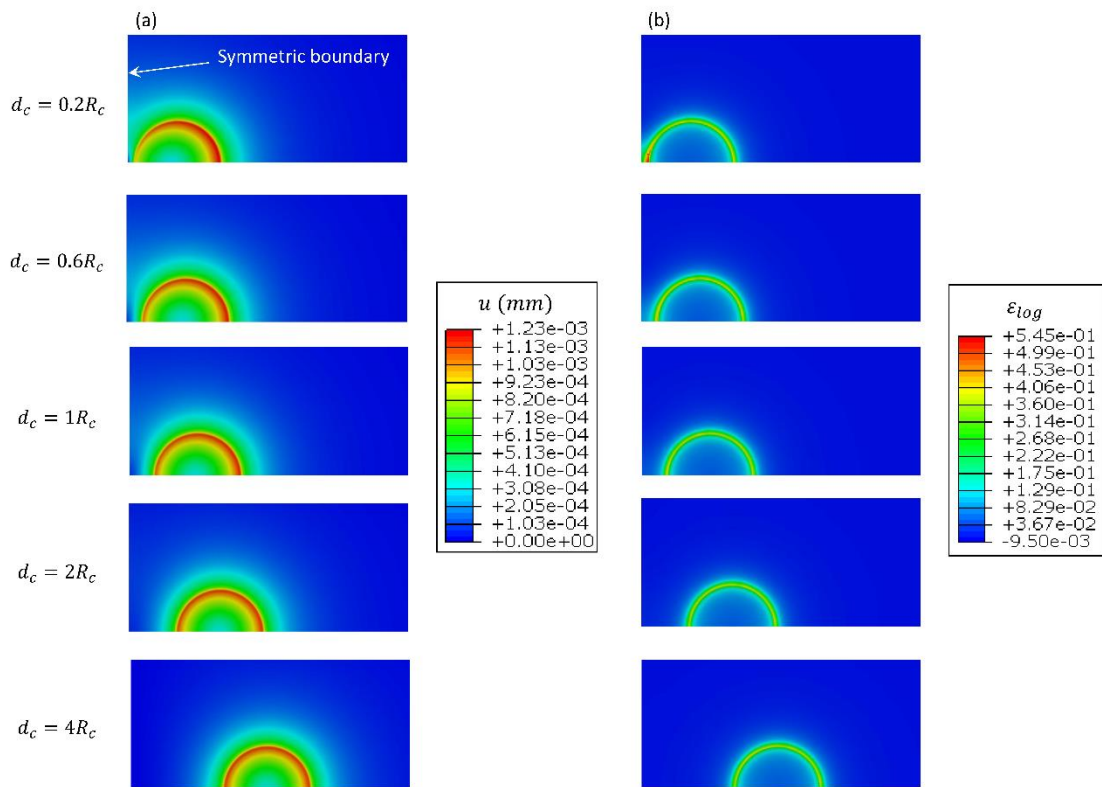
Figure 6.11 Contour plot of (a) displacement and (b) maximum principal logarithmic strain in the substrates with different cell-cell distances.

6.4 Discussion

In current study, the effect of laterally fixed boundary and a neighbouring cell on the SF and FA formation of a cell are investigated. The results show the centre of SF concentration and SF active principal stress patterns are shifted towards the fixed boundary, implying that the cell responds to the physical boundary condition. This lateral boundary sensing phenomena could be analogous to the cell 'durotaxis' (directed cell migration) on substrate with stiffness gradient (Lo *et al.*, 2000). The substrate fixed at the lateral side can be considered as a stiffness gradient with a step change from a soft region to a rigid region. It has been demonstrated that higher stiffness gradient strength enhances the cell durotaxis speed (Isenberg *et al.*, 2009; Vincent *et al.*, 2013). Therefore, such a rigid boundary will significantly influence the adjacent cell behaviour. Cell SFs are polarized towards the fixed boundary (Figure 6.8). As a consequence, the orientation of the FAs could be regulated and finally change the cell polarization (Prager-Khoutorsky *et al.*, 2011). This result is consistent with experimental observations that cells orient in the direction of stiffness gradient (Vincent *et al.*, 2013). Our prediction demonstrates that the cell SF orientation is influenced by the fixed boundary within distance of $d = R_c$ on substrate with stiffness of 1 kPa.
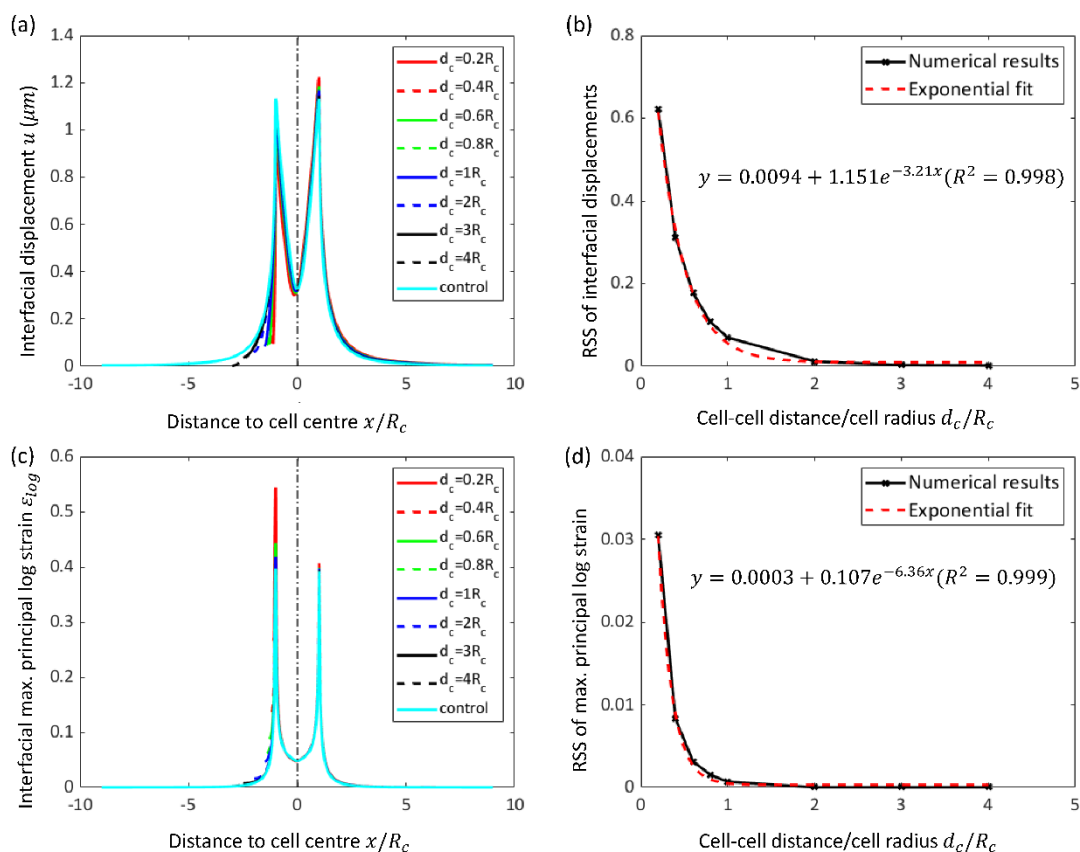
Figure 6.12 Substrate interfacial (a) displacements and (c) maximum principal logarithmic strains along the radial direction of the cell with different cell-cell distances. The lateral boundary is located at the negative side of x axis. Residual sum of squares (RSS) of (b) interfacial displacements and (d) maximum principal logarithmic strains along the radial direction of the cell compared to the values induced by a single cell on substrate. The red dashed lines are the exponential fittings of RSS values with equations shown nearby.

When the cells encounter other cells on the same substrate, they can sense the other cells through the underlying substrate. It has been reported that pairs of endothelial cells keep disconnecting and reconnecting on elastic gels with stiffness of 2.5~5.5 kPa (Reinhart-King *et al.*, 2008). Cells sense the adjacent cells within the displacement field created by themselves. As shown in our results, the displacement field connect to the symmetric part to talk to the other cell with appropriate cell-cell distance (Figure 6.11). The lateral mechanical cues created by other cells induce the SF orientation, which ultimately changes the cell shape. The cell shape has been reported to regulate the traction forces (Rape *et al.*, 2011), which could provide the migration driving force for the cells (Zhong and Ji, 2013). In contrast to the cells on soft gels, the cells on stiff gels (33 kPa) only contact once and move away from each other, implicating that higher substrate stiffness undermines the cell-cell communication. It is demonstrated that the deformation field created by the cell do

not propagate a detectable distance from the cell edge on stiff substrate (Reinhart-King *et al.*, 2008). This is confirmed our results in Figure 6.18, which shows the attenuated propagation of displacement and strains on the stiff substrate. The detectable displacement field for the endothelial cell is ~31.2 µm with cell size ~100 µm. It gives a sensing distance of ~$0.6R_c$, which is comparable with the estimation (0.36~$0.71R_c$,) by the 10% of RSS (Figure 6.17). Although the sensing distance is cell type dependent, the contractility of endothelial cells and fibroblast are comparable based on the experiment measurement (Kolodney and Wysolmerski, 1992).
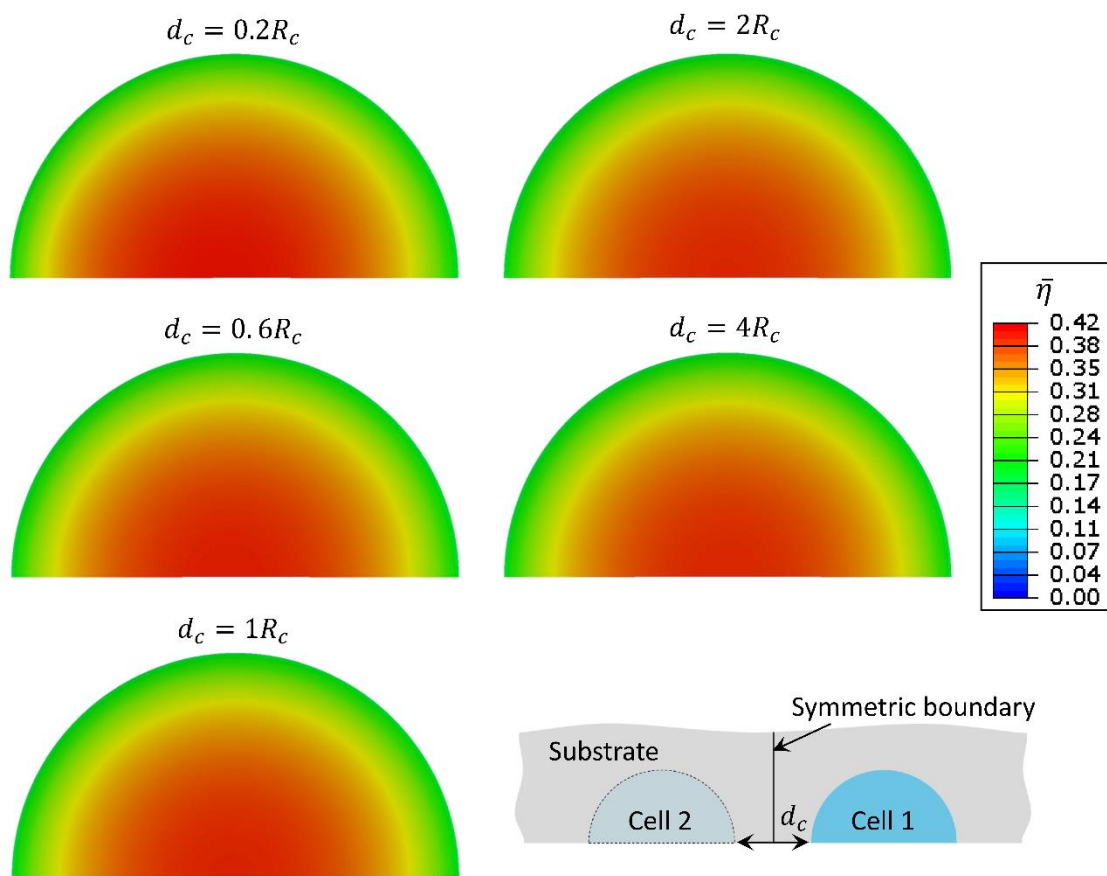
Figure 6.13 Contour plot of SF concentration of the cell with different cell-cell distances. The bottom right figure shows the schematic of cell-cell communication position.
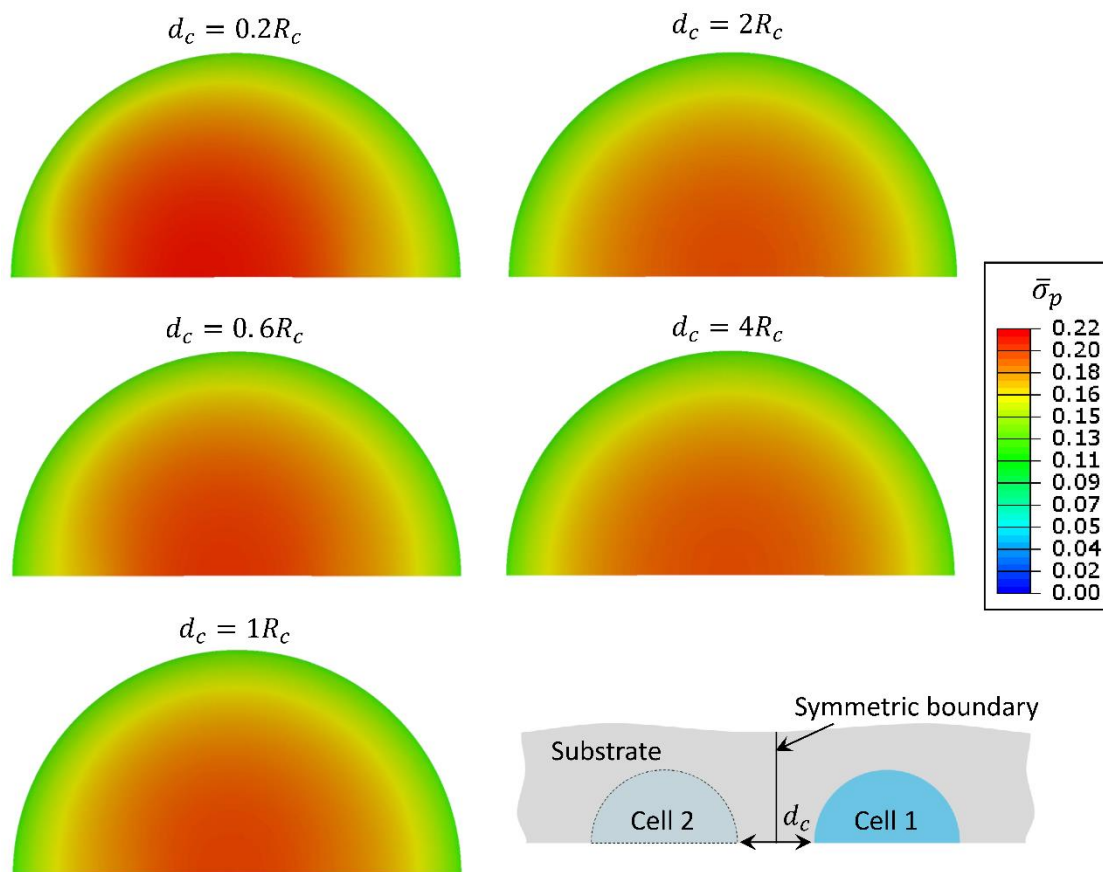
Figure 6.14 Contour plot of SF active maximum principal stress of the cell with different cell-cell distances. The bottom right figure shows the schematic of cell-cell communication position.

Cell-cell communication depends on the material types of the substrate. For example, the non-linear strain-stiffening fibrin gels enable the cells to communicate with other cells of hundred microns away (Winer *et al.*, 2009). Recent studies have focused on how far the cell could sense laterally on fibrous matrix (Wang *et al.*, 2014; Humphries *et al.*, 2017). Wang et al. have reported that cells sense other cells located at distances ~20 times their size in fibrous 3D matrices (Wang *et al.*, 2014). On 2D fibrous matrix, the displacements propagate to distance of 10 times cell radius, while the cells on linear and neo-Hookean material only propagate to 4 times cell radius (comparable to our prediction in Figure 6.12a). The fibres in the substrate are aligned and compacted and in turn modulate the cell contraction. However, the lateral boundaries could interrupt the fibre alignment process in small cell culture grid (Mohammadi *et al.*, 2014).
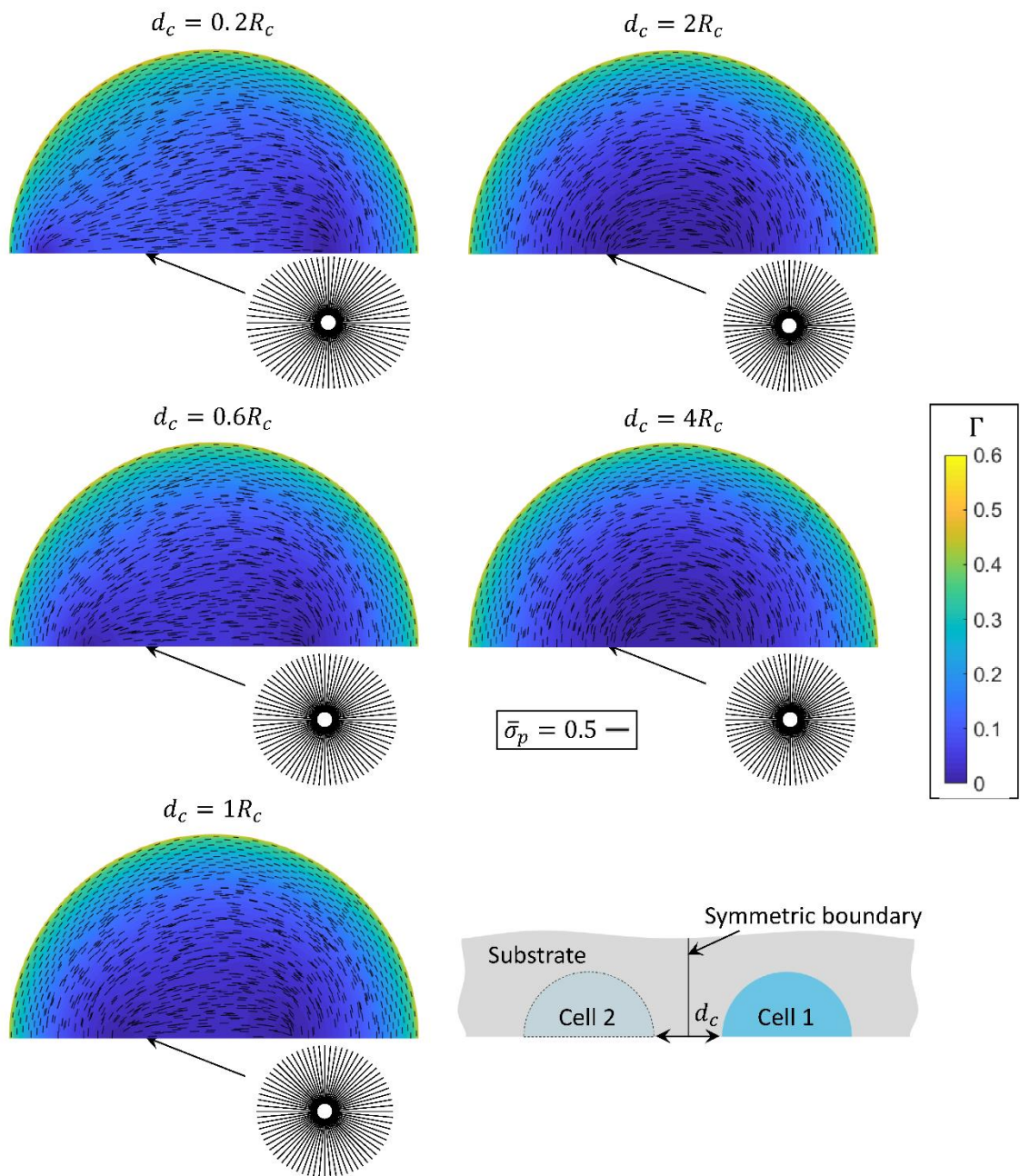
Figure 6.15 Contour plot of SF variance of the cell with different cell-cell distances. The bottom right figure shows the schematic of cell-cell communication position. The line segments denote the magnitude of the active maximum principal stresses ($\bar{\sigma}_p$) and their directions. The circular histogram plots represent the SF stress in each direction at the indicated point.

6.5 Conclusions

In current work, the cell SF concentration, SF active principal stress, SF orientation and integrin density are investigated with the effect of laterally fixed boundary and neighbouring cell on elastic substrates. SF concentration and SF active principal stress centres are shifted towards the fixed boundary. SF orientation is regulated and directed towards the boundary. The fibroblast cell could sense the lateral boundary

within distance $d = 0.4R_c$. However, the boundary can influence the SF orientation within the distance $d = R_c$. Cell SF concentration and stress centres bias towards the neighbouring cell, similar to the response to laterally fixed boundary. Cell orients its SFs in the direction of another cell. Cell-cell communication on elastic substrate is restricted in distance of d_c =0.36~0.71R_c. These predictions provide information for guiding the material design in tissue engineering.
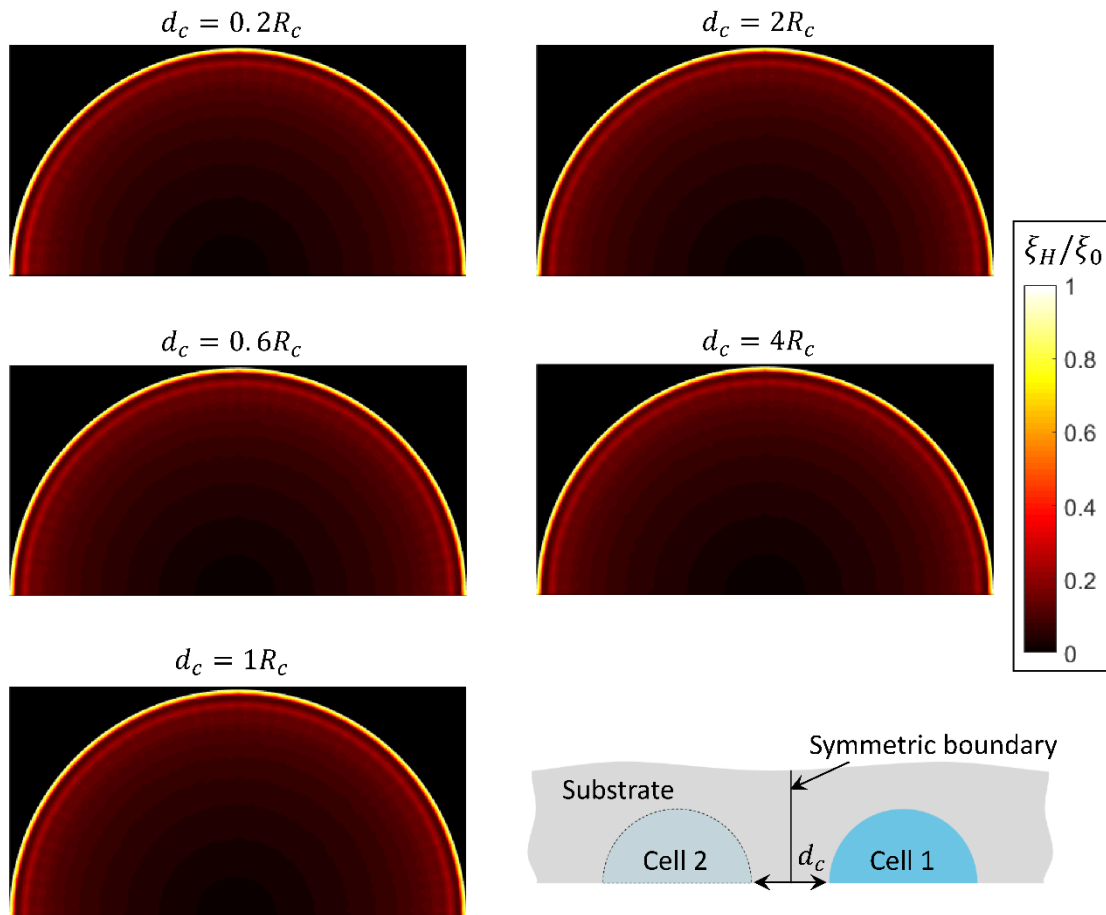
Figure 6.16 Contour plot of integrin density within the cell with different cell-cell distances. The bottom right figure shows the schematic of cell-cell communication position.
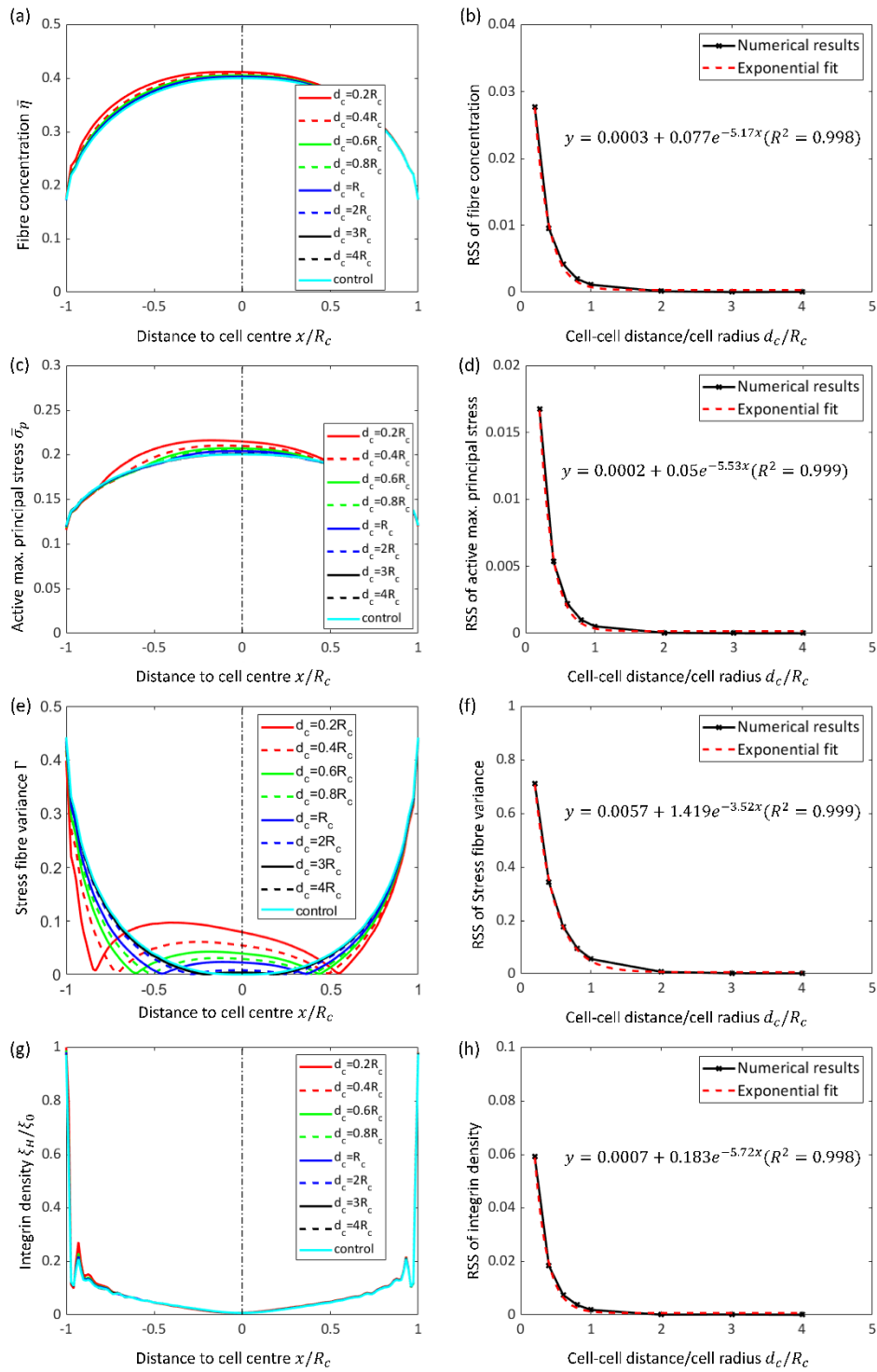
Figure 6.17 (a) SF concentration, (c) SF active maximum principal stress, (e) SF concentration variance, and (g) integrin density along the cell radius with different cell-cell distances. The other cell is located at the negative side of x axis. Residual sum of squares (RSS) of (b) SF concentration, (d) SF active maximum principal stress, (f) SF concentration variance, and (h) integrin density, compared to the values of a single cell on substrate. The red dashed lines are the exponential fittings of RSS values with equations shown nearby.
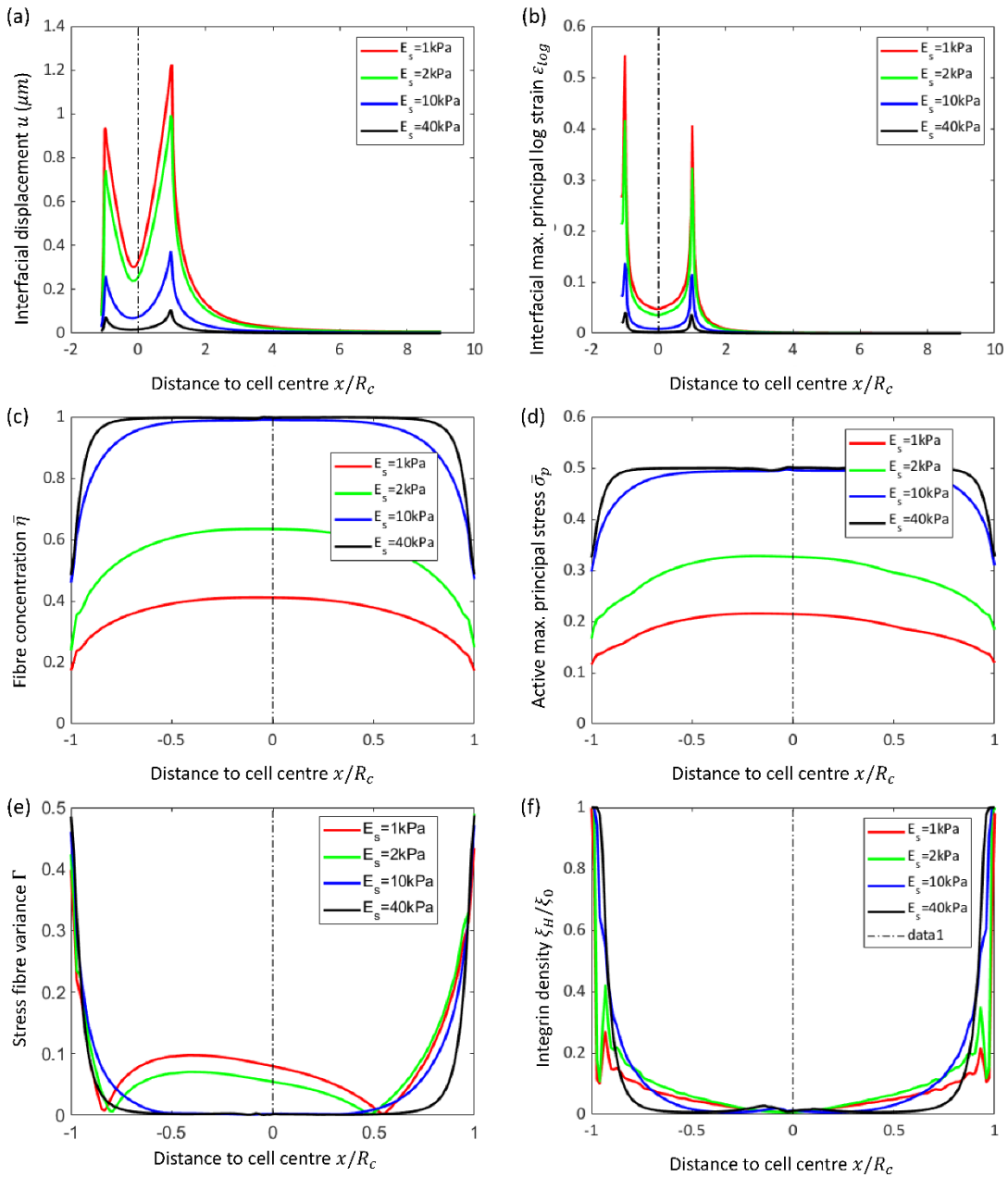
Figure 6.18 (a) Substrate interfacial displacements, (b) substrate interfacial maximum principal strain, (c) SF concentration, (d) SF active maximum principal stress, (e) SF concentration variance, and (f) integrin density along the cell radius with the cell placed $0.2R_c$ away from the other cell on substrate with varied stiffness (E_s=1, 2, 10, 40 kPa). The dash-dotted lines denote the centre of the cell. The other cell is located at the negative side of x axis.

Chapter 7. Conclusions and Future Work

7.1 Conclusions

In current study, we have employed a structure-based cell model to investigate the roles of subcellular components in nano-indentation process to obtain apparent cell elasticity. We have revealed the contributions of the cytoskeleton components to the apparent elasticity. Large indenter sizes attenuate the effect of subcellular heterogeneity and average the contributions from all cell components. Small and sharp indenters could sense the local heterogeneity of cells. Specifically, the sharp indenters amplified the contributions of stiff cellular component including actin cortex, stress fibres (SFs) and microtubules. This structure-based cell model provides a clear understanding of cell mechanics during nano-indentation process, which will also guide the practitioners to better interpret their nanoindentation results of cell using different test protocols.

As SFs are important in cell mechanics presented in our nano-indentation simulation, the role of SF in cell-material interactions are studied. However, it is difficult to describe the formation and self-organization of SFs with structure-based model. Therefore, a continuum-based bio-chemo-mechanical model has been developed. This model has revealed the physical insights of SF and focal adhesion (FA) formation when the cell senses the rigid surface underneath the elastic substrate with finite thickness (in other words, thickness sensing process). Furthermore, we have also explored how the concentration and orientation of SFs change in the presence of a rigid surface perpendicular to cell. This will enable us to understand cell's mechanical sensing capacity in lateral direction. The modelling parameters were calibrated for a typical fibroblast cell. It has demonstrated that   fibroblast cell senses deeper into the substrate with lower stiffness. In a more quantitative manner, the cell is more sensitive (in terms of variations in SF and FA formation) to substrate stiffness under 10 kPa, while insensitive to further increase of stiffness. In general, the level of SF and FA formation is proportional to cell size. The bigger cell, the more deformation of the underlying elastic substrate. For the lateral mechanical cues, the cell senses the lateral boundary within distance of cell radius and orients its SFs towards the rigid surface (simplified as fixed boundary). The cell can regulate the SF orientation of its neighbouring cell within distance of one cell radius, which is comparable to the displacements field created by the cell.

These studies have enabled the quantitative prediction of SF and FA formation of a cell in response to mechanical properties of the elastic substrate. These predictions can potentially guide a bespoke design of biomaterials in tissue engineering to achieve desirable cellular functions.

7.2 Future work

Although the structural based finite element has merits in understanding the spatial dependent mechanical properties of a cell, it has several limitations. For example, the equilibrium moduli were adopted for all the subcellular components. In principle, all these sub-cellular components can exhibit time-dependent behaviour. Therefore, the model can be improved by adopting biphasic model for cytoplasm, viscoelastic properties for nucleus and cytoskeleton. Furthermore, the tension in the actin cortex may induce the depth-dependent variation of apparent elasticity, it will be considered in the updated model to investigate its role in structural cell indentation process. But we also need to be aware that some of those viscoelastic properties of the subcellular component are very difficult to be directly measured experimentally.

Despite of the capacity of robust predictions of how cells sense the physical properties of elastic substrate and substrate mediated cell-cell sensing, there are also several limitations in the modelling. For instance, the integrin densities in the continuum-based model have little difference in response to lateral mechanical cues due to the maximum density restriction. Therefore, the model can be further improved by considering the FA protein transportation which can be accumulate at cell edge. Additionally, the cell model does not consider the effect of nucleus in cell-material interaction. Thus, the computational model could be extended to a fully 3D cell model (rather than cell layer) to give a comprehensive understanding of SF formation during cell-material interaction. The SF response to the substrate is cell type dependent. Therefore, we could also extend the modelling framework to other cell types such as muscle cell, mesenchymal stem cell and osteoblast.

Finally, part of the *in vivo* connective tissues consists of fibrous components such as collagen, fibronectin, and elastin. Such fibrous extracellular matrix has been reported to enhance the cell response. Ideally, it will be exciting to extend the model to predict the interaction between a cell and fibrous materials.

Reference

An, S.S., Fabry, B., Trepat, X., Wang, N. and Fredberg, J.J. (2006) 'Do biophysical properties of the airway smooth muscle in culture predict airway hyperresponsiveness?', *American journal of respiratory cell and molecular biology*, 35(1), pp. 55-64.

Armstrong, J.P.K., Puetzer, J.L., Serio, A., Guex, A.G., Kapnisi, M., Breant, A., Zong, Y., Assal, V., Skaalure, S.C. and King, O. (2018) 'Engineering anisotropic muscle tissue using acoustic cell patterning', *Advanced Materials*, 30(43), p. 1802649.

Aryaei, A. and Jayasuriya, A.C. (2013) 'Mechanical properties of human amniotic fluid stem cells using nanoindentation', *J Biomech*, 46(9), pp. 1524-30.

Balaban, N.Q., Schwarz, U.S., Riveline, D., Goichberg, P., Tzur, G., Sabanay, I., Mahalu, D., Safran, S., Bershadsky, A., Addadi, L. and Geiger, B. (2001) 'Force and focal adhesion assembly: a close relationship studied using elastic micropatterned substrates', *Nature Cell Biology*, 3(5), pp. 466-472.

Barreto, S., Clausen, C.H., Perrault, C.M., Fletcher, D.A. and Lacroix, D. (2013) 'A multi-structural single cell model of force-induced interactions of cytoskeletal components', *Biomaterials*, 34(26), pp. 6119-26.

Barreto, S., Perrault, C.M. and Lacroix, D. (2014) 'Structural finite element analysis to explain cell mechanics variability', *J Mech Behav Biomed Mater*, 38, pp. 219-31.

Bell, G.I. (1978) 'Models for the specific adhesion of cells to cells', *Science*, 200(4342), pp. 618-627.

Bell, G.I., Dembo, M. and Bongrand, P. (1984) 'Cell adhesion. Competition between nonspecific repulsion and specific bonding', *Biophysical journal*, 45(6), pp. 1051-1064.

Besser, A. and Schwarz, U.S. (2007) 'Coupling biochemistry and mechanics in cell adhesion: a model for inhomogeneous stress fiber contraction', *New Journal of Physics*, 9(11), p. 425.

Bhadriraju, K. and Hansen, L.K. (2002) 'Extracellular matrix- and cytoskeleton-dependent changes in cell shape and stiffness', *Exp Cell Res*, 278(1), pp. 92-100.

Booth-Gauthier, E.A., Alcoser, T.A., Yang, G. and Dahl, K.N. (2012) 'Force-induced changes in subnuclear movement and rheology', *Biophys J*, 103(12), pp. 2423-31.

Bouzid, T., Kim, E., Riehl, B.D., Esfahani, A.M., Rosenbohm, J., Yang, R., Duan, B. and Lim, J.Y. (2019) 'The LINC complex, mechanotransduction, and mesenchymal stem cell function and fate', *Journal of Biological Engineering*, 13(1), pp. 1-12.

Butler, J.P., Tolić-Nørrelykke, I.M., Fabry, B. and Fredberg, J.J. (2002) 'Traction fields, moments, and strain energy that cells exert on their surroundings', *American Journal of Physiology-Cell Physiology*, 282(3), pp. C595-C605.

Buxboim, A., Rajagopal, K., Brown, A.E.X. and Discher, D.E. (2010) 'How deeply cells feel: methods for thin gels', *Journal of Physics-Condensed Matter*, 22(19), p. 10.

Cai, X. and Bangert, H. (1995) 'Hardness measurements of thin films-determining the critical ratio of depth to thickness using FEM', *Thin Solid Films*, 264(1), pp. 59-71.

Caille, N., Tardy, Y. and Meister, J.J. (1998) 'Assessment of strain field in endothelial cells subjected to uniaxial deformation of their substrate', *Annals of biomedical engineering*, 26(3), pp. 409-416.

Canetta, E., Duperray, A., Leyrat, A. and Verdier, C. (2005) 'Measuring cell viscoelastic properties using a force-spectrometer: Influence of protein–cytoplasm interactions', *Biorheology*, 42(5), pp. 321-333.

Carl, P. and Schillers, H. (2008) 'Elasticity measurement of living cells with an atomic force microscope: data acquisition and processing', *Pflugers Arch*, 457(2), pp. 551-9.

Chantre, C.O., Hoerstrup, S.P. and Parker, K.K. (2019) 'Engineering biomimetic and instructive materials for wound healing and regeneration', *Current Opinion in Biomedical Engineering*, 10, pp. 97-106.

Charras, G.T. and Horton, M.A. (2002) 'Single cell mechanotransduction and its modulation analyzed by atomic force microscope indentation', *Biophysical journal*, 82(6), pp. 2970-2981.

Chaudhuri, O. and Mooney, D.J. (2012) 'Stem-cell differentiation: Anchoring cell-fate cues', *Nat Mater*, 11(7), pp. 568-9.

Chen, C.S., Mrksich, M., Huang, S., Whitesides, G.M. and Ingber, D.E. (1997) 'Geometric control of cell life and death', *Science*, 276(5317), pp. 1425-8.

Chen, C.S., Mrksich, M., Huang, S., Whitesides, G.M. and Ingber, D.E. (1998) 'Micropatterned surfaces for control of cell shape, position, and function', *Biotechnol Prog*, 14(3), pp. 356-63.

Chen, J. (2013) 'Understanding the nanoindentation mechanisms of a microsphere for biomedical applications', *Journal of Physics D: Applied Physics*, 46(49), p. 495303.

Chen, J. (2014) 'Nanobiomechanics of living cells: a review', *Interface Focus*, 4(2), p. 20130055.

Chen, J. and Bull, S.J. (2009) 'On the factors affecting the critical indenter penetration for measurement of coating hardness', *Vacuum*, 83(6), pp. 911-920.

Chen, J. and Lu, G. (2012) 'Finite element modelling of nanoindentation based methods for mechanical properties of cells', *J Biomech*, 45(16), pp. 2810-6.

Chen, W.L., Likhitpanichkul, M., Ho, A. and Simmons, C.A. (2010) 'Integration of statistical modeling and high-content microscopy to systematically investigate cell-substrate interactions', *Biomaterials*, 31(9), pp. 2489-97.

Cheng, C.M., Steward, R.L., Jr. and LeDuc, P.R. (2009) 'Probing cell structure by controlling the mechanical environment with cell-substrate interactions', *J Biomech*, 42(2), pp. 187-92.

Chrzanowska-Wodnicka, M. and Burridge, K. (1996) 'Rho-stimulated contractility drives the formation of stress fibers and focal adhesions', *J Cell Biol*, 133(6), pp. 1403-15.

Chuah, Y.J., Zhang, Y., Wu, Y., Menon, N.V., Goh, G.H., Lee, A.C., Chan, V., Zhang, Y. and Kang, Y. (2015) 'Combinatorial effect of substratum properties on mesenchymal stem cell sheet engineering and subsequent multi-lineage differentiation', *Acta Biomater*, 23, pp. 52-62.

Clark, Andrew G., Dierkes, K. and Paluch, Ewa K. (2013) 'Monitoring Actin Cortex Thickness in Live Cells', *Biophysical Journal*, 105(3), pp. 570-580.

Coceano, G., Yousafzai, M.S., Ma, W., Ndoye, F., Venturelli, L., Hussain, I., Bonin, S., Niemela, J., Scoles, G. and Cojoc, D. (2015) 'Investigation into local cell mechanics by atomic force microscopy mapping and optical tweezer vertical indentation', *Nanotechnology*, 27(6), p. 065102.

Curtis, A.S. (1964) 'The Mechanism of Adhesion of Cells to Glass. A Study by Interference Reflection Microscopy', *J Cell Biol*, 20(2), pp. 199-215.

Dalby, M.J., Gadegaard, N., Tare, R., Andar, A., Riehle, M.O., Herzyk, P., Wilkinson, C.D.W. and Oreffo, R.O.C. (2007) 'The control of human mesenchymal cell differentiation using nanoscale symmetry and disorder', *Nature materials*, 6(12), pp. 997-1003.

Dao, M., Lim, C.T. and Suresh, S. (2003) 'Mechanics of the human red blood cell deformed by optical tweezers', *Journal of the Mechanics and Physics of Solids*, 51(11-12), pp. 2259-2280.

Dartsch, P.C. and Betz, E. (1989) 'Response of cultured endothelial cells to mechanical stimulation', *Basic Res Cardiol*, 84(3), pp. 268-81.

De Santis, G., Lennon, A.B., Boschetti, F., Verhegghe, B., Verdonck, P. and Prendergast, P.J. (2011) 'How can cells sense the elasticity of a substrate? an

analysis using a cell tensegrity model', *European Cells and Materials*, 22, pp. 202-213.

De Vos, W.H., Houben, F., Kamps, M., Malhas, A., Verheyen, F., Cox, J., Manders, E.M.M., Verstraeten, V.L.R.M., van Steensel, M.A.M. and Marcelis, C.L.M. (2011) 'Repetitive disruptions of the nuclear envelope invoke temporary loss of cellular compartmentalization in laminopathies', *Human molecular genetics*, p. ddr344.

Deguchi, S., Ohashi, T. and Sato, M. (2006) 'Tensile properties of single stress fibers isolated from cultured vascular smooth muscle cells', *Journal of Biomechanics*, 39(14), pp. 2603-2610.

Deshpande, V.S., McMeeking, R.M. and Evans, A.G. (2006) 'A bio-chemo-mechanical model for cell contractility', *Proceedings of the National Academy of Sciences*, 103(38), pp. 14015-14020.

Deshpande, V.S., McMeeking, R.M. and Evans, A.G. (2007) 'A model for the contractility of the cytoskeleton including the effects of stress-fibre formation and dissociation', *Proceedings of the Royal Society A: Mathematical, Physical and Engineering Science*, 463(2079), pp. 787-815.

Deshpande, V.S., Mrksich, M., McMeeking, R.M. and Evans, A.G. (2008) 'A bio-mechanical model for coupling cell contractility with focal adhesion formation', *Journal of the Mechanics and Physics of Solids*, 56(4), pp. 1484-1510.

Ding, Y., Wang, J., Xu, G.-K. and Wang, G.-F. (2018) 'Are elastic moduli of biological cells depth dependent or not? Another explanation using a contact mechanics model with surface tension', *Soft matter*, 14(36), pp. 7534-7541.

Ding, Y., Xu, G.K. and Wang, G.F. (2017) 'On the determination of elastic moduli of cells by AFM based indentation', *Sci Rep*, 7, p. 45575.

Dingal, P.C.D.P., Bradshaw, A.M., Cho, S., Raab, M., Buxboim, A., Swift, J. and Discher, D.E. (2015) 'Fractal heterogeneity in minimal matrix models of scars modulates stiff-niche stem-cell responses via nuclear exit of a mechanorepressor', *Nature materials*, 14(9), pp. 951-960.

Diz-Munoz, A., Fletcher, D.A. and Weiner, O.D. (2013) 'Use the force: membrane tension as an organizer of cell shape and motility', *Trends Cell Biol*, 23(2), pp. 47-53.

Dowling, E.P., Ronan, W., Ofek, G., Deshpande, V.S., McMeeking, R.M., Athanasiou, K.A. and McGarry, J.P. (2012) 'The effect of remodelling and contractility of the actin cytoskeleton on the shear resistance of single cells: a computational and experimental investigation', *Journal of The Royal Society Interface*, 9(77), pp. 3469-3479.

Dumbauld, D.W., Lee, T.T., Singh, A., Scrimgeour, J., Gersbach, C.A., Zamir, E.A., Fu, J., Chen, C.S., Curtis, J.E., Craig, S.W. and Garcia, A.J. (2013) 'How vinculin regulates force transmission', *Proc Natl Acad Sci U S A*, 110(24), pp. 9788-93.

Dupont, S., Morsut, L., Aragona, M., Enzo, E., Giulitti, S., Cordenonsi, M., Zanconato, F., Le Digabel, J., Forcato, M. and Bicciato, S. (2011) 'Role of YAP/TAZ in mechanotransduction', *Nature*, 474(7350), pp. 179-183.

Efremov, Y.M., Velay-Lizancos, M., Weaver, C.J., Athamneh, A.I., Zavattieri, P.D., Suter, D.M. and Raman, A. (2019) 'Anisotropy vs isotropy in living cell indentation with AFM', *Sci Rep*, 9(1), p. 5757.

Efremov, Y.M., Wang, W.H., Hardy, S.D., Geahlen, R.L. and Raman, A. (2017) 'Measuring nanoscale viscoelastic parameters of cells directly from AFM force-displacement curves', *Sci Rep*, 7(1), p. 1541.

Emerman, J.T. and Pitelka, D.R. (1977) 'Maintenance and induction of morphological differentiation in dissociated mammary epithelium on floating collagen membranes', *In Vitro*, 13(5), pp. 316-28.

Engler, A., Bacakova, L., Newman, C., Hategan, A., Griffin, M. and Discher, D. (2004a) 'Substrate compliance versus ligand density in cell on gel responses', *Biophys J*, 86(1 Pt 1), pp. 617-28.

Engler, A.J., Richert, L., Wong, J.Y., Picart, C. and Discher, D.E. (2004b) 'Surface probe measurements of the elasticity of sectioned tissue, thin gels and polyelectrolyte multilayer films: correlations between substrate stiffness and cell adhesion', *Surface Science*, 570(1), pp. 142-154.

Engler, A.J., Sen, S., Sweeney, H.L. and Discher, D.E. (2006) 'Matrix elasticity directs stem cell lineage specification', *Cell*, 126(4), pp. 677-89.

Fischer-Cripps, A.C. (2000) 'A review of analysis methods for sub-micron indentation testing', *Vacuum*, 58(4), pp. 569-585.

Fletcher, D.A. and Mullins, R.D. (2010a) 'Cell mechanics and the cytoskeleton', *Nature*, 463(7280), pp. 485-92.

Fletcher, D.A. and Mullins, R.D. (2010b) 'Cell mechanics and the cytoskeleton', *Nature*, 463(7280), pp. 485-492.

Floren, M., Bonani, W., Dharmarajan, A., Motta, A., Migliaresi, C. and Tan, W. (2016) 'Human mesenchymal stem cells cultured on silk hydrogels with variable stiffness and growth factor differentiate into mature smooth muscle cell phenotype', *Acta Biomater*, 31, pp. 156-66.

Franke, R.P., Gräfe, M., Schnittler, H., Seiffge, D., Mittermayer, C. and Drenckhahn, D. (1984) 'Induction of human vascular endothelial stress fibres by fluid shear stress', *Nature*, 307(5952), p. 648.

Fu, J., Wang, Y.K., Yang, M.T., Desai, R.A., Yu, X., Liu, Z. and Chen, C.S. (2010) 'Mechanical regulation of cell function with geometrically modulated elastomeric substrates', *Nat Methods*, 7(9), pp. 733-6.

Galbraith, C.G., Skalak, R. and Chien, S. (1998) 'Shear stress induces spatial reorganization of the endothelial cell cytoskeleton', *Cell Motil Cytoskeleton*, 40(4), pp. 317-30.

Garcia, P.D. and Garcia, R. (2018) 'Determination of the Elastic Moduli of a Single Cell Cultured on a Rigid Support by Force Microscopy', *Biophys J*, 114(12), pp. 2923-2932.

Gavara, N. and Chadwick, R.S. (2016) 'Relationship between cell stiffness and stress fiber amount, assessed by simultaneous atomic force microscopy and live-cell fluorescence imaging', *Biomechanics and modeling in mechanobiology*, 15(3), pp. 511-523.

Geiger, B. and Yamada, K.M. (2011) 'Molecular architecture and function of matrix adhesions', *Cold Spring Harbor perspectives in biology*, 3(5), p. a005033.

Ghibaudo, M., Saez, A., Trichet, L., Xayaphoummine, A., Browaeys, J., Silberzan, P., Buguin, A. and Ladoux, B. (2008) 'Traction forces and rigidity sensing regulate cell functions', *Soft Matter*, 4(9), pp. 1836-1843.

Ghosh, K., Pan, Z., Guan, E., Ge, S., Liu, Y., Nakamura, T., Ren, X.D., Rafailovich, M. and Clark, R.A. (2007) 'Cell adaptation to a physiologically relevant ECM mimic with different viscoelastic properties', *Biomaterials*, 28(4), pp. 671-9.

Guck, J., Schinkinger, S., Lincoln, B., Wottawah, F., Ebert, S., Romeyke, M., Lenz, D., Erickson, H.M., Ananthakrishnan, R. and Mitchell, D. (2005) 'Optical deformability as an inherent cell marker for testing malignant transformation and metastatic competence', *Biophys J*, 88(5), pp. 3689-3698.

Guerrero, C.R., Garcia, P.D. and Garcia, R. (2019) 'Subsurface Imaging of Cell Organelles by Force Microscopy', *ACS Nano*, 13(8), pp. 9629-9637.

Guilak, F., Tedrow, J.R. and Burgkart, R. (2000) 'Viscoelastic properties of the cell nucleus', *Biochem Biophys Res Commun*, 269(3), pp. 781-6.

Gupta, M., Sarangi, B.R., Deschamps, J., Nematbakhsh, Y., Callan-Jones, A., Margadant, F., Mège, R.-M., Lim, C.T., Voituriez, R. and Ladoux, B. (2015) 'Adaptive

rheology and ordering of cell cytoskeleton govern matrix rigidity sensing', *Nature communications*, 6, p. 7525.

Guz, N., Dokukin, M., Kalaparthi, V. and Sokolov, I. (2014) 'If cell mechanics can be described by elastic modulus: study of different models and probes used in indentation experiments', *Biophys J*, 107(3), pp. 564-575.

Hall, M.S., Alisafaei, F., Ban, E., Feng, X., Hui, C.-Y., Shenoy, V.B. and Wu, M. (2016) 'Fibrous nonlinear elasticity enables positive mechanical feedback between cells and ECMs', *Proceedings of the National Academy of Sciences*, 113(49), pp. 14043-14048.

Harris, A.R. and Charras, G.T. (2011) 'Experimental validation of atomic force microscopy-based cell elasticity measurements', *Nanotechnology*, 22(34), p. 345102.

Haugh, M.G., Murphy, C.M., McKiernan, R.C., Altenbuchner, C. and O'Brien, F.J. (2011) 'Crosslinking and mechanical properties significantly influence cell attachment, proliferation, and migration within collagen glycosaminoglycan scaffolds', *Tissue Engineering Part A*, 17(9-10), pp. 1201-1208.

He, S.J., Su, Y.W., Ji, B.H. and Gao, H.J. (2014) 'Some basic questions on mechanosensing in cell-substrate interaction', *Journal of the Mechanics and Physics of Solids*, 70, pp. 116-135.

Hertz, H. (1882) 'Ueber die Berührung fester elastischer Körper', *Journal für die reine und angewandte Mathematik*, 1882(92), pp. 156-171.

Ho, C.Y., Jaalouk, D.E., Vartiainen, M.K. and Lammerding, J. (2013) 'Lamin A/C and emerin regulate MKL1-SRF activity by modulating actin dynamics', *Nature*, 497(7450), pp. 507-511.

Hofmann, U.G., Rotsch, C., Parak, W.J. and Radmacher, M. (1997) 'Investigating the cytoskeleton of chicken cardiocytes with the atomic force microscope', *J Struct Biol*, 119(2), pp. 84-91.

Huebsch, N., Arany, P.R., Mao, A.S., Shvartsman, D., Ali, O.A., Bencherif, S.A., Rivera-Feliciano, J. and Mooney, D.J. (2010) 'Harnessing traction-mediated manipulation of the cell/matrix interface to control stem-cell fate', *Nat Mater*, 9(6), pp. 518-26.

Humphries, D.L., Grogan, J.A. and Gaffney, E.A. (2017) 'Mechanical cell–cell communication in fibrous networks: the importance of network geometry', *Bulletin of mathematical biology*, 79(3), pp. 498-524.

Ingber, D.E. (2003) 'Tensegrity I. Cell structure and hierarchical systems biology', *J Cell Sci*, 116(Pt 7), pp. 1157-73.

Ingber, D.E. and Folkman, J. (1989) 'Mechanochemical switching between growth and differentiation during fibroblast growth factor-stimulated angiogenesis in vitro: role of extracellular matrix', *The Journal of cell biology*, 109(1), pp. 317-330.

Irgens, F. (2008) *Continuum mechanics*. Springer Science & Business Media.

Isenberg, B.C., Dimilla, P.A., Walker, M., Kim, S. and Wong, J.Y. (2009) 'Vascular smooth muscle cell durotaxis depends on substrate stiffness gradient strength', *Biophys J*, 97(5), pp. 1313-22.

Isermann, P. and Lammerding, J. (2013) 'Nuclear Mechanics and Mechanotransduction in Health and Disease', *Current Biology*, 23(24), pp. R1113-R1121.

Johnson, K. (1985) 'Contact Mechanics Cambridge University Press London', *UK*.

Johnson, K.L. and Johnson, K.L. (1987) *Contact mechanics*. Cambridge university press.

Khatau, S.B., Hale, C.M., Stewart-Hutchinson, P.J., Patel, M.S., Stewart, C.L., Searson, P.C., Hodzic, D. and Wirtz, D. (2009a) 'A perinuclear actin cap regulates nuclear shape', *Proceedings of the National Academy of Sciences*, 106(45), pp. 19017-19022.

Khatau, S.B., Hale, C.M., Stewart-Hutchinson, P.J., Patel, M.S., Stewart, C.L., Searson, P.C., Hodzic, D. and Wirtz, D. (2009b) 'A perinuclear actin cap regulates nuclear shape', *Proceedings of the National Academy of Sciences*, 106(45), pp. 19017-22.

Kilian, K.A., Bugarija, B., Lahn, B.T. and Mrksich, M. (2010) 'Geometric cues for directing the differentiation of mesenchymal stem cells', *Proceedings of the National Academy of Sciences*, 107(11), pp. 4872-4877.

Kilian, K.A. and Mrksich, M. (2012) 'Directing Stem Cell Fate by Controlling the Affinity and Density of Ligand-Receptor Interactions at the Biomaterials Interface', *Angewandte Chemie-International Edition*, 51(20), pp. 4891-4895.

Kolodney, M.S. and Wysolmerski, R.B. (1992) 'Isometric contraction by fibroblasts and endothelial cells in tissue culture: a quantitative study', *The Journal of cell biology*, 117(1), pp. 73-82.

Kuo, C.H., Xian, J., Brenton, J.D., Franze, K. and Sivaniah, E. (2012) 'Complex stiffness gradient substrates for studying mechanotactic cell migration', *Adv Mater*, 24(45), pp. 6059-64.

Lee, H.-H. (2020) *Finite Element Simulations with ANSYS Workbench 2020*. SDC Publications.

Lee, J., Abdeen, A.A. and Kilian, K.A. (2014) 'Rewiring mesenchymal stem cell lineage specification by switching the biophysical microenvironment', *Sci Rep*, 4, p. 5188.

Lekka, M., Laidler, P., Gil, D., Lekki, J., Stachura, Z. and Hrynkiewicz, A.Z. (1999) 'Elasticity of normal and cancerous human bladder cells studied by scanning force microscopy', *Eur Biophys J*, 28(4), pp. 312-6.

Leong, W.S., Tay, C.Y., Yu, H., Li, A., Wu, S.C., Duc, D.H., Lim, C.T. and Tan, L.P. (2010) 'Thickness sensing of hMSCs on collagen gel directs stem cell fate', *Biochem Biophys Res Commun*, 401(2), pp. 287-92.

Lepelletier, Y., Moura, I.C., Hadj-Slimane, R., Renand, A., Fiorentino, S., Baude, C., Shirvan, A., Barzilai, A. and Hermine, O. (2006) 'Immunosuppressive role of semaphorin-3A on T cell proliferation is mediated by inhibition of actin cytoskeleton reorganization', *European journal of immunology*, 36(7), pp. 1782-1793.

Leung, T., Chen, X.-Q., Manser, E. and Lim, L. (1996) 'The p160 RhoA-binding kinase ROK alpha is a member of a kinase family and is involved in the reorganization of the cytoskeleton', *Molecular and cellular biology*, 16(10), pp. 5313-5327.

Li, Q.S., Lee, G.Y., Ong, C.N. and Lim, C.T. (2008) 'AFM indentation study of breast cancer cells', *Biochem Biophys Res Commun*, 374(4), pp. 609-13.

Li, S., Zhao, F., Zhan, Y., Liu, X., Hun, T., Zhang, H., Qiu, C., He, J., Yi, Z. and Sun, Y. (2018) 'How Deep Might Myoblasts Sense: The Effect of Substrate Stiffness and Thickness on the Behavior of Myoblasts', *Journal of Medical and Biological Engineering*, 38(4), pp. 596-606.

Lim, C.T., Zhou, E.H. and Quek, S.T. (2006) 'Mechanical models for living cells--a review', *J Biomech*, 39(2), pp. 195-216.

Lin, Y.C., Tambe, D.T., Park, C.Y., Wasserman, M.R., Trepat, X., Krishnan, R., Lenormand, G., Fredberg, J.J. and Butler, J.P. (2010) 'Mechanosensing of substrate thickness', *Physical Review E*, 82(4), p. 6.

Liu, H., Sun, Y. and Simmons, C.A. (2013) 'Determination of local and global elastic moduli of valve interstitial cells cultured on soft substrates', *J Biomech*, 46(11), pp. 1967-71.

Liu, Y., Mollaeian, K. and Ren, J. (2019) 'Finite element modeling of living cells for AFM indentation-based biomechanical characterization', *Micron*, 116, pp. 108-115.

Lo, C.M., Wang, H.B., Dembo, M. and Wang, Y.L. (2000) 'Cell movement is guided by the rigidity of the substrate', *Biophysical Journal*, 79(1), pp. 144-152.

Lodish, H., Berk, A., Kaiser, C.A., Krieger, M., Scott, M.P., Bretscher, A., Ploegh, H. and Matsudaira, P. (2008) *Molecular cell biology*. Macmillan.

Lombardi, M.L., Jaalouk, D.E., Shanahan, C.M., Burke, B., Roux, K.J. and Lammerding, J. (2011) 'The interaction between nesprins and sun proteins at the nuclear envelope is critical for force transmission between the nucleus and cytoskeleton', *Journal of Biological Chemistry*, 286(30), pp. 26743-26753.

Lovett, D.B., Shekhar, N., Nickerson, J.A., Roux, K.J. and Lele, T.P. (2013) 'Modulation of Nuclear Shape by Substrate Rigidity', *Cellular and Molecular Bioengineering*, 6(2), pp. 230-238.

Mahaffy, R.E., Shih, C.K., MacKintosh, F.C. and Kas, J. (2000) 'Scanning probe-based frequency-dependent microrheology of polymer gels and biological cells', *Phys Rev Lett*, 85(4), pp. 880-3.

Maloney, J.M., Walton, E.B., Bruce, C.M. and Van Vliet, K.J. (2008) 'Influence of finite thickness and stiffness on cellular adhesion-induced deformation of compliant substrata', *Phys Rev E Stat Nonlin Soft Matter Phys*, 78(4 Pt 1), p. 041923.

Marcotti, S., Reilly, G.C. and Lacroix, D. (2019) 'Effect of cell sample size in atomic force microscopy nanoindentation', *Journal of the Mechanical Behavior of Biomedical Materials*.

Marina, K., Joost te, R. and Katarina, W. (2013) 'Probing the compressibility of tumor cell nuclei by combined atomic force–confocal microscopy', *Physical Biology*, 10(6), p. 065002.

Mathur, A.B., Collinsworth, A.M., Reichert, W.M., Kraus, W.E. and Truskey, G.A. (2001) 'Endothelial, cardiac muscle and skeletal muscle exhibit different viscous and elastic properties as determined by atomic force microscopy', *J Biomech*, 34(12), pp. 1545-1553.

McGarry, J.P., Fu, J., Yang, M.T., Chen, C.S., McMeeking, R.M., Evans, A.G. and Deshpande, V.S. (2009) 'Simulation of the contractile response of cells on an array of micro-posts', *Philos Trans A Math Phys Eng Sci*, 367(1902), pp. 3477-97.

McNamara, L.E., Burchmore, R., Riehle, M.O., Herzyk, P., Biggs, M.J.P., Wilkinson, C.D.W., Curtis, A.S.G. and Dalby, M.J. (2012) 'The role of microtopography in cellular mechanotransduction', *Biomaterials*, 33(10), pp. 2835-2847.

Merkel, R., Kirchgeßner, N., Cesa, C.M. and Hoffmann, B. (2007) 'Cell Force Microscopy on Elastic Layers of Finite Thickness', *Biophysical Journal*, 93(9), pp. 3314-3323.

Mohammadi, H., Janmey, P.A. and McCulloch, C.A. (2014) 'Lateral boundary mechanosensing by adherent cells in a collagen gel system', *Biomaterials*, 35(4), pp. 1138-1149.

Morimoto, A., Shibuya, H., Zhu, X., Kim, J., Ishiguro, K.-i., Han, M. and Watanabe, Y. (2012) 'A conserved KASH domain protein associates with telomeres, SUN1, and dynactin during mammalian meiosis', *J Cell Biol*, 198(2), pp. 165-172.

Msc, M. (2004) 'Software Manual Volume A: Theory and User Information (Version 2005)', *MSC Software Corporation, Santa Ana, CA, USA*.

Mullen, C.A., Haugh, M.G., Schaffler, M.B., Majeska, R.J. and McNamara, L.M. (2013) 'Osteocyte differentiation is regulated by extracellular matrix stiffness and intercellular separation', *J Mech Behav Biomed Mater*, 28, pp. 183-94.

Mullen, C.A., Vaughan, T.J., Billiar, K.L. and McNamara, L.M. (2015) 'The effect of substrate stiffness, thickness, and cross-linking density on osteogenic cell behavior', *Biophys J*, 108(7), pp. 1604-12.

Multiphysics, C. (2014) 'COMSOL solver theory guide 4.4', *Burlington, MA, USA: COMSOL Inc*.

Nam, K.-H., Jamilpour, N., Mfoumou, E., Wang, F.-Y., Zhang, D.D. and Wong, P.K. (2014) 'Probing Mechanoregulation of Neuronal Differentiation by Plasma Lithography Patterned Elastomeric Substrates', *Scientific Reports*, 4, p. 6965.

Nash, G.B., O'Brien, E., Gordon-Smith, E.C. and Dormandy, J.A. (1989) 'Abnormalities in the mechanical properties of red blood cells caused by Plasmodium falciparum', *Blood*, 74(2), pp. 855-61.

Ng, L., Hung, H.-H., Sprunt, A., Chubinskaya, S., Ortiz, C. and Grodzinsky, A. (2007) 'Nanomechanical properties of individual chondrocytes and their developing growth factor-stimulated pericellular matrix', *J Biomech*, 40(5), pp. 1011-1023.

Ni, Y. and Chiang, M.Y.M. (2007) 'Cell morphology and migration linked to substrate rigidity', *Soft Matter*, 3(10), pp. 1285-1292.

Nisenholz, N., Rajendran, K., Dang, Q., Chen, H., Kemkemer, R., Krishnan, R. and Zemel, A. (2014) 'Active mechanics and dynamics of cell spreading on elastic substrates', *Soft Matter*, 10(37), pp. 7234-46.

Notbohm, J., Kim, J.H., Asthagiri, A.R. and Ravichandran, G. (2012) 'Three-dimensional analysis of the effect of epidermal growth factor on cell-cell adhesion in epithelial cell clusters', *Biophysical journal*, 102(6), pp. 1323-1330.

Novak, I.L., Slepchenko, B.M., Mogilner, A. and Loew, L.M. (2004) 'Cooperativity between cell contractility and adhesion', *Phys Rev Lett*, 93(26 Pt 1), p. 268109.

O'Brien, F.J. (2011) 'Biomaterials & scaffolds for tissue engineering', *Materials today*, 14(3), pp. 88-95.

Ofek, G., Natoli, R.M. and Athanasiou, K.A. (2009) 'In situ mechanical properties of the chondrocyte cytoplasm and nucleus', *J Biomech*, 42(7), pp. 873-7.

Pablo Rodríguez, J., González, M., Ríos, S. and Cambiazo, V. (2004) 'Cytoskeletal organization of human mesenchymal stem cells (MSC) changes during their osteogenic differentiation', *Journal of cellular biochemistry*, 93(4), pp. 721-731.

Pajerowski, J.D., Dahl, K.N., Zhong, F.L., Sammak, P.J. and Discher, D.E. (2007) 'Physical plasticity of the nucleus in stem cell differentiation', *Proceedings of the National Academy of Sciences*, 104(40), pp. 15619-15624.

Pampaloni, F. and Florin, E.L. (2008) 'Microtubule architecture: inspiration for novel carbon nanotube-based biomimetic materials', *Trends Biotechnol*, 26(6), pp. 302-10.

Panich, N. and Sun, Y. (2004) 'Effect of penetration depth on indentation response of soft coatings on hard substrates: a finite element analysis', *Surface and Coatings Technology*, 182(2-3), pp. 342-350.

Park, J.S., Chu, J.S., Tsou, A.D., Diop, R., Tang, Z., Wang, A. and Li, S. (2011) 'The effect of matrix stiffness on the differentiation of mesenchymal stem cells in response to TGF-beta', *Biomaterials*, 32(16), pp. 3921-30.

Parsons, J.T., Horwitz, A.R. and Schwartz, M.A. (2010) 'Cell adhesion: integrating cytoskeletal dynamics and cellular tension', *Nat Rev Mol Cell Biol*, 11(9), pp. 633-43.

Pathak, A., Deshpande, V.S., McMeeking, R.M. and Evans, A.G. (2008) 'The simulation of stress fibre and focal adhesion development in cells on patterned substrates', *Journal of The Royal Society Interface*, 5(22), pp. 507-524.

Pelham, R.J., Jr. and Wang, Y. (1997) 'Cell locomotion and focal adhesions are regulated by substrate flexibility', *Proceedings of the National Academy of Sciences*, 94(25), pp. 13661-5.

Pellegrin, S. and Mellor, H. (2007) 'Actin stress fibres', *Journal of cell science*, 120(20), pp. 3491-3499.

Plotnikov, Sergey V., Pasapera, Ana M., Sabass, B. and Waterman, Clare M. (2012) 'Force Fluctuations within Focal Adhesions Mediate ECM-Rigidity Sensing to Guide Directed Cell Migration', *Cell*, 151(7), pp. 1513-1527.

Poh, Y.-C., Shevtsov, S.P., Chowdhury, F., Wu, D.C., Na, S., Dundr, M. and Wang, N. (2012) 'Dynamic force-induced direct dissociation of protein complexes in a nuclear body in living cells', *Nature communications*, 3, p. 866.

Pollard, T.D., Earnshaw, W.C., Lippincott-Schwartz, J. and Johnson, G. (2016) *Cell Biology E-Book*. Elsevier Health Sciences.

Prager-Khoutorsky, M., Lichtenstein, A., Krishnan, R., Rajendran, K., Mayo, A., Kam, Z., Geiger, B. and Bershadsky, A.D. (2011) 'Fibroblast polarization is a matrix-rigidity-dependent process controlled by focal adhesion mechanosensing', *Nature cell biology*, 13(12), pp. 1457-1465.

Puig-de-Morales-Marinkovic, M., Turner, K.T., Butler, J.P., Fredberg, J.J. and Suresh, S. (2007) 'Viscoelasticity of the human red blood cell', *Am J Physiol Cell Physiol*, 293(2), pp. C597-605.

Qu, X., Zhu, W., Huang, S., Li, Y.S., Chien, S., Zhang, K. and Chen, S. (2013) 'Relative impact of uniaxial alignment vs. form-induced stress on differentiation of human adipose derived stem cells', *Biomaterials*, 34(38), pp. 9812-8.

Rape, A.D., Guo, W.-h. and Wang, Y.-l. (2011) 'The regulation of traction force in relation to cell shape and focal adhesions', *Biomaterials*, 32(8), pp. 2043-2051.

Reinhart-King, C.A., Dembo, M. and Hammer, D.A. (2008) 'Cell-Cell Mechanical Communication through Compliant Substrates', *Biophysical Journal*, 95(12), pp. 6044-6051.

Reynolds, N.H. and McGarry, J.P. (2015) 'Single cell active force generation under dynamic loading – Part II: Active modelling insights', *Acta Biomaterialia*, 27, pp. 251-263.

Rheinlaender, J. and Schäffer, T.E. (2013) 'Mapping the mechanical stiffness of live cells with the scanning ion conductance microscope', *Soft Matter*, 9(12), pp. 3230-3236.

Ridley, A.J. and Hall, A. (1992) 'The small GTP-binding protein rho regulates the assembly of focal adhesions and actin stress fibers in response to growth factors', *Cell*, 70(3), pp. 389-399.

Riveline, D., Zamir, E., Balaban, N.Q., Schwarz, U.S., Ishizaki, T., Narumiya, S., Kam, Z., Geiger, B. and Bershadsky, A.D. (2001) 'Focal contacts as mechanosensors', *The Journal of cell biology*, 153(6), pp. 1175-1186.

Roduit, C., Sekatski, S., Dietler, G., Catsicas, S., Lafont, F. and Kasas, S. (2009) 'Stiffness tomography by atomic force microscopy', *Biophys J*, 97(2), pp. 674-7.

Ronan, W., Deshpande, V.S., McMeeking, R.M. and McGarry, J.P. (2011) *ASME 2011 Summer Bioengineering Conference*. American Society of Mechanical Engineers.

Ronan, W., Deshpande, V.S., McMeeking, R.M. and McGarry, J.P. (2012a) 'Investigation of Stress Fiber and Focal Adhesion Evolution Under Applied Mechanical Loading', *ASME 2012 Summer Bioengineering Conference*, (44809), pp. 689-690.

Ronan, W., Deshpande, V.S., McMeeking, R.M. and McGarry, J.P. (2012b) 'Numerical investigation of the active role of the actin cytoskeleton in the compression resistance of cells', *Journal of the Mechanical Behavior of Biomedical Materials*, 14, pp. 143-157.

Ronan, W., Deshpande, V.S., McMeeking, R.M. and McGarry, J.P. (2014) 'Cellular contractility and substrate elasticity: a numerical investigation of the actin cytoskeleton and cell adhesion', *Biomechanics and Modeling in Mechanobiology*, 13(2), pp. 417-435.

Rowlands, A.S., George, P.A. and Cooper-White, J.J. (2008) 'Directing osteogenic and myogenic differentiation of MSCs: interplay of stiffness and adhesive ligand presentation', *American Journal of Physiology-Cell Physiology*, 295(4), pp. C1037-C1044.

Sagadevan, S. and Murugasen, P. (2014) 'Novel Analysis on the Influence of Tip Radius and Shape of the Nanoindenter on the Hardness of Materials', *Procedia materials science*, 6, pp. 1871-1878.

Schillers, H., Walte, M., Urbanova, K. and Oberleithner, H. (2010) 'Real-time monitoring of cell elasticity reveals oscillating myosin activity', *Biophys J*, 99(11), pp. 3639-46.

Sen, S., Engler, A.J. and Discher, D.E. (2009) 'Matrix Strains Induced by Cells: Computing How Far Cells Can Feel', *Cellular and Molecular Bioengineering*, 2(1), pp. 39-48.

Shenoy, V.B., Wang, H. and Wang, X. (2016) 'A chemo-mechanical free-energy-based approach to model durotaxis and extracellular stiffness-dependent contraction and polarization of cells', *Interface Focus*, 6(1), p. 20150067.

Shimi, T., Pfleghaar, K., Kojima, S., Pack, C.G., Solovei, I., Goldman, A.E., Adam, S.A., Shumaker, D.K., Kinjo, M., Cremer, T. and Goldman, R.D. (2008) 'The A- and

B-type nuclear lamin networks: microdomains involved in chromatin organization and transcription', *Genes Dev*, 22(24), pp. 3409-21.

Sneddon, I.N. (1965) 'The relation between load and penetration in the axisymmetric Boussinesq problem for a punch of arbitrary profile', *International journal of engineering science*, 3(1), pp. 47-57.

Solon, J., Levental, I., Sengupta, K., Georges, P.C. and Janmey, P.A. (2007) 'Fibroblast Adaptation and Stiffness Matching to Soft Elastic Substrates', *Biophysical Journal*, 93(12), pp. 4453-4461.

Soufivand, A.A., Navidbakhsh, M. and Soleimani, M. (2014) 'Is it appropriate to apply Hertz model to describe cardiac myocytes' mechanical properties by atomic force microscopy nanoindentation?', *Micro & Nano Letters*, 9(3), pp. 153-156.

Stricker, J., Falzone, T. and Gardel, M.L. (2010) 'Mechanics of the F-actin cytoskeleton', *Journal of Biomechanics*, 43(1), pp. 9-14.

Subramanian, A. and Lin, H.Y. (2005) 'Crosslinked chitosan: its physical properties and the effects of matrix stiffness on chondrocyte cell morphology and proliferation', *J Biomed Mater Res A*, 75(3), pp. 742-53.

Sun, Y., Yong, K.M., Villa-Diaz, L.G., Zhang, X., Chen, W., Philson, R., Weng, S., Xu, H., Krebsbach, P.H. and Fu, J. (2014) 'Hippo/YAP-mediated rigidity-dependent motor neuron differentiation of human pluripotent stem cells', *Nat Mater*, 13(6), pp. 599-604.

Suresh, H., Shishvan, S.S., Vigliotti, A. and Deshpande, V.S. (2019) 'Free-energy-based framework for early forecasting of stem cell differentiation', *J R Soc Interface*, 16(161), p. 20190571.

Suzuki, S., Narita, Y., Yamawaki, A., Murase, Y., Satake, M., Mutsuga, M., Okamoto, H., Kagami, H., Ueda, M. and Ueda, Y. (2010) 'Effects of extracellular matrix on differentiation of human bone marrow-derived mesenchymal stem cells into smooth muscle cell lineage: utility for cardiovascular tissue engineering', *Cells Tissues Organs*, 191(4), pp. 269-80.

Swift, J., Ivanovska, I.L., Buxboim, A., Harada, T., Dingal, P.C., Pinter, J., Pajerowski, J.D., Spinler, K.R., Shin, J.W., Tewari, M., Rehfeldt, F., Speicher, D.W. and Discher, D.E. (2013) 'Nuclear lamin-A scales with tissue stiffness and enhances matrix-directed differentiation', *Science*, 341(6149), p. 1240104.

Systemes, D. (2015) 'Abaqus 6.14 documentation–theory guide', *Providence, RI*.

Takagi, J., Petre, B.M., Walz, T. and Springer, T.A. (2002) 'Global Conformational Rearrangements in Integrin Extracellular Domains in Outside-In and Inside-Out Signaling', *Cell*, 110(5), pp. 599-611.

Takebayashi, T., Horii, T., Denno, H., Nakamachi, N., Otomo, K., Kitamura, S., Miyamoto, K., Horiuchi, T. and Ohta, Y. (2013) 'Human mesenchymal stem cells differentiate to epithelial cells when cultured on thick collagen gel', *Bio-Medical Materials and Engineering*, 23(1-2), pp. 143-153.

Tan, J.L., Tien, J., Pirone, D.M., Gray, D.S., Bhadriraju, K. and Chen, C.S. (2003) 'Cells lying on a bed of microneedles: an approach to isolate mechanical force', *Proc Natl Acad Sci U S A*, 100(4), pp. 1484-9.

Tan, S.J., Li, Q. and Lim, C.T. (2010) 'Manipulation and isolation of single cells and nuclei', in *Methods in cell biology*. Elsevier, pp. 79-96.

Tay, C.Y., Pal, M., Yu, H., Leong, W.S., Tan, N.S., Ng, K.W., Venkatraman, S., Boey, F., Leong, D.T. and Tan, L.P. (2011) 'Bio‑inspired Micropatterned Platform to Steer Stem Cell Differentiation', *Small*, 7(10), pp. 1416-1421.

Tojkander, S., Gateva, G. and Lappalainen, P. (2012) 'Actin stress fibers–assembly, dynamics and biological roles', *J Cell Sci*, 125(8), pp. 1855-1864.

Trappmann, B., Gautrot, J.E., Connelly, J.T., Strange, D.G.T., Li, Y., Oyen, M.L., Stuart, M.A.C., Boehm, H., Li, B. and Vogel, V. (2012) 'Extracellular-matrix tethering regulates stem-cell fate', *Nature materials*, 11(7), pp. 642-649.

Trichet, L., Le Digabel, J., Hawkins, R.J., Vedula, S.R.K., Gupta, M., Ribrault, C., Hersen, P., Voituriez, R. and Ladoux, B. (2012) 'Evidence of a large-scale mechanosensing mechanism for cellular adaptation to substrate stiffness', *Proceedings of the National Academy of Sciences*, 109(18), pp. 6933-6938.

Trickey, W.R., Lee, G.M. and Guilak, F. (2000) 'Viscoelastic properties of chondrocytes from normal and osteoarthritic human cartilage', *J Orthop Res*, 18(6), pp. 891-8.

Tusan, C.G., Man, Y.H., Zarkoob, H., Johnston, D.A., Andriotis, O.G., Thurner, P.J., Yang, S., Sander, E.A., Gentleman, E., Sengers, B.G. and Evans, N.D. (2018) 'Collective Cell Behavior in Mechanosensing of Substrate Thickness', *Biophys J*, 114(11), pp. 2743-2755.

Vailhé, B., Ronot, X., Tracqui, P., Usson, Y. and Tranqui, L. (1997) 'In vitro angiogenesis is modulated by the mechanical properties of fibrin gels and is related to α ν β 3 integrin localization', *In Vitro Cellular & Developmental Biology-Animal*, 33(10), pp. 763-773.

van Oers, R.F., Rens, E.G., LaValley, D.J., Reinhart-King, C.A. and Merks, R.M. (2014) 'Mechanical cell-matrix feedback explains pairwise and collective endothelial cell behavior in vitro', *PLoS Comput Biol*, 10(8), p. e1003774.

Vargas-Pinto, R., Gong, H., Vahabikashi, A. and Johnson, M. (2013) 'The effect of the endothelial cell cortex on atomic force microscopy measurements', *Biophys J*, 105(2), pp. 300-9.

Vernerey, F.J. and Farsad, M. (2011) 'A constrained mixture approach to mechano-sensing and force generation in contractile cells', *Journal of the Mechanical Behavior of Biomedical Materials*, 4(8), pp. 1683-1699.

Vichare, S., Inamdar, M.M. and Sen, S. (2012) 'Influence of cell spreading and contractility on stiffness measurements using AFM', *Soft Matter*, 8(40), pp. 10464-10471.

Vincent, L.G., Choi, Y.S., Alonso-Latorre, B., del Alamo, J.C. and Engler, A.J. (2013) 'Mesenchymal stem cell durotaxis depends on substrate stiffness gradient strength', *Biotechnol J*, 8(4), pp. 472-84.

Wang, H., Abhilash, A.S., Chen, C.S., Wells, R.G. and Shenoy, V.B. (2014) 'Long-range force transmission in fibrous matrices enabled by tension-driven alignment of fibers', *Biophys J*, 107(11), pp. 2592-603.

Wang, N., Tytell, J.D. and Ingber, D.E. (2009) 'Mechanotransduction at a distance: mechanically coupling the extracellular matrix with the nucleus', *Nature reviews Molecular cell biology*, 10(1), pp. 75-82.

Wang, Y., Wang, G., Luo, X., Qiu, J. and Tang, C. (2012) 'Substrate stiffness regulates the proliferation, migration, and differentiation of epidermal cells', *Burns*, 38(3), pp. 414-20.

Wang, Z. and Newman, W.H. (2003) 'Smooth muscle cell migration stimulated by interleukin 6 is associated with cytoskeletal reorganization', *Journal of Surgical Research*, 111(2), pp. 261-266.

Watanabe, N., Kato, T., Fujita, A., Ishizaki, T. and Narumiya, S. (1999) 'Cooperation between mDia1 and ROCK in Rho-induced actin reorganization', *Nature cell biology*, 1(3), pp. 136-143.

Watanabe, N., Madaule, P., Reid, T., Ishizaki, T., Watanabe, G., Kakizuka, A., Saito, Y., Nakao, K., Jockusch, B.M. and Narumiya, S. (1997) 'p140mDia, a mammalian homolog of Drosophila diaphanous, is a target protein for Rho small GTPase and is a ligand for profilin', *The EMBO journal*, 16(11), pp. 3044-3056.

Weafer, P.P., Reynolds, N.H., Jarvis, S.P. and McGarry, J.P. (2015) 'Single cell active force generation under dynamic loading – Part I: AFM experiments', *Acta Biomaterialia*, 27, pp. 236-250.

Wen, J.H., Vincent, L.G., Fuhrmann, A., Choi, Y.S., Hribar, K.C., Taylor-Weiner, H., Chen, S. and Engler, A.J. (2014) 'Interplay of matrix stiffness and protein tethering in stem cell differentiation', *Nat Mater*, 13(10), pp. 979-87.

Winer, J.P., Oake, S. and Janmey, P.A. (2009) 'Non-linear elasticity of extracellular matrices enables contractile cells to communicate local position and orientation', *PloS one*, 4(7), p. e6382.

Wingate, K., Floren, M., Tan, Y., Tseng, P.O. and Tan, W. (2014) 'Synergism of matrix stiffness and vascular endothelial growth factor on mesenchymal stem cells for vascular endothelial regeneration', *Tissue Eng Part A*, 20(17-18), pp. 2503-12.

Xu, Z.-H. and Rowcliffe, D. (2004) 'Finite element analysis of substrate effects on indentation behaviour of thin films', *Thin Solid Films*, 447, pp. 399-405.

Yang, M.T., Sniadecki, N.J. and Chen, C.S. (2007) 'Geometric Considerations of Micro‐to Nanoscale Elastomeric Post Arrays to Study Cellular Traction Forces', *Advanced Materials*, 19(20), pp. 3119-3123.

Yim, E.K.F., Darling, E.M., Kulangara, K., Guilak, F. and Leong, K.W. (2010) 'Nanotopography-induced changes in focal adhesions, cytoskeletal organization, and mechanical properties of human mesenchymal stem cells', *Biomaterials*, 31(6), pp. 1299-1306.

Yoshigi, M., Hoffman, L.M., Jensen, C.C., Yost, H.J. and Beckerle, M.C. (2005) 'Mechanical force mobilizes zyxin from focal adhesions to actin filaments and regulates cytoskeletal reinforcement', *J Cell Biol*, 171(2), pp. 209-15.

Zaidel-Bar, R., Cohen, M., Addadi, L. and Geiger, B. (2004) 'Hierarchical assembly of cell–matrix adhesion complexes'. Portland Press Limited.

Zemel, A., Rehfeldt, F., Brown, A.E.X., Discher, D.E. and Safran, S.A. (2010) 'Optimal matrix rigidity for stress-fibre polarization in stem cells', *Nat Phys*, 6(6), pp. 468-473.

Zhang, X., Schaefer, A.W., Burnette, D.T., Schoonderwoert, V.T. and Forscher, P. (2003) 'Rho-dependent contractile responses in the neuronal growth cone are independent of classical peripheral retrograde actin flow', *Neuron*, 40(5), pp. 931-944.

Zhong, Y. and Ji, B. (2013) 'Impact of cell shape on cell migration behavior on elastic substrate', *Biofabrication*, 5(1), p. 015011.

Zienkiewicz, O.C., Taylor, R.L. and Zhu, J.Z. (2005) *The finite element method: its basis and fundamentals*. Elsevier.

Appendix A. Fortran User Material (UMAT)

```
   SUBROUTINE UMAT(STRESS,STATEV,DDSDDE,SSE,SPD,SCD,
 1 RPL,DDSDDT,DRPLDE,DRPLDT,
 2 STRAN,DSTRAN,TIME,DTIME,TEMP,DTEMP,PREDEF,DPRED,CMNAME,
 3 NDI,NSHR,NTENS,NSTATV,PROPS,NPROPS,COORDS,DROT,PNEWDT,
 4 CELENT,DFGRD0,DFGRD1,NOEL,NPT,LAYER,KSPT,JSTEP,KINC)
C
   INCLUDE 'ABA_PARAM.INC'
C
   CHARACTER*80 CMNAME
   DIMENSION STRESS(NTENS),STATEV(NSTATV),
 $ DDSDDE(NTENS,NTENS),DDSDDT(NTENS),DRPLDE(NTENS),
 $ STRAN(NTENS),DSTRAN(NTENS),TIME(2),PREDEF(1),DPRED(1),
 $ PROPS(NPROPS),COORDS(3),DROT(3,3),DFGRD0(3,3),DFGRD1(3,3),
 $ PHI(37),PHIS(37),RKETA(6),DDS(3,3),DDFGRD0(NTENS,NTENS),
 $ VF0(2,2),DVGRD(2,2),VGRD(2,2),GS0(2,2),GS1(2,2),PAVSTRESS0(2,2),
 $ PAVSTRESS1(2,2),DPSTRESS(3),DELTA(2,2),SIGMA_E(37),STRESSINC(3),
 $ ETA_S(37),ETA_E(37),DDE(3,3),FJ11(37),FJ12(37),
 $ FJ13(37),FJ21(37),FJ22(37),FJ23(37),FJ31(37),FJ32(37),FJ33(37)
C
*DEFINITIONS OF VARIABLES IN THE MODEL
* SIGMA_E --- ACTIVE STRESS AT THE END OF INCREMENT
* ETA_S,ETA_E --- AVERAGE FIBRE CONCENTRATION AT THE START, END OF
INCREMENT
* PHI --- ANGLES OF EACH FIBRE FROM -PI/2 TO PI/2
```

* RKETA --- ITERATION ITEMS IN RUNGE-KUTTA METHOD

* DDS --- PASSIVE STRESS JACOBIAN

* SIC --- ACTIVE STRESS INCREMENT IN CURRENT ANALYSIS INCREMENT

* STATE VARIABLES PASSED ON TO NEXT INCREMENT AS INITIAL

* VALUES OF ETA (ETA_S) AND STRESS (SIGMA_S).

*---------------------- STATE VARIABLES STORAGE ----------------------

* 1-37 STORE THE FIBRE DENSITY ETA VALUE;

* 38-74 STORE THE CORRESPONDING FIBRE STRESS SIGMA VALUE;

* 75-111 STORE THE ROTATED ANGLE PHIS

* 112 STORES THE AVERAGE VALUE OF ETA.

* 113 STORES THE PRINCIPAL STRESS.

* 114 STORES THE FIBRE VARIANCE TO REPRESENT THE STRESS FIBRE
FORMATION.

* 115-117 STORES THE ACTIVE PRINCIPAL STRESS COMPONENTS, WHICH
ARE USED

* TO CALCULATE THE ACTIVE PRINCIPAL STRESS TENSOR.

*--

C

      PARAMETER (ZERO=0.D0, ONE=1.D0, TWO=2.D0, RKV=7.D0,

   $ THETA=70.D0, RKF=10.D0, RKB=1.D0, SX=3.5D-3,NEL=4924,

   $ D_EPS0=3.D-4, PI=3.1416D0,CLAMBDA=100.D0,HALF=0.5D0)

      DIMENSION ANGSFLV1(NEL,37),ANGSFLV2(NEL,37),

   & ANGSFLV3(NEL,37),ANGSFLV4(NEL,37)

      COMMON/SFDENSITY/ANGSFLV1,ANGSFLV2,ANGSFLV3,ANGSFLV4

C********************* Intialization **************************

133

```fortran
      IF (TIME(2).EQ.0) THEN

        DO K=1,NTENS

          STRESS(K)=ZERO

        END DO

        !NSTATV=73

        DO K=1,NSTATV

          STATEV(K)=ZERO

        END DO

      END IF

      ASINC1=ZERO

      ASINC2=ZERO

      ASINC3=ZERO

      PSINC1=ZERO

      PSINC2=ZERO

      PSINC3=ZERO

C======================= PASSIVE STRESS
===========================

      !PASSIVE PART OF STRESS

      !Second Piola–Kirchhoff stress calculated by Green-Lagrange Strain

      !CAUCHY STRESS CONVERTED BY PK2 STRESS

      !THIS PART IS SCRIPTED ACCORDING TO THE FORMULATIONS IN PAPER

      E=PROPS(1)

      ANU=PROPS(2)

      ALAM1=E*ANU/(ONE-ANU**TWO)

      ALAM2=E/(ONE+ANU)
```

```fortran
C********** CALCULATE STRAIN RATE BY VELOCITY GRADIENT *********
      DO I=1,2
        DO J=1,2
          !DEFORMATION GRADIENT INCREMENT
          DDFGRD0(I,J)=(DFGRD1(I,J)-DFGRD0(I,J))/DTIME
        END DO
      END DO
      A11=DFGRD0(1,1) !DEFORMATION GRADIENT PARTS
      A12=DFGRD0(1,2)
      A21=DFGRD0(2,1)
      A22=DFGRD0(2,2)


      B11=DFGRD1(1,1)
      B12=DFGRD1(1,2)
      B21=DFGRD1(2,1)
      B22=DFGRD1(2,2)


      !DETERMINANT OF DEFORMATION GRADIENT
      DETF0=A11*A22-A12*A21
      DETF1=B11*B22-B12*B21


      VF0(1,1)=A22/DETF0
      VF0(1,2)=(-1.0)*A12/DETF0
      VF0(2,1)=(-1.0)*A21/DETF0
      VF0(2,2)=A11/DETF0
```

!VELOCITY GRADIENT

VGRD(1,1)=DDFGRD0(1,1)*VF0(1,1)+DDFGRD0(1,2)*VF0(2,1)

VGRD(1,2)=DDFGRD0(1,1)*VF0(1,2)+DDFGRD0(1,2)*VF0(2,2)

VGRD(2,1)=DDFGRD0(2,1)*VF0(1,1)+DDFGRD0(2,2)*VF0(2,1)

VGRD(2,2)=DDFGRD0(2,1)*VF0(1,2)+DDFGRD0(2,2)*VF0(2,2)

!SYMMETRIC PART OF VELOCITY GRADIENT

!TO OBTAIN STRAIN RATE(D_EPS) USED IN ACTIVE STRESS
INTEGRATION

DVGRD(1,1)=VGRD(1,1)

DVGRD(2,2)=VGRD(2,2)

DVGRD(1,2)=(VGRD(1,2)+VGRD(2,1))/TWO

DVGRD(2,1)=DVGRD(1,2)

!GREEN STRAIN

GS0(1,1)=ONE/TWO*(A11*A11+A21*A21-ONE)

GS0(1,2)=ONE/TWO*(A11*A12+A21*A22)

GS0(2,1)=GS0(1,2)

GS0(2,2)=ONE/TWO*(A12*A12+A22*A22-ONE)

GS1(1,1)=ONE/TWO*(B11*B11+B21*B21-ONE)

GS1(1,2)=ONE/TWO*(B11*B12+B21*B22)

GS1(2,1)=GS1(1,2)

GS1(2,2)=ONE/TWO*(B12*B12+B22*B22-ONE)

```fortran
EKK0=GS0(1,1)+GS0(2,2)

EKK1=GS1(1,1)+GS1(2,2)

DELTA(1,1)=ONE

DELTA(2,2)=ONE

DELTA(1,2)=ZERO

DELTA(2,1)=ZERO


DO I=1,2

  DO J=1,2

    DO M=1,2

      DO N=1,2

      !PASSIVE STRESS AT THE BEGINNING OF THE TIME INCREMENT

      PAVSTRESS0(I,J)=PAVSTRESS0(I,J)+(ALAM1*EKK0*DELTA(M,N)+

1     ALAM2*GS0(M,N))*DFGRD0(I,M)*DFGRD0(J,N)/DETF0

      END DO

    END DO

  END DO

END DO


DO I=1,2

  DO J=1,2

    DO M=1,2

      DO N=1,2

      !PASSIVE STRESS AT THE END OF THE TIME INCREMENT
```

```fortran
      PAVSTRESS1(I,J)=PAVSTRESS1(I,J)+(ALAM1*EKK1*DELTA(M,N)
    1     +ALAM2*GS1(M,N))*DFGRD1(I,M)*DFGRD1(J,N)/DETF1
        END DO
       END DO
      END DO
     END DO


     !INCREMENT OF PASSIVE STRESS

     DPSTRESS(1)=PAVSTRESS1(1,1)-PAVSTRESS0(1,1)

     DPSTRESS(2)=PAVSTRESS1(2,2)-PAVSTRESS0(2,2)

     DPSTRESS(3)=PAVSTRESS1(1,2)-PAVSTRESS0(1,2)


********STRESS INCREMENTS CALCULATED BY DSTRAN********************
     DDS(1,1)=E/(ONE-ANU**TWO)

     DDS(2,2)=E/(ONE-ANU**TWO)

     DDS(3,3)=E/TWO/(ONE+ANU)

     DDS(1,2)=E*ANU/(ONE-ANU**TWO)

     DDS(1,3)=ZERO

     DDS(2,3)=ZERO

     DDS(2,1)=E*ANU/(ONE-ANU**TWO)

     DDS(3,1)=ZERO

     DDS(3,2)=ZERO


C************** INTEGRATION OF THE ACTIVE STRESS ************
     !36 INTERVALS TO INTEGRATE THE INTEGRATION POINT
```

```
      ANG=PI/36.0  !ANGLE INCREMENT

      DO K=1,37

        PHI(K)=PI/TWO*(-1.0)+(K-1)*ANG

      END DO


      IF (KINC.LE.1) THEN

        DO K=1,37

          PHIS(K) = PHI(K)+1./4.*(DFGRD1(2,1)-DFGRD0(2,1)-DFGRD1(1,2)
     $    +DFGRD0(1,2))

          STATEV(74+K) = PHIS(K)

        END DO

       ELSE

        DO K=1,37

          PHIS(K) = STATEV(74+K)+1./4.*(DFGRD1(2,1)-DFGRD0(2,1)-
     $    DFGRD1(1,2)+DFGRD0(1,2))

          STATEV(74+K) = PHIS(K)

        END DO

       END IF


      !METHODS TO CALCULATE STRAIN RATE: BY VELOCITY GRADIENT

c      D_EPS11=DVGRD(1,1) !STRAIN RATE COMPONENTS

c      D_EPS22=DVGRD(2,2)

c      D_EPS12=DVGRD(1,2)

      !DSTRAN HAS THE SAME VALUE AS (DVGRD*DTIME)

      D_EPS11=DSTRAN(1)/DTIME  !STRAIN RATE COMPONENTS
```

```
      D_EPS22=DSTRAN(2)/DTIME

      D_EPS12=DSTRAN(3)/TWO/DTIME


   DO I=1,37

     !STRAIN RATE AT ANGLE PHI

     D_EPS=D_EPS11*((COS(PHIS(I)))**TWO)+D_EPS22*
   1  ((SIN(PHIS(I)))**TWO)+D_EPS12*SIN(TWO*PHIS(I))


     STNR=D_EPS/D_EPS0  !INDICATOR TO DETERMINE HILL LIKE RELATION

     ETA_S(I)=STATEV(I)   !STRESS FIBRE CONCENTRATION


CC     FIFTH ORDER RUNGE KUTTA CALCULATE ETA IN NEXT INCREMENT

     H=DTIME

     ETAIN=ETA_S(I)

     ETK=(-1.0)*ETAIN/RKV

     TIMEIN=TIME(2)


     !K(1)

     IF (STNR.LT.ETK) THEN

       IF (KINC.LE.1) THEN

         RSX=ZERO  !CUZ ETA=ZERO AT TIME=0

       ELSE

         RSX=(ONE+RKV/ETAIN*STNR)/CLAMBDA

       END IF

       RKETA(1)=(ONE-ETAIN)*RKF/THETA*EXP(-ONE*TIMEIN/THETA)-
```

140

```
 1    ETAIN*RKB/THETA

    ELSE IF (STNR.GT.ZERO) THEN

     IF (KINC.LE.1) THEN

       RSX=ZERO

     ELSE

       RSX=ONE+RKV/ETAIN*STNR/CLAMBDA

     END IF

     RKETA(1)=(ONE-ETAIN)*RKF/THETA*EXP(-ONE*TIMEIN/THETA)

    ELSE

     IF (KINC.LE.1) THEN

       RSX=ZERO

     ELSE

       RSX=ONE+RKV/ETAIN*STNR

     END IF

     RKETA(1)=(ONE-ETAIN)*RKF/THETA*EXP(-ONE*TIMEIN/THETA)-

 1    (ONE-RSX)*ETAIN*RKB/THETA

    END IF


    !K(2)

    TIMEIN=TIME(2)+1.0/2.0*H

    ETAIN=ETA_S(I)+1.0/2.0*RKETA(1)

    ETK=(-ONE)*ETAIN/RKV


    IF (STNR.LT.ETK) THEN

     RSX=(ONE+RKV/ETAIN*STNR)/CLAMBDA
```

```fortran
      RKETA(2)=(ONE-ETAIN)*RKF/THETA*EXP(-ONE*TIMEIN/THETA)-
1    ETAIN*RKB/THETA
      ELSE IF (STNR.GT.ZERO) THEN
       RSX=ONE+RKV/ETAIN*STNR/CLAMBDA
       RKETA(2)=(ONE-ETAIN)*RKF/THETA*EXP(-ONE*TIMEIN/THETA)
      ELSE
       RSX=ONE+RKV/ETAIN*STNR
       RKETA(2)=(ONE-ETAIN)*RKF/THETA*EXP(-ONE*TIMEIN/THETA)-
1    (ONE-RSX)*ETAIN*RKB/THETA
      END IF

      !K(3)
      TIMEIN=TIME(2)+1.0/2.0*H
      ETAIN=ETA_S(I)+1.0/2.0*RKETA(2)
      ETK=(-ONE)*ETAIN/RKV
      IF (STNR.LT.ETK) THEN
       RSX=(ONE+RKV/ETAIN*STNR)/CLAMBDA
       RKETA(3)=(ONE-ETAIN)*RKF/THETA*EXP(-ONE*TIMEIN/THETA)-
1    ETAIN*RKB/THETA
      ELSE IF (STNR.GT.ZERO) THEN
       RSX=ONE+RKV/ETAIN*STNR/CLAMBDA
       RKETA(3)=(ONE-ETAIN)*RKF/THETA*EXP(-ONE*TIMEIN/THETA)
      ELSE
       RSX=ONE+RKV/ETAIN*STNR
       RKETA(3)=(ONE-ETAIN)*RKF/THETA*EXP(-ONE*TIMEIN/THETA)-
```

```
1   (ONE-RSX)*ETAIN*RKB/THETA

    END IF


    !K(4)

    TIMEIN=TIME(2)+H

    ETAIN=ETA_S(I)+RKETA(3)

    ETK=(-ONE)*ETAIN/RKV

    IF (STNR.LT.ETK) THEN

      RSX=(ONE+RKV/ETAIN*STNR)/CLAMBDA

      RKETA(4)=(ONE-ETAIN)*RKF/THETA*EXP(-ONE*TIMEIN/THETA)-
1     ETAIN*RKB/THETA

    ELSE IF (STNR.GT.ZERO) THEN

      RSX=ONE+RKV/ETAIN*STNR/CLAMBDA

      RKETA(4)=(ONE-ETAIN)*RKF/THETA*EXP(-ONE*TIMEIN/THETA)

    ELSE

      RSX=ONE+RKV/ETAIN*STNR

      RKETA(4)=(ONE-ETAIN)*RKF/THETA*EXP(-ONE*TIMEIN/THETA)-
1     (ONE-RSX)*ETAIN*RKB/THETA

    END IF


    ETA_E(I)=ETA_S(I)+H/6.0*(RKETA(1)+TWO*RKETA(2)+TWO*
1   RKETA(3)+RKETA(4))

    STATEV(I)=ETA_E(I) !UPDATE THE ETA AT ANGLE PHIS


    !CALCULATE THE STRESS AND STRESS INCREMENT FOR EACH FIBER
```

```fortran
      !STORE DATA IN STATE VARIABLES AND PASS TO NEXT TIME STEP

      ETK=(-ONE)*ETA_E(I)/RKV

      IF (STNR.LT.ETK) THEN

       SIGMA_E(I)=(ETA_E(I)+RKV*STNR)/CLAMBDA*SX

       STATEV(I+37)=SIGMA_E(I)

      ELSE IF (STNR.GT.ZERO) THEN

       SIGMA_E(I)=(ETA_E(I)+RKV/CLAMBDA*STNR)*SX

       STATEV(I+37)=SIGMA_E(I)

      ELSE

       SIGMA_E(I)=(ETA_E(I)+RKV*STNR)*SX

       STATEV(I+37)=SIGMA_E(I)

      END IF

     END DO  !END OF LOOP
C*********************************************************************



C******CALCULATE THE AVERAGE VALUE OF ETA (TRAPEZOIDAL
INTEGRATION)*****

     ETA_AVG=(ETA_E(1)+ETA_E(37))*ANG/TWO/PI

     DO I=2,36

      ETA_AVG=ETA_AVG+ETA_E(I)*ANG/PI

     END DO

     STATEV(112)=ETA_AVG

     STATEV(114) = ONE-ETA_AVG/MAXVAL(ETA_E)
C******TRAPEZOIDAL METHOD TO CALCULATE ACTIVE STRESS INCREMENT
********

     DO I=1,36
```

```fortran
      !ACTIVE STRESS COMPONENTS AT THE END OF INCREMENT
       TSIGMA11=TSIGMA11+(SIGMA_E(I)*((COS(PHIS(I)))**TWO)+
     1  SIGMA_E(I+1)*((COS(PHIS(I+1)))**TWO))*ANG/TWO/PI
       TSIGMA22=TSIGMA22+(SIGMA_E(I)*((SIN(PHIS(I)))**TWO)+
     2  SIGMA_E(I+1)*((SIN(PHIS(I+1)))**TWO))*ANG/TWO/PI
       TSIGMA12=TSIGMA12+(SIGMA_E(I)*SIN(TWO*PHIS(I))+SIGMA_E(I+1)*
     3  SIN(TWO*PHIS(I+1)))*ANG/TWO/PI/TWO
      END DO

      !ACTIVE STRESS INCREMENT FOR STRESS COMPONENTS
      SIGMA11 = TSIGMA11-STATEV(115)
      SIGMA22 = TSIGMA22-STATEV(116)
      SIGMA12 = TSIGMA12-STATEV(117)
      !STORE THE ACTIVE STRESS
      STATEV(115)=TSIGMA11
      STATEV(116)=TSIGMA22
      STATEV(117)=TSIGMA12

      !ACTIVE PRINCIPAL STRESS DIRECTION
      PTHETA=0.5*ATAN(TWO*TSIGMA12/(TSIGMA11-TSIGMA22))
      PCSTRESS=MAX((TSIGMA11+TSIGMA22)/TWO+SQRT(((TSIGMA11-
     TSIGMA22)
     1 /TWO)**TWO+TSIGMA12**TWO),(TSIGMA11+TSIGMA22)/TWO-
     SQRT(((TSIGMA11
     2 -TSIGMA22)/TWO)**TWO+TSIGMA12**TWO))   !ACTIVE PRINCIPAL STRESS
```

```fortran
      STATEV(113)=PCSTRESS/SX


C****** CALCULATE THE TOTAL STRESS ***************************


      !TOTAL STRESS

      STRESS(1)=PAVSTRESS1(1,1)+TSIGMA11

      STRESS(2)=PAVSTRESS1(2,2)+TSIGMA22

      STRESS(3)=PAVSTRESS1(1,2)+TSIGMA12


      STRESSINC(1) = DPSTRESS(1)+SIGMA11

      STRESSINC(2) = DPSTRESS(2)+SIGMA22

      STRESSINC(3) = DPSTRESS(3)+SIGMA12


C****** UPDATE JACOBIAN MATRIX *********************************

      !ACTIVE JACOBIAN CALCULATION

      !THE CALCULATION OF PARA1 AND PARA2 REFERS TO DERIVATIONS IN
THE WORD FILE.

      PARA1=TWO*RKV*SX/CLAMBDA/D_EPS0/DTIME

      CS=EXP(-ONE*(TIME(2)+DTIME/TWO)/THETA)

      PARA2=(ONE+RKB/(TWO*THETA/DTIME+RKF*CS))*
    1 TWO*SX*RKV/D_EPS0/DTIME


      !MUST INITIALIZE THE VARS

      DO I=1,NTENS

       DO J=1,NTENS
```

146

```fortran
      DDSDDE(I,J)=ZERO

       DDE(I,J)=ZERO

     END DO

    END DO


    !CALCULATE THE FIBRE JACOBIAN AT EACH ANGLE.
    DO I=1,37
     D_EPS=D_EPS11*((COS(PHIS(I)))**TWO)+D_EPS22*
 &   ((SIN(PHIS(I)))**TWO)+D_EPS12*SIN(TWO*PHIS(I))
     STNR=D_EPS/D_EPS0
     IF ((STNR.LT.(-1.0*ETA_S(I)/RKV)).OR.(STNR.GT.ZERO)) THEN
      FJ11(I)=PARA1/PI*((COS(PHIS(I)))**4.0)
      FJ12(I)=PARA1/PI*((COS(PHIS(I)))**2.0)*((SIN(PHIS(I)))**2.0)
      FJ13(I)=PARA1/PI*((COS(PHIS(I)))**3.0)*(SIN(PHIS(I)))
      FJ21(I)=PARA1/PI*((SIN(PHIS(I)))**2.0)*((COS(PHIS(I)))**2.0)
      FJ22(I)=PARA1/PI*((SIN(PHIS(I)))**4.0)
      FJ23(I)=PARA1/PI*((SIN(PHIS(I)))**3)*(COS(PHIS(I)))
      FJ31(I)=PARA1/PI*((COS(PHIS(I)))**3.0)*(SIN(PHIS(I)))
      FJ32(I)=PARA1/PI*((SIN(PHIS(I)))**3)*(COS(PHIS(I)))
      FJ33(I)=PARA1/PI*((COS(PHIS(I)))**2.0)*((SIN(PHIS(I)))**2.0)
     ELSE
      FJ11(I)=PARA2/PI*((COS(PHIS(I)))**4.0)
      FJ12(I)=PARA2/PI*((COS(PHIS(I)))**2.0)*((SIN(PHIS(I)))**2.0)
      FJ13(I)=PARA2/PI*((COS(PHIS(I)))**3.0)*(SIN(PHIS(I)))
      FJ21(I)=PARA2/PI*((SIN(PHIS(I)))**2.0)*((COS(PHIS(I)))**2.0)
```

147

```
FJ22(I)=PARA2/PI*((SIN(PHIS(I)))**4.0)

FJ23(I)=PARA2/PI*((SIN(PHIS(I)))**3)*(COS(PHIS(I)))

FJ31(I)=PARA2/PI*((COS(PHIS(I)))**3.0)*(SIN(PHIS(I)))

FJ32(I)=PARA2/PI*((SIN(PHIS(I)))**3)*(COS(PHIS(I)))

FJ33(I)=PARA2/PI*((COS(PHIS(I)))**2.0)*((SIN(PHIS(I)))**2.0)

END IF

END DO

!TRAPEZOIDAL METHOD TO ADD THE JACOBIAN CONTRIBUTIONS FROM

!EACH FIBRE.

DO I=1,36

DDE(1,1)=DDE(1,1)+HALF*ANG*(FJ11(I)+FJ11(I+1))

DDE(1,2)=DDE(1,2)+HALF*ANG*(FJ12(I)+FJ12(I+1))

DDE(1,3)=DDE(1,3)+HALF*ANG*(FJ13(I)+FJ13(I+1))

DDE(2,1)=DDE(2,1)+HALF*ANG*(FJ21(I)+FJ21(I+1))

DDE(2,2)=DDE(2,2)+HALF*ANG*(FJ22(I)+FJ22(I+1))

DDE(2,3)=DDE(2,3)+HALF*ANG*(FJ23(I)+FJ23(I+1))

DDE(3,1)=DDE(3,1)+HALF*ANG*(FJ31(I)+FJ31(I+1))

DDE(3,2)=DDE(3,2)+HALF*ANG*(FJ32(I)+FJ32(I+1))

DDE(3,3)=DDE(3,3)+HALF*ANG*(FJ33(I)+FJ33(I+1))

END DO

!TOTAL JACOBIAN MATRIX COMPRISES ACTIVE PART AND PASSIVE PART

DDSDDE(1,1)=DDS(1,1)+DDE(1,1)

DDSDDE(1,2)=DDS(1,2)+DDE(1,2)

DDSDDE(1,3)=DDS(1,3)+DDE(1,3)

DDSDDE(2,1)=DDS(2,1)+DDE(2,1)
```

```fortran
      DDSDDE(2,2)=DDS(2,2)+DDE(2,2)

      DDSDDE(2,3)=DDS(2,3)+DDE(2,3)

      DDSDDE(3,1)=DDS(3,1)+DDE(3,1)

      DDSDDE(3,2)=DDS(3,2)+DDE(3,2)

      DDSDDE(3,3)=DDS(3,3)+DDE(3,3)
C***************.DAT OUTPUT***************
      !BOTTOM LEFT AND BOTTOM RIGHT ELEMENT

      DO I=1,37

      IF (NPT.EQ.1) THEN

      ANGSFLV1(NOEL,I)=ETA_E(I)

      ELSEIF (NPT.EQ.2) THEN

      ANGSFLV2(NOEL,I)=ETA_E(I)

      ELSEIF (NPT.EQ.3) THEN

      ANGSFLV3(NOEL,I)=ETA_E(I)

      ELSEIF (NPT.EQ.4) THEN

      ANGSFLV4(NOEL,I)=ETA_E(I)

      END IF

      END DO


      RETURN

      END

***************************** END *********************************
```

Appendix B. Fortran User Interface (UINTER)

********************* INTERFACIAL BEHAVIOUR **************************

* RELATIVE DISPLACEMENTS ARE CALCULATED BY RDISP AND GLOBAL COORDINATES.

* STRESS CONVERTED INTO LOCAL COORDINATE.

* PASSED IN RELATIVE DISPLACEMENTS ARE DEFIEND IN LOCAL COORDINATES, BUT

* THEY ARE ASSUMED TO BE IN GLOBAL COORDINATES. SEE PPT FOR DETAIL.

```
      SUBROUTINE
UINTER(STRESS,DDSDDR,DVISCOUS,DSTRUCTURAL,FLUX,DDFDDT,
   1 DDSDDT,DDFDDR,STATEV,SED,SFD,SPD,SVD,SCD,PNEWDT,RDISP,
   2 DRDISP,
   3 TEMP,DTEMP,PREDEF,DPRED,TIME,DTIME,FREQR,CINAME,SLNAME,
   4 MSNAME,
   5
PROPS,COORDS,ALOCALDIR,DROT,AREA,CHRLNGTH,NODE,NDIR,NSTATV,
   6 NPRED,NPROPS,MCRD,KSTEP,KINC,KIT,LINPER,LOPENCLOSE,LSTATE,
   7 LSDI,LPRINT)
C
      INCLUDE 'ABA_PARAM.INC'
C
*================= DEFINITIONS OF PARAMETERS
=========================
*- UNITS: mm, Newton, MPa, SECOND, TONNE, mJ, Kelvin
*- TP: TEMPERATURE.
*- RKSI_0: TOTAL INTEGRIN DENSITY AT TIME=0.
```

*- CKS: INTEGRIN-LIGAND BOND STIFFNESS.

*- DN: MAXIMUM STRETCH OF INTEGRIN-LIGAND BOND.

*- BKZ: BOLTZMANN CONSTANT.

*- RAT_DENS: RATIO OF LOW AFFINITY INTEGRIN DENSITY TO HIGH AFFINITY

*   INTEGRIN DENSITY AT TIME=0.

*- RKSIH_MAT: HIGH AFFINITY INTEGRIN DENSITY MATRIX.

*- COORDS_MAT: COORDINATES OF ALL THE NODES AT CURRENT TIME.

*- NNODE: USED IN WRITING OUTPUT ONLY.

*- RDISP: AN ARRAY CONTAINING THE CURRENT RELATIVE POSITIONS BETWEEN

*   THE TWO SURFACES AT THE END OF THE INCREMENT.

*- DRDISP: AN ARRAY CONTAINING THE INCREMENTS IN RELATIVE

*   POSITIONS BETWEEN THE TWO SURFACES.

*- STATEV: 1:HIGH AFFINITY INTEGRIN DENSITY;2~3: X,Y END POINTS COORDS OF

* DISPLACEMENT VECTOR; 4~5: DISPLACEMENT VECTOR OF CURRENT NODE;

*==
=======

     CHARACTER*80 CINAME,SLNAME,MSNAME,ASIGN

     DIMENSION STRESS(NDIR),DDSDDR(NDIR,NDIR),FLUX(2),DDFDDT(2,2),

   $ DDSDDT(NDIR,2),DDFDDR(2,NDIR),STATEV(NSTATV),

   $ RDISP(NDIR),DRDISP(NDIR),TEMP(2),DTEMP(2),PREDEF(2,NPRED),

   $ DPRED(2,NPRED),TIME(2),PROPS(NPROPS),COORDS(MCRD),

151

```fortran
     $ ALOCALDIR(3,3),DROT(2,2),DVISCOUS(NDIR,NDIR),F(2),D(2),

     $ DSTRUCTURAL(NDIR,NDIR),

     $ DELTA(2,2),PART1(2,2),PART2(2,2),UD(2)


c~      !CHECK THE NODE NUMBER OF THE CELL PART

      PARAMETER (ZERO=0.D0, ONE=1.D0,
TWO=2.D0,HALF=0.5D0,THREE=3.D0,

    1 TP=310.D0,RKSI_0=1.D9,CKS=1.5D-8,DN=1.3D-4,TOLE=1.D30,

    2 BKZ=1.3806485D-20,RAT_DENS=150.D0,NODENUM=5041,P0=5.D-11,

    & DP=1.3D-4,DLT0=1.3D-8)



      DIMENSION RKSIH_MAT(NODENUM,4)

      COMMON/INTEGRINS/RKSIH_MAT



*========================= INITIALIZATION
===========================



      DELTA(1,1)=ONE

      DELTA(2,2)=ONE

      DELTA(1,2)=ZERO

      DELTA(2,1)=ZERO


      COS11 = ALOCALDIR(1,2)

      COS12 = ALOCALDIR(2,2)

      COS21 = ALOCALDIR(1,3)

      COS22 = ALOCALDIR(2,3)
```

152

```fortran
      !DIFFERENCE IN CHEMICAL POTENTIAL DCHEM=KAI_H-KAI_L

      DCHEM = 5.0*BKZ*TP

      ENERGY0 = CKS*(DN**TWO)
*---------------------- DEFINITIONS OF SIGNS --------------------------
* THE SURFACES HAVE THREE CONTACT SITUATIONS: CONTACT,
TRANSITION AND
* NON-CONTACT.
* IN CONTACT MODE, ONE SURFACE KEEPS SLIDING RELATIVE TO THE
OTHER
* SURFACE. THE INTEGRINS ARE STRETCHED OR SLIDING.
* IN TRANSITION STATE, THE INTEGRINS ARE STRETCHED TO THE LIMIT OF
2*DN.
* IN NON-CONTACT STATE, THE SURFACES DO NOT CONTACT.
*-  SGNSURF = 0: NON-CONTACT
*-  SGNSURF = 1: CONTACT WITH MASTER SURFACE
*-  ASIGN = 'CONTACT'. SURFACE CONTACT OR SLIDING
*-  ASIGN = 'TRANSFORM'. CONTACT TRANSFORMED INTO NON-CONTACT
*-  ASIGN = 'NONCONTACT'. STAY IN NON-CONTACT.
*-----------------------------------------------------------------------


      IF (ABS(RDISP(1)).LT.TOLE) THEN !CONTACT IN CURRENT KINC

         TDISP = SQRT(RDISP(1)**TWO+RDISP(2)**TWO+RDISP(3)**TWO)

         BL=DN+DLT0

         ESTH = TDISP-DLT0

         IF (ESTH.LT.ZERO) THEN
```

!Force in the bond

FF = ZERO

!Bound high affinity integrin density

RKSI_H = ZERO

!Calculate passive normal traction

FNM = P0/(DP**TWO)*RDISP(1)*EXP(-RDISP(1)/DP)

!Calculate shear and normal FA forces

FTNM = ZERO !Normal FA force

F(1) = ZERO

F(2) = ZERO

!Calculate total tractions

STRESS(1) = FNM

STRESS(2) = ZERO

STRESS(3) = ZERO

RKSI_H=ZERO

!Update Jacobian

HD1=RDISP(1)-HALF*DRDISP(1)

DDSDDR(1,1)=P0/(DP**TWO)*(ONE-HD1/DP)*EXP(-HD1/DP)

DDSDDR(1,2)=ZERO

DDSDDR(1,3)=ZERO

DDSDDR(2,1)=ZERO

DDSDDR(2,2)=ZERO

DDSDDR(2,3)=ZERO

```fortran
      DDSDDR(3,1)=ZERO

      DDSDDR(3,2)=ZERO

      DDSDDR(3,3)=ZERO


      STATEV(2) = COORDS(1)  !CURRENT COORDS

      STATEV(3) = COORDS(2)

      STATEV(4) = RDISP(1)   !STORE CURRENT VECTOR

      STATEV(5) = ZERO

      STATEV(6) = ZERO


      ELSEIF ((ESTH.LT.DN).AND.(ESTH.GE.ZERO)) THEN

!========== Stretch until length reaches peak length ==========

!Effective stretch

      DE = ESTH

!Energy in the bond

      ENERGY = HALF*CKS*(DE**TWO)

!Force in the bond

      FF = CKS*DE

!Bound high affinity integrin density

      RKSI_H = RKSI_0/(EXP((DCHEM+ENERGY-CKS*(DE**TWO))/BKZ/
     $   TP)+ONE)

!Calculate passive normal traction

      FNM = P0/(DP**TWO)*RDISP(1)*EXP(-RDISP(1)/DP)

!Calculate shear and normal FA forces

      FTNM = (RDISP(1)/TDISP)*FF  !Normal force
```

F(1) = RDISP(2)/TDISP*FF !Tangential force

F(2) = RDISP(3)/TDISP*FF

!Calculate total tractions

STRESS(1) = FNM+FTNM*RKSI_H

STRESS(2) = F(1)*RKSI_H

STRESS(3) = F(2)*RKSI_H

!Update Jacobian

TIMEIN=TIME(1)+HALF*DTIME

HD1=RDISP(1)-HALF*DRDISP(1)

HD2=RDISP(2)-HALF*DRDISP(2)

HD3=RDISP(3)-HALF*DRDISP(3)

DTOT=SQRT(HD1**TWO+HD2**TWO+HD3**TWO)

Q = EXP((DCHEM-HALF*CKS*((DTOT-DLT0)**TWO))/BKZ/TP)

DDSDDR(1,1)=P0/(DP**TWO)*(ONE-HD1/DP)*EXP(-HD1/DP)+CKS*

&   RKSI_0/(Q+ONE)*(ONE-DLT0*(HD2**TWO+HD3**TWO)/(DTOT**THREE))+

&   ((HD1*CKS*(DTOT-DLT0)/DTOT/(Q+ONE))**TWO)*RKSI_0*Q/BKZ/TP

DDSDDR(1,2)=CKS*DLT0*HD1*HD2*RKSI_0/(DTOT**THREE)/(Q+ONE)+

&   ((CKS*(DTOT-DLT0)/DTOT/(Q+ONE))**TWO)*RKSI_0*Q*HD1*HD2/BKZ/TP

DDSDDR(1,3)=CKS*DLT0*HD1*HD3*RKSI_0/(DTOT**THREE)/(Q+ONE)+

&   ((CKS*(DTOT-DLT0)/DTOT/(Q+ONE))**TWO)*RKSI_0*Q*HD1*HD3/BKZ/TP

DDSDDR(2,1)=DDSDDR(1,2)

DDSDDR(2,2)=CKS*RKSI_0/(Q+ONE)*(ONE-DLT0/DTOT+DLT0*

&   (HD2**TWO)/(DTOT**THREE))+((CKS*(DTOT-DLT0)/DTOT/(Q+ONE))

&   **TWO)*RKSI_0*Q*(HD2**TWO)/BKZ/TP

DDSDDR(2,3)=CKS*HD3*HD2*DLT0*RKSI_0/(DTOT**THREE)/(Q+ONE)+((

156

```fortran
     &    CKS*(DTOT-DLT0)/DTOT/(Q+ONE))**TWO)*RKSI_0*Q*HD2*HD3/BKZ/TP

      DDSDDR(3,1)=DDSDDR(1,3)

      DDSDDR(3,2)=DDSDDR(2,3)

      DDSDDR(3,3)=CKS*RKSI_0/(Q+ONE)*(ONE-
     DLT0/DTOT+DLT0*(HD3**TWO)

     &    /(DTOT**THREE))+((CKS*(DTOT-DLT0)/DTOT/(Q+ONE))**TWO)

     &    *RKSI_0*Q*(HD3**TWO)/BKZ/TP


      STATEV(2) = COORDS(1)   !CURRENT COORDS

      STATEV(3) = COORDS(2)

      STATEV(4) = RDISP(1)   !CURRETN VECTOR

      STATEV(5) = RDISP(2)

      STATEV(6) = RDISP(3)  !CURRENT NORMAL VECTOR


      ELSEIF ((ESTH.GE.DN).AND.(ABS(RDISP(1)).LE.BL)) THEN

!========== Sliding until bond perpendicular to the substrate while

!maintaining effective stretch value DN. ==========

!Effective stretch

      DE = DN

!Energy in the bond

      ENERGY = HALF*CKS*(DN**TWO)

!Force in the bond

      FF = CKS*DE

!Bound high affinity integrin density

      RKSI_H = RKSI_0/(EXP((DCHEM+ENERGY-CKS*(DN**TWO))/BKZ/TP)
```

```
$    +ONE)

     !Calculate passive normal traction

     FNM = P0/(DP**TWO)*RDISP(1)*EXP(-RDISP(1)/DP)

     !Calculate shear and normal FA forces

     FTNM = (RDISP(1)/(DN+DLT0))*FF  !Normal force

     TTF = SQRT(FF**TWO-FTNM**TWO)

     UD(1) = STATEV(5)+DRDISP(2)

     UD(2) = STATEV(6)+DRDISP(3)

     F(1) = (UD(1)/SQRT(UD(1)**TWO+UD(2)**TWO))*TTF

     F(2) = (UD(2)/SQRT(UD(1)**TWO+UD(2)**TWO))*TTF


     !Calculate total tractions

     STRESS(1) = FNM+FTNM*RKSI_H

     STRESS(2) = F(1)*RKSI_H

     STRESS(3) = F(2)*RKSI_H


     !Update Jacobian

     TIMEIN=TIME(1)+HALF*DTIME

     HD1=RDISP(1)-HALF*DRDISP(1)

     HD2=RDISP(2)-HALF*DRDISP(2)

     HD3=RDISP(3)-HALF*DRDISP(3)


     Q = EXP((DCHEM-HALF*CKS*(DN**TWO))/BKZ/TP)


     DDSDDR(1,1)=P0/(DP**TWO)*(ONE-HD1/DP)*EXP(-HD1/DP)+CKS*DN/
```

```fortran
     &    (DN+DLT0)*RKSI_0/(Q+ONE)

          DDSDDR(1,2)=ZERO

          DDSDDR(1,3)=ZERO

          DDSDDR(2,1)=-CKS*DN*HD2/SQRT(HD2**TWO+HD3**TWO)*HD1/((DN
     &    +DLT0)**TWO)/SQRT(ONE-(HD1/(DN+DLT0))**TWO)*RKSI_0/(Q+ONE)

          DDSDDR(2,2)=CKS*DN*SQRT(ONE-(HD1/(DN+DLT0))**TWO)*(HD3**TWO)
     &    /((HD2**TWO+HD3**TWO)**(HALF*THREE))

          DDSDDR(2,3)=CKS*DN*SQRT(ONE-(HD1/(DN+DLT0))**TWO)*(-HD2*HD3)
     &    /((HD2**TWO+HD3**TWO)**(HALF*THREE))

          DDSDDR(3,1)=-CKS*DN*HD3*SQRT(HD2**TWO+HD3**TWO)*HD1/((DN
     &    +DLT0)**TWO)/SQRT(ONE-(HD1/(DN+DLT0))**TWO)*RKSI_0/(Q+ONE)

          DDSDDR(3,2)=CKS*DN*SQRT(ONE-(HD1/(DN+DLT0))**TWO)*(-HD2*HD3)
     &    /((HD2**TWO+HD3**TWO)**(HALF*THREE))

          DDSDDR(3,3)=CKS*DN*SQRT(ONE-(HD1/(DN+DLT0))**TWO)*(HD2**TWO)
     &    /((HD2**TWO+HD3**TWO)**(HALF*THREE))


          STATEV(2) = COORDS(1)  !COORDS

          STATEV(3) = COORDS(2)

          STATEV(4) = RDISP(1)   !CURRENT VECTOR

          STATEV(5) = RDISP(2)

          STATEV(6) = RDISP(3)


          ELSEIF ((ESTH.GE.DN).AND.(ABS(RDISP(1)).GT.BL))THEN

!========== Stretch beyond peak length ==========

!Sliding and perpendicular to the substrate
```

IF (ESTH.LE.(TWO*DN)) THEN

!the bond maintains perpendicular to the substrate and slipping

!Effective stretch

DE = ABS(RDISP(1))-DLT0

!Energy in the bond

ENERGY = -CKS*(DN**TWO)+TWO*CKS*DN*DE-HALF*CKS*(DE**TWO)

!Force in the bond

FF = TWO*CKS*DN-CKS*DE

!Bound high affinity integrin density

RKSI_H = RKSI_0/(EXP((DCHEM+ENERGY-FF*DE)/BKZ/TP)+ONE)

!Calculate passive normal traction

FNM = P0/(DP**TWO)*RDISP(1)*EXP(-RDISP(1)/DP)

!Calculate shear and normal FA forces

FTNM = FF !Normal FA force

F(1) = ZERO

F(2) = ZERO

!Calculate total tractions

STRESS(1) = FNM+FTNM*RKSI_H

STRESS(2) = ZERO

STRESS(3) = ZERO

!Update Jacobian

TIMEIN=TIME(1)+HALF*DTIME

```fortran
      HD1=RDISP(1)-HALF*DRDISP(1)

      HD2=RDISP(2)-HALF*DRDISP(2)

      HD3=RDISP(3)-HALF*DRDISP(3)


      Q = EXP((DCHEM-CKS*DN**TWO+HALF*CKS*(HD1-DLT0))/BKZ/TP)


      DDSDDR(1,1)=P0/(DP**TWO)*(ONE-HD1/DP)*EXP(-HD1/DP)-CKS*
     &   RKSI_0/(Q+ONE)-(TWO*DN-HD1+DLT0)*((CKS/Q+ONE)**TWO)*RKSI_0*Q
     &   *(HD1-DLT0)/BKZ/TP
      DDSDDR(1,2)=ZERO

      DDSDDR(1,3)=ZERO

      DDSDDR(2,1)=ZERO

      DDSDDR(2,2)=ZERO

      DDSDDR(2,3)=ZERO

      DDSDDR(3,1)=ZERO

      DDSDDR(3,2)=ZERO

      DDSDDR(3,3)=ZERO


      STATEV(2) = COORDS(1)  !CURRENT COORDS

      STATEV(3) = COORDS(2)

      STATEV(4) = RDISP(1)   !Current vector

      STATEV(5) = RDISP(2)

      STATEV(6) = RDISP(3)


      ELSEIF ((ESTH.GT.(TWO*DN))) THEN
```

```fortran
!Force in the bond

FF = ZERO

!Bound high affinity integrin density

RKSI_H = ZERO

!Calculate passive normal traction

FNM = P0/(DP**TWO)*RDISP(1)*EXP(-RDISP(1)/DP)

!Calculate shear and normal FA forces

FTNM = ZERO  !Normal FA force

F(1) = ZERO

F(2) = ZERO


!Calculate total tractions

STRESS(1) = FNM+FTNM*RKSI_H

STRESS(2) = F(1)*RKSI_H

STRESS(3) = F(2)*RKSI_H

RKSI_H=ZERO


!Update Jacobian

HD1=RDISP(1)-HALF*DRDISP(1)

DDSDDR(1,1)=P0/(DP**TWO)*(ONE-HD1/DP)*EXP(-HD1/DP)

DDSDDR(1,2)=ZERO

DDSDDR(1,3)=ZERO

DDSDDR(2,1)=ZERO

DDSDDR(2,2)=ZERO

DDSDDR(2,3)=ZERO
```

```fortran
      DDSDDR(3,1)=ZERO

      DDSDDR(3,2)=ZERO

      DDSDDR(3,3)=ZERO


      STATEV(2) = COORDS(1)  !VECTOR ORIGIN

      STATEV(3) = COORDS(2)

      STATEV(4) = RDISP(1)   !CURRENT COORDS

      STATEV(5) = RDISP(2)

      STATEV(6) = RDISP(3)


      END IF

      END IF

      END IF
*------------------------- UPDATE VARIABLES --------------------------
      !RECORD INTEGRIN DENSITY AND NODES

      RKSIH_MAT(NODE,1) = NODE

      RKSIH_MAT(NODE,2) = RKSI_H/RKSI_0

      RKSIH_MAT(NODE,3) = COORDS(1)

      RKSIH_MAT(NODE,4) = COORDS(2)

      STATEV(1)=RKSI_H/RKSI_0

      RETURN

      END

****************************** END ********************************


*************** USER OUTPUT AT INTEGRATION POINTS *********************
```

```fortran
      SUBROUTINE UVARM(UVAR,DIRECT,T,TIME,DTIME,CMNAME,ORNAME,
     1 NUVARM,NOEL,NPT,LAYER,KSPT,KSTEP,KINC,NDI,NSHR,COORD,
     2 JMAC,JMATYP,MATLAYO,LACCFLA)
      INCLUDE 'ABA_PARAM.INC'
C
      CHARACTER*80 CMNAME,ORNAME
      CHARACTER*3 FLGRAY(120)
      DIMENSION UVAR(NUVARM),DIRECT(3,3),T(3,3),TIME(2)
      DIMENSION ARRAY(120),JARRAY(120),JMAC(*),JMATYP(*),COORD(*)
C
      CALL GETVRM('SDV',ARRAY,JARRAY,FLGRAY,JRCD,JMAC,JMATYP,
     1 MATLAYO,LACCFLA)
      UVAR(1)=ARRAY(112)   !AVERAGE OF ETA
      UVAR(2)=ARRAY(113) !ACTIVE PRINCIPAL STRESS
      UVAR(3)=ARRAY(114)   !FIBRE VARIANCE
      UVAR(4)=ARRAY(115)  !AS11
      UVAR(5)=ARRAY(116)   !AS22
      UVAR(6)=ARRAY(117)    !AS12
      RETURN
      END
```

***************************** END ********************************

Appendix C. Fortran User Element Output (UVARM)

*************** USER OUTPUT AT INTEGRATION POINTS **********************

```fortran
      SUBROUTINE UVARM(UVAR,DIRECT,T,TIME,DTIME,CMNAME,ORNAME,
     1 NUVARM,NOEL,NPT,LAYER,KSPT,KSTEP,KINC,NDI,NSHR,COORD,
     2 JMAC,JMATYP,MATLAYO,LACCFLA)
      INCLUDE 'ABA_PARAM.INC'
C
      CHARACTER*80 CMNAME,ORNAME
      CHARACTER*3 FLGRAY(120)
      DIMENSION UVAR(NUVARM),DIRECT(3,3),T(3,3),TIME(2)
      DIMENSION ARRAY(120),JARRAY(120),JMAC(*),JMATYP(*),COORD(*)
C
      CALL GETVRM('SDV',ARRAY,JARRAY,FLGRAY,JRCD,JMAC,JMATYP,
     1 MATLAYO,LACCFLA)

      UVAR(1)=ARRAY(112)   !AVERAGE OF ETA
      UVAR(2)=ARRAY(113) !ACTIVE PRINCIPAL STRESS
      UVAR(3)=ARRAY(114)   !FIBRE VARIANCE
      UVAR(4)=ARRAY(115)  !AS11
      UVAR(5)=ARRAY(116)   !AS22
      UVAR(6)=ARRAY(117)    !AS12

      RETURN
      END
```

*************************** END ********************************

Appendix D. Fortran User External Database (UEXTERNALDB)

*************************** EXTERNAL OUTPUT DATABASE ******************

```
      SUBROUTINE UEXTERNALDB(LOP,LRESTART,TIME,DTIME,KSTEP,KINC)
C

      INCLUDE 'ABA_PARAM.INC'

C

*================== USER SUBROUTINE INFORMATION

======================

* user coding to set up the FORTRAN environment, open files, close files,

* calculate user-defined model-independent history information,

* write history information to external files,

* recover history information during restart analyses, etc.

* do not include calls to utility routine XIT


*-The user subroutine is called once each at the beginning of the

* analysis, at the beginning of each increment, at the end of each

* increment, and at the end of the analysis (in addition, the user

* subroutine is also called once at the beginning of a restart analysis).


*-This subroutine can be used to open external files needed for other

* user subroutines at the beginning of the analysis and to close those

* files at the end of the analysis.


*-Can be used to calculate or read history information at the beginning

* of each increment. This information can be written to user-defined
```

* COMMON block variables or external files for use during the analysis

* by other user subroutines.

*-Can be used to write the current values of the user-calculated history

* information to external files.

*==
======

*============================ VARIABLES
============================

* LOP=2 indicates that the user subroutine is being called at the end

* of the current analysis increment.

*==
=======

```fortran
      CHARACTER*80 FNAME1,SFNAME1,SFNAME2,SFNAME3,SFNAME4

      CHARACTER*20 POSTFIX

      PARAMETER (NEL=4924,NODENUM=5041)


      DIMENSION ANGSFLV1(NEL,37),ANGSFLV2(NEL,37),

    & ANGSFLV3(NEL,37),ANGSFLV4(NEL,37)

      COMMON/SFDENSITY/ANGSFLV1,ANGSFLV2,ANGSFLV3,ANGSFLV4

      DIMENSION RKSIH_MAT(NODENUM,4)

      COMMON/INTEGRINS/RKSIH_MAT
C
      IF (LOP.EQ.2) THEN  !IN THE END OF CURRENT INCREMENT
```

```fortran
WRITE(6,*)'****EXTERNAL DB CALLED AT END OF INCREMENT*****'


!WRITE TO FILES

IF (MOD(KINC,100).EQ.0) THEN

IF (KSTEP.EQ.1) THEN


SELECT CASE(KINC)

!I1--------------------------------------------------

CASE(:9)

WRITE(POSTFIX,'(I1,A4)')KINC,'.txt'

FNAME1='E:\Abaqus Work\TK\TK5-INTEGRIN-DENSITY-'//POSTFIX

SFNAME1='E:\Abaqus Work\TK\TK5-ANGSFLV1-'//POSTFIX

SFNAME2='E:\Abaqus Work\TK\TK5-ANGSFLV2-'//POSTFIX

SFNAME3='E:\Abaqus Work\TK\TK5-ANGSFLV3-'//POSTFIX

SFNAME4='E:\Abaqus Work\TK\TK5-ANGSFLV4-'//POSTFIX


OPEN(UNIT=111,FILE=FNAME1)

OPEN(UNIT=112,FILE=SFNAME1)

OPEN(UNIT=113,FILE=SFNAME2)

OPEN(UNIT=114,FILE=SFNAME3)

OPEN(UNIT=115,FILE=SFNAME4)


!WRITE THE STRESS FIBRE DENSITY

DO I=1,NEL

DO J=1,37
```

```fortran
          WRITE(112,'(E25.15)')ANGSFLV1(I,J)

          WRITE(113,'(E25.15)')ANGSFLV2(I,J)

          WRITE(114,'(E25.15)')ANGSFLV3(I,J)

          WRITE(115,'(E25.15)')ANGSFLV4(I,J)

       END DO

       END DO


       !WRITE THE INTEGRIN DENSITY

       DO I=1,NODENUM

       WRITE(111,'(F8.1,E25.15,E25.15,E25.15)')RKSIH_MAT(I,1),
     & RKSIH_MAT(I,2),RKSIH_MAT(I,3),RKSIH_MAT(I,4)

       END DO


       !I2------------------------------------------------

       CASE(10:99)

       WRITE(POSTFIX,'(I2,A4)')KINC,'.txt'

       FNAME1='E:\Abaqus Work\TK\TK5-INTEGRIN-DENSITY-'//POSTFIX

       SFNAME1='E:\Abaqus Work\TK\TK5-ANGSFLV1-'//POSTFIX

       SFNAME2='E:\Abaqus Work\TK\TK5-ANGSFLV2-'//POSTFIX

       SFNAME3='E:\Abaqus Work\TK\TK5-ANGSFLV3-'//POSTFIX

       SFNAME4='E:\Abaqus Work\TK\TK5-ANGSFLV4-'//POSTFIX


       OPEN(UNIT=111,FILE=FNAME1)

       OPEN(UNIT=112,FILE=SFNAME1)

       OPEN(UNIT=113,FILE=SFNAME2)
```

```fortran
OPEN(UNIT=114,FILE=SFNAME3)

OPEN(UNIT=115,FILE=SFNAME4)


!WRITE THE STRESS FIBRE DENSITY

DO I=1,NEL

DO J=1,37

  WRITE(112,'(E25.15)')ANGSFLV1(I,J)

  WRITE(113,'(E25.15)')ANGSFLV2(I,J)

  WRITE(114,'(E25.15)')ANGSFLV3(I,J)

  WRITE(115,'(E25.15)')ANGSFLV4(I,J)

END DO

END DO


!WRITE THE INTEGRIN DENSITY

DO I=1,NODENUM

WRITE(111,'(F8.1,E25.15,E25.15,E25.15)')RKSIH_MAT(I,1),

& RKSIH_MAT(I,2),RKSIH_MAT(I,3),RKSIH_MAT(I,4)

END DO


!I3--------------------------------------------------

CASE(100:999)

WRITE(POSTFIX,'(I3,A4)')KINC,'.txt'

FNAME1='E:\Abaqus Work\TK\TK5-INTEGRIN-DENSITY-'//POSTFIX

SFNAME1='E:\Abaqus Work\TK\TK5-ANGSFLV1-'//POSTFIX

SFNAME2='E:\Abaqus Work\TK\TK5-ANGSFLV2-'//POSTFIX
```

170

```
SFNAME3='E:\Abaqus Work\TK\TK5-ANGSFLV3-'//POSTFIX

SFNAME4='E:\Abaqus Work\TK\TK5-ANGSFLV4-'//POSTFIX


OPEN(UNIT=111,FILE=FNAME1)

OPEN(UNIT=112,FILE=SFNAME1)

OPEN(UNIT=113,FILE=SFNAME2)

OPEN(UNIT=114,FILE=SFNAME3)

OPEN(UNIT=115,FILE=SFNAME4)


!WRITE THE STRESS FIBRE DENSITY

DO I=1,NEL

DO J=1,37

  WRITE(112,'(E25.15)')ANGSFLV1(I,J)

  WRITE(113,'(E25.15)')ANGSFLV2(I,J)

  WRITE(114,'(E25.15)')ANGSFLV3(I,J)

  WRITE(115,'(E25.15)')ANGSFLV4(I,J)

END DO

END DO


!WRITE THE INTEGRIN DENSITY

DO I=1,NODENUM

WRITE(111,'(F8.1,E25.15,E25.15,E25.15)')RKSIH_MAT(I,1),

& RKSIH_MAT(I,2),RKSIH_MAT(I,3),RKSIH_MAT(I,4)

END DO
```

```fortran
!I4-------------------------------------------------

CASE(1000:9999)

WRITE(POSTFIX,'(I4,A4)')KINC,'.txt'

FNAME1='E:\Abaqus Work\TK\TK5-INTEGRIN-DENSITY-'//POSTFIX

SFNAME1='E:\Abaqus Work\TK\TK5-ANGSFLV1-'//POSTFIX

SFNAME2='E:\Abaqus Work\TK\TK5-ANGSFLV2-'//POSTFIX

SFNAME3='E:\Abaqus Work\TK\TK5-ANGSFLV3-'//POSTFIX

SFNAME4='E:\Abaqus Work\TK\TK5-ANGSFLV4-'//POSTFIX


OPEN(UNIT=111,FILE=FNAME1)

OPEN(UNIT=112,FILE=SFNAME1)

OPEN(UNIT=113,FILE=SFNAME2)

OPEN(UNIT=114,FILE=SFNAME3)

OPEN(UNIT=115,FILE=SFNAME4)


!WRITE THE STRESS FIBRE DENSITY

DO I=1,NEL

DO J=1,37

  WRITE(112,'(E25.15)')ANGSFLV1(I,J)

  WRITE(113,'(E25.15)')ANGSFLV2(I,J)

  WRITE(114,'(E25.15)')ANGSFLV3(I,J)

  WRITE(115,'(E25.15)')ANGSFLV4(I,J)

END DO

END DO
```

```fortran
!WRITE THE INTEGRIN DENSITY

DO I=1,NODENUM

WRITE(111,'(F8.1,E25.15,E25.15,E25.15)')RKSIH_MAT(I,1),
& RKSIH_MAT(I,2),RKSIH_MAT(I,3),RKSIH_MAT(I,4)

END DO


!I5---------------------------------------------------

CASE(10000:99999)

WRITE(POSTFIX,'(I5,A4)')KINC,'.txt'

FNAME1='E:\Abaqus Work\TK\TK5-INTEGRIN-DENSITY-'//POSTFIX

SFNAME1='E:\Abaqus Work\TK\TK5-ANGSFLV1-'//POSTFIX

SFNAME2='E:\Abaqus Work\TK\TK5-ANGSFLV2-'//POSTFIX

SFNAME3='E:\Abaqus Work\TK\TK5-ANGSFLV3-'//POSTFIX

SFNAME4='E:\Abaqus Work\TK\TK5-ANGSFLV4-'//POSTFIX


OPEN(UNIT=111,FILE=FNAME1)

OPEN(UNIT=112,FILE=SFNAME1)

OPEN(UNIT=113,FILE=SFNAME2)

OPEN(UNIT=114,FILE=SFNAME3)

OPEN(UNIT=115,FILE=SFNAME4)


!WRITE THE STRESS FIBRE DENSITY

DO I=1,NEL

DO J=1,37

 WRITE(112,'(E25.15)')ANGSFLV1(I,J)
```

173

```fortran
    WRITE(113,'(E25.15)')ANGSFLV2(I,J)

    WRITE(114,'(E25.15)')ANGSFLV3(I,J)

    WRITE(115,'(E25.15)')ANGSFLV4(I,J)

  END DO

  END DO


  !WRITE THE INTEGRIN DENSITY

  DO I=1,NODENUM

  WRITE(111,'(F8.1,E25.15,E25.15,E25.15)')RKSIH_MAT(I,1),

& RKSIH_MAT(I,2),RKSIH_MAT(I,3),RKSIH_MAT(I,4)

  END DO


  END SELECT

  CLOSE(111)

  CLOSE(112)

  CLOSE(113)

  CLOSE(114)

  CLOSE(115)

  END IF

  END IF

  END IF


  RETURN

  END
```